ISSN 2408-2384 (ONLINE)

Environment and Natural Resources Journal

Volume 22 Number 2 March- April 2024

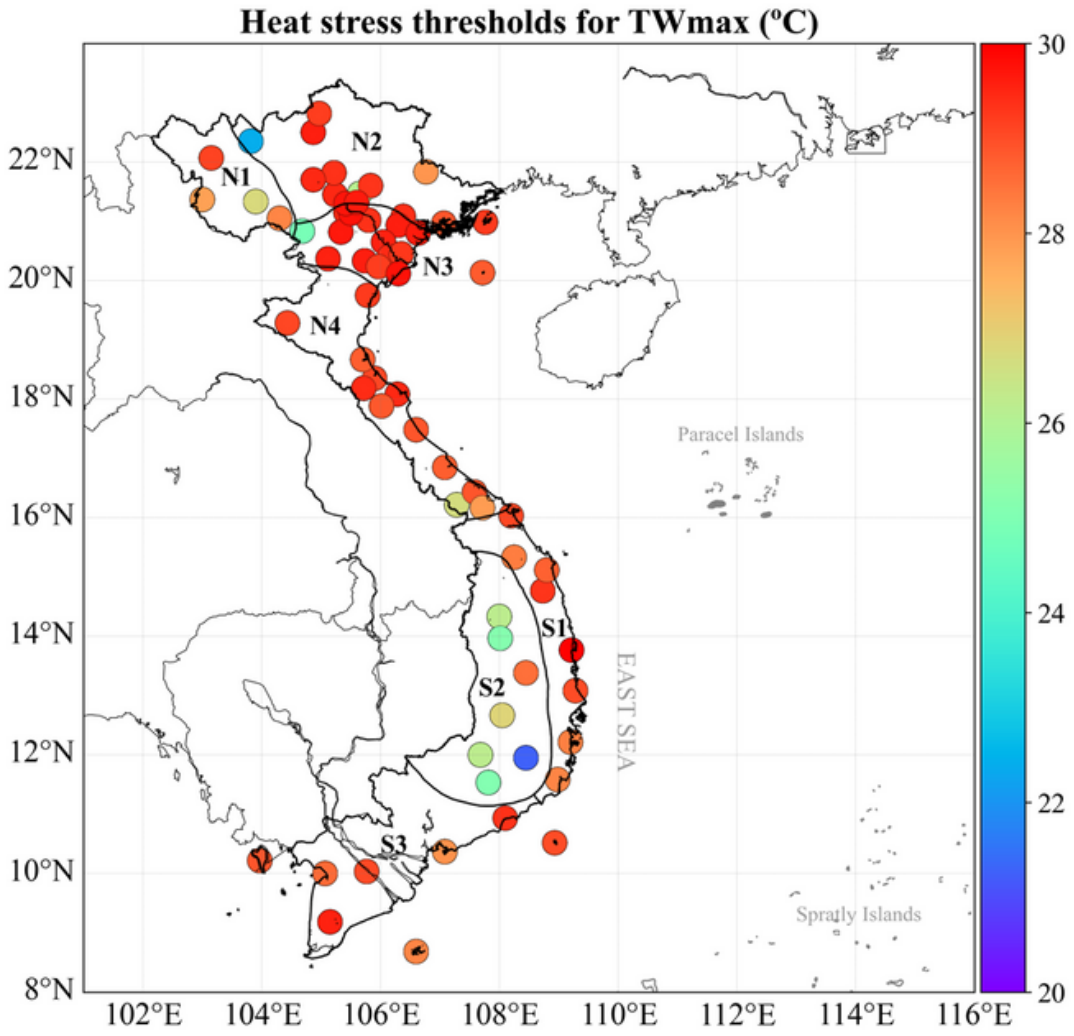

Heat stress thresholds at 68 station in Vietnam, identified as the 95th percentile value of daily TWmax for the period 1979-1998

Source: Vu N, Ngo-Duc T. Spatial Distribution and Trends of Heat Stress in Vietnam. Page 93-104.

Environment and Natural Resources Journal (EnNRJ)
Volume 22, Number 2, March - April 2024 ISSN: 2408-2384 (Online)

AIMS AND SCOPE

The Environment and Natural Resources Journal is a peer-reviewed journal, which provides insight scientific knowledge into the diverse dimensions of integrated environmental and natural resource management. The journal aims to provide a platform for exchange and distribution of the knowledge and cutting-edge research in the fields of environmental science and natural resource management to academicians, scientists and researchers. The journal accepts a varied array of manuscripts on all aspects of environmental science and natural resource management. The journal scope covers the integration of multidisciplinary sciences for prevention, control, treatment, environmental clean-up and restoration. The study of the existing or emerging problems of environment and natural resources in the region of Southeast Asia and the creation of novel knowledge and/or recommendations of mitigation measures for sustainable development policies are emphasized.

The subject areas are diverse, but specific topics of interest include:

- Biodiversity
- Climate change
- Detection and monitoring of polluted sources e.g., industry, mining
- Disaster e.g., forest fire, flooding, earthquake, tsunami, or tidal wave
- Ecological/Environmental modelling
- Emerging contaminants/hazardous wastes investigation and remediation
- Environmental dynamics e.g., coastal erosion, sea level rise
- Environmental assessment tools, policy and management e.g., GIS, remote sensing, Environmental Management System (EMS)
- Environmental pollution and other novel solutions to pollution
- Remediation technology of contaminated environments
- Transboundary pollution
- Waste and wastewater treatments and disposal technology

Schedule
Environment and Natural Resources Journal (EnNRJ) is published 6 issues per year in January-February, March-April, May-June, July-August, September-October, and November-December.

Publication Fees
There is no cost of the article-processing and publication.

Ethics in publishing
EnNRJ follows closely a set of guidelines and recommendations published by Committee on Publication Ethics (COPE).

Environment and Natural Resources Journal (EnNRJ)
Volume 22, Number 2, March - April 2024 ISSN: 2408-2384 (Online)

Editorial Office Address
Research Management and Administration Section,
Faculty of Environment and Resource Studies, Mahidol University
999, Phutthamonthon Sai 4 Road, Salaya, Phutthamonthon, Nakhon Pathom, Thailand, 73170
Phone +662 441 5000 ext. 2108 Fax. +662 441 9509-10
Website: https://ph02.tci-thaijo.org/index.php/ennrj/index
E-mail: ennrjournal@gmail.com

Environment and Natural Resources Journal (EnNRJ)

Volume 22, Number 2, March - April 2024 ISSN: 2408-2384 (Online)

CONTENT

Environment and Natural Resources Journal

Volume 22
Issue 2
2024

Spatial Distribution and Trends of Heat Stress in Vietnam

Nhung Vu[1,2] and Thanh Ngo-Duc[3*]

[1]*School of Interdisciplinary Studies, Vietnam National University, Hanoi, Vietnam*
[2]*Medical Committee Netherlands-Vietnam, Hanoi, Vietnam*
[3]*Department of Space and Applications, University of Science and Technology of Hanoi (USTH), Vietnam Academy of Science and Technology (VAST), Hanoi, Vietnam*

ARTICLE INFO

Received: 25 Aug 2023
Received in revised: 19 Dec 2023
Accepted: 26 Dec 2023
Published online: 30 Jan 2024
DOI: 10.32526/ennrj/22/20230227

Keywords:
Heat stress/ Wet-bulb temperature/ Climate change/ Trend analysis/ Vietnam

*** Corresponding author:**
E-mail:
thanh.ngo-duc@usth.edu.vn

ABSTRACT

This study investigated the spatial distribution and trend of heat stress in Vietnam using data from 68 meteorological stations between 1979 and 2018. Daily maximum wet-bulb temperature (TWmax), an indicator of heat stress, was computed based on the daily maximum air temperature (Tx) and relative humidity at 13:00 LST (RH13). The results indicate a strong positive correlation (>0.72) between daily TWmax and Tx and a weak relationship between daily TWmax and RH13. Tx and TWmax generally increased across most stations over the study period, while RH13 displayed both negative and positive trends. The heat stress thresholds for each station are defined using the 95th percentile values of TWmax during the baseline period 1979-1998. We found that most parts of Vietnam experienced an increase in heat stress days, with the interquartile range across all stations spanning from 0.8 to 4.2 days per decade. Among seasons, summer contributed the most (typically 52-80%) to the annual number of heat stress days in most sub-regions, except for the Central Highlands and the South, where spring contributed the most (44% and 41%, respectively). Overall, this study provides useful benchmark values for future research on heat stress in Vietnam.

1. INTRODUCTION

Climate change affects human health, well-being, livelihoods, and various aspects of society in multiple ways, from increasing the risk of extreme events to increasing the risk of infectious diseases. Biologically, the human body regulates its internal temperature by maintaining a delicate balance between hot and cold temperatures. However, when exposed to excessive heat, the body's ability to regulate its temperature is compromised, resulting in adverse effects on human health (Petkova et al., 2013). Both hotter and colder temperatures have been associated with an increased risk of death and disease (Perkins, 2015; Glaser et al., 2016). The Intergovernmental Panel on Climate Change's (IPCC) special report on 1.5°C global warming (Hoegh-Guldberg et al., 2018) reported a global increase in heat stress due to surface heating, which exacerbates exposure and vulnerability to climate-related stress (Cramer et al., 2014). The topic of heat stress has attracted considerable attention and research efforts in recent decades. Some studies have focused solely on temperature data (e.g., Dong et al., 2015; Liu et al., 2017; Harrington and Otto, 2018), while others have also employed humidity besides temperature due to its critical role in heat stress discomfort (e.g., Matthews et al., 2017; Mora et al., 2017; Coffel et al., 2018).

Vietnam, located in the tropical monsoon region of Southeast Asia, is among the countries most affected by climate change (MONRE, 2012; Vu Duy et al., 2022). Temperatures in Vietnam have increased by approximately 0.78ºC from 1981 to 2018, which is equivalent to about 0.21ºC per decade (Espagne et al., 2021). It is noteworthy that even moderate shifts in mean temperatures can significantly change the risk of extreme events (Arias et al., 2021). Thus, a seemingly moderate increase of 0.78ºC in mean temperatures in Vietnam can dramatically elevate the frequency of

Citation: Vu N, Ngo-Duc T. Spatial distribution and trends of heat stress in Vietnam. Environ. Nat. Resour. J. 2024;22(2):93-104. (https://doi.org/10.32526/ennrj/22/20230227)

extremes, including heat stress, occurring in the country. To date, there have been no specific studies on the changes in heat stress in response to the temperature increase across Vietnam, except for some studies focusing on local impacts. For instance, Opitz-Stapleton et al. (2016) analyzed trends in day and night temperatures from 1970-2011 and examined several heat indices to determine the degree of heat stress among workers in Danang. Their findings suggested that nighttime temperatures were excessively high after hot days, preventing workers from recovering and leading to heat stress. Dang et al. (2019) focused on the association of temperature with mortality and hospitalization in Ho Chi Minh City. They found that heat waves significantly increase the risk of death in the elderly and people with respiratory disease.

To address the gap in the literature outlined above, this study examined the relationship between temperature, relative humidity, and heat stress in Vietnam. Specifically, the study addressed two questions: (1) How do temperature and relative humidity interact to affect heat stress in Vietnam? (2) How has heat stress in Vietnam changed over the past four decades in response to the increase in temperature, and what is the spatial distribution of these changes? The remainder of this paper consists of four sections. In Section 2, we describe the data and methods of analysis utilized in our study. Sections 3 and 4 present the results obtained from the analysis and the associated discussion, respectively. Finally, the study's conclusions are presented in Section 5.

2. METHODOLOGY

2.1 Station data

The daily maximum temperature (Tx) and daily relative humidity at 13:00 LT (RH13) during the period 1979-2018 at 68 meteorological stations of the Vietnam Meteorological Hydrological Administration (VNMHA) were used in this study (Figure 1, Table S1). We analyzed the changes over the seven climatic sub-regions of Vietnam: Northwest (N1), Northeast (N2), North Delta (N3), North Central (N4), South Central (S1), Central Highlands (S2), and South (S3). These climatic sub-regions were identified based on radiation, temperature, and rainfall characteristics (Nguyen and Nguyen, 2004) and have been widely used in climate studies of Vietnam (Phan et al., 2009; Ngo-Duc et al., 2014; Le et al., 2019).

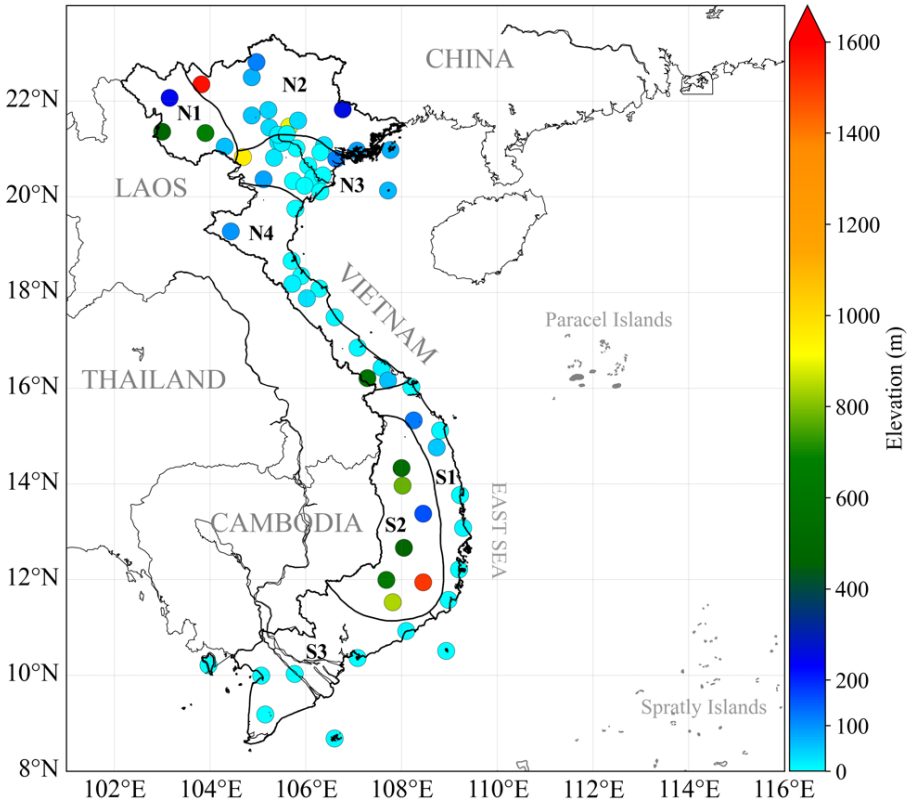

Figure 1. Locations of the 68 meteorological stations (blue-filled circles) used in the study and the seven climatic sub-regions of Vietnam

2.2 Daily maximum wet-bulb temperature

Various heat stress indicators have been developed to quantify the level of heat danger. Most indicators use air temperature and relative humidity as inputs (Morabito et al., 2014; Coffel et al., 2018; Wang and Zhu, 2020). Here we utilized the daily maximum wet-bulb temperature (TWmax) index to represent extreme heat stress. Unlike other indices, TWmax establishes a clear thermodynamic limit on heat transfer that cannot be offset by adaptations (Davies-Jones, 2008; Pal and Eltahir, 2016; Im et al., 2017). Higher values of TWmax imply hot and humid conditions while lower values indicate less extreme conditions. We estimated the TWmax index using a mathematical formulation based on daily Tx and RH13, as shown below (Stull, 2011):

$$\begin{aligned} \mathrm{TWmax} = {} & \mathrm{Tx} \times \operatorname{atan}\left[0.151977 \times (\mathrm{RH13\%} + 8.313659)^{\frac{1}{2}}\right] \\ & + \operatorname{atan}(\mathrm{Tx} + \mathrm{RH13\%}) - \operatorname{atan}(\mathrm{RH13\%} - 1.676331) \\ & + 0.00391838 \times (\mathrm{RH13\%})^{\frac{3}{2}} \times \operatorname{atan}(0.023101 \times \\ & \mathrm{RH13\%}) - 4.686035 \end{aligned} \quad (1)$$

Where; the arctangent function (atan) uses argument values as if they are in radians.

It is important to note that TWmax is best estimated when Tx is reached around 13:00 local time (LT), the same time as the RH13 measurement. Since hourly station data are not available, we used the hourly 2m-temperature (T2m) data of the ERA5-land reanalysis (Muñoz-Sabater et al., 2021) for the summer months of June, July, and August (JJA) in 2019. The data were used to estimate the difference between hourly T2m and the daily average T2m at each latitude band in Vietnam (see supplementary Figure S1). The analysis confirmed that Tx is generally reached around 13:00 LT across Vietnam. Therefore, combining Tx and RH13 to compute TWmax was a reasonable choice for our study.

2.3 Heat stress criteria

The health impacts of heat vary considerably depending on population demographics, acclimation, socioeconomic status, physical activities, clothing, and other factors. As such, the threshold for heat stress is merely an approximation (Kjellstrom et al., 2009; Spector and Sheffield, 2014; Xiao et al., 2015). To date, there has been no predefined absolute threshold for identifying heat stress using the wet-bulb temperature index (Schwingshackl et al., 2021). The only defined threshold is 35°C, identified as a limit for survivability (Sherwood and Huber, 2010). To account for the fact that human beings acclimate to their environment, percentile values are commonly used instead of absolute quantities (e.g., Meehl and Tebaldi, 2004; Peng et al., 2011; Grundstein et al., 2015). In this study, we defined heat stress thresholds for each local station in Vietnam using the 95th percentile values of TWmax for the baseline period 1979-1998. The 95th percentile allows for capturing the higher end of the TWmax distribution while minimizing the influence of outliers in the data. This choice was based on previous research that suggests that temperatures over the 80th percentile at specific locations can threaten human health (Meehl and Tebaldi, 2004; McMichael et al., 2006; Anderson and Bell, 2011; Peng et al., 2011). Some studies even proposed relative thresholds ranging from the 90th to the 99th percentiles (Robinson, 2001; Hajat et al., 2006; Grundstein et al., 2015). Kang and Eltahir (2018) employed the 95th percentile value of TWmax as a metric to assess the intensity of extreme heatwaves. Using the baseline period of 1979-1998 enabled us to assess how heat stress has changed over the past two decades (1999-2018) compared to the earlier period.

2.4 Seasonal selection and trend analysis

We computed and assessed the characteristics of Tx, RH13, and TWmax for the annual average and for spring (March-April-May, MAM), summer (June-July-August, JJA), autumn (September-October-November, SON), and winter (December-January-February, DJF).

The Sen's method (Sen, 1968) was employed for trend analysis. The statistical significance levels of the Sen's slope were obtained using the nonparametric Mann-Kendall test (Kendall, 1975).

3. RESULTS AND DISCUSSION

3.1 Spatial distribution and trends of Tx, RH13, and TWmax

Figure 2 indicates the spatial distribution and trends of the daily maximum temperature (Tx) in Vietnam. It shows that the annual average of Tx ranges between 19-31.8ºC and generally increases from the North to the South. Annual Tx averages under 25ºC are found in the mountainous areas in the Northwest (N1) (e.g., SaPa Station [103.82ºE, 22.35ºN], 19.0ºC) and Central Highlands (S2) (DaLat Station [108.45ºE, 11.95ºN], 23.3ºC), where temperatures decrease with higher elevation. Annual Tx averages above 31ºC occur at stations in South Central (S1) (e.g., PhanRang Station [108.98ºE, 11.58ºN], 31.8ºC), Central Highlands (S2) (Ayunpa Station [108.45ºE, 13.4ºN],

31.65ºC), and South (S3) (e.g., CaMau Station [105.15ºE, 9.18ºN], 31.7ºC). The distribution of Tx across the seven climatic sub-regions varies by season (Figure 2(b-e)). In DJF, low Tx values of less than 23ºC are found in the Northern regions. In JJA, high Tx values are observed in almost all stations across Vietnam, particularly in the Central Coast regions, where the values reach around 34.5ºC.

An increasing trend of Tx during the analysis period was observed across Vietnam (Figure 2(f-j)). Tx increases over almost all areas of Vietnam, except for QuyNhon Station [109.22ºE, 13.77ºN] in the South Central region and some stations in the Central Highlands with a slight decreasing and non-significant trend. The average increasing trend peaks at 0.32ºC/decade in the North Delta (N3), followed by the South (S3) with an average trend of 0.24ºC/decade, although the trends in the South are not homogeneous among stations. Among seasons, the Tx increases in MAM and SON are highest in the Northern and Southern domains, respectively.

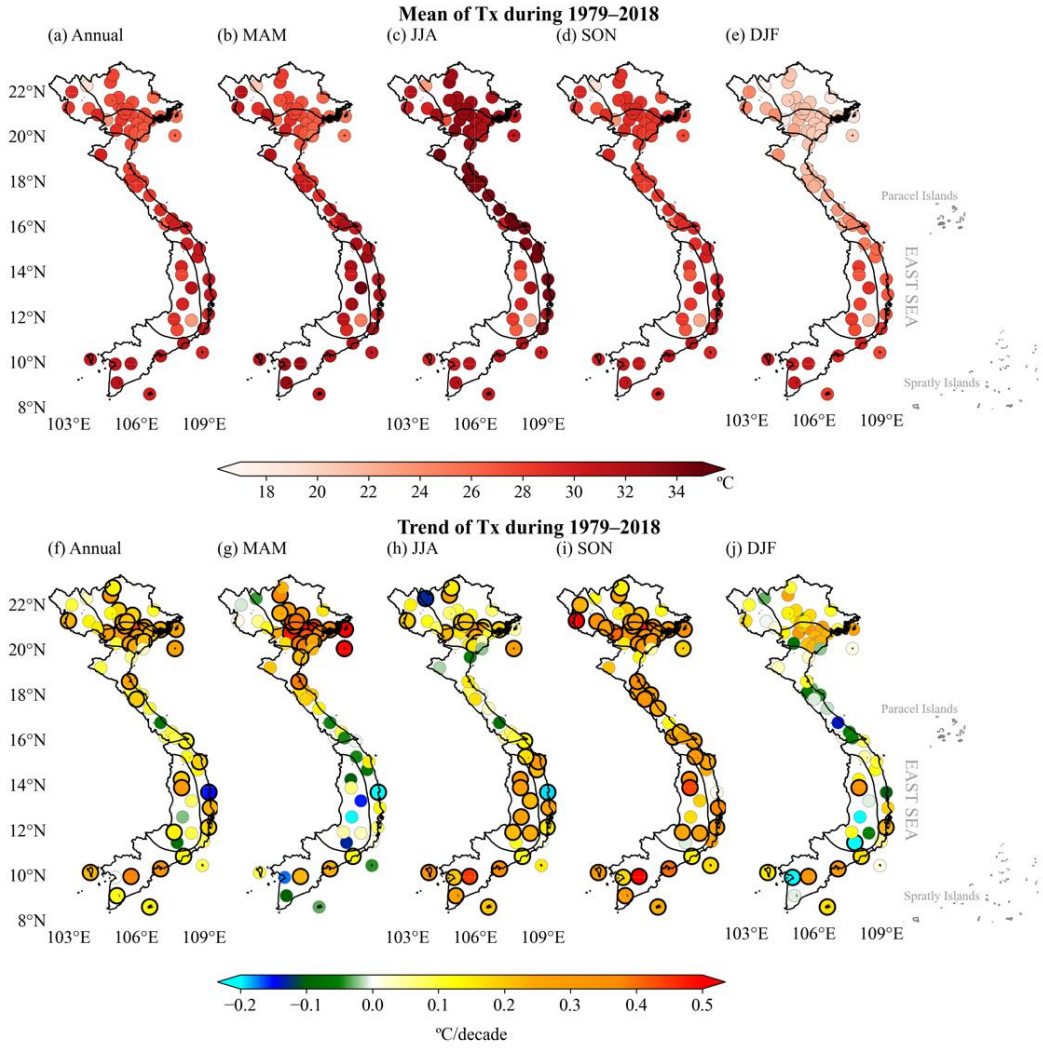

Figure 2. Spatial distributions of the mean (upper panel) and trend (lower panel) of Tx during 1979-2018 for the annual average and the four seasons. The circles with black contours in the lower panel indicate where the trend is statistically significant at the 95% level

Figure 3 shows the spatial distribution of the mean and trend of annual and seasonal averages of relative humidity at 13:00 LST. RH13 values below 60% are found in the Northwest (N1) and Central Highlands (S2) regions. The coastal areas experience more humid conditions with RH13 values above 80%. Similar to Tx, the RH13 values are also seasonally dependent (Figure 3(b-h)). For example, the RH13 values at some stations in the Central Coast are relatively high (>70%) in autumn and winter but low (<60%) in summer. This can be explained by the foehn effect caused by the Truong Son mountain range in the western part of the region.

Unlike Tx, which has increasing trends at almost all stations, RH13 displays both negative and positive trends for the period 1979-2018, varying from -1.63%/decade to 2.23%/decade (Figure 3(f-j)). RH13 decreases by -0.79%/decade in the North Delta region, with the largest decrease of -1.63%/decade at Hanoi Station [105.8ºE, 21.02ºN]. RH13 increases by around 0.25%/decade in the North Central region, reaching up to 2.23 %/decade at Nam Dong Station [107.72ºE, 16.17ºN]. RH13 trends vary by climatic sub-region and season. Significantly decreasing RH13 trends are seen in the North Delta in MAM, the Central Highlands in JJA, and the South region in JJA and SON. Meanwhile, significantly increasing RH13 trends are recorded at some stations in the North Central region in all four seasons and in the Central Highlands in MAM and DJF.

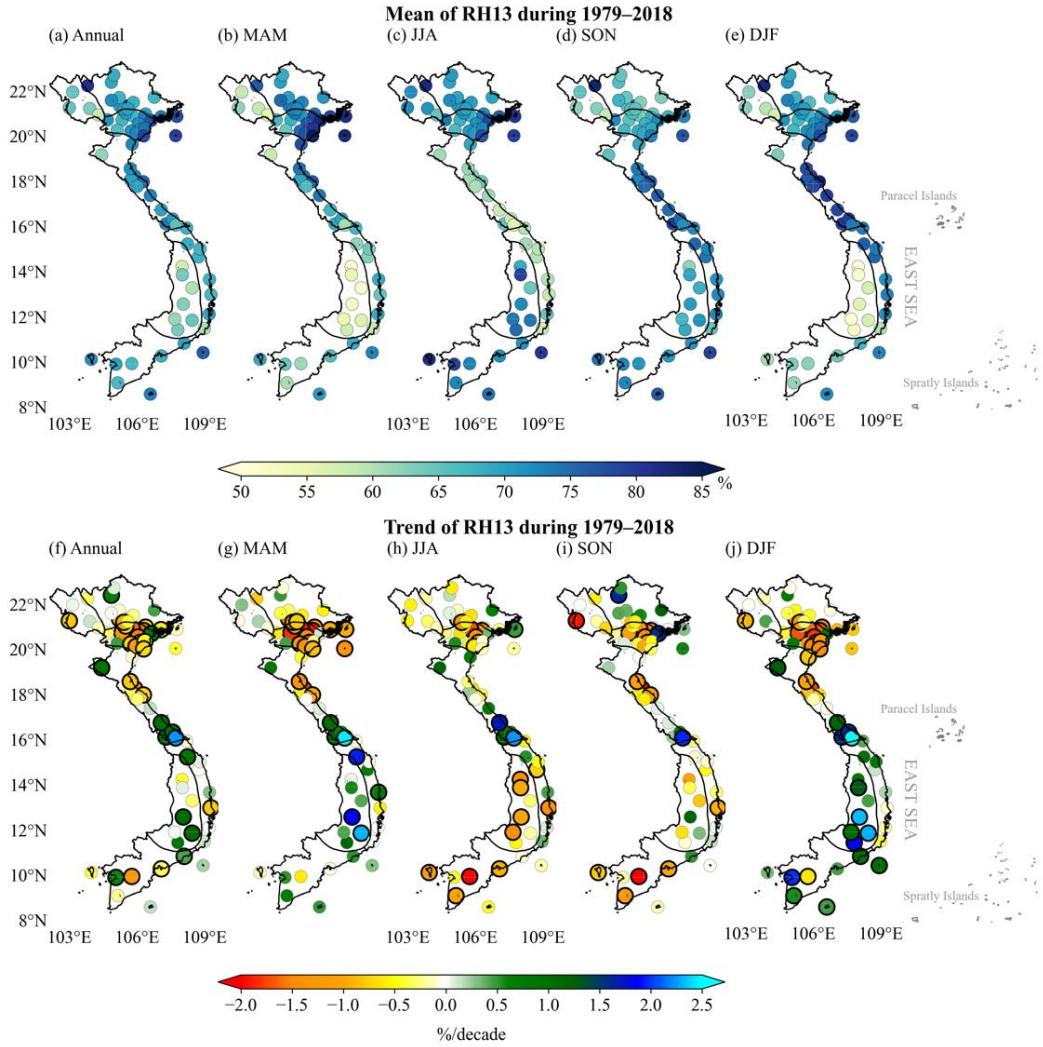

Figure 3. As in Figure 2 except for RH13 rather than for Tx

There are large regional and seasonal variabilities of TWmax across Vietnam (Figure 4). Similar to Tx, the annual TWmax generally increases from the North to the South. TWmax strongly depends on topography, with relatively lower values in the mountainous areas. The lowest annual TWmax of 16.5ºC was recorded at SaPa Station [103.82ºE, 22.35ºN, 1,570 m] in the Northwest; the highest value of 26.6ºC was observed at PhanThiet Station [108.1ºE, 10.93ºN, 9 m] in the South Central region (Figure 4(a)). Concerning seasonal variability, lower TWmax values are generally found in DJF; higher values are recorded in JJA for most sub-regions and in MAM for the Central Highlands and the South. The highest TWmax in JJA of 28.7ºC was measured at PhuLien Station [106.63ºE, 20.8ºN] in the North Delta, while the lowest TWmax in DJF of 11.0ºC was observed at SaPa Station [103.82ºE, 22.35ºN].

Figure 4(f) shows a general significant increasing trend in annual TWmax during 1979-2018.

The trends are more pronounced in the North Delta sub-region than in other sub-regions. Only QuyNhon Station displays a significant decreasing trend of TWmax (of -0.08ºC/decade); this can be explained by the observed downtrend in Tx (Figure 2(f)). Figure 4(g-j) depicts the TWmax trends for each season. TWmax increases most rapidly during MAM in the North Delta (>0.23ºC/decade) and increases significantly in almost all sub-regions during SON. The slightly increasing trends in DJF are not statistically significant at most stations, except for some stations mainly located in the South. In JJA, the increasing TWmax trends, with maximum rates greater than 0.2ºC/decade, are more pronounced in the Central Coast region.

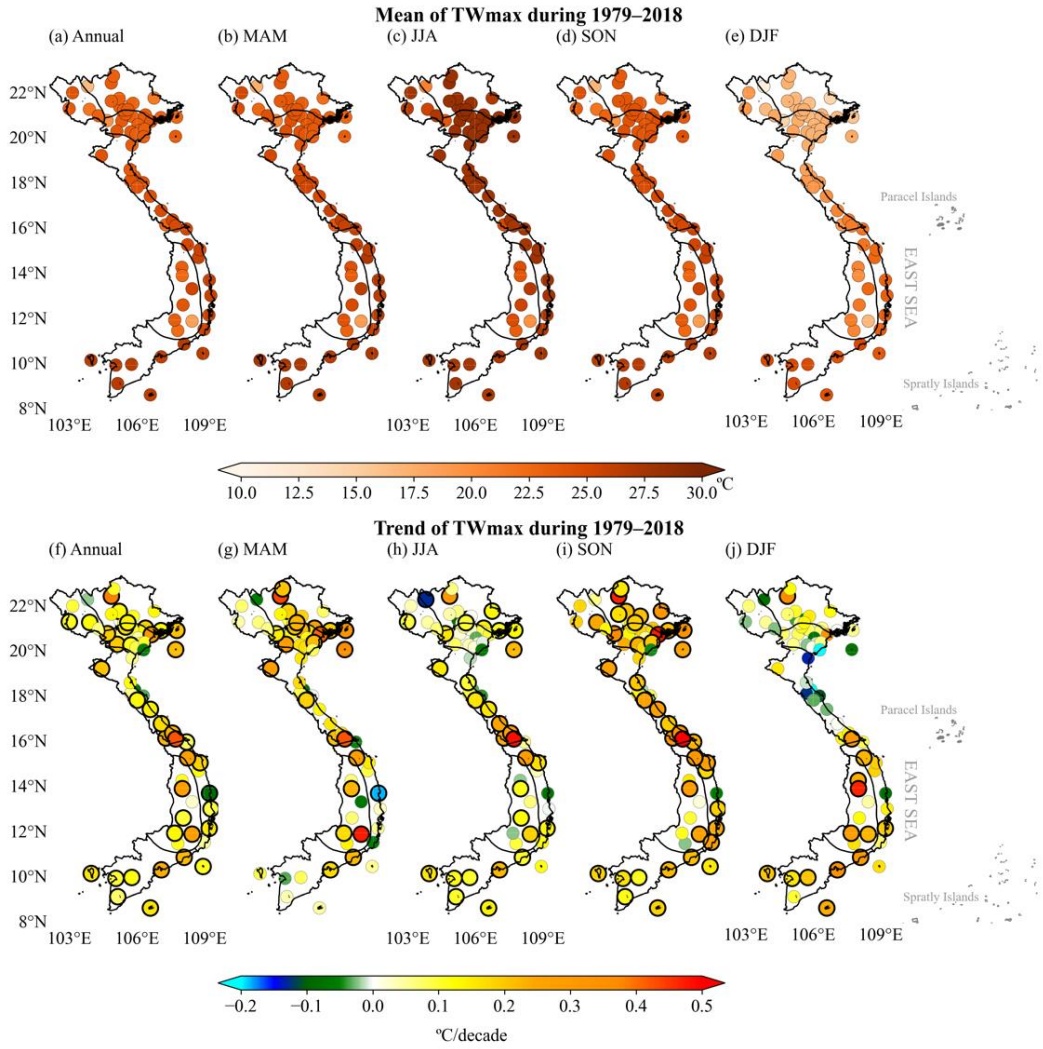

Figure 4. As in Figure 2 except for TWmax rather than for Tx

Since TWmax is calculated from Tx and RH13 (Equation 1), the spatial distribution and trend of TWmax shown in Figure 4 can be interpreted through the values of Tx and RH13. Figure 5 illustrates the relationships between TWmax and the daily Tx and RH13 values of the 68 stations for the period 1979-2018. The results indicate negative correlations between Tx and RH13, e.g., r=-0.72 in summer (Figure 5(a)). These negative correlations can be explained by the capacity of the atmosphere to hold more water vapor in a warmer climate, leading to lower relative humidity. The correlations between TWmax and RH13 are weak: r ranges from -0.05 in summer to 0.24 in autumn. Figure 5(c) demonstrates a robust association between TWmax and Tx, indicating that Tx plays a crucial and more dominant role in determining TWmax, i.e., heat stress, compared to RH13. The results strongly indicate that the seasonality of TWmax is closely tied to the seasonality of Tx, with the highest correlation observed in winter (r=0.9) and the lowest correlation observed in summer (r=0.72).

3.2 Heat stress characteristics and trends

According to the heat stress criteria proposed in Section 2.3, the days with TWmax values exceeding the 95th percentile of the 1979-1998 daily series are considered heat stress days. Figure 6 shows how these 95th percentile thresholds vary across 68 stations in Vietnam. The heat stress threshold is high (≥28ºC) at most stations in the North Delta and Central regions, with the highest recorded value of 29.9ºC at QuyNhon Station [109.22ºE, 13.77ºN]. By contrast, lower heat stress thresholds (≤26ºC) are observed in high-elevation areas, such as in the Northwest and Central Highlands. The lowest heat stress threshold of 21.3ºC is observed at DaLat Station [108.45ºE, 11.95ºN]. In the North Delta region, the typical heat stress thresholds range between 28.8-29.8ºC, while in the South, these values are slightly lower, ranging between 28.0-29.6ºC.

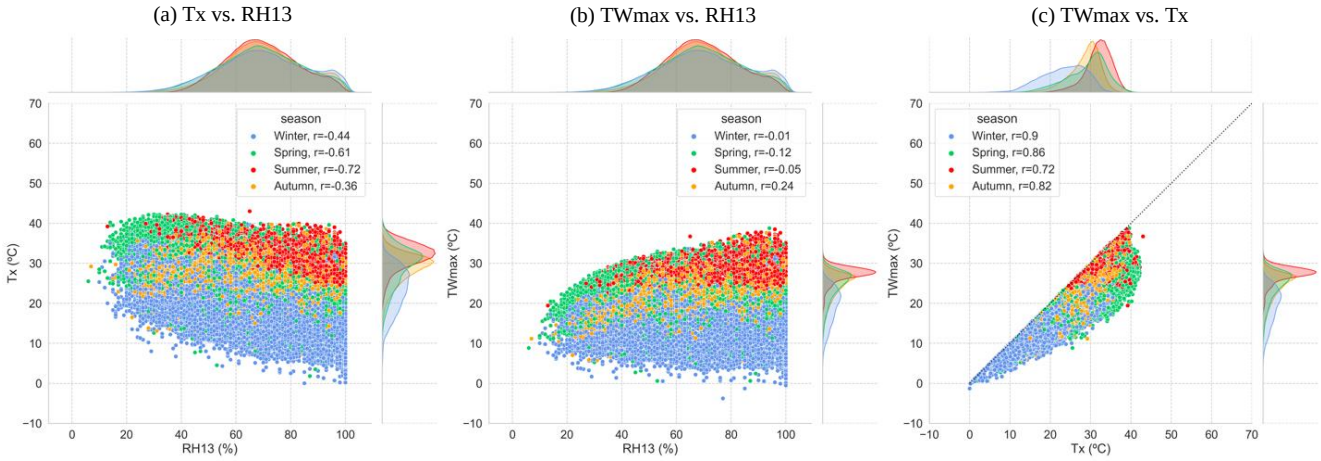

Figure 5. Relationship between (a) Tx and RH13, (b) TWmax and RH13, and (c) TWmax and Tx for the four seasons. The probabilistic distributions for each variable and the Pearson r correlation coefficients for each pair and season are also displayed.

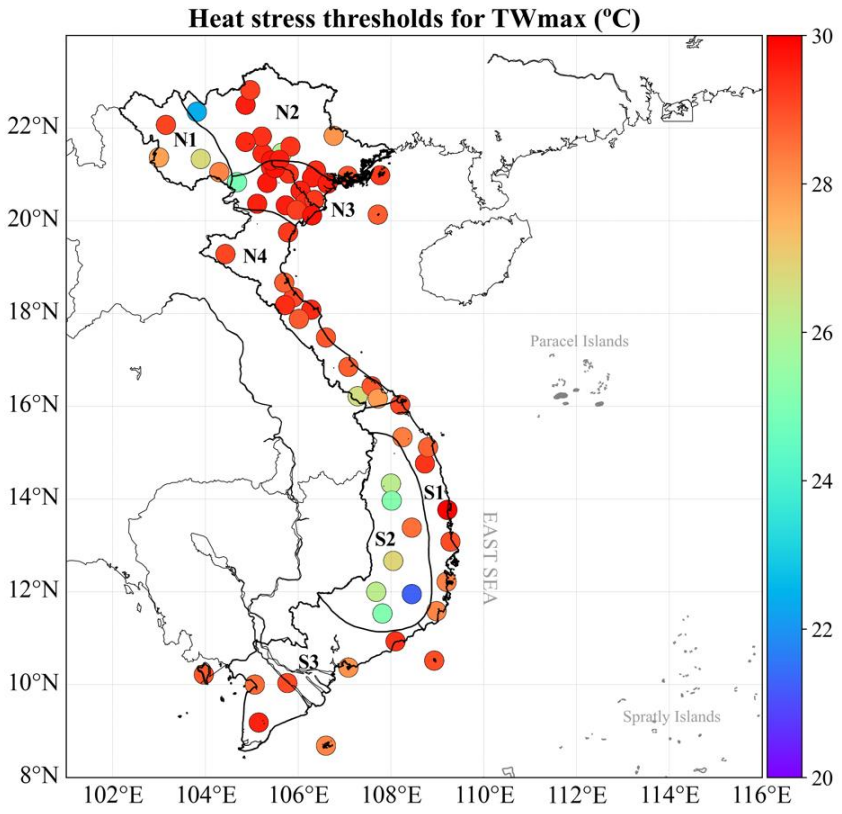

Figure 6. Heat stress thresholds at each station, identified as the 95th percentile value of daily TWmax for the period 1979-1998

Applying the heat stress criteria depicted in Figure 6, the number of heat stress days (DOH) was estimated for each year and each season. While the 95th percentile value of daily TWmax corresponds to about 18 DOH for an average year between 1979 and 1998, Figure 7(a) indicates higher DOH values, generally exceeding 18.5 days per year, for many stations over 1979-2018. Across all stations, NamDong Station [107.72ºE, 160.77ºN] exhibits the highest annual DOH of around 47.8 days, followed by TraMy Station [108.25ºE, 15.33ºN] with 31.7 days. Conversely, the lowest annual DOH values are found in the South Central region, with the minimum of 10.8 days at PhanRang Station [108.98ºE, 11.58ºN].

The annual DOH varies greatly by season, with the largest contribution of JJA found in most regions, except for the Central Highlands and the South. The Northern regions show the highest average JJA contribution to the annual DOH, with percentages of 79.5%, 77.9%, and 67.6% in the Northeast, North Delta, and Northwest, respectively. This is followed by the North Central and South Central regions with contributions of 54.6% and 51.6%, respectively. Meanwhile, the Central Highlands and South regions experience an average JJA contribution of only about 38%.

The average MAM contribution to the annual DOH is approximately 44.4% for the Central Highlands stations, 41.0% for the South stations, and around 36.1% for the stations in the Central regions. In the Northern regions, the average MAM contribution is approximately 22% for the Northwest and only about 13% at Northeast and North Delta stations.

The SON contribution to the annual DOH is relatively small, ranging from 3.7 to 25.2% for all stations. For DJF, the contribution to the annual DOH is negligible (mostly <1%) for most regions of Vietnam, except for the South region where the DJF contribution reached 2.1% at Phu Quoc Station [103.97ºE, 10.22ºN].

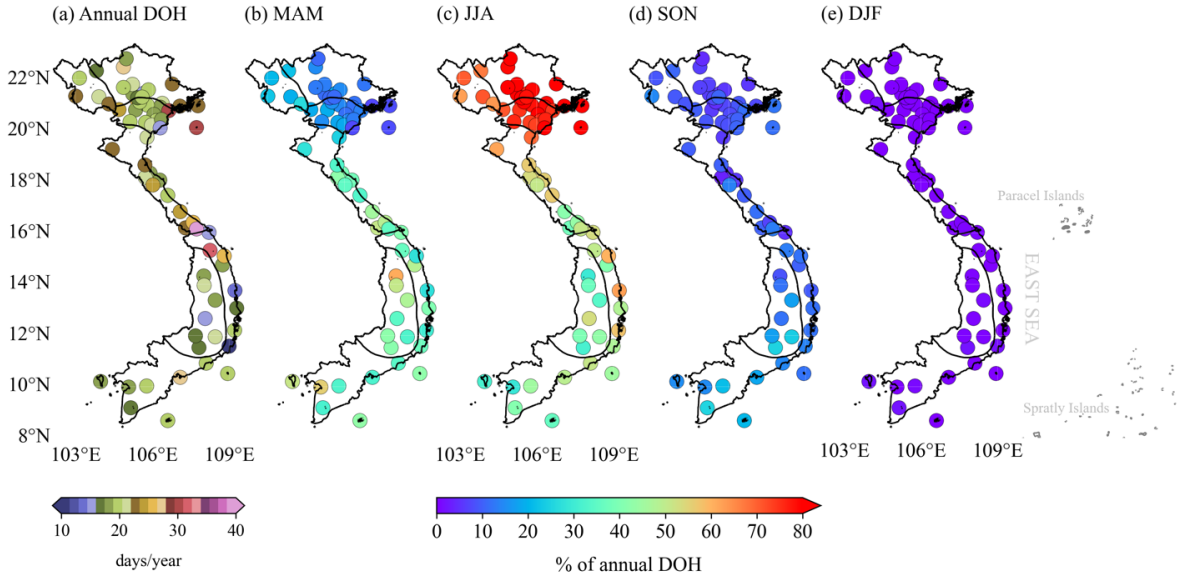

Figure 7. Spatial distributions of (a) the average annual number of DOH during 1979-2018 and (b-e) the contribution percentages by season.

Figure 8 displays the trends of annual and seasonal DOH for the 68 stations. We observe significant increases in annual DOH at most stations. NamDong Station [107.72ºE, 16.77ºN] in the North Central region has the highest DOH increase of 28.9 days/decade, followed by TraMy Station [108.25ºE, 15.333ºN] in the Central Highlands with 12.5 days/decade and BachLongVi Station [107.72ºE, 20.13ºN] in the North Delta with 11.4 days/decade. The stations in the North Central region have relatively higher DOH trends compared to those in other regions. DOH tends to decrease at some stations, such as PhuHo Station [105.23ºE, 21.45ºN] in the Northeast and BMThuot Station [108.05ºE, 12.67ºN] in the Central Highlands, which experience downward trends of -2.0 and -2.2 days/decade, respectively. However, these trends are not statistically significant. The DOH numbers during the MAM, JJA, and SON seasons also exhibit increasing trends at many stations. Since DOH is negligible in winter, most stations in Vietnam do not show pronounced DOH trends in DJF. Similar to the annual DOH, some stations exhibit

downward trends in seasonal DOH, although these are not statistically significant at the 95% level. The number of DOH shows faster trends in JJA than in other seasons, suggesting enhanced severe heat stress during summer under climate change conditions.

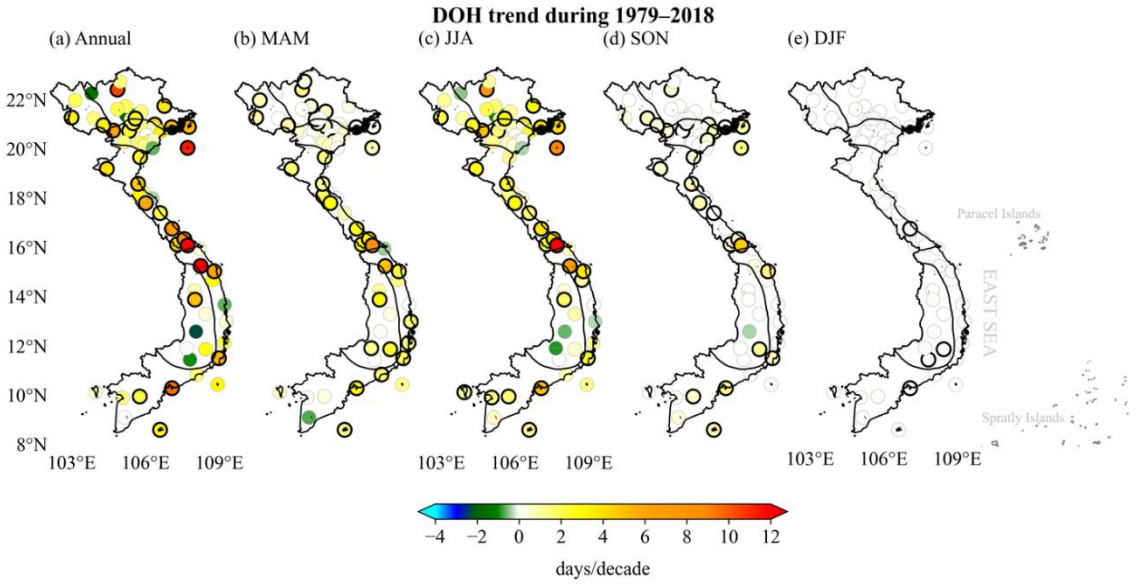

Figure 8. DOH trend during 1979-2018 for the annual average and the four seasons. The circles with black contours indicate where the trend is statistically significant at the 95% level.

4. DISCUSSION

According to the National Report on Climate Change and Sea Level Rise Scenario for Vietnam published in 2016 by the Ministry of Natural Resources and Environment (MONRE, 2016), Vietnam's temperature had increased by approximately 0.62ºC between 1958 and 2014. The report indicates that Tx had increased in most regions, except for some southern stations that experienced a decreasing trend. The updated 2020 scenario report (MONRE, 2020) revealed an increasing trend in the highest annual temperature (TXx) across most of the country, ranging from 0.2 to 1.7ºC during the period 1961-2018. However, in certain areas of the Northwest and Central Highlands, the annual average of Tx had decreased by 0.2 to 0.6ºC over 58 years (1961-2018).

It is worth noting that the reports mentioned above did not provide the statistical significance of the trends. Furthermore, comparing the increasing and decreasing trends between stations in the reports could lead to incoherent findings since the data period is not uniform for all the stations used in MONRE (2016) and MONRE (2020). Some stations, mainly in the North of Vietnam, have data collected since the 1960s, whereas many other stations in the Central and Southern regions have data only after 1975, when North and South Vietnam were unified after the war.

Our study has the advantage of using daily Tx and RH13 values that have been collected and processed uniformly between 1979 and 2018 across all stations. This uniformity enabled us to compare trends among stations and calculate average trends across each climatic sub-region and for the entire country. We also applied the Mann-Kendall test to determine the statistical significance of the trends. This analysis enabled us to identify significant increases in Tx at nearly all stations in Vietnam in autumn, in the North Delta in spring, and in the Central Highlands and the South in summer (Figure 2).

Concerning past humidity trends in Vietnam, Ngo-Duc and Phan-Van (2012) first explored the trend of daily minimum relative humidity during 1961-2007. However, their study was based on a limited number of monitoring stations, and they found no systematic change in the minimum humidity during the study period. In our analysis (Figure 3), we revisited their work using more up-to-date data from more stations to obtain a more comprehensive understanding of the distribution and trend of humidity in Vietnam.

Our study has revealed two significant features of RH13. Firstly, RH13 values in the Central Coast and Central Highlands regions are lower than in other regions during summer and winter/spring, respectively

(Figure 3). This can be explained by the foehn effect, which occurs when moist air rises over a mountain range and loses its moisture as it descends on the leeward side. This results in lower relative humidity in the Central Coast region during summer and in the Central Highlands during winter and spring (Nguyen-Le et al., 2014; Nguyen-Le et al., 2015). Secondly, the decreasing (increasing) trends of RH13 at various stations are possibly associated with the corresponding increasing (decreasing) trends of Tx, as depicted in Figures 2 and 4. This finding can be partly explained by the Clausius-Clapeyron relationship (Held and Soden, 2006), which states that in a warmer (cooler) climate, the atmosphere holds more (less) humidity, thereby resulting in a decrease (increase) in relative humidity.

It is worth noting that, to the best of our knowledge, this is the first time that the heat stress index has been calculated and analyzed using data sources from the network of meteorological stations in Vietnam. The heat stress thresholds determined in this study, which are based on the 95th percentile of TWmax values, are generally above 27ºC across most stations in Vietnam, in line with the findings of Kang and Eltahir (2018). These results provide useful benchmark values for future studies on heat stress in Vietnam.

In the context of global warming, the number of heat stress days has increased significantly in most parts of Vietnam over the past four decades. The typical increase, i.e. the interquartile range of values across all stations, ranges from 0.8 to 4.2 days per decade, and possibly even up to 28.9 days per decade. The results of this study indicate that there is an increasing risk of heat stress on health and productivity in Vietnam, particularly for outdoor workers (Parsons et al., 2022) during the summer months.

5. CONCLUSION

In this study, we examined the relationship between the daily maximum temperature Tx, the relative humidity RH13, and the heat stress index TWmax in Vietnam, with a focus on the spatial distribution and trends of these variables from 1979 to 2018. Our results revealed a close relationship between Tx and TWmax, whereas the impact of RH13 on TWmax was weak. We also observed a general increasing trend in Tx and TWmax across most stations, with RH13 showing both negative and positive trends. The heat stress thresholds used in this study resulted in a range of 10.5-36.1 heat stress days per year for the study period, with most stations experiencing more than 18.5 heat stress days per year. We also identified a significant increase in heat stress days over the past four decades across most of Vietnam, particularly in summer, which contributes the most to the annual number of heat stress days in most sub-regions.

Our study has established useful benchmark values for future research on heat stress in Vietnam and has provided a comprehensive understanding of the spatial distribution and trends of heat stress over the past four decades. In future work, we plan to project heat stress under different greenhouse gas scenarios in the 21st century using multiple downscaling experiments. As heat stress can have critical impacts on society, our findings are expected to provide insights for policymakers and researchers concerned with this issue in Vietnam.

ACKNOWLEDGEMENTS

This study is supported by the Vietnam National Foundation for Science and Technology Development (NAFOSTED) under Grant 105.06-2021.14. The author would like to express gratitude to the two anonymous reviewers and editors for their useful comments and suggestions.

REFERENCES

Anderson GB, Bell ML. Heat waves in the United States: Mortality risk during heat waves and effect modification by heat wave characteristics in 43 U.S. Communities. Environmental Health Perspectives 2011;119(2):210-8.

Arias PA, Bellouin N, Coppola E, Jones RG, Krinner G, Marotzke J, et al. Technical Summary. In: Masson-Delmotte V, Zhai P, Pirani A, Connors SL, Péan C, Berger S, et al, editors. Climate Change 2021: The Physical Science Basis. Contribution of Working Group I to the Sixth Assessment Report of the Intergovernmental Panel on Climate Change. Cambridge, UK and New York, USA: Cambridge University Press; 2021. p. 33-144.

Coffel ED, Horton RM, de Sherbinin A. Temperature and humidity based projections of a rapid rise in global heat stress exposure during the 21st century. Environmental Research Letters 2018;13(1):Article No. 014001.

Cramer W, Yohe G, Aufhammer M, Huggel C, Molau U, da Silva Dias MAF, et al. Detection and attribution of observed impacts. In: Field CB, Barros VR, Dokken DJ, Mach KJ, Mastrandrea MD, Bilir TE, et al, editors. Climate Change 2014: Impacts, Adaptation, and Vulnerability. Part A: Global and Sectoral Aspects. Contribution of Working Group II to the Fifth Assessment Report of the Intergovernmental Panel on Climate Change. Cambridge, UK and New York, USA: Cambridge University Press; 2014. p. 979-1037.

Dang TN, Honda Y, Van Do D, Pham ALT, Chu C, Huang C, et al. Effects of extreme temperatures on mortality and hospitalization in Ho Chi Minh City, Vietnam. International

Journal of Environmental Research Public Health 2019;16(3):Article No. 432.

Davies-Jones R. An efficient and accurate method for computing the wet-bulb temperature along Pseudoadiabats. Monthly Weather Review 2008;136(7):2764-85.

Dong W, Liu Z, Liao H, Tang Q, Li X. New climate and socio-economic scenarios for assessing global human health challenges due to heat risk. Climate Change 2015;130(4): 505-18.

Espagne E, Ngo-Duc T, Nguyen MH, Pannier E, Woillez MN, Drogoul A, et al. Climate Change in Viet Nam; Impacts and Adaptation. A COP26 Assessment Report of the GEMMES Viet Nam Project. Paris: Agence Française de Développement; 2021.

Glaser J, Lemery J, Rajagopalan B, Diaz HF, García-Trabanino R, Taduri G, et al. Climate change and the emergent epidemic of CKD from heat stress in rural communities: The case for heat stress nephropathy. Clinical Journal of the American Society of Nephrology 2016;11(8):1472-83.

Grundstein A, Williams C, Phan M, Cooper E. Regional heat safety thresholds for athletics in the contiguous United States. Applied Geography 2015;56:55-60.

Hajat S, Armstrong B, Baccini M, Biggeri A, Bisanti, L, Russo A, et al. Impact of high temperatures on mortality: Is there an added heat wave effect? Epidemiology 2006;17(6):632-8.

Harrington LJ, Otto FEL. Changing population dynamics and uneven temperature emergence combine to exacerbate regional exposure to heat extremes under 1.5ºC and 2.0ºC of warming. Environmental Research Letters 2018;13(3):Article No. 034011.

Held IM, Soden BJ. Robust responses of the hydrological cycle to global warming. Journal of Climate 2006;19:5686-99.

Hoegh-Guldberg O, Jacob D, Taylor M, Bindi M, Brown S, Camilloni I, et al. Impacts of 1.5ºC global warming on natural and human systems. In: Masson-Delmotte V, Zhai P, Pörtner H-O, Roberts D, Skea J, Shukla PR, et al, editors. Global Warming of 1.5ºC: An IPCC Special Report on the Impacts of Global Warming of 1.5ºC Above Pre-industrial Levels and Related Global Greenhouse Gas Emission Pathways, in the Context of Strengthening the Global Response to the Threat of Climate Change, Sustainable Development, and Efforts to Eradicate Poverty. Cambridge, UK and New York, USA: Cambridge University Press; 2018. p. 175-312.

Im ES, Pal JS, Eltahir EAB. Deadly heat waves projected in the densely populated agricultural regions of South Asia. Science Advances 2017;3(8):1-7.

Kang S, Eltahir EAB. North China Plain threatened by deadly heatwaves due to climate change and irrigation. Nature Communications 2018;9:Article No. 2894.

Kendall MG. Rank Correlation Methods. 4th ed. London: Griffin; 1975.

Kjellstrom T, Holmer I, Lemke B. Workplace heat stress, health and productivity: An increasing challenge for low and middle-income countries during climate change. Global Health Action 2009;2(1):Article No. 2047.

Le VVP, Phan-Van T, Mai VK, Tran QD. Space-time variability of drought over Vietnam. International Journal of Climatology 2019;39(14):5437-51.

Liu Z, Anderson B, Yan K, Dong W, Liao H, Shi P. Global and regional changes in exposure to extreme heat and the relative contributions of climate and population change. Scientific Report 2017;7(1):Article No. 43909.

Matthews TKR, Wilby RL, Murphy C. Communicating the deadly consequences of global warming for human heat stress. Proceedings of the National Academy of Sciences 2017; 114(15):3861-6.

McMichael AJ, Woodruff RE, Hales S. Climate change and human health: Present and future risks. The Lancet 2006; 367(9513):859-69.

Meehl GA, Tebaldi C. More intense, more frequent, and longer lasting heat waves in the 21st century. Science 2004; 305(5686):994-7.

Ministry of Natural Resources and Environment (MONRE). Climate Changes and Sea Level Rise Scenarios for Vietnam. Viet Nam Natural Resources, Environment and Mapping Publishing House; 2012 (in Vietnamese).

Ministry of Natural Resources and Environment (MONRE). Climate Changes and Sea Level Rise Scenarios for Vietnam. Viet Nam Natural Resources, Environment and Mapping Publishing House; 2016 (in Vietnamese).

Ministry of Natural Resources and Environment (MONRE). Climate Changes Scenarios. Viet Nam Natural Resources, Environment and Mapping Publishing House; 2020 (in Vietnamese).

Mora C, Dousset B, Caldwell IR, Powell FE, Geronimo RC, Bielecki CR, et al. Global risk of deadly heat. Nature Climate Change 2017;7(7):501-6.

Morabito M, Crisci A, Messeri A, Capecchi V, Modesti PA, Gensini GF, et al. Environmental temperature and thermal indices: What is the most effective predictor of heat-related mortality in different geographical contexts? The Scientific World Journal 2014;2014:Article No. 961750.

Muñoz-Sabater J, Dutra E, Agustí-Panareda A, Albergel C, Arduini G, Balsamo G, et al. ERA5-Land: A state-of-the-art global reanalysis dataset for land applications. Earth System Science Data 2021;13(9):4349-83.

Ngo-Duc T, Phan-Van T. Non-parametric test for trend detection of some meteorological elements for the period 1961-2007. VNU Journal of Science: Natural Sciences and Technology 2012;28(3S):129-35 (in Vietnamese).

Ngo-Duc T, Kieu C, Thatcher M, Nguyen-Le D, Phan-Van T. Climate projections for Vietnam based on regional climate models. Climate Research 2014;60(3):199-213.

Nguyen DN, Nguyen TH. Vietnamese Climate and Climatic Resources. Hanoi: Hanoi Agriculture Press; 2004 (in Vietnamese).

Nguyen-Le D, Matsumoto J, Ngo-Duc T. Climatological onset date of summer monsoon in Vietnam. International Journal of Climatology 2014;34:3237-50.

Nguyen-Le D, Matsumoto J, Ngo-Duc T. Onset of the rainy seasons in the eastern Indochina Peninsula. Journal of Climate 2015;28(14):5645-66.

Opitz-Stapleton S, Sabbag L, Hawley K, Tran P, Hoang L, Nguyen PH. Heat index trends and climate change implications for occupational heat exposure in Da Nang, Vietnam. Climate Services 2016;2-3:41-51.

Pal JS, Eltahir EAB. Future temperature in southwest Asia projected to exceed a threshold for human adaptability. Nature Climate Change 2016;6(2):197-200.

Parsons LA, Masuda YJ, Kroeger T, Shindell D, Wolff NH, Spector JT. Global labor loss due to humid heat exposure underestimated for outdoor workers. Environmental Research Letters 2022;17(1):Article No. 014050.

Peng RD, Bobb JF, Tebaldi C, McDaniel L, Bell ML, Dominici F. Toward a quantitative estimate of future heat wave mortality under global climate change. Environmental Health Perspectives 2011;119(5):701-6.

Perkins SE. A review on the scientific understanding of heatwaves—Their measurement, driving mechanisms, and changes at the global scale. Atmospheric Research 2015;164-165:242-67.

Petkova E, Horton R, Bader D, Kinney P. Projected heat-related mortality in the U.S. Urban Northeast. International Journal of Environmental Research and Public Health 2013; 10(12):6734-47.

Phan VT, Ngo-Duc T, Ho TMH. Seasonal and interannual variations of surface climate elements over Vietnam. Climate Research 2009;40(1):49-60.

Robinson PJ. On the definition of a heat wave. Journal of Applied Meteorology and Climatology 2001;40:762-75.

Schwingshackl C, Sillmann J, Vicedo-Cabrera AM, Sandstad M, Aunan K. Heat stress indicators in CMIP6: Estimating future trends and exceedances of impact-relevant thresholds. Earth's Future 2021;9:e2020EF001885.

Sen PK. Estimates of the regression coefficient based on Kendall's Tau. Journal of the American Statistical Association 1968; 63(324):1379-89.

Sherwood SC, Huber M. An adaptability limit to climate change due to heat stress. Proceedings of the National Academy of Sciences 2010;107(21):9552-5.

Spector JT, Sheffield PE. Re-evaluating occupational heat stress in a changing climate. The Annals of Occupational Hygiene 2014;58(8):936-42.

Stull R. Wet-bulb temperature from relative humidity and air temperature. Journal of Applied Meteorology and Climatology 2011;50(11):2267-9.

Vu Duy V, Ouillon S, Nguyen Minh H. Sea surface temperature trend analysis by Mann-Kendall test and Sen's slope estimator: A study of the Hai Phong coastal area (Vietnam) for the period 1995-2020. Vietnam Journal of Earth Sciences 2022;44(1):73-91.

Wang S, Zhu J. Amplified or exaggerated changes in perceived temperature extremes under global warming. Climate Dynamics 2020;54(1-2):117-27.

Xiao J, Peng J, Zhang Y, Liu T, Rutherford S, Lin H, et al. How much does latitude modify temperature-mortality relationship in 13 eastern US cities? International Journal of Biometeorology 2015;59(3):365-72.

Environment and Natural Resources Journal

Volume 22
Issue 2
2024

Fine Scale Modeling for Potential Distribution of Dengue Fever in Tampan District, Indonesia

Eggy Arya Giofandi[1*] Dhanu Sekarjati[2], Cipta Estri Sekarrini[3], and Yuska Nelva Sari[4]

[1]*Graduate Program of Regional Planning Science, Faculty of Agriculture, IPB University, West Java 16680, Indonesia*
[2]*Geoinformatics, Department of Computer Science, College of Computing, Khon Kaen University, Khon Kaen 40000, Thailand*
[3]*Doctoral Program of Geography Education, Faculty of Social Science, Universitas Negeri Malang, East Java 65145, Indonesia*
[4]*Pekanbaru City Health Office, Riau Province 28288, Indonesia*

ARTICLE INFO

Received: 24 Jul 2023
Received in revised: 31 Dec 2023
Accepted: 17 Jan 2024
Published online: 5 Feb 2024
DOI: 10.32526/ennrj/22/20230196

Keywords:
Epidemic/ Kernel-density estimation/ Neighboring algorithm/ Surveillance/ Tampan District

*** Corresponding author:**
E-mail: eggyarya@apps.ipb.ac.id

ABSTRACT

Larvisiding is one common way used to reduce mosquito density in breeding areas before metamorphosizing into adults. Despite numerous eradication efforts, the outcomes have not met expectations, leading to additional issues such as environmental pollution in urban areas. In the context of dengue hemorrhagic fever (DHF), addressing the challenge of mitigating the endemic outbreak entails formulating an effective strategy through a vector eradication approach. Therefore, this study explored the spatial pattern of DHF and estimated the potential spread of outbreaks. A geographic information system approach, with nearest neighbor analysis and kernel density estimation (KDE), was used to generate information regarding the pattern and potential for transmission of *Aedes aegypti* mosquitoes. The results showed that in 2019, a random pattern was observed, while in 2020, a clustered pattern of virus spread occurred. Furthermore, in terms of the potential transmission, an exposed zone of 9.73 km² was identified in 2019, and this increased to 15.72 km² in 2020. In this study, several important actions were implemented with a spatial approach, enabling the detection and polarization of events. However, the limitations included not being comprehensive in addressing the hygiene, sanitation, drainage, and population density aspects.

1. INTRODUCTION

Dengue hemorrhagic fever (DHF) is a seasonal disease, posing an unresolved health issue with significant social and economic dimensions. The spatial connections to environmental aspects, particularly cleanliness, play a crucial role in the impact of DHF outbreaks (Lawson and Williams, 2001). Efforts to reduce disease transmission have been undertaken by various scientific groups with diverse perspectives, but the results obtained have not been optimal (Sekarrini et al., 2022a). The estimation of transmission through *Aedes aegypti* mosquitoes is derived from patient data history associated with the population, collected from health agencies. The detailed tracking of the population has been recorded and is assumed as the basis for calculating transmission cases (Firdous et al., 2017).

The rapid spread of the virus over 2-7 days is facilitated by the movement of *Aedes aegypti* mosquitoes, resulting in symptoms such as high fever, weakness, and red spots on the skin (Murray and Smith, 2013; Sekarrini et al., 2020). The transmission is enhanced by environmental conditions characterized by minimal vegetation, low transportation density, lowlands, and rapid urban development, allowing for the uncontrollable proliferation of *Aedes aegypti* mosquitoes (Hii et al., 2012). This information is also substantiated by the impact of anthropogenic growth on the natural environment, leading to various issues concerning ecosystem damage (Wijayanti et al., 2016). The measurement of DHF outbreak transmission can be conducted using a mapping tool derived from the results of transmission detection, incident detection,

Citation: Giofandi EA, Sekarjati D, Sekarrini CE, Sari YN. Fine scale modeling for potential distribution of Dengue Fever in Tampan District, Indonesia. Environ. Nat. Resour. J. 2024;22(2):105-118. (https://doi.org/10.32526/ennrj/22/20230196)

and prevention coverage implemented by health agencies (Rushton, 2003; Waller and Gotway, 2004; Sekarrini et al., 2022b). The effect of weather variables on the magnitude of dengue fever distribution has been established in several previous studies. These studies explored changes in infectivity and vector survival rates, showing the sensitivity of climatic factors to dengue transmission (Negev et al., 2015). Furthermore, the lack of sanitation, poor activity patterns, declining water quality, and existing health conditions interact with the growth of *Aedes aegypti* mosquito vector, forming a common challenge in relation to the prevention and control of DHF (Devine and Furlong, 2007; Bansal et al., 2011).

The impact of DHF transmission on health investigations is reflected through the utilization of geographic information systems methodologies (Giofandi et al., 2023). Scientific application of geographic information systems enables the determination of a case location and the assessment of its influence pattern on the surrounding area (Gatrell and Luytonen, 2003). The role of geographic information systems in managing and analyzing environmental health surveillance data is recognized as changes are occurring in the presentation of information in the field of public health. Furthermore, the potential for DHF transmission through the bite of *Aedes aegypti* mosquitoes can be estimated using the kernel density estimation (KDE) approach. This approach uses a calculation technique based on the relative location of incidents through spatial devices, considering various environmental aspects. The results can be applied to policy and interactive planning of event estimates to address the increased population activity associated with transmission (Spencer and Angeles, 2007; King et al., 2016). The KDE algorithm, with locations monitored at high spatial resolution and population incident data, produces a favorable output for the development of a spatial transmission method based on field observation. In this context, the problem of modifiable unit area is addressed by associating each event with a fixed zone setting (Arifin et al., 2016). The challenge in implementing KDE lies in the selection of parameter clusters, enabling the adaptation of network density settings for problem-solving.

In the western part of Indonesia, dengue fever issues based on a geospatial approach are seldom addressed by a few studies. In most cases, global assessments are the main focus, with less attention given to crucial problems at a more detailed level. The utilization of surveillance data for local observations is one of the calculations used to estimate the future incidence of dengue fever, in line with the Sustainable Development Goals (SDGs) program. Pekanbaru City is one of the urban areas with the highest incidence of dengue fever cases. The characteristics of lowland areas, with an altitude of <100 meters above sea level, increase the prevalence of *Aedes aegypti* (Molina et al., 2022), The similarity in these topographic conditions is one factor in selecting the Tampan District as an observation area. In recent periods, an increase in built-up land in urban areas without corresponding improvement in sanitary environmental conditions and drainage channels has led to a higher potential for the presence of *Aedes aegypti* mosquito habitats (Liu et al., 2022).

This study aimed to determine the spatial pattern of dengue fever incidence and estimate the potential spread of outbreaks. The spatial pattern of incidence was identified using nearest-neighbor analysis in the form of clusters. This part is essential for representing the regional intensity of dengue fever incidence within the cluster. To estimate the potential for transmission, geographic information system (GIS) techniques through a KDE approach were used. Public health resources continue to be burdened by the incidence of this epidemic, and the transmission of DHF changes dynamically, necessitating more effective monitoring and control strategies. Therefore, this model is expected to provide a better understanding of DHF incidence problem. It can also be implemented as one of the approaches at the urban scale, specifically in areas with morphological conditions and other aspects similar to sustainable development.

2. METHODOLOGY

2.1 Study area

This study was conducted at the Tampan District of Pekanbaru City, located in the center of Sumatra Island, Indonesia, as illustrated in Figure 1. Geographically, the observation area is situated at 101°22'45"-101°23'09" East Longitude and 0°28'41"-0°29'09" North Latitude, covering an area of 57 km^2 and falling within a densely populated region. One of the primary reasons for selecting this location is the relatively flat to undulating topographic conditions and high air humidity, reaching 89%. In addition, this area is known for having a high potential for dengue fever cases, as shown by recent reports.

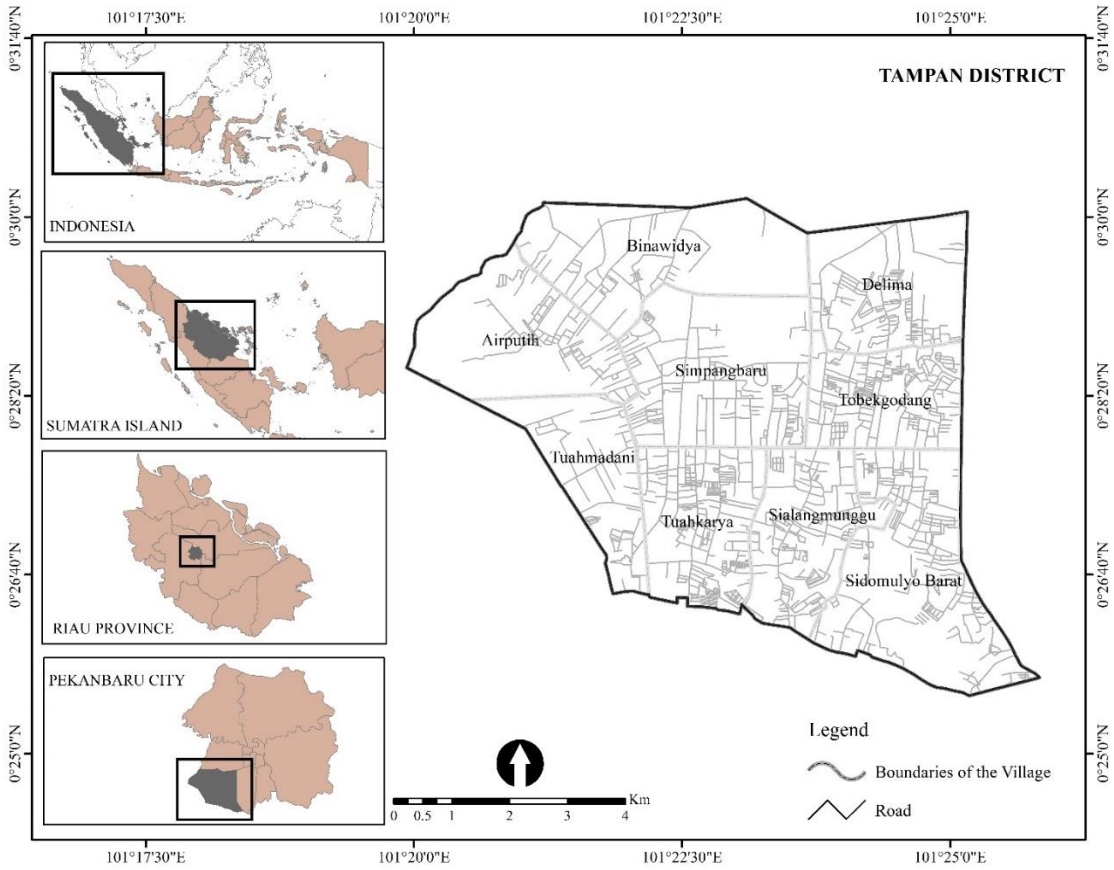

Figure 1. Study site

2.2 DHF epidemiological data

Monthly reports of dengue fever cases were collected from the surveillance database of the Riau Provincial Health Office representative in Tampan District, Pekanbaru City. Monthly dengue incidence reports from nine villages were observed from January 2019 to December 2020. The surveillance system data were initiated from reports by hospital inpatients, health centers, and pharmacies, which were then detected by officers. The report did not include information on the burden of infection and manifestations of dengue fever but provided the coordinates of the residence and age of patients (Table 1). Therefore, reports confirmed by health agency officials were used in this study, and all the data were spatially processed using the nearest neighbor statistical index and kernel density estimation (KDE). All processing was carried out with the Spatial Statistics and Geographic Information Systems (GIS) software (Figure 2).

Table 1. Age categories of patients infected with *Aedes aegypti* mosquitoes

Age group	Category	2020	(%)	2019	(%)
<5	Toddler	4	0.05	3	0.10
6-11	Childhood	8	0.10	6	0.20
12-16	Early Adolescence	13	0.16	6	0.20
17-25	Late Adolescence	29	0.36	6	0.20
26-35	Early Adulthood	14	0.18	2	0.07
36-45	Late Adulthood	8	0.10	4	0.13
46-55	Early Old Age	1	0.01	2	0.07
>55	Late Old Age	3	0.04	1	0.03
	Total	80	1.00	30	1.00

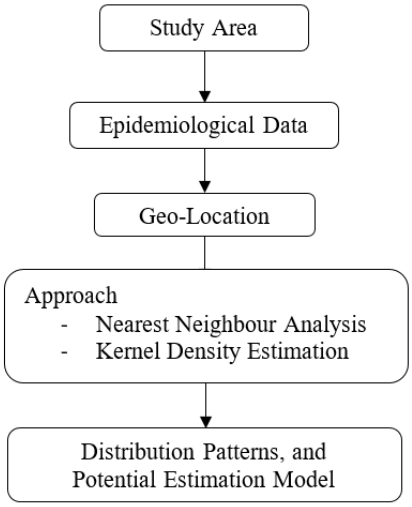

Figure 2. Flow chart of the methodology

2.3 Detection of incidence distribution and potential transmission of *Aedes aegypti*

The processing carried out to detect clusters of distribution linkages between incident locations aimed to discover distribution patterns and help filter out irrelevant information. The neighboring statistical algorithm used to detect the distribution pattern of Dengue hemorrhagic fever (DHF) incidence was calculated using the formula:

$$R = Ju/Jh \quad (1)$$

Where; R is the target, Ju is the average observed distance between each object to be measured, and Jh is the expected distance in a distribution. This analysis required data on the distance between one settlement and another, considered a point in space used to assess the spread pattern of geographical phenomena. Furthermore, the estimation of potential transmission considered the flying capabilities of mosquitoes with an average of 50 meters to 50 km, depending on the species. The migration range of mosquitoes significantly influences the ecology and physiology of the species, irrespective of the disturbance situation. When the flight is related to disturbance, the species tend to cover shorter distances ranging from 25 meters to 6 km^2 (Verdonschot and Lototskaya, 2014).

In the context of *Aedes aegypti* mosquitoes, the flight distance was estimated to be about 400 meters (Satoto et al., 2019). The relatively simple formula for KDE was used with a conceptual method that could be simplified according to the phenomenon under examination. The application of physics analogies could be used to understand how the density estimation kernel works. The algorithm for KDE in determining potential areas for DHF outbreaks was calculated using the formula:

$$f(x) = \frac{1}{nh} \sum_{t}^{n} = 1K\left(\frac{X - Xt}{h}\right) \quad (2)$$

$$K(x) = \frac{3}{4}(1 - x^2), |x| \leq 1 \quad (3)$$

$$\text{Bandwidth} = 0.9 * \min\left(SD, \sqrt{\frac{1}{\ln(2)} \times Dm}\right) \quad (4)$$

Where; h is the bandwidth, n is the number of cases, X-Xt is the distance from the center of the incident, and K is the quadratic kernel function of the equation. Bandwidth refers to the shorter value of the height from the output level in a spatial reference (Sun et al., 2019). Meanwhile, the bandwidth value of the standard distance has been derived from SD of the distance between each point. Dm is the medium distance value of the point distribution pattern (Wang et al., 2019).

Vector formats are used majorly for making disease maps based on aggregated data but the major drawback is the limited availability of detailed disease case data. This is important because data acquisition is subject to high subjectivity and low precision (Shi, 2010). To overcome these challenges, a KDE simulation was conducted to cover multi-modal distributions with minimal errors. In this study, one circle of data was uniformly randomized from a uniform distribution, incorporating either normal bivariate distribution or a combination of two or three. The density value function can estimate the excess of points or compare to the underlying value of each point (Donthu and Rust, 1989).

The results between boundary coverage and geolocation of Point of Interest (POI) events were assessed to understand the rationality and traceability effectiveness of the kernel density estimation approach. The area within the POI with high estimation potential was considered to have the most frequent transmission. Therefore, the calculation of the accuracy was based on a precision indicator, which entailed dividing the delimited area by the identical area and multiplying the result by 100%. This value was used in the process of calculating the area ratio of points found within the radius of the incident POIs.

3. RESULTS AND DISCUSSION

3.1 Distribution of DHF patients

This study focused on location information, specifically the proximity or distance of an activity from the surroundings. Location information in this study was conducted to discover the distribution of Dengue hemorrhagic fever (DHF) events which was limited by an administrative scale, namely Tampan District, Pekanbaru City with spatial distribution patterns of incident locations through statistical analysis of nearest neighbor.

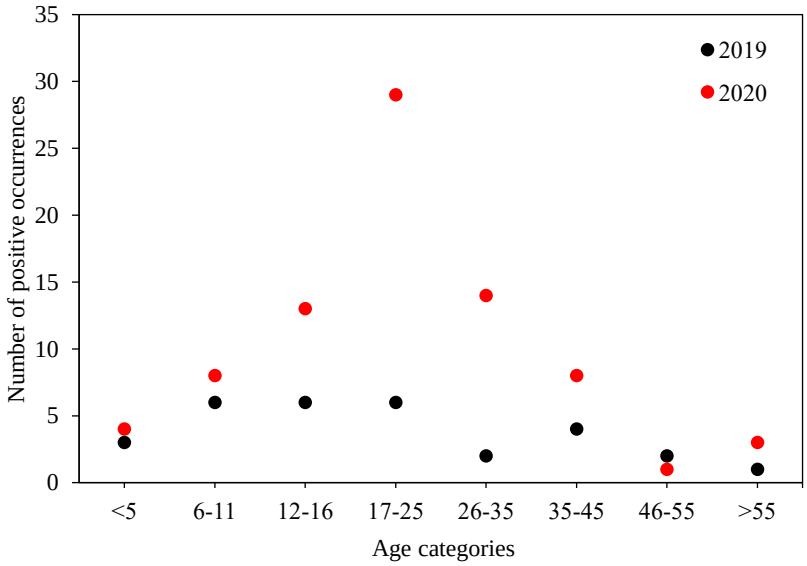

Figure 3. Age distribution of patients with DHF incidence in Tampan District

Based on the results, patients infected with *Aedes aegypti* mosquitoes varied, with a dominance of late adolescence to children (six cases each), in 2019. Meanwhile, in 2020, most patients were found in the age category of early adulthood to adolescence, between 17-25 years, as shown in Figure 3. Therefore, it is recommended that the surveillance of virus transmission age in the Tampan District be further strengthened, and a highly sensitized emergency response to control transmission be established. The continued implementation of health education programs focused on infectious diseases at the school level and suitable for both children and adults is also essential (Portella and Kraenkel, 2021). The results further showed that the peak period for acute infectious diseases in the Tampan District was between June to December, coinciding with the rainy season in the island of Sumatra, Indonesia. Moreover, a more responsive tracking system in the specific identification process can minimize potential breeding sites, contributing to the prevention and control of mosquito habitats (Zhang et al., 2023).

Information related to the distribution pattern of DHF sufferers was measured by the statistical value of the nearest neighbor index, ranging from 0 to 2.15. Values approaching 0 are included in the category of clustered pattern, while those approaching 2.15 are identified as a uniform pattern. An index value of 1.0 positioned in the middle, suggests a random pattern without bias toward clustering or uniformity.

The statistical calculation of the nearest neighbor index for the location of the patients in 2019 yielded a value of 1.0622. A total of 30 location points were identified, forming the second quadrant with a random distribution pattern. This spatial information is evident in the irregular pattern represented by the yellow 1-point figure, which separates from the surrounding locations. Meanwhile, the nearest neighbor statistical index value for events in 2020 was estimated at 0.6505. A total of 80 location points were identified, forming a clustered distribution pattern. When observed spatially, these incidents form a clustered pattern, as illustrated in Figure 4. Information related to the pattern of incident groups includes proximity among certain locations, suggesting a potential vulnerability in the transmission of DHF. The results were consistent with a study conducted in other Southeast Asian countries where the highest incidence occurred in the productive age, attributed to climatological conditions (Masrani et al., 2022). Some estimates of increased vector transmission occur during the journey to school or work (Ragab et al., 2023).

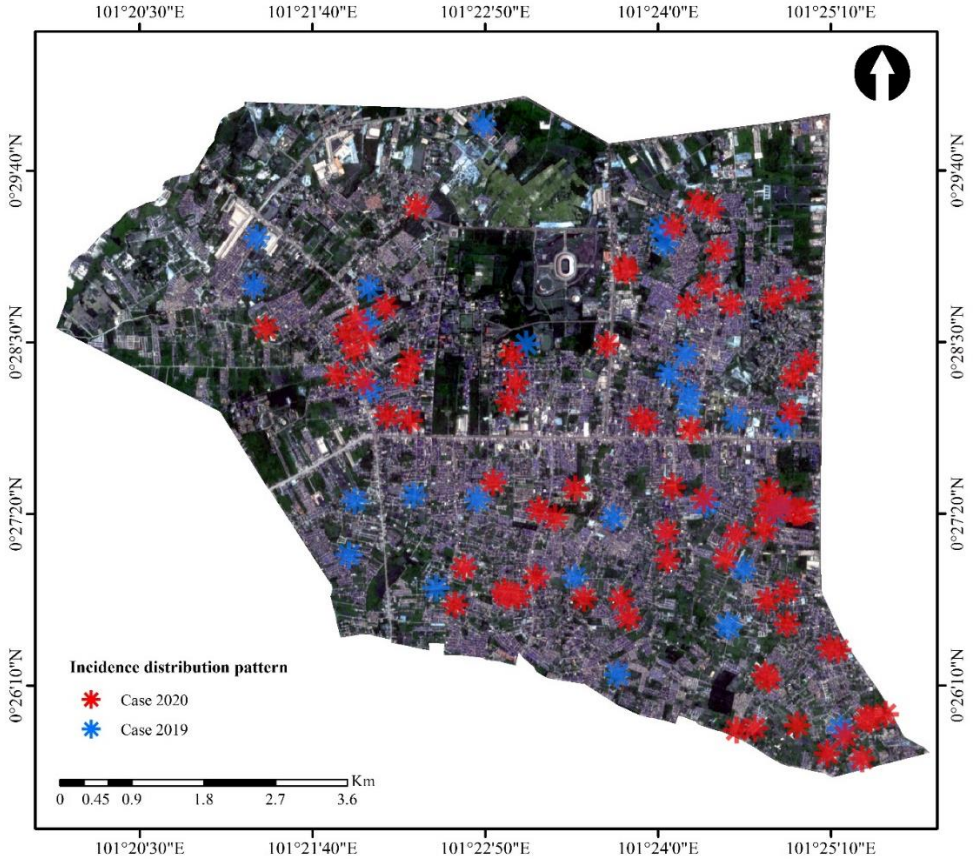

Figure 4. Distribution pattern in 2019 and 2020

The 2019 nearest neighbor statistical index value is marked in yellow, representing a random pattern category. Meanwhile, data obtained from the nearest neighbor statistical index value for 2020 showed a clustered pattern marked in blue (Figure 5). Information regarding the condition of the house and the surrounding environment is needed in structured and visual analyses to determine the conditions of *Aedes aegypti* mosquito habitats.

These results were corroborated by data from the surrounding climatological station detailed in the yearbook, indicating a significant increase in surface temperature from 2020 with an average temperature of 28.83°C to 34.80°C in 2021 (SoPM, 2021). This increase enhances the suitability for the existence of *Aedes aegypti* mosquitoes as also described by (Lubinda et al., 2019) who identified the most suitable temperature range for the environmental habitat to be 28-35°C. Another study (Setiawati, 2019) stated that urban development provided an expansion of movement for dengue vectors including *Aedes aegypti* and *Aedes albopictus* mosquitoes. Response variables such as climate factors were reported to affect the incidence of dengue fever by 66.1%. The peak of the strongest variable was found from rainfall followed by the surface temperature. The presence of *Aedes aegypti* larvae adapts well to poor water and overpopulated areas, effectively breeding in such habitats (Ramadona et al., 2023).

The observed change pattern was attributed to extreme temperature changes resulting from increased greenhouse gas emissions, deforestation, sea level rise, and global warming. Although environments with increased temperatures are more prone to *Aedes aegypti* mosquitoes (Ferraguti et al., 2023), current conditions are reducing the distribution, leading to adaptive clustering.

3.2 Potential of *Aedes aegypti* transmission

Clustering of potential transmission was performed through KDE and data types used in the analysis were derived from the coordinates of event location, categorized by sex ratio (Figure 6) and age category (Figure 8). The primary analysis of potential transmission through statistical estimation illustrated the influence of high infection density during the observation year. Therefore, this area should be considered when planning strategic actions for incidence control in anthropogenic activity land use areas.

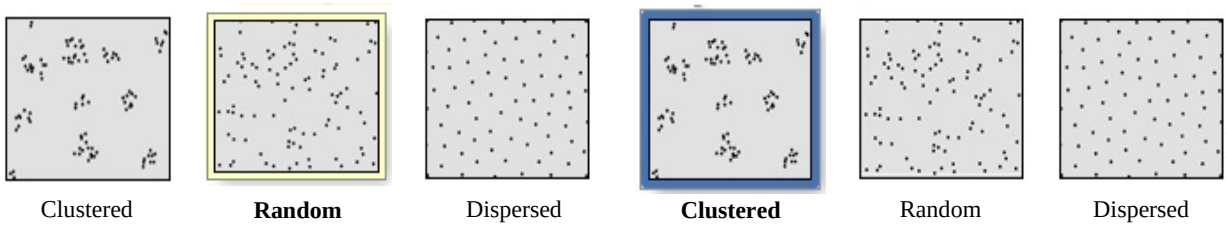

Figure 5. The results of the closest neighbor analysis pattern in 2019 and 2020

The KDE showed the existence of a centralized dengue transmission location and the calculation was based on the sex ratio for 2019 and 2020, as shown in Figure 6. Significant movement was observed among females in 2020, totaling 38 incidents, while groupings were formed in several parts for the movement of transmission events based on the male gender, reaching 42 incidents (Figure 6(a)). In the female gender, transmission occurred widely and randomly, as observed from the movement of the incidence in 2019. In 2020, this transmission occurred in clusters represented in blue (Figure 6(b)). Each result of KDE not only describes the orientation of the incident locations during the observation period but also shows valuable insights for surveillance surveyors to respond promptly to ongoing events.

The analysis showed that based on the sex ratio, the risk of transmission was higher in females compared to males. These results are expected to aid in the identification of populations in vulnerable areas and in conducting early diagnoses for appropriate treatments to reduce the number of incidents, specifically in females. In general, the total vulnerable area observed increased for both male and female incidents, as shown in Figure 7. The potential area for the male gender increased significantly from 6.65 km^2 to 15 km^2. Within the <100-meter range, the area increased by 76 hectares, in the 100-200-meter range, there was a rise of 200 hectares. Furthermore, in the 200-300-meter radius, there was a broader expansion of 263 hectares, and in the farthest 300-400-meter radius, the increase amounted to 296 hectares.

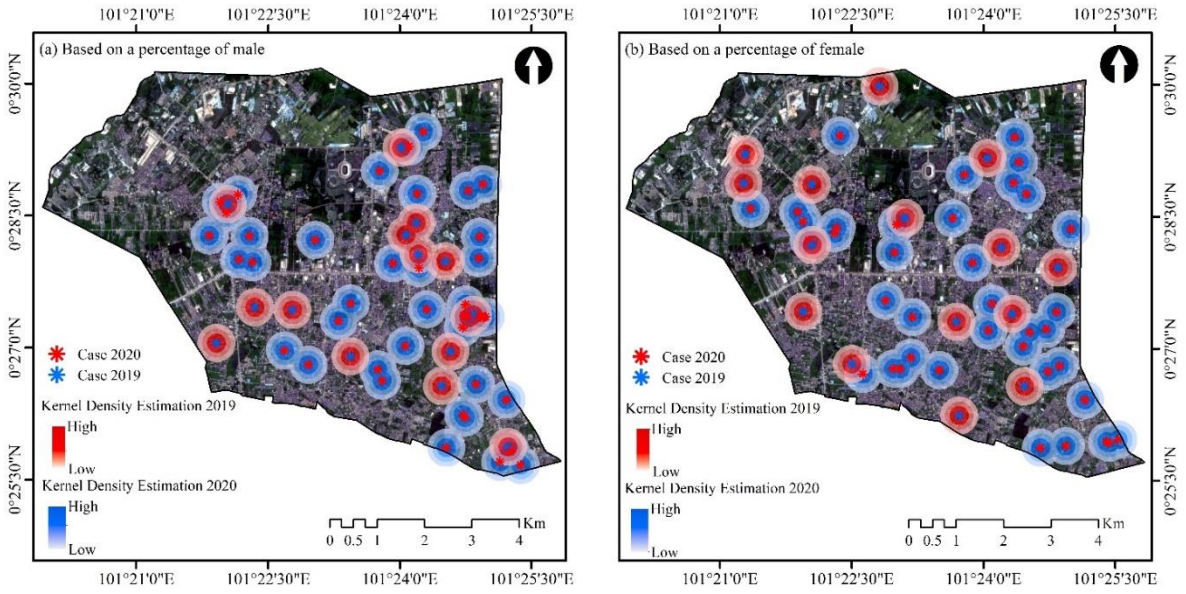

Figure 6. Kernel density estimation based on gender ratio in 2019 and 2020

The incidence rate in females was found to also increase but not significantly compared to males. This was observed in the rise from 7.31 km^2 to 7.47 km^2 in 2019 and further to 14.78 km^2 in 2020. The observation was grounded in the proximity of transmission events and the influence of climatology, which shortened the range of mosquitoes. The estimated area of the exposed zone in the <100-meter radius increased to 69 hectares, the 100-200-meter radius covered 181 hectares, the 200-300-meter radius had a coverage area of 237 hectares, and the farthest radius of 300-400 meters resulted in a reachable area

of 244 hectares. Furthermore, the KDE approach was used to assess the eight age categories. This consideration was used to determine the number and distribution of events in each age grouping of patients infected with *Aedes aegypti* mosquitoes.

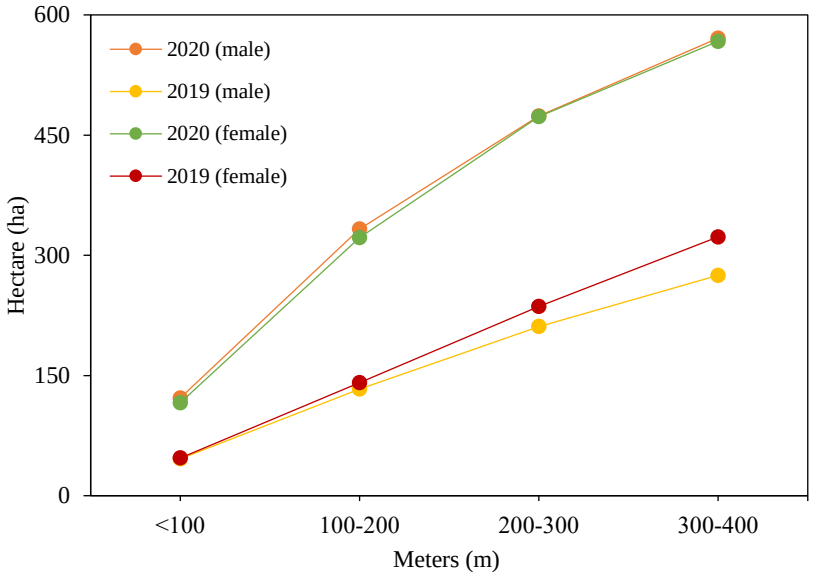

Figure 7. The curve of DHF spread based on gender ratio in 2019 and 2020

In general, the total incidence of dengue fever varied in age categories from Early Adolescence to Early Adulthood (Figure 8). In this age category, individuals are in the productive age, actively engaging in daily activities, while fewer cases were found in the growing age group. This was illustrated in Figure 8(a) and (b), respectively, showing an increase in cases with the incident initially changing randomly to a clustering pattern. As explained previously, the flying range and the presence of wind acting as factors affecting movement speed contribute to mosquito transmission occurring in closer proximity. This phenomenon was also observed in vulnerable age groups such as the Early Old and Late Old, where transmission movement activities occurred far apart, potentially starting with the presence of new breeding habitats. Furthermore, the Late Adolescence group was identified as the most vulnerable age for dengue fever transmission incidents. This result is evident in Figure 7(d), which interprets the movement of *Aedes aegypti* mosquitoes from the previous year. It was found that almost all incidents had intersections with the year 2020, creating a pattern of incidents occurring in close proximity, and designating this area as a red zone. The estimated transmission in 2020, represented by blue, overlaps with that of the previous year. When interpreted more broadly, the potential for incidents in the following year did not change significantly within the transmission area.

Various age categories were considered to determine the potential transmission of dengue fever outbreaks. When examined individually, specifically in the Toddler age category (<5 years), an initial random pattern of occurrence was observed, later shifting into groups. The potential coverage area varied, starting from a radius of <100 meters with an area of 13 hectares, to 37 hectares at 100-200 meters, 55 hectares at 200-300 meters, and 73 hectares at the farthest radius in 2020. In the previous year, smaller areas were observed in the potential range, namely 9 hectares for a radius of <100 meters, 28 hectares at 100-200 meters, 47 hectares at 200-300 meters, and 66 hectares at the farthest radius of 300-400 meters. Furthermore, in the Childhood age category (6-11 years old), the same movement pattern model was observed as the previous age category, but there were differences in the coverage area. In 2020, the potential coverage area started with 25 hectares at a radius of <100 meters, 75 hectares at 100-200 meters, 126 hectares at 200-300 meters, and 169 hectares at 300-400 meters. For 2019, the movement of the potential transmission area was lower at 298 hectares, with coverage of 19 hectares at a radius of <100 meters, 57 hectares at 100-200 meters, 94 hectares at 200-300 meters, and 129 hectares at 300-400 meters.

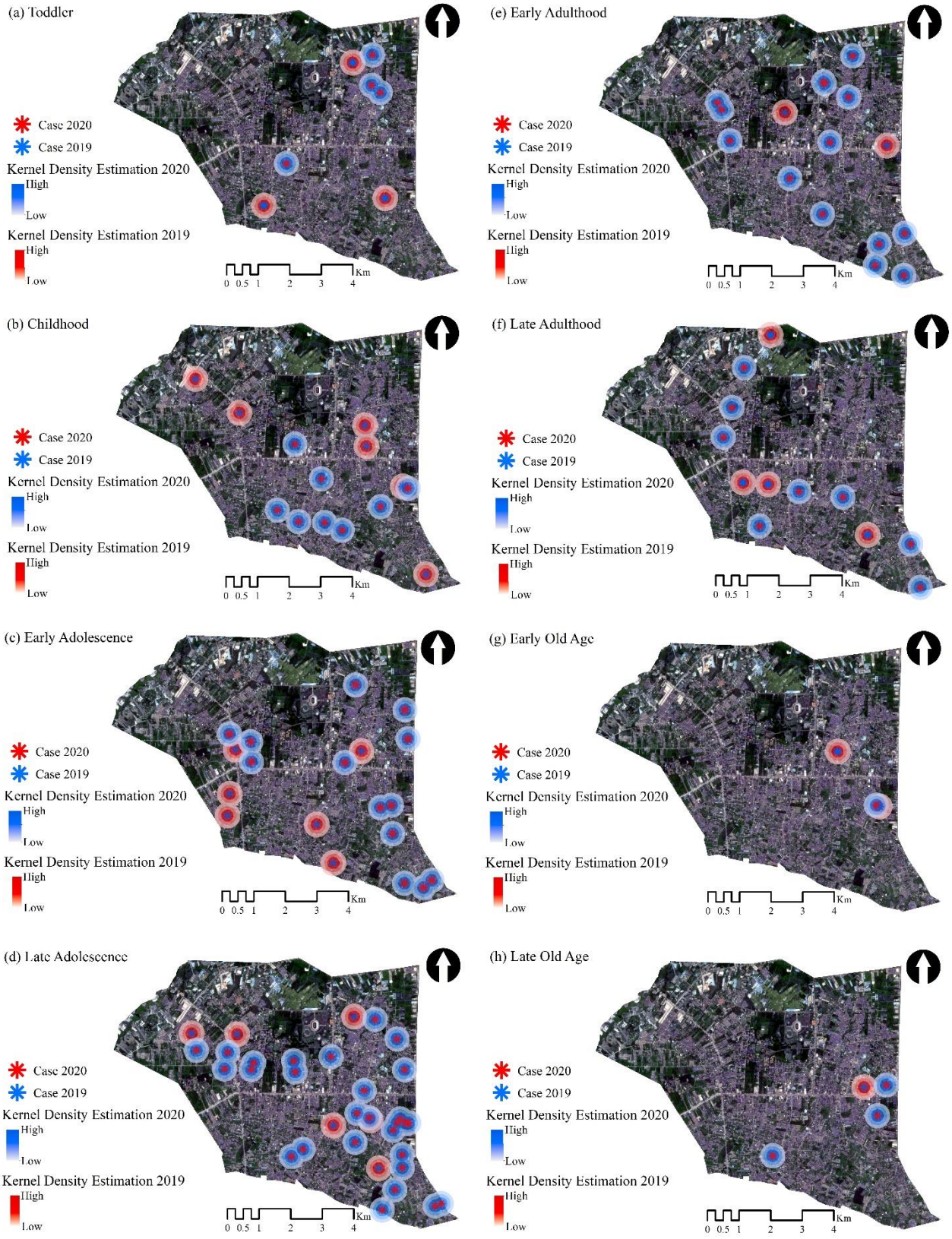

Figure 8. Kernel density estimation based on age category in 2019 and 2020

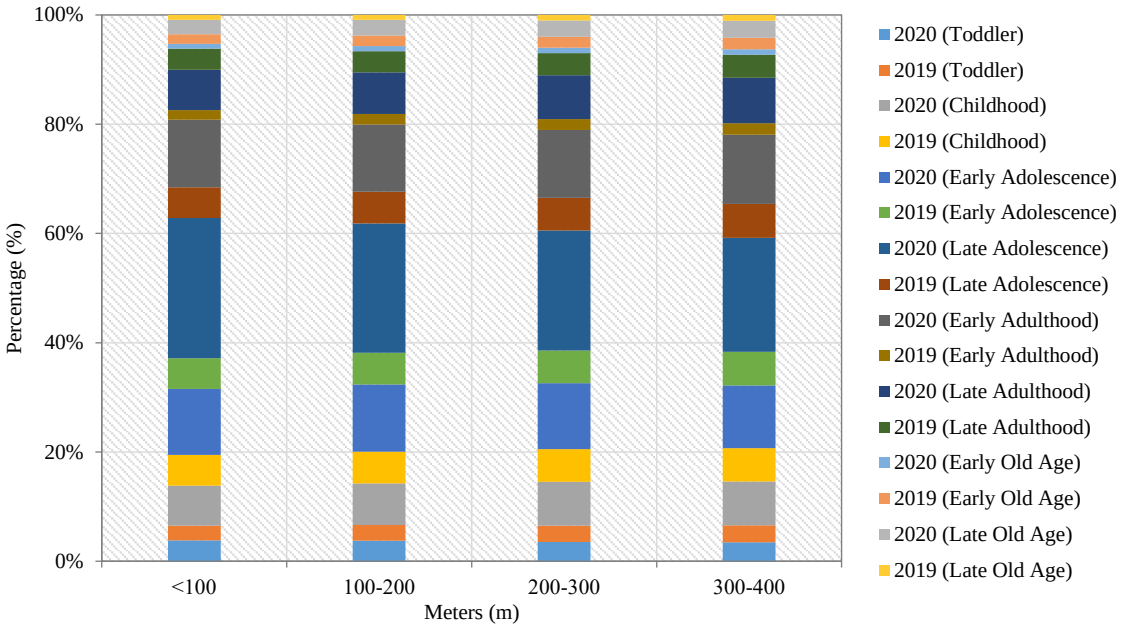

Figure 9. The percentage of DHF spread by age category in 2019 and 2020

In Early Adolescence (11-16 years), differences in movement patterns were observed compared to the two previous age categories. The movement was slightly initiated by transmission from the same vector, evidenced by a non-overlapping flight radius, preventing mutual influence or initiation from different sources. Regarding coverage at this age level, 41 hectares were recorded at a radius of <100 meters, 121 hectares at 100-200 meters, 189 hectares at 200-300 meters, and 243 hectares at the farthest radius of 300-400 meters in 2020. Compared to the potential coverage of the previous year, 19 hectares, 57 hectares, 94 hectares, and 129 hectares were found in the four radius categories namely <100 meters, 100-200 meters, 200-300 meters, and 300-400 meters respectively. This indicated that the coverage in 2019 was lower than in 2020. Additionally, in the Late Adolescence age category (17-25 years), the highest incidence of dengue fever was recorded with a four times increase observed from 302 hectares in 2019 to almost 1,104 hectares or 1.1 km^2 in 2020. At this age level, serious attention is needed to reduce the incidence rate, starting with vaccination or an ideal form of environmental protection easily adapted by the community.

In the Early Adulthood age category (26-35 years), which initially had two incidents, an increase to 14 incidents was observed. New transmission activities were found in this age group, increasing the potential area of transmission to 525 hectares. The changes in coverage area included 36 hectares at <100 meters, 102 hectares at 100-200 meters, 164 hectares at 200-300 meters, and 223 hectares at 300-400 meters, derived from the difference in potential area between both years. For the Late Adulthood age category (36-45 years old), a random transmission pattern with a systematic phenomenon was observed. An increase in potential transmission reaching an area of 200 hectares was recorded, with a distribution of radius coverage including 12 hectares at <100 meters around, 37 hectares at 100-200 meters, 63 hectares at 200-300 meters, and 88 hectares at 300-400 meters.

In the Early Old Age category (46-55 years), a decrease in the potential area reaching half of the previous year was observed throughout the entire radius of the potential range of transmission. This was attributed to the decrease in the incidence rate, approaching the absence of case findings throughout the observation period. Similar results were observed in the Late Old Age category (>55 years) with a less significant incidence rate but expanded area, reaching 100 hectares from the beginning of 2019 to the end of 2020. Subsequently, the entire site unit was subjected to a KDE approach, divided into two-year categories to analyze the density of *Aedes aegypti* mosquito infection in the observation area.

The estimated density for DHF transmission through the flight distance of *Aedes aegypti* mosquitoes is shown in Figure 5. The potential level of DHF transmission was denoted by a red overlay, indicating areas with high kernel density as the proximity of patients increased. This signifies a virus-

prone region where the red area is susceptible to dengue virus infection, potentially facilitating its transmission to the surroundings (Chen, 2018). Furthermore, the location of DHF cases correlated with the habitat of *Aedes aegypti* mosquitoes. Areas with close proximity to breeding sites are more prone to experiencing DHF incidence due to heightened susceptibility. Mitigating measures, such as closing water reservoirs, recycling or burying mosquito breeding items, and effectively managing drained reservoirs can help reduce the risk of transmission in these areas (Saita et al., 2022).

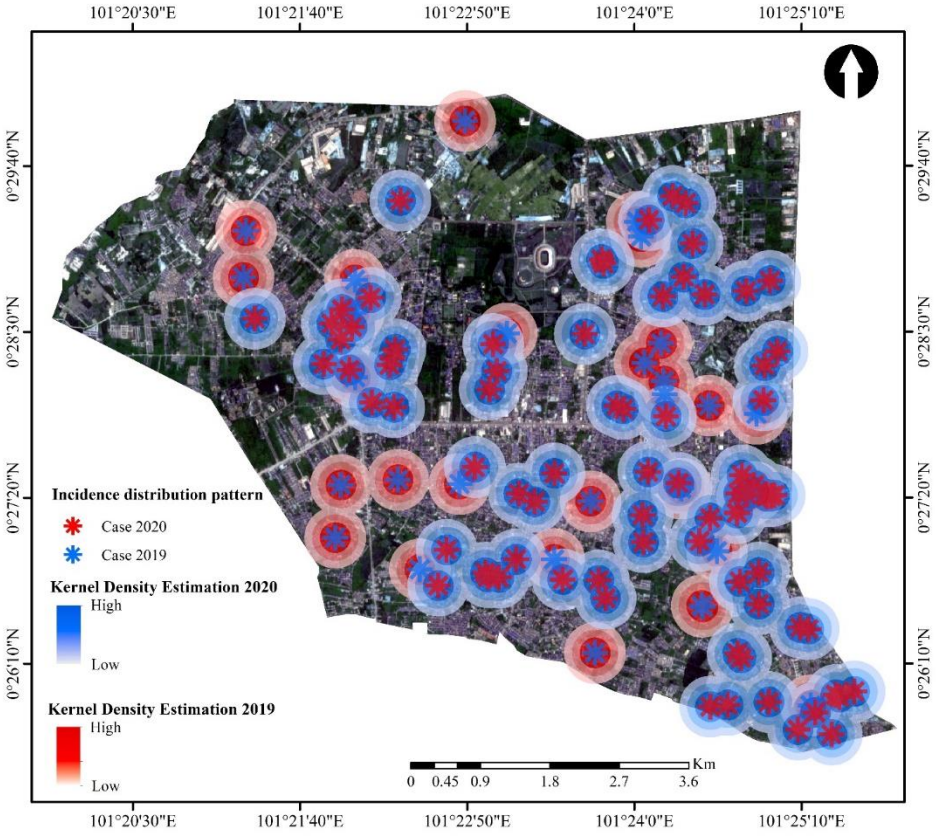

Figure 10. Kernel density estimation in 2019 and 2020

Based on the results of the validity assessment, a significant increase was observed based on the KDE approach, from 0.30% in 2019 to 0.63% in 2020, as shown in Table 2. The boundaries of areas with the potential for disease transmission, calculated considering geolocation, were closely related to the incidence data in the observation area. However, an increase in the number of DHF virus cases was observed. This was reflected in the number of DHF cases, with 30 reported in 2019 and 80 in 2020, showing an increase of 50 cases within one year.

Regarding patients affected by dengue hemorrhagic fever, when prevention and control measures are not swiftly initiated, the virus will spread more rapidly, potentially leading to death. Furthermore, this study found that poor environmental conditions and inadequate solid waste management result from the uncontrolled growth of urbanized areas, providing space for breeding sites. This factor is responsible for the indiscriminate disposal of plastic and bottle waste, forming pools suitable for the oviposition of *Aedes aegypti* mosquitoes (Souza et al., 2022).

Table 2. Assessment of the model in terms of validity

Description	Kernel Density Estimation	
	2020	2019
Potential of disease area (km^2)	22	13
Unpotential of disease area (km^2)	35	44
Validity (%)	0.63	0.30

This section discusses the areas affected by potential exposure to dengue virus bites from *Aedes aegypti* mosquitoes for one year. Based on the results, an increase was observed in the location of DHF cases in 2020. The potential area in 2019 was approximately 973.13 hectares, increasing to 1,572.36 hectares in 2020, as shown in Figure 6. Information related to the distance of the exposed zone was divided into four categories ranging from <100 meters, 100 to 200 meters, 200 to 300 meters, and 300 to 400 meters. As shown in Figure 11, the zone category of <100 meters had coverage of exposed area amounting to 53.14 hectares in 2019, which was higher compared to 2020, at 24,83 hectares. At a radius of 100-200 meters, the exposed area expanded, reaching 254.06 hectares in 2019 and 187.69 hectares in 2020. Extending to a larger radius of 200-300 meters in 2020, the area significantly increased to approximately 579.22 hectares, while in 2019, it was comparatively lower at 237.05 hectares. Finally, at the farthest radius of 300-400 meters, the increase in the number of cases in 2020 yielded the most significant area, reaching 780.62 hectares, compared to 2019, which had 428.88 hectares.

The distinction between each category corresponds to the distance from the location of the incident, estimating how far *Aedes aegypti* mosquitoes can fly without being disturbed by weather conditions and wind direction. The existence of broad categories of potential transmission zones was affected by the location of each patient acting as a host based on a high estimated kernel density. Additionally, areas with few or no cases of DHF were marked by color degradation, particularly faded red in the furthest zone from the flying distance of *Aedes aegypti* mosquitoes. Changes in land configuration, such as land use and urban development, including road networks and waste management systems directly or indirectly impact the transmission of dengue fever to the community (Andreo et al., 2021). The presence of excess water reservoirs also increases the abundance of mosquito vector species, creating suitable ecological spaces for the habitat and resulting in the potential for clustered transmission (Naqvi et al., 2021).

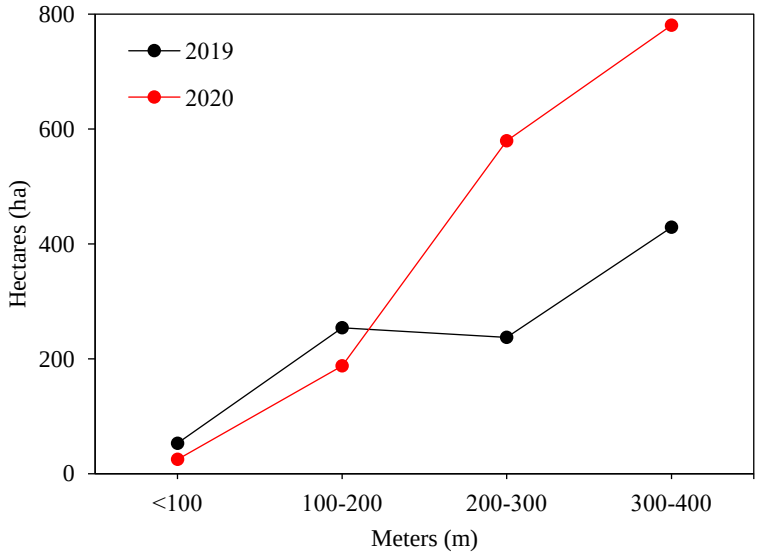

Figure 11. The curve of DHF spread in 2019 and 2020

The growth of new event points during the observation period in the designated area was illustrated by the utilization of the KDE approach. The estimation process algorithm for the pattern of changes in the incidence point was influenced by comparing to the existence of other events. The resulting interpretation suggests a significant increase in the number of incidence cases with the addition of an increasingly widespread potential transmission area. Furthermore, the development of anthropogenic activities in an area contributes to the potential presence of mosquito larvae and drives the demand for affordable health facilities, enhancing overall comfort in human living spaces. This in turn ensures community resilience in responding to *Aedes aegypti* mosquito outbreaks. The diversity of dengue virus transmission in the observation area was spatially influenced by complex interactions between humans and environmental factors of *Aedes aegypti* mosquitoes and climatology. In a particular phase,

climate anomalies influence the abundance of vector species, as well as the density and behavior of humans in the area. This was further compounded by high population and residential density, which reduced the distance between infected individuals, thereby accelerating transmission.

This study has certain limitations, such as not considering climate and other environmental variables. Incorporating these variables on a detailed scale could produce more complex zoning with a specific unit scale. This information is crucial for pinpointing locations expected to be part of the transmission area for *Aedes aegypti* mosquitoes. Special treatment is needed to understand how to anticipate dengue fever events in densely populated areas with building structures. In addition, it is necessary to build literacy about endemic outbreak mitigation in the community based on a sustainable environmental approach, coupled with the inclusion of climate change dynamics scenarios.

4. CONCLUSION

In conclusion, the analysis of DHF incidence using the nearest neighbor analysis and kernel density estimation (KDE) equation found distinct distribution patterns. The movement from random events to clustered groups underscored the impact of public awareness in maintaining clean conditions and prioritizing sanitation, hygiene, and drainage. This shift in distribution was indicative of improved community practices. Moreover, when estimating the transmission potential of *Aedes aegypti* mosquitoes based on the radius of the flight distance, weather conditions, and wind direction must be considered. Although this study observed a downward trend in the incidence of DHF, identifying potential areas of occurrence further reflected the history of vector control. The results obtained during the observation can be used to inform and guide future studies on environmental epidemiological ecology and the implementation of appropriate measures in disease control.

ACKNOWLEDGEMENTS

The authors are grateful to the Riau Province Health Office for granting permission to use surveillance data, as well as everyone who has reviewed and helped improve this paper.

CONFLICTS OF INTEREST

The authors declare that there is no conflict of interest regarding the publication of this manuscript.

ETHICAL APPROVAL

This study used secondary surveillance data, which included routine reports from (Riau Provincial Health Office) based on geospatial data containing geolocation information in the Tampan District area, Pekanbaru City. Therefore, the use of humans or animals as subjects of observation was unnecessary.

REFERENCES

Andreo V, Ximena P, Claudio G, Laura L, Carlos MS. Spatial distribution of *Aedes aegypti* oviposition temporal patterns and their relationship with environment and dengue incidence. Insects 2021;12(10):1-18.

Arifin, Niaz SM, Madey GR, Frank H, Collins. Spatial Agent-Based Simulation Modeling in Public Health. Canada: John Wiley and Sons, Inc; 2016.

Bansal SK, Karam VS, Sapna S, Sherwani MRK. Comparative larvicidal potential of different plant parts of *Withania somnifera* against vector mosquitoes in the semi-arid region of Rajasthan. Journal of Environmental Biology 2011;32(1):71-5.

Statistics of Pekanbaru Municipality (SoPM). Annual Report of Pekanbaru Municipality in Figures 2021. Pekanbaru: Statistics of Pekanbaru Municipality; 2021.

Chen WJ. Dengue outbreaks and the geographic distribution of dengue vectors in Taiwan: A 20-Year epidemiological analysis. Biomedical Journal 2018;41(5):283-9.

Devine, Gregor J, Michael J, Furlong. Insecticide use: Contexts and ecological consequences. Agriculture and Human Values 2007;(24):281-306.

Donthu, Naveen, Roland TR. Estimating geographic customer densities using kernel density estimation. Marketing Science 1989;8(2):191-203.

Ferraguti M, Martínez-de la Puente J, Brugueras S, Millet JP, Rius C, Valsecchi A, et al. Spatial distribution and temporal dynamics of invasive and native mosquitoes in a large Mediterranean city. Science of the Total Environment 2023;896:Article No. 165322.

Firdous, Jannathul, Ariza M, Muhammad AA, Muhamad I, Muhammad FI, et al. Knowledge, attitude and practice regarding dengue infection among Ipoh Community, Malaysia. Journal of Applied Pharmaceutical Science 2017;7(8):99-103.

Gatrell, Anthony C, Markku L. GIS and Health. Philadelphia: Taylor and Francis Inc; 2003.

Giofandi EA, Khursatul M, Kraugusteeliana K, Amira N, Cipta ES. The comparison of vector and raster data for the calculation of landscape environment using a geographic information system approach. IT Journal Research and Development 2023;7(2):209-19.

Hii, Yien L, Huaiping Z, Nawi N, Lee CN, Joacim R. Forecast of dengue incidence using temperature and rainfall. PLoS Neglected Tropical Diseases 2012;6(11):1-9.

King, Tania L, Rebecca JB, Lukar ET, Anne MK. Using kernel density estimation to understand the influence of neighbourhood destinations on BMI. BMJ Open 2016;6:1-8.

Lawson AB, Williams FLR. An introductory guide to disease mapping. American Journal of Epidemiology 2001; 154(9):881-2.

Liu, Wen H, Chen S, Ying L, Lei L, Chun QO. Epidemiological characteristics of imported acute infectious diseases in

Guangzhou, China, 2005-2019. PLoS Neglected Tropical Diseases 2022;16(12):1-12.

Lubinda, Jailos, Jesús ATC, Mallory RW, Adrian JM, Ahmad AHB, et al. Environmental suitability for *Aedes aegypti* and *Aedes albopictus* and the spatial distribution of major arboviral infections in Mexico. Parasite Epidemiology and Control 2019;6:e00116.

Masrani, Afiqah S, Nik RNH, Kamarul IM, Ahmad SY. Trends and spatial pattern analysis of dengue cases in Northeast Malaysia. Journal of Preventive Medicine and Public Health 2022;55(1):80-7.

Molina G, Licet P, Lina AGB, Leonardo ARO. Models of spatial analysis for vector-borne diseases studies: A systematic review. Veterinary World 2022;15(8):1975-89.

Murray, Natasha EA, Mikkel BQ, Annelies WS. Epidemiology of dengue: Past, present and future prospects. Clinical Epidemiology 2013;5(1):299-309.

Naqvi, Syed AA, Muhammad S, Liaqat AW, Shoaib K, Saima S, et al. Integrating spatial modelling and space-time pattern mining analytics for vector disease-related health perspectives: A case of dengue fever in Pakistan. International Journal of Environmental Research and Public Health 2021;18(22):1-30.

Negev, Maya, Shlomit P, Alexandra C, Noemie GPO, Uri S, et al. Impacts of climate change on vector borne diseases in the Mediterranean Basin — Implications for preparedness and adaptation policy. International Journal of Environmental Research and Public Health 2015;12(6):6745-70.

Portella, Tatiana P, Roberto AK. Spatial–Temporal pattern of cutaneous leishmaniasis in Brazil. Infectious Diseases of Poverty 2021;10(1):1-11.

Ragab, Sanad H, Mostafa AK, Riham HT, Mohamed ET. Spatial distribution of appropriate aquatic mosquitos' larval sites occurrence using integration of field data and GIS techniques. Egyptian Journal of Aquatic Biology and Fisheries 2023;27(4):355-71.

Ramadona, Aditya L, Yesim T, Jonas W, Lutfan L, Adi U, et al. Predicting the dengue cluster outbreak dynamics in Yogyakarta, Indonesia: A modelling study. The Lancet Regional Health - Southeast Asia 2023;15:1-8.

Rushton G. Public health, GIS, and spatial analytic tools. Annual Review of Public Health 2003;24:43-56.

Saita, Sayambhu, Sasithan M, Tassanee S. Temporal variations and spatial clusters of dengue in Thailand: Longitudinal study before and during the coronavirus disease (COVID-19) pandemic. Tropical Medicine and Infectious Disease 2022;7(8):1-14.

Satoto TBT, Nur AP, Wida P, Hari KJ, Purwono, Rumbiwati, et al. Occurrence of natural vertical transmission of Zika like virus in *Aedes aegypti* mosquito in Jambi City. Kesmas: National Public Health Journal 2019;13(4):189-94.

Sekarrini CE, Sumarmi, Syamsul B, Didik T. Fuzzy set model of dengue using imageries and the geographic information system in Palembang. International Journal of Innovation, Creativity and Change 2020;13(10):1264-93.

Sekarrini CE, Sumarmi S, Syamsul B, Didik T, Eggy AG. The application of geographic information system for dengue epidemic in Southeast Asia: A review on trends and opportunity. Journal of Public Health Research 2022a; 11(3):1-6.

Sekarrini CE, Syamsul B, Didik T, Giofandi EA. Spatial temporal analysis of dengue hemorrhagic fever occurrence (Case study of Palembang City, South Sumatera Province, Indonesia). Malaysian Journal of Medical Sciences 2022b;18(17):39-45.

Setiawati MD. The effect of climate variables on dengue Burden in Indonesia: A case study from Medan City. Journal of Geoscience and Environment Protection 2019;7(10):80-94.

Shi X. Selection of bandwidth type and adjustment side in kernel density estimation over inhomogeneous backgrounds. International Journal of Geographical Information Science 2010;24(5):643-60.

Souza SJP, André CG, Nildimar AH, Daniel CPC, Natali MS, Sarita TM, et al. Spatial and temporal distribution of *Aedes aegypti* and *Aedes albopictus* oviposition on the Coast of Paraná, Brazil, a recent area of dengue virus transmission. Tropical Medicine and Infectious Disease 2022;7(9):1-14.

Spencer J, Gustavo A. Kernel density estimation as a technique for assessing availability of health services in Nicaragua. Health Services and Outcomes Research Methodology 2007;7: 145-57.

Sun Q, Sijie W, Kaiqi Z, Fei M, Xiaozhuang G, Tingzhen L. Spatial pattern of urban system based on gravity model and whole network analysis in eight urban agglomerations of China. Mathematical Problems in Engineering 2019;2019: Article No. 6509726.

Verdonschot PFM, Anna ABL. Flight distance of mosquitoes (culicidae): A metadata analysis to support the management of barrier zones around rewetted and newly constructed wetlands. Limnologica 2014;45:69-79.

Waller LA, Carol AG. Applied Spatial Statistics for Public Health Data. New Jersey, United States: John Wiley and Sons, Inc; 2004.

Wang Z, Lin L, Hanlin Z, Minxuan L. How is the confidentiality of crime locations affected by parameters in kernel density estimation? ISPRS International Journal of Geo-Information 2019;8(12):1-12.

Wijayanti SPM, Thibaud P, Margo CT, Stephanie MR, Melanie M, Esther S, et al. The importance of socio-economic versus environmental risk factors for reported dengue Cases in Java, Indonesia. PLoS Neglected Tropical Diseases 2016; 10(9):1-15.

Zhang Y, Lei W, Guozhen W, Jiabao X, Tianxing Z. An ecological assessment of the potential pandemic threat of dengue virus in Zhejiang Province of China. BMC Infectious Diseases 2023;23(473)1-10.

Environment and Natural Resources Journal

Volume 22
Issue 2
2024

Faunal Diversity and the Ecological Aspects of a Community-Based Fragmented Lowland Rainforest Patch in Western Province, Sri Lanka

Buddhika Abeyrathne[1,2*], Nilanga Ranatunga[3], Sahani Chandrasiri[2], and Indrakheela Madola[4]

[1]Centre for Water Quality and Algae Research, Department of Zoology, Faculty of Applied Sciences, University of Sri Jayewardenepura, Sri Lanka
[2]Faculty of Graduate Studies, University of Sri Jayewardenepura, Sri Lanka
[3]Department of Biotechnology, Faculty of Agriculture and Plantation Management, Wayamba University of Sri Lanka, Makandura, Gonawila (NWP), Sri Lanka
[4]Department of Horticulture & Landscape Gardening, Faculty of Agriculture and Plantation Management, Wayamba University of Sri Lanka, Sri Lanka

ARTICLE INFO

Received: 17 Aug 2023
Received in revised: 9 Jan 2024
Accepted: 17 Jan 2024
Published online: 1 Feb 2024
DOI: 10.32526/ennrj/22/20230220

Keywords:
Faunal diversity/ Rainforest fragmentation/ Ecological aspects/ Water quality/ Wawekale rainforest reserve

*** Corresponding author:**
E-mail: bpabeyrathne@gmail.com

ABSTRACT

Wawekale Rainforest Reserve (WRR) is a primary lowland tropical rainforest area in the Western Province of Sri Lanka, established with diversity, but disturbed by human activities such as rubber cultivation, logging, poaching, chemical release, and the collection of firewood. Visual Encounter Surveys (VES) were conducted for 100 hours in the year 2022, which covered wide habitat distribution. The herpetofaunal diversity was measured in the WRR which can indicate broader ecological shifts, environmental changes, or habitat degradation. Water quality was measured in the WRR area to determine the ecosystem health and human impact. The study reports 171 species in 73 families, including two Critically Endangered (1.17%), six Endangered (3.51%), 16 Vulnerable (9.36%), and 14 Near Threatened (8.19%) species according to the IUCN Red List. The study area showed 51 endemic faunal species in Sri Lanka, which represented 29.83% of endemism. Based on the observations conducted on the herpetofauna diversity, the Shannon-Wiener diversity index (H) was calculated and the overall herpetofauna (H'_H) showed high diversity within the forest premises. The water quality of the forest fragment had an influence from anthropogenic activities such as removing forest cover, bathing, washing vehicles, and releasing agro-chemical compounds resulting in high water temperature, basic pH level, high electrical conductivity, and high total dissolved solid conditions. The WRR, designated under protection, exhibits the need for immediate remedial actions to mitigate human-induced pollution and deforestation, emphasizing the critical importance of implementing proactive conservation measures to sustain ecological integrity and preserve biodiversity.

1. INTRODUCTION

Sri Lanka is a tropical island situated in the Indian Ocean with a total land area of 65,610 km^2 (Weerakoon, 2012; Manawaduge et al., 2020). It is considered a global diversity hotspot along the Western Ghats (Bossuyt et al., 2004; Narayanan et al., 2021). The abundant biodiversity in Sri Lanka is a consequence of the diverse climatic, topographical, and soil conditions present on the island, which have given rise to a wide range of aquatic and terrestrial habitats. This region comprises a natural forest that still accounts for slightly more than 12% of the total land area (Premakantha et al., 2021). Environmental factors, including substantial rainfall, humidity, and dense undergrowth, are prevalent in these areas, providing a conducive environment for a diverse array of fauna (Karunarathna and Amarasinghe, 2011; Ranagalage et al., 2020). Nonetheless, the island's

Citation: Abeyrathne B, Ranatunga N, Chandrasiri S, Madola I. Faunal diversity and the ecological aspects of a community-based fragmented lowland rainforest patch in Western Province, Sri Lanka. Environ. Nat. Resour. J. 2024;22(2):119-128. (https://doi.org/10.32526/ennrj/22/20230220)

native forests are rapidly declining due to the expansion of settlements and agricultural land, resulting in detrimental effects on its rich biodiversity (Rodrigo and Manamendra-Arachchi, 2020). The loss of natural forests and other causes over the past 100 years, has led to the extinction of lots of fauna species.

Over 60% of Sri Lanka's native fauna find habitat within the Wet Zone forests (Rodrigo and Manamendra-Arachchi, 2020). Additionally, the southwest lowland forests exhibit a significant level of endemism, with nearly 90% of endemic vertebrate species concentrated in this region (Rodrigo and Manamendra-Arachchi, 2020). The wet zone forest reserves are scattered through the Central and Rakwana Mountain ranges. So from the inter-monsoon rain, Southwest-monsoon Season and Northeast-monsoon Season provide plenty of water and maintain a precious climate to the fauna habitat in this area. For example, 59 freshwater fish species have been recorded in these wet zone forest areas and 27 of them are endemic to Sri Lanka (Sudasinghe et al., 2021).

However, efforts to conserve forests are severely hampered by the existing state of forest fragmentation. Large, continuous forest regions can be broken up into smaller, isolated parts as a result of human activities like logging, farming, and urbanisation. This process is known as forest fragmentation. The interconnection of forest habitats is disrupted by this fragmentation, which results in a loss of biodiversity, decreased genetic variety in plant and animal populations, and greater susceptibility to invading species and diseases (De Matos et al., 2021). The fragmented forest sections are also more vulnerable to environmental stressors like climate change and severe weather. Numerous plant and animal species may experience growth and survival issues due to these fragmented areas' changed microclimates, which may result in population decreases and local extinctions. Whole ecosystems may be adversely affected by changes in wildlife migration patterns, pollination dynamics, and nutrient cycling, which can undermine their adaptability and resilience to environmental change (Valenzuela-Aguayo et al., 2020).

Wewekele Rainforest Reserve (WRR) is located in the Avissawella area in Sri Lanka, one of the fragmented forest patches in the lowland Wet Zone of Sri Lanka (Abeyrathne et al., 2020). The forest is situated in a dense community area that is frequently affected by anthropogenic interactions. Fragmentation can be seen by separating this forest from contacting Labugama-Kalatuwawa, Meethirigala or Yatiyanthota lowland rainforest areas. This study reports the data on faunal diversity, ecological aspects, community interactions and the threats posed to the animal species of Wewekele. It aims to enhance the current knowledge of biodiversity and conservation implications in this unique forest habitat.

2. METHODOLOGY

2.1 Study area

The WRR is situated within the Northern boundary of Ratnapura District in Sabaragamuwa Province and belongs to Western Province, Sri Lanka. It is located 1 km away from Avissawella Town. The study area is located between 06°56'30"-06°56'50"N and 80°12'30"-80°12'50"E (Figure 1), and also in the elevation 94 m-111 m a.s.1 (Ranatunga et al., 2019). The forest ecosystem, which also forms an important part of the forest cover within the Avissawella area, covers an area of more than 45 acres within the Seethawakapura Urban Council area and can be categorised as a lowland evergreen rainforest. The forest is situated in the Kotahera Grama Niladhari (GN) division surrounded by 1,465 population. This lowland wet forest consists of dominant tree species *Mesua* sp., *Doona* sp., *Dipterocarpus* sp., *Trichadenia zeylanica*, *Calamus thwaitesii*, *Entada pursaetha*, and *Coscinium fenestratum* (Ministry of Environment in Sri Lanka, 2012). The general forest floor is covered with cascading large boulders and leaf litter. The area is supported by rich waterways. Two main streams start from the mountain in the middle of the forest and finally, it terminates with the creation of Seetha Ella near the Avissawella Town. There is a rich water reservoir at the entrance of the forest with 4.05×10^{-3} km^2. The annual rainfall averages approximately 3,662 mm, with the majority of precipitation falling between November and May. From April to December, the weather undergoes a gradual transition to dry conditions, coinciding with the period of highest recorded temperatures. The WRR experiences an average annual temperature of 27.2°C, ranging from a maximum of 32.9°C to a minimum of 21.6°C. Access to the study area can be attained via either the Colombo-Rathnapura Road or the Kagalle-Avissawella Road.

2.2 Data collection

Dates of the field works were conducted in random numbered tables. A total of 15 field visits were conducted including day and night visiting, of a total of 100 hours in the year 2022. Visual encounter

surveys (VES) were conducted in 200 m line transects through 10 pathways. Night visits were conducted with the help of headlamps. Visual observations were conducted by searching 20 cm deep into the leaf litter (Figure 1). A comprehensive exploration was conducted across diverse habitats, encompassing water bodies, rock crevices, logs, trees, decaying vegetation, and bushes up to 5 metres in height, as well as the tree canopy, to detect reptiles, birds, mammals, fish, butterflies, dragonflies, snails, and amphibians (Karunarathna and Amarasinghe, 2011). The identification process involves the comparative method which allows a systematic approach used in faunal diversity studies especially compares the physical characteristics, behaviours and genetic details (Early-Capistrán et al., 2020; Munari and Mistri, 2008), and all species and colour variations were documented in live photographs using digital single-lens reflex cameras (Canon 80D and 600D). Three sites were identified and water samples for identifying the water quality variation in the WRR. Site 01: aquifer and a natural pool inside the WRR, Site 02: Reservoir of the WRR, and Site 03: Water-consuming pool for human use as follows. Onsite water quality measurements were conducted on water pH, temperature, total dissolved solid (TDS), electrical conductivity (EC), and relative dissolved oxygen (RDO) using a Thermo Scientific multimeter. Surface water samples were collected within the period of April-June, 2022 for the water quality analysis.

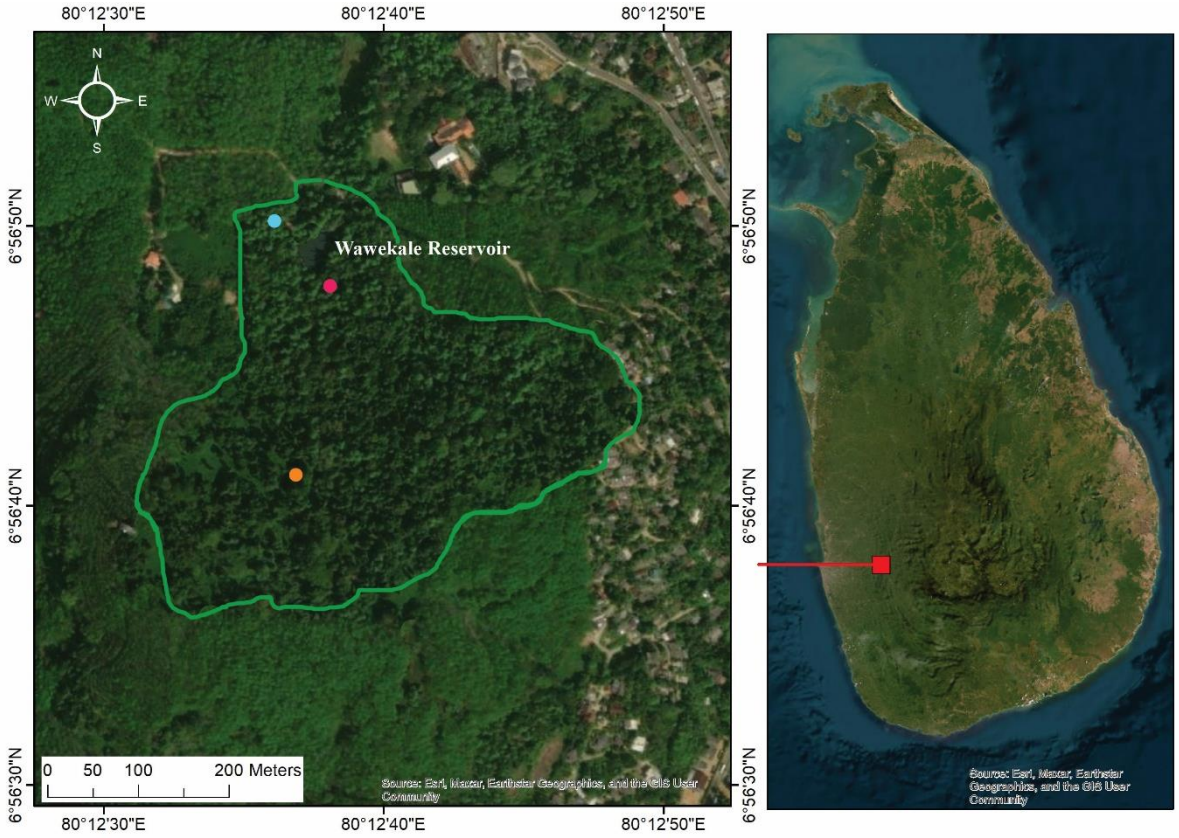

Figure 1. Geographical location and map of WRR (● Site 1: source of the stream and the natural pool, ● Site 2: the reservoir of WRR, ● Site 3: natural water pool with human activities and consumption)

2.3 Data analysis

The Shannon-Wiener Index [$H' = -\sum (pi \ln pi)$] was used to determine the herpetofauna diversity of species heterogeneity using the data about reptiles and amphibians (where, H'=species diversity, and pi=proportional frequency of the i^{th} species). Herpetofauna are the indicators of the ecological system functioning and can be used to create ecological indices (Trimurti et al., 2020). All the percentage values were calculated and graphed using Microsoft Excel 2013. The Geographical map was created using ArcGIS 10.8 software. One-way ANOVA was used to find out the variation in water quality measurements. When ANOVA was significant, the Tukey Pairwise post hoc comparison test was used to determine which means were significantly different. All statistical analyses were performed in Minitab 19™: statistical software for Windows (Minitab Inc, USA.)

2.4 Species identification

All the species identifications and classifications were conducted using standard guidebooks, expertise ideas and social media platforms. The standard guidebooks included Ukuwela and De Silva (2021), De Silva et al. (2015), De Silva (2009), Chathuranga et al. (2022), De Silva (2021), De Silva (2008), Warakagoda et al. (2012), Gamage (2013), Sumanapala (2017), Somaweera et al. (2023), Gunathilaka (2007), and the lists of Threatened species were based on the national Red List (Ministry of Environment in Sri Lanka, 2012). Also, the expertise group and page formed on Facebook named "Reptiles and Amphibians of Sri Lanka, and Snakes of Sri Lanka" contributed to identifying some reptile and amphibian species.

3. RESULTS AND DISCUSSION

3.1 Faunal species diversity

During this survey, 171 different fauna species were recorded in 73 families (Table 1) at the WRR. From the total number of recorded species, there were 51 species endemic to Sri Lanka.

During this survey, there were 68 (39.77%) different bird species recorded in 34 different families and 6 of them were endemic to Sri Lanka. Among them, *Dinopium benghalense*, *Megalaima flavifrons*, *Megalaima rubricapillus*, *Ocyceros gingalensis*, *Loriculus beryllinus*, and *Argya rufescens* were listed as endemic to Sri Lanka. Five species of birds were migrants. They were *Muscicapa muttui*, *Muscicapa latirostris*, *Pitta brachyura*, *Phylloscopus trochiloides*, and *Lanius cristatus.* During this study, the endemism of the birds of WRR was 8.82% and the endemism of birds in Sri Lanka was 2.50% (BirdLife International, 2023) respectively. Five migrant bird species were identified during the study.

From the recorded number of the reptiles, 33 (19.30%) species were recorded in 9 different families and 18 of them were endemic to Sri Lanka. From them *Otocryptis wiegmanni*, *Fowlea asperrima*, *Peltopeler trigonocephalus*, *Ahaetulla nasuta*, *Lycodon carinatus*, *Boiga ceylonensis*, *Boiga ranawanei*, *Bungarus ceylonicus*, *Calotes liolepis*, *Oligodon sublineatus*, *Aspidura guentheri*, *Hypnale zara*, *Hemidactylus depressus*, *Lankascincus fallax*, and *Lankascincus dorsicatenatus* are endemic to Sri Lanka. Furthermore, two diurnal geckoes were identified in the WRR and they were possibly *Cnemaspis tropidogaster* and *Cnemespis pava.* The endemism of reptiles in WRR was 54.55% and the endemism of reptiles in Sri Lanka was 8.53% accordingly (Ministry of Environment in Sri Lanka, 2012).

From this survey 11 (6.43%) amphibians have been recorded with 5 different families. There were 10 endemic species are among them as follows, *Indosylvirana temporalis*, *Hydrophylax gracilis*, *Indosylvirana serendipi*, *Indosylvirana serendipi*, *Minervarya kirtisinghei*, *Polypedates cruciger*, *Pseudophilautus folicola*, *Pseudophilautus popularis*, *Pseudophilautus stictomerus*, *Pseudophilautus schneideri*, and *Nannophrys ceylonensis*. In the WRR 90.91% of the amphibians were endemic to Sri Lanka. Furthermore, 9.01% of the Amphibians in Sri Lanka are endemic (Ministry of Environment in Sri Lanka, 2012).

During this survey, 13 (7.60%) freshwater fish species were recorded in six different families. Six of them were endemic to Sri Lanka as follows, *Channa orientalis*, *Belontia signata*, *Schistura notostigma*, *Puntius kelumi*, *Roshanella titteya*, and *Aplocheilus dayi*. Endemism of fish in WRR was 46.15% and endemism in Sri Lanka was 6.59% (Ministry of Environment in Sri Lanka, 2012) appropriately.

From the mammal records of 10 (6.06%) different species with 8 different families. Four species have been recorded endemic to Sri Lanka as follows, *Macaca sinica*, *Semnopithecus vetulus* ssp. *nestor*, *Loris tardigradus* ssp. *tardigradus*, *and Paradoxurus zeylonensis.* Altogether 40% of the mammal species were endemic to WRR. According to the Ministry of Environment in Sri Lanka (2012), 3.2% of the mammals in Sri Lanka have been recorded as endemic.

In this study, 22 (12.87%) different butterfly species were recorded in 4 different families with 2 endemic records as follows, *Pachliopta jophon* and *Troides darsius*. The endemism of the butterfly species at the WRR is 9.09%. Entirely 0.82% (Ministry of Environment in Sri Lanka, 2012) of the butterflies are endemic to Sri Lanka. From this survey, 11 dragonfly species were recorded in 5 different families. In the WRR 18.18% of the dragonflies are endemic. Altogether 1.69% (Ministry of Environment in Sri Lanka, 2012) of the dragonflies in Sri Lanka are endemic.

There were 3 (1.75%) air-breathing snail species recorded that belong to the *Acavidae* and *Ariophantidae* families. They are *Acavus superbus*, *Acavus phoenix*, and *Ariophanta chenui.* All the species were endemic to Sri Lanka. Endemism of the land snails in Sri Lanka was 1.19% according to the Red List (Ministry of Environment in Sri Lanka, 2012).

Out of the 171 species recorded during this study, 14 (8.19%) species were in the Near Threatened (NT) category, 16 (9.36%) species were in the Vulnerable (VU) category and 6 (3.51%) species were in the Endangered (EN) category, and 2 (1.17%) species were in the Critically Endangered (CR) species among them according to the IUCN Red Data List.

Table 1. Summary of Faunal species recorded during this survey

Faunal group	No. of families	No. of species	No. of endemic species	Endemism to the WRR (%)	Endemism to the Sri Lanka (%)
Birds	34	68	6	8.82	2.50
Reptiles	9	33	18	54.55	8.53
Amphibians	5	11	10	90.91	9.01
Fish	6	13	6	46.15	6.59
Mammals	8	10	4	40.00	3.20
Butterflies	4	22	2	9.09	0.82
Dragonflies	5	11	2	18.18	1.69
Snails	2	3	3	100.00	1.19
Total	73	171	51	29.82	3.66

3.2 Diversity of the forest with herpetofauna distribution

Herpetological diversity was measured with the amphibian and reptile distribution throughout the WRR. According to the classification scheme for the Shannon-Wiener Diversity Index (Table 2), overall herpetofauna (H'_H) was 3.29, indicating high diversity. The Shannon-Wiener Index for amphibian diversity (H'_A) was 2.56 and this value shows moderate diversity. The diversity value of the reptiles (H'_R) 3.15 shows high diversity inside the WRR. Most of the amphibian distribution was identified beside the walking paths and the stream banks. Most of the *Ranidae* and *Dicroglossidae* family amphibians dwelled through the steam channels and *Rhacophoridae* family amphibians were found at the shrub forest areas above the ground level 0.3-1.6 m.

Table 2. The Classification scheme for the Shannon Diversity Index (Baliton et al., 2020)

Relative values	Shannon-Wiener diversity index (H')
Very high	3.50 and above
High	3.00-3.49
Moderate	2.50-2.99
Low	2.00-2.49
Very low	1.99 and below

Reptile distribution was high in the area, especially *Peltopeler trigonocephalus*, *Hypnale hypnale*, *Hypnale zara*, and *Daboia russelii* were in high abundance in the WRR (Figure 2), and *Naja naja* in the forest entrance area. These species belong to the *Elapidae* and *Viperidae* families that hold venom that can do potential damage to humans. So, the villagers used to catch and relocate these species into WRR after rescuing these snakes within their livelihood or household premises. That may result in the moderate diversity level of amphibians within the WRR due to the high predator capacity for the prey. Most of the *Gekkonidae* family species were found in the walls of the research centre building and the large tree trunks.

Edge effects resulting from forest fragmentation can significantly impact faunal diversity. As forests are broken into smaller, isolated patches, the boundaries between these fragments become critical zones of change. These edges often exhibit altered microclimates, increased vulnerability to predation, and disruptions in habitat structure (Andriatsitohaina et al., 2020). Some species may thrive in these edge habitats, while others struggle to adapt. The overall result is a complex interplay of species shifts, reduced genetic diversity, and potential declines in animal populations. To conserve and enhance faunal diversity in fragmented landscapes, it is essential to understand and mitigate these edge effects through thoughtful conservation planning and habitat management strategies (Andriatsitohaina et al., 2020). In the study of WRR, edge effects were particularly pronounced, revealing how herpetofauna diversity suffered along the forest edges. These edges, intertwined with rubber plantation areas and those adjacent to the nearby village around 50 m away, showcased the profound ecological transformations resulting from forest fragmentation. Most of the forest edges are separated 2 m away from the rubber state boundary and are

mostly affected by chemical exposure and wood cuttings for human consumption. The altered microclimates and increased human activity near these edges disrupted the delicate balance between amphibians and reptiles, leading to declines in species richness and population numbers. This research underscores the critical importance of understanding and addressing edge effects in forest fragmentation scenarios, emphasising the need for holistic conservation strategies to safeguard the diverse and often fragile herpetofauna communities that inhabit these ecosystems.

Figure 2. Most abundant *Viperidae* family snake species in WRR [(a) *Peltopeler trigonocephalus*, (b) *Hypnale hypnale*, (c) *Daboia russelii*, (d) *Hypnale zara*]

3.3 Water quality study and fish ecology in WRR

The water quality of the WRR was analysed by identifying three major sites related to the WRR water stream. Water quality significantly affects the growth, reproduction, and overall ecosystem balance of aquatic organisms, making it crucial for their health and well-being. pH, TDS, and EC levels are three important variables that have a big impact on water quality (Sarda and Sadgir, 2015). A good environment for aquatic life is ensured by adequate pH levels within the ideal range, often between 6.5 and 8.5, by preventing severe acidity or alkalinity that can stress or injure species (Asante et al., 2008). The preservation of proper TDS levels, which indicate the concentration of dissolved minerals, aids in maintaining osmotic balance and guarantees that organisms' physiological processes are not jeopardised. A balanced electrical conductivity is also essential since it measures the water's electrical conductivity and shows whether or not it has the necessary ions for aquatic life (Jordan and Benson, 2015). These sensitive aquatic habitats can be disturbed by pollution-induced changes to these characteristics, which can result in a loss in species diversity, hampered reproduction, and unstable ecosystems. To protect aquatic environments and maintain the diversity and health of aquatic creatures, it is crucial to regularly monitor and adjust pH, TDS, and EC levels. Regular monitoring of the water quality in the resources is necessary to determine the overall health of the ecosystems (Jiang et al., 2020). Poor water quality, caused by factors such as water contamination and pollution effects can directly impact aquatic ecosystems, with the destruction of habitats and their well-being (Odume, 2017).

Site no 1 was the initial water aquifer fountain that initiated the water stream, which appeared as a natural pool with swallowed water with slow-moving

water flow. Moreover, the water body was filled with leaf debris, especially from the trees *Artocarpus nobilis*, *Ochlandra stridula*, and *Dipterocarpus zeylanicus*. According to the results site, No. 1 showed the acidic condition of the water that may be an effect of the leaf debris degradation and black water formation. Therefore that was an ideal place for fish ecology by forming small microhabitats. Specifically *Channa orientalis*, *Channa kelaartii*, *Roshanella titteya*, *Aplocheilus dayi*, and *Schistura notostigma* were abundant in this water body. The offspring were well distributed throughout the leaf debris which indicated that the pile of leaf debris provided a breeding ground for the fish species. These fish species prefer the high quality of water for the continuation of their breeding habitats, especially the *Roshanella titteya* presence in this area (Ranatunga and Abeyrathne, 2019; Abeyrathne et al., 2022). Site No. 2 is described as the reservoir that was a man-made water lake continuing from the British colonial era. That reservoir provided a home for aquatic reptiles, amphibians and some fish species. As fish species *Channa orientalis*, *Belontia signata*, *and Heteropneustes fossilis* frequently occurred in the lake banks. The lake was filled with leaf debris and soil weathered from the forest streams. As introduced and become invasive fish species *Oreochromis mossambicus* and *Osphronemus goramy* were highly identified in the lake area which may affect less native fish species occurrence in the observed water body. It is believed that invasive species are a major cause of the current decline in biodiversity. They can directly reduce native species' variety through predation or the spread of pathogens, but they can also have an indirect impact on native species by altering the distribution and accessibility of vital biological resources, such as food and breeding sites (Gracida-Juárez et al., 2022). Invasive species like *Oreochromis* sp. and *Osphronemus* sp. pose a significant threat to native fish and their ecosystems worldwide. They compete for vital resources, such as food and habitat, often outcompeting native species due to their adaptability. Invasive fish also act as aggressive predators, harming native populations and disrupting ecosystem balance. Their habitat alterations, disease transmission, and potential hybridization further jeopardize native fish. This disruption extends to ecosystem dynamics, impacting food webs and nutrient cycles. Economically, invasive species reduce native fish stocks, affecting livelihoods and availability. Mitigation efforts involve early detection, control, education, habitat restoration, and regulation. Addressing invasive species comprehensively is crucial to safeguard native fish populations and their habitats (Sunarto et al., 2022).

Site 3 is an anthropogenic consuming area that is frequently used for bathing, washing vehicles and less drinking purposes. The location was less covered with a tree canopy as a result of human influence in deforestation and with clear water flowing. There was a lack of presence of native fish species in this area but it was highly incorporated with schools of *Oreochromis mossambicus*.

According to the water quality variations throughout the stream (Table 3), there was a huge parameter variation that occurred in the water pH, TDS, and EC levels. From site 1 to site 3 water pH varied from acidic condition to basic condition with mainly effect from human interaction. There was particle contamination that occurred at site 3, which was highly affected by anthropogenic activities. Moreover, that water body is frequently polluted by polyethene, detergents, vehicle lubrication and oils. Water temperature (ANOVA $F=98.43$, $P<0.001$), Water pH (ANOVA $F=43.21$, $P<0.001$) and total dissolved solids (ANOVA $F=19463.36$, $P<0.001$) of the three sites were significantly different. These values were significantly higher in site 3 (ANOVA $F=144.61$, $P<0.001$). The electric conductivity of site 3 was significantly higher than the other two sites. Electric conductivity did not vary between site 1 and site 2. The lowest water temperature was recorded on site 2. The lowest water pH and total dissolved solids were recorded in site 1.

Table 3. Water quality variations in WRR

Water quality measurement	Site 1	Site 2	Site 3
Water temperature (°C)	29.70 ± 0.64^{b}	26.38 ± 0.36^{c}	31.12 ± 0.73^{a}
Water pH	4.95 ± 0.10^{c}	6.83 ± 0.06^{b}	8.00 ± 0.98^{a}
Electrical conductivity (µS/cm)	14.33 ± 1.51^{b}	22.00 ± 2.61^{b}	194.80 ± 35.9^{a}
Total dissolved solids (ppm)	7.17 ± 0.75^{c}	12.33 ± 1.03^{b}	220.00 ± 3.46^{a}

*Means that do not share a letter are significantly different.

3.4 Anthropogenic influence and conservation needs

A considerable land area of the WRR has been lost due to habitat fragmentation, and plant and animal pest invasion. Especially *Oreochromis mossambicus*, *Osphronemus goramy*, and *Trachemys scripta* through human involvement and hunting animals for flesh and engaging in irresponsible human actions. This may disrupt the balance of plant and animal ecosystems, potentially causing harm to various species and even leading to the degradation of the environment. This can occur notably through activities like deforestation for firewood and the indiscriminate collection of medicinal plants such as *Coscinium fenestratum*. Moreover, the WRR is surrounded by plantations of *Hevea brasiliensis* that provide economic stability to the area that may be influenced by excess run-off of sediment, fertiliser, industrial waste, chemicals and pesticides. Moreover, the extensive use of agrochemicals poses a significant menace to the local biodiversity, particularly impacting environmentally fragile amphibian species. The chronic overapplication of agrochemicals in agriculture can result in fatalities, deformities, and irregularities among amphibians (Rout et al., 2016). This poses a grave threat to the numerous endemic and endangered species confined to closed forests, placing them in imminent danger of extinction within the region. A specific concern is the practice of vehicle washing within the Western Rainforest Reserve (WRR) forest stream, which leads to the leakage of materials into local waterways. This not only exacerbates the adverse effects on biodiversity but also jeopardises the health of communities residing downstream. Materials such as non-biodegradable polyethene bags are indiscriminately dispersed within the monastery premises and along forest footpaths, causing disruptions to the delicate ecological equilibrium within the forest ecosystem (Fu et al., 2023). The WRR is a community-based forest fragment that mainly provides a water supply for the nearby villagers. As Seethawakapura Urban Council records 1465 villagers are staying in the nearby area of the WRR, especially because they rely on drinking, bathing and their day-to-day water usage through WRR water streams. Within the study, some of the common issues that occur in a forest were observed. In the Wawekale forest area, there were no proper forest boundaries. So illegal entrances, deforestation and illegal specimen collecting were observed within this study period. Also, the reservoir is filled with leaf debris and sand. Habitat loss and deterioration remain the dominant threat to all faunal populations at present.

These suggestions can keep the forest maintained at best as are they, developing the current building as a research station with a dormitory and lecture hall to provide facilities for research and education activities, maintaining a trail through the forest, providing identification checklist boards for birds, butterflies, and snakes, establishing a security point and ticket counter to stop illegal entering and finally carrying out awareness programs for people and students about the biodiversity of Wewekele and importance of protecting this hotspot. Habitat loss and deterioration remain the dominant threat to all faunal populations at present.

4. CONCLUSION

Based on the comprehensive findings of the present study, a firm conclusion can be drawn regarding the WRR as an exceptionally biodiverse region characterised by the highest levels of endemism and remarkable diversity across various taxonomic groups. The substantial presence of aquatic environments within the reserve fosters ideal habitats for a wide array of fauna. However, this study also brings to light a critical concern, indicating the forest's vulnerability to human encroachment primarily due to its proximity to anthropogenic areas. The burgeoning expansion of the town of Avissawella, driven by the textile industry and the establishment of the Seethawaka Export Promotion Zone (an industrial precinct), amplifies this threat. Consequently, the imperative arises for the formulation and implementation of comprehensive and integrated management strategies aimed at rationalising the protection of this invaluable natural asset. To achieve this, competent authorities must develop a well-structured strategy and action plan specifically designed to curtail human intrusion into the protected areas. Furthermore, the introduction of ecotourism initiatives should be considered, as they have the potential to yield long-term societal benefits, transcending short-term gains. By harmonising conservation efforts with sustainable human activities, the WRR can continue to thrive as an exemplar of biodiversity preservation and ecological stewardship.

ACKNOWLEDGEMENTS

We extend our sincere gratitude to the Seethawakapura Urban Council for their invaluable support in conducting the faunal diversity study in the

WRR. Their assistance greatly contributed to the success of our research. We appreciate their collaboration and commitment to environmental conservation. Moreover, we would like to express our gratitude to the villagers of the Kotahera area which is located near the WRR for all their tremendous support throughout the research work.

APPENDIX A. SUPPLEMENTARY DATA

Supplementary material related to this article can be found starting from Tables S1 to S8.

REFERENCES

Abeyrathne PABP, Ranatunga RAGN, Madola GKIS. Revealing study of faunal diversity in a fragmented lowland evergreen rain forest patch: Wawekele Reserve Forest, Avissawella, Sri Lanka. Journal of the Wildlife and the Nature Protection Society of Sri Lanka 2020;29:18-25.

Abeyrathne PABP, Ranatunga RAGN, Madola GKIS. Habitat and breeding ground preferences of the vulnerable fish species Sri Lankan Cherry Barb (*Puntius titteya*) according to the water quality in aquatic habitats in lowland wet zone, Sri Lanka. Proceedings of the International Research Conference of SLTC; 2022 Sep 29-30; Sri Lanka; 2022. p. 180-2.

Andriatsitohaina B, Romero-Mujalli D, Ramsay MS, Kiene F, Rasoloharijaona S, Rakotondravony R, et al. Effects of habitat edges on vegetation structure and the vulnerable golden-brown mouse lemur (*Microcebus ravelobensis*) in northwestern Madagascar. BMC Ecology 2020;20:1-13.

Asante KA, Quarcoopome T, Amevenku FYK. Water quality of the Weija Reservoir after 28 years of impoundment. West African Journal of Applied Ecology 2008;13:125-31.

Baliton R, Landicho L, Cabahug RE, Paelmo RF, Laruan K, Rodriguez R, et al. Ecological services of agroforestry systems in selected upland farming communities in the Philippines. Biodiversitas Journal of Biological Diversity 2020;21:707-17.

BirdLife International. Country profile: Sri Lanka [Internet]. 2023 [cited 2023 Sep 10] Available from: http://datazone.birdlife.org/country/sri-lanka.

Bossuyt F, Meegaskumbura M, Beenaerts N, Gower DJ, Pethiyagoda R, Roelants K, et al. Local endemism within the Western Ghats-Sri Lanka biodiversity hotspot. Science 2004;15:479-81.

Chathuranga D, De Silva A, Ukuwela K. A Photographic Field Guide to the Amphibians of Sri Lanka. Oxford, England: John Beaufoy Publishing; 2022.

De Matos TPV, De Matos VPV, De Mello K, Valente RA. Protected areas and forest fragmentation: Sustainability index for prioritizing fragments for landscape restoration. Geology, Ecology, and Landscapes 2021;5:19-31.

De Silva A. Snakes of Sri Lanka: A Coloured Atlas, with Accounts on Snakes in Archaeology, History, Folklore, Venomous Snakes, and Snakebite. Colombo, Sri Lanka: Amphibian and Reptile Research Organization of Sri Lanka; 2009.

De Silva M, Hapuarachchi N, Jayaratne T. Sri Lankan Freshwater Fishes: Wildlife Conservation Society, Galle. Sri Lanka: Vijitha Yapa Publications; 2015.

De Silva WG. A Naturalist's Guide to the Mammals of Sri Lanka. Oxford, England: John Beaufoy Publishing; 2021.

De Silva WG. A Photographic Guide to Mammals of Sri Lanka. Australia: New Holland; 2008.

Early-Capistrán MM, Solana-Arellano E, Abreu-Grobois FA, Narchi NE, Garibay-Melo G, Seminoff JA, et al. Quantifying local ecological knowledge to model historical bundance of long-lived, heavily-exploited fauna. PeerJ 2020;8:Article No. 9494.

Fu Y, Oduor AM, Jiang M, Liu Y. Live soil ameliorated the negative effects of biodegradable but not non-biodegradable microplastics on the growth of plant communities. bioRxiv 2023;2023:Article No. 10

Gamage R. An Illustrated Field Guide to the Fauna of Sri Lanka. Volume 1. Rajika Gamage; 2013.

Gracida-Juárez CA, Ioannou CC, Genner MJ. Competitive dominance and broad environmental tolerance favour invasive success of *Nile tilapia*. Hydrobiologia 2022;849:1161-76.

Gunathilaka SA. Freshwater Fishes of Sri Lanka. Colombo 4, Sri Lanka: Wildlife Heritage Trust of Sri Lanka; 2007.

Jiang J, Tang S, Han D, Fu G, Solomatine D, Zheng Y. A comprehensive review on the design and optimization of surface water quality monitoring networks. Environmental Modelling and Software 2020;132:Article No. 104792.

Jordan SJ, Benson WH. Sustainable watersheds: Integrating ecosystem services and public health. Environmental Health Insights 2015;9:1-7.

Karunarathna DMS, Amarasinghe AA. Reptile diversity of a fragmented lowland rain forest patch in Kukulugala, Ratnapura District, Sri Lanka. TAPROBANICA: The Journal of Asian Biodiversity 2011;2:86-94.

Manawaduge CG, Yakandawala D, Yakandawala K. Does the IUCN Red-Listing 'Criteria B'do justice for smaller aquatic plants? A case study from Sri Lankan Aponogetons. Biodiversity and Conservation 2020;29:115-27.

Ministry of Environment in Sri Lanka. The National Red List of Sri Lanka; Conservation Status of the Fauna and Flora. Colombo, Sri Lanka: Ministry of Environment (MOE); 2012.

Munari C, Mistri M. Biodiversity of soft-sediment benthic communities from Italian transitional waters. Journal of Biogeography 2008;35:1622-37.

Narayanan SP, Kumari S, Kurien VT, Thomas AP, Paliwal R, Julka JM. A comprehensive checklist of the earthworms (Annelida: Clitellata: Megadrili) of Sri Lanka, a component of the Western Ghats-Sri Lanka biodiversity hotspot. The Journal of "Grigore Antipa" National Museum of Natural History 2021;64:7-36.

Odume ON. Ecosystem approach to managing water quality. In: Water Quality. London, United Kingdom: IntechOpen; 2017.

Premakantha KT, Chandani RPDS, Kingsly SAD, Dias HU, Kekulandara NSB. Forest cover assessment in Sri Lanka using high resolution satellite images. The Sri Lanka Forester 2021;40:1-16.

Ranagalage M, Gunarathna MHJP, Surasinghe TD, Dissanayake D, Simwanda M, Murayama Y, et al. Multi-decadal forest-cover dynamics in the tropical realm: Past trends and policy insights for forest conservation in dry zone of Sri Lanka. Forests 2020;11:Article No. 836.

Ranatunga RAGN, Abeyrathne PABP, Madola GKIS. A preliminary study of the faunal diversity in a fragmented lowland evergreen rain forest patch: Wawekele Reserve Forest, Avissawella, Sri Lanka. Proceedings of the International Research Conference of the Uva Wellassa

University of Sri Lanka; 2019 Feb 7-8; Uva Wellassa University: Sri Lanka; 2019.

Ranatunga RAGN, Abeyrathne PABP. Importance of *Puntius titteya* as a biomarker to determine the water quality of aquatic habitats in the low and mid-country wet zone of Sri Lanka. Proceedings of 24th International Forestry and Environment Symposium; University of Sri Jayewardenepura, Sri Lanka; 2019. Article No. 24.

Rodrigo K, Manamendra-Arachchi K. Reconsidering the palaeo-environmental reconstruction of the wet zone of Sri Lanka: A zooarchaeological perspective. International Journal of Environmental and Ecological Engineering 2020;14:284-94.

Rout S, Baruah B, Mishra N, Panda T. Diversity of herpetofaunal community in Kuldiha wildlife sanctuary, Odisha, India. Current Life Sciences 2016;2:9-14.

Sarda P, Sadgir P. Assessment of multi parameters of water quality in surface water bodies: A review. International Journal for Research in Applied Science and Engineering Technology 2015;3:331-6.

Somaweera R, Wijayasekara S, Bandara S. Snakes of Sri Lanka (Sinhala language). 2nd ed. Colombo: Ruchira Somaweera; 2023.

Sudasinghe H, Raghavan R, Dahanukar N, Pethiyagoda R, Rüber L, Meegaskumbura M. Diversification and biogeography of Dawkinsia (Teleostei: Cyprinidae) in the Western Ghats-Sri Lanka Biodiversity Hotspot. Organisms Diversity and Evolution 2021;21:795-820.

Sumanapala AP. A Field Guide to the Dragonflies and Damselflies of Sri Lanka. Peliyagoda, Sri Lanka: Dilmah Conservation; 2017.

Sunarto A, Grimm J, McColl KA, Ariel E, Nair KK, Corbeil S, et al. Bioprospecting for biological control agents for invasive tilapia in Australia. Biological Control 2022:174;Article No. 105020.

Trimurti S, Sarina A, Lariman. Herpetofauna distribution and ecology in East Kutai District, East Kutai, East Kalimantan. International Journal of Innovative Science and Research Technology 2020;5:279-84.

Ukuwela K, De Silva A. A Naturalist's Guide to the Reptiles of Sri Lanka. 2nd ed. Oxford, England: John Beaufoy Publishing Ltd; 2021.

Valenzuela-Aguayo F, McCracken GR, Manosalva A, Habit E, Ruzzante DE. Human-induced habitat fragmentation effects on connectivity, diversity, and population persistence of an endemic fish, *Percilia irwini*, in the Biobío River basin (Chile). Evolutionary Applications 2020;13:794-807.

Warakagoda D, Inskipp C, Inskipp T, Grimmett R. Birds of Sri Lanka. London, United Kingdom: Helm; 2012.

Weerakoon DK. Brief overview of the biodiversity of Sri Lanka. In: Weerakoon DK, Wijesundara S, editors. The National Red List 2012 of Sri Lanka: Conservation Status of the Fauna and Flora. Colombo, Sri Lanka: Ministry of Environment; 2012.

Environment and Natural Resources Journal

Volume 22
Issue 2
2024

Composite Layered Double Hydroxide Zn-Al/Magnetic Biochar Modified for Highly Effective Malachite Green Adsorption

Erni Salasia Fitri[1], Risfidian Mohadi[2,3], Neza Rahayu Palapa[2], Susila Arita Rachman[4], and Aldes Lesbani[2,3*]

[1]Magister Programme in Environment Management, Sriwijaya University, Palembang 30139, Indonesia
[2]Research Center of Inorganic Materials and Coordination Complexes, Universitas Sriwijaya, Palembang 30139, Indonesia
[3]Master Program of Material Science, Graduate School Universitas Sriwijaya, Palembang 30139, Indonesia
[4]Department of Chemical Engineering, Universitas Sriwijaya, Palembang 30662, Indonesia

ARTICLE INFO

Received: 4 Oct 2023
Received in revised: 12 Jan 2024
Accepted: 18 Jan 2024
Published online: 20 Feb 2024
DOI: 10.32526/ennrj/22/20230276

Keywords:
Composite/ Malachite green/ Magnetic/ Biochar/ Layered double hydroxide/ Regeneration

*** Corresponding author:**
E-mail:
aldeslesbani@pps.unsri.ac.id

ABSTRACT

One of the main needs of humans is water, one source of water pollutantion is from dyes. Adsorption is the most popular method in removing pollutants as it is proven to be efficient. One of the dyes harmful to living things is malachite green. In this study, malachite green dye was removed using a layered double hydroxide (LDH) Zn-Al/magnetic biochar composite. The XRD, FTIR, BET, and VSM analyses show that the LDH Zn-Al, magnetic biochar, and LDH Zn-Al/magnetic biochar composite were successfully produced. The surface area of the Zn-Al/magnetic biochar composite made up of LDH increased from 9.621 m^2/g to 99.473 m^2/g. The point of zero charge of LDH Zn-Al and magnetic biochar were at pH 6, whereas the composite of these two materials was at pH 7. For LDH Zn-Al, magnetic biochar, and composite LDH Zn-Al/magnetic biochar, pH 8 is the ideal value for adsorption of malachite green. PSO (pseudo-second order) kinetics is the best-fit model. LDH Zn-Al, magnetic biochar, and LDH Zn-Al/magnetic biochar composite had adsorption capacities of 14.472, 15.552, and 25.907 mg/g, respectively, at a temperature of 60°C. Regeneration showed the LDH Zn-Al/magnetic biochar composite had superior and more effective ability compared to LDH Zn-Al and magnetic biochar.

1. INTRODUCTION

One of the main human needs is water. Rivers are one of the water sources used for daily human life. Therefore, river water must be clean from pollutants. One source of pollutants is dyes from the textile industry (Mahmoodi et al., 2018; Mokhtari-Shourijeh et al., 2020; Hosseinabadi-Farahani et al., 2015). The textile industry uses about 10,000 color pigments. Dye is lost during the drying process, and as much as 1-15% of the dye is released into wastewater (Lv et al., 2022). Dye effluent contains suspended particles and a high pH, and dyes are also hazardous to health because they have carcinogenic, genotoxic, mutagenic, and teratogenic properties (Hasanah et al., 2022; Yan et al., 2022; Mahmoodi et al., 2017). These problems can cause negative effects on the environment and health so ways are needed to overcome them. Many methods can be used to overcome liquid waste, especially dyes, such as precipitation, chemical degradation, photo-degradation, biodegradation, coagulation, and adsorption (Dai et al., 2022; Faggio et al., 2022; Li et al., 2022; Selvanathan et al., 2017; Mahmoodi and Mokhtari-Shourijeh, 2016; Mahmoodi et al., 2017). Among these methods, adsorption is the most popular method as it is proven to be efficient in removing pollutants from effluents (Palapa et al., 2020; dos Santos et al., 2021).

Adsorption is the most widely used technique for pollutant removal. This is due to its efficiency in removing very low amounts of contaminants from aqueous solutions, speed, cost-effectiveness,

Citation: Fitri ES, Mohadi R, Palapa NR, Rachman SA, Lesbani A. Composite layered double hydroxide Zn-Al/magnetic biochar modified for highly effective malachite green adsorption. Environ. Nat. Resour. J. 2024;22(2):129-144. (https://doi.org/10.32526/ennrj/22/20230276)

universality among numerous water treatment systems, ease of handling, excellent selectivity, and adsorbent regeneration (Badhai et al., 2020; Ho and Adnan, 2021; Liao et al., 2022; Rabeie and Mahmoodi, 2024). Layered double hydroxide is one of the materials that can be utilized in the adsorption method to purify water. This substance has been developed considerably because it is distinct and has good absorption. Due to its low cost and substantial surface area, it has a lot of potential for use as an adsorbent in the treatment of water (Bouteraa et al., 2020; Cheng et al., 2022; Zubair et al., 2022). According to Vithanage et al. (2020), stacked double hydroxide can be utilized as an adsorbent to remove organic and inorganic species, colors, and hazardous metal pollutants from water. Rathee et al. (2019) reported that layered double hydroxide applied as an adsorbent has limitations in the regeneration process. According to Normah et al. (2021) and Yuliasari et al. (2022), LDH tends to have unstable adsorption effectiveness due to damage to the layer structure during the application process. To create a composite, layered double hydroxide must be changed with supporting elements made of carbon. Composites are materials formed through the combination of two or more different materials and become one material microscopically where the forming material is still visible and does not change the properties of each material (Lee et al., 2019).

According to the research of Wijaya et al. (2021) malachite green was adsorbed using composite layered double hydroxide Cu-Al/carbon with an adsorption capacity of 49.505 mg/g. Congo red was adsorbed using layered double hydroxide Ni-Al with an adsorption capacity of 61.728 mg/g (Siregar et al., 2021). Research Mohadi et al. (2021) reported a malachite green dye using LDH Ca/Al had a maximum adsorption capacity of 43.860 mg/g, while Ca/Al which had been composited with biochar has an increase in maximum adsorption capacity to 71.429 mg/g. Layered double hydroxide CuAl and CuAl/biochar composites adsorb malachite green dye at an optimum pH of 9 with adsorption capacities of 20 mg/g and 25 mg/g, respectively (Palapa et al., 2020). Layered double hydroxide modified using carbon to improve performance stability in adsorbing dyes can also be used repeatedly (Palapa et al., 2019).

Zn-Al layered double hydroxide magnetic composites have been carried out by Ahmad et al. (2023) to adsorb congo red dye and produced better regeneration than using pristine layered double hydroxide. Making magnetic composites by combining layered double hydroxide with activated carbon, can combine the advantages of both types of materials, such as high adsorption capacity and good separation efficiency (Ahmad et al., 2023). Some of the advantages of using magnetic layered double hydroxide composite materials are efficient separation, efficient regeneration, and targeted control to direct adsorbents to specific areas using magnetic fields improves control over the adsorption process, especially in the case of dye removal. In addition, the use of magnetic materials can simplify the separation and adsorption process, reducing operational complexity. As for the disadvantage of using these materials, namely production costs, magnetic materials are often more expensive to produce compared to conventional adsorbents, and this can be an obstacle to their application. The selection of suitable magnetic materials that have good adsorption properties for certain dyes is a key factor in the success of adsorption (Ahmad et al., 2023). The first regeneration of a Zn-Al layered double hydroxide magnetic composite recovered up to 100% activity compared to Zn-Al layered double hydroxide at only 76.99% (Ahmad et al., 2023). In this study, LDH Zn-Al was composited with biochar magnets which were then characterized using XRD, FT-IR, BET, and VSM. Malachite green dye's ability to bind to different materials was determined by evaluating factors like pH, pHpzc, time, concentration, temperature, and material regeneration.

2. METHODOLOGY

2.1 Chemicals and instrumentation

Materials and tools used are zinc nitrate hexahydrate $Zn(NO_3)_2{\cdot}6H_2O$, aluminum nitrate nonahydrate ($Al(NO_3)_3{\cdot}9H_2O$) (Sigma-Aldrich, 375.13 g/mol), sulfuric acid (H_2SO_4), graphite, sodium hydroxide (NaOH) (EMSURE® ACS, 40 g/mol), sodium carbonate (Na_2CO_3) (EMSURE® ACS, 105.99 g/mol), sodium nitrate ($NaNO_3$), ferrous sulfate heptahydrate ($FeSO_4{\cdot}7H_2O$), ammonia (NH_3), hydrogen peroxide (H_2O_2), hydrochloric acid (HCl) (MallinckrodtAR®, 37%), distilled water (H_2O), biochar, malachite green ($C_{23}N_2H_{25}Cl$). The tools used were a magnetic stir bar, separatory funnel, hotplate, filter paper, analytical balance, oven, pH meter, shaker, standard glassware including Erlenmeyer, beaker, measuring cup, drip pipettes, and volumetric pipettes, analysis XRD Rigaku Miniflex-6000, Spectro-photometer FT-IR Shimadzu Prestige-21, BET

equipment Quantachrome Instruments, Spectrophotometer UV-Vis Biobase BK- UV 1800 PC, and VSM250-P2F.

2.2 Synthesis of Zn-Al LDH

Zn-Al layered double hydroxide synthesis was carried out with 100 mL of 0.75 M $Zn(NO_3)_2 \cdot 6H_2O$ mixed with 100 mL of 0.25 M $Al(NO_3)_3 \cdot 9H_2O$, then dripped into 50 mL of 2 M NaOH solution. NaOH was used to get the mixture's pH to 10, after which it was agitated for four hours at 80°C (Rahmadan et al., 2021; Palapa et al., 2019). The precipitate was stirred, then filtered and washed with distilled water to get rid of any contaminants. XRD analysis, FTIR spectrophotometer, BET, and VSM was utilized to characterize the solid produced after the precipitate was oven-dried.

2.3 Preparation of magnetic biochar

To make magnetic biochar, as much as 1 g of $FeCl_3$ dissolved in 3 mL of distilled water was mixed with 0.6 g of $FeSO_4 \cdot 7H_2O$ dissolved in 3 mL of distilled water. One gram of biochar was added to the mixed solution and then stirred for three hours. The mixture formed was slowly dripped with 3.5 mL NH_3 solution and then stirred for 30 min at 75°C. The solution formed was put into a 100 mL hydrothermal stainless steel autoclave. After that, the mixture was then heated for three hours at 150°C. Magnetite biochar solid product was filtered and dried at 40°C. Magnetite biochar solids were characterized using XRD, FT-IR, BET, and VSM tools (Ahmad et al., 2023; Cheng et al., 2022).

2.4 Preparation of composite magnetic biochar-modified layered double hydroxide Zn-Al

Fifteen mL each of 0.75 M Zn and 0.25 M Al solutions were combined, and the pH was then brought to 10 by adding 15 mL of NaOH solution. Three grams of biochar was then added after the mixture had been agitated for an hour to become homogenous and form a gel. $FeCl_3$ was added in the amount of 2 g, dissolved in 3 mL of distilled water, together with 1.6 g of $FeSO_4 \cdot 7H_2O$, and agitated for three hours at room temperature to create solution A. For 72 h, the solution was kept at 80°C. The mixture formed was slowly dripped with 7 mL NH_3 solution and stirred at 75°C for 30 min so that solution B was formed. Thirty minutes of stirring followed by adding solution B to solution A. The created solution was heated at 150°C for 72 h in a 100 mL hydrothermal stainless autoclave. The solid obtained was filtered washed with distilled water and dried in the oven at 100°C for 24 h. The dried Zn-Al/magnetite biochar composite was crushed and analyzed by XRD, FT-IR, BET, and VSM (Ahmad et al., 2023; Cheng et al., 2022; Siregar et al., 2021; Dai et al., 2022).

2.5 Performance of pH optimum

A total of 20 mL of dye at a concentration of 45 mg/L was put into a 100 mL beaker and the pH adjusted using NaOH and HCl solutions with pH variations of 2, 3, 4, 5, 6, 7, 8, 9, 10, and 11. Then the initial absorbance of each solution was measured using a UV-Vis spectrophotometer to determine the initial concentration at various pHs. A total of 0.02 g of materials was added to the malachite green dye selective solution and stirred for two hours. Centrifugation was used for the separation procedure, and a UV-Vis spectrophotometer was used to measure the filtrate (Wijaya et al., 2021; Normah et al., 2021; Lesbani et al., 2020).

2.6 Performance of pH point zero charges (pHpzc)

LDH Zn-Al, biochar, composite layered double hydroxide Zn-Al/Biochar, and magnetic Zn-Al/Biochar, were added in amounts of up to 0.02 g to 20 mL of a 0.1 M NaCl solutions that had been adjusted to pH values of 2, 3, 4, 5, 6, 7, 8, 9, 10, and 11. NaOH and HCl solutions with a concentration of 0.1 M were added to the NaCl solution to change the pH. A pH meter was used to test the final pH of the mixture after it had been agitated for 24 h. The correlation between the initial and final pHs was then plotted on a graph (Hasanah et al., 2022; Rathee et al., 2019; Siregar et al., 2022).

2.7 Adsorption of color substances

The adsorption process was carried out by adding 0.02 g of adsorbent to as much as 20 mL of a 60 mg/L malachite green dye solution, then stirring with adsorption contact times of 0, 5, 10, 15, 20, 30, 60, 90, 100, 120, 150, and 180 min. In the variation of concentration and temperature, concentrations of 60 mg/L, 70 mg/L, 80 mg/L, 90 mg/L, and 100 mg/L with temperature variations of 30°C, 40°C, 50°C, and 60°C were used (Zubair et al., 2022; Yuliasari et al., 2022; Liao et al., 2022). The solutions were stirred for two hours. After the stirring was complete, the adsorbent was separated from each dye solution using centrifugation. The separated solution was measured for absorbance value using a UV-Vis spectrophotometer.

2.8 Regeneration

By introducing adsorbents that have undergone the desorption process an ultrasonic instrument, the regeneration process is carried out. First, 1 g of adsorbent was added to 20 mL of a 50 mg/L solution of malachite green dye. Next, the mixture was agitated for two hours. The adsorbent that had been used was dried. After drying, 0.2 g of the residue was added to 10 mL of water solvent and desorbed for two hours using an ultrasonic device. The next regeneration process was carried out by mixing 0.2 g of desorbed adsorbent with as much as 20 mL of 50 mg/L of dye solution. The mixture was stirred for two hours and the residual concentration was measured using a UV-Vis spectrophotometer. The adsorbent then underwent the next regeneration (Mohadi et al., 2021; Palapa et al., 2020).

3. RESULTS AND DISCUSSION

3.1 Point of zero charge (PZC) of the adsorbent materials

In determining the state of zero-charged material on LDH Zn-Al, magnetic biochar, and LDH ZnAl/magnetic biochar composites, the pH pzc method was used. The pH pzc measurement was done by making 15 mL of a 0.1 M NaCl solution as and then adding 0.015 g of ZnAl layered double hydroxide material, magnetic biochar, or ZnAl/magnetic biochar layered double hydroxide composite. Then, the pH condition was adjusted by adding 0.1 M HCl and 0.1 M NaOH, and the solution was shaken for 24 h. Then, filtrates were taken and a pH meter recorded final pH from each material.

Figure 1 shows the state of the pH pzc graphs of ZnAl layered double hydroxide material, magnetic biochar, and ZnAl/magnetic biochar layered double hydroxide composite. The line intersection at pH pzc of layered double hydroxide ZnAl and magnetic biochar is seen at pH 6 and pH pzc of layered double hydroxide ZnAl/magnetic biochar composite is pH 7. At pH conditions from pH 6-7 for layered double hydroxide ZnAl and magnetic biochar materials, and layered double hydroxide ZnAl/magnetic biochar composite shows that pH > pH pzc. At pH < pH pzc, this indicates a positive charge on the adsorbent surface, so this can increase the adsorption capacity due to the attractive force between the positive charge of the adsorbent and the negative charge on the dye (Ahmad et al., 2023). Based on the research by Amri and Hanifah (2023) on the adsorption of malachite green using graphene oxide, the optimum pH > pHpzc on graphene oxide material. This suggests that the graphene oxide surface has a large number of negative charges. Due to the difference in charge between graphene oxide and the positively charged malachite green dye, there is an electrostatic interaction between the two materials.

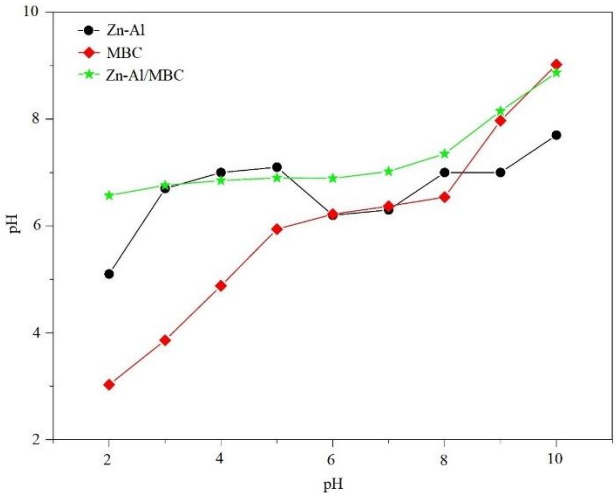

Figure 1. Pzc of adsorbent materials

3.2 Effect of pH

The effect of pH variation on the adsorption of malachite green on LDH adsorbent Zn-Al, magnetic biochar, and LDH composite Zn-Al / magnetic biochar is presented in Figure 2. Figure 2 shows an increase in the adsorbed concentration of LDH adsorbent Zn-Al, magnetic biochar, and LDH composite Zn-Al/ magnetic biochar. Figure 2 graph shows that the greatest adsorbed concentration of malachite green dye solution on LDH Zn-Al adsorbent, magnetic biochar, and LDH Zn-Al/magnetic biochar composite occurs at pH 8. The optimum pH of malachite green dye is at neutral pH, this is due to the effect of equilibrium on the solution. At the optimum pH, too acidic or too basic conditions will experience protonation and the complexes formed will dissociate. It can be seen that the pH pzc and pH optimum have a difference, this can mean that the adsorption that occurs is chemical. Zain et al. (2023) reported that at pH 8 a biocomposite made of chitosan, sepiolite clay, and algae absorbed malachite green with a maximum adsorption capacity of 515.7 mg/g. Malachite green dye adsorption on the surface of chitosan/sepiolite clay/algae biocomposite is thought to be caused by a variety of interactions, including electrostatic, H-bonding, and n- interactions. As a result, by altering the solution's pH, this pH-

sensitive chitosan/sepiolite clay/algae biocomposite exhibits a strong affinity for capturing both cationic and anionic dyes (Zain et al., 2023).

3.3 Characterization

The successful development of Zn-Al LDH adsorbent material, magnetic biochar, and Zn-Al LDH composite/ magnetic biochar is shown from the characterization results of XRD, FT-IR, BET, and VSM analysis. Synthesis of Zn-Al LDH material, magnetic biochar, and Zn-Al LDH composite/ magnetic biochar has diffractogram peaks of layered double hydroxide matched with JCPDS No. 48.2023 data for Zn-Al (Siregar et al., 2022). The characterization results of Zn-Al LDH, magnetic biochar, and composite LDH Zn-Al/magnetic biochar are presented in Figure 3.

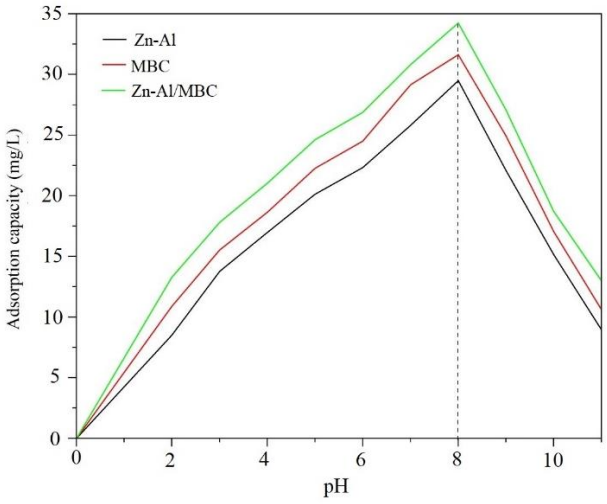

Figure 2. pH on adsorption of malachite green

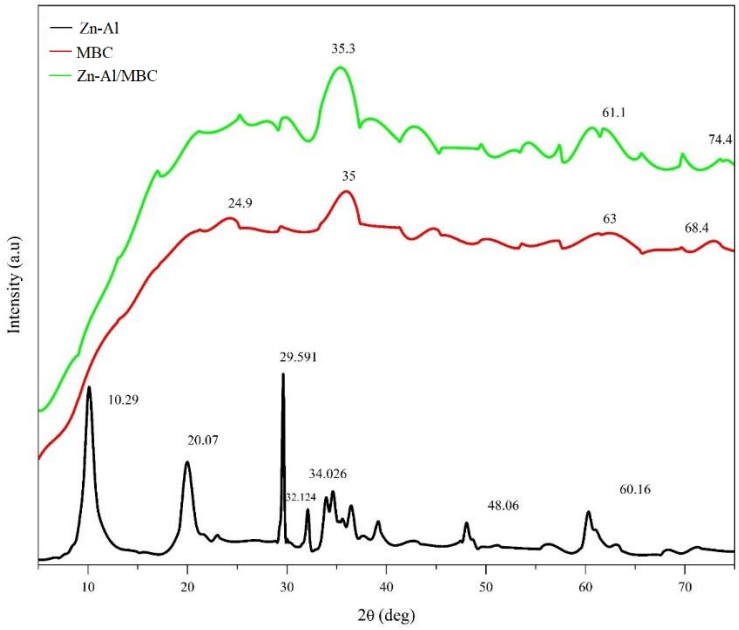

Figure 3. X-ray diffractogram of adsorbents

Typical diffractogram patterns of Zn-Al layered double hydroxide material with angles at 2θ, namely, diffraction peaks at 10.29°, 20.07°, 29.59°, 32.12°, 34.02°, 48.06°, and 60.16° allocated to planes (003), (006), (101), (012), (015), (107), and (110), were detected from XRD patterns. Based on the diffraction peaks the formation of the Zn-Al material structure follows the JCPDS file No 48-1023. According to Palapa et al. (2019), the double diffraction peak found at an angle of 60° is a typical diffraction pattern indicating that the Zn-Al layered double hydroxide material contains anions in the interlayer. Figure 3 explains that the biochar magnet has an angle at 2θ, namely the diffraction peaks at 24.9°, 35°, 63°, and 68.4° for the planes (220), (311), (422), and (440), respectively, while in the layered double hydroxide Zn-Al/magnetic biochar composite, the diffraction angle peaks are shown at 35.3° and 61.1° for the planes (311), and (110), respectively. This explains that magnetic biochar and layered double hydroxide Zn-Al/magnetic biochar composite have been successfully synthesized based on JCPDS file No.19-0619 (Ahmad et al., 2023; Fitri and Ardiansyah, 2023).

The successful synthesis of Zn-Al LDH material, magnetic biochar, and Zn-Al/magnetic biochar layered double hydroxide composite is also supported through FT-IR spectra presented in Figure

4. In Figure 4, there are vibrational peaks at wave numbers 3,441 cm^{-1}, 3,425 cm^{-1}, and 3,448 cm^{-1} this indicates the presence of O-H groups from water molecules in Zn-Al, magnetic biochar, and composite LDH Zn-Al/magnetic biochar. Wave numbers 2,376 cm^{-1} and 2,422 cm^{-1} on composite LDH Zn-Al/magnetic biochar, magnetic biochar, and Zn-Al indicate the presence of C≡C. In the composite LDH Zn-Al/magnetic biochar and magnetic biochar, there are wave numbers of 1,620 cm^{-1} and 1,635 cm^{-1} on the LDH indicating the presence of carbonyl groups C=O (Siregar et al., 2021).

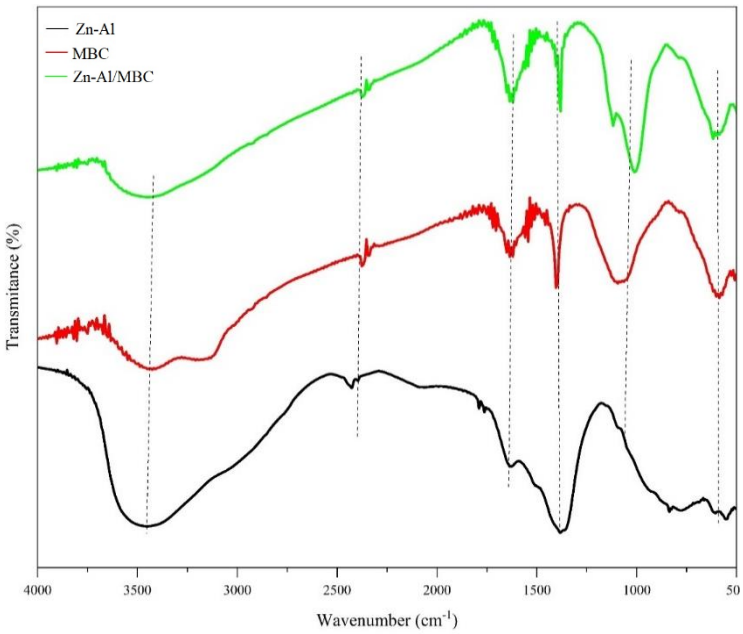

Figure 4. FTIR of adsorbents

In the Zn-Al layered double hydroxide, there is a wave number of 1,381 cm^{-1} indicating the vibration of the NO_3^- group, and wave numbers from 609 to 840 cm^{-1} indicating the presence of M-O vibrations in the form of Zn-O and Al-O. The wave number at 1,404 cm^{-1} in magnetic biochar indicates the presence of C-H carbon groups, at wave number 1,095 cm^{-1} there are C-O vibrations, and at wave number 586 cm^{-1} indicates the presence of magnetic Fe-O. The layered double hydroxide Zn-Al/magnetic biochar composite has wave numbers 1,110-1,120 cm^{-1} indicating the presence of aliphatic amines and wave numbers 580 cm^{-1} indicating the presence of M-O vibrations in Zn-O and Al-O. So it can be said that the synthesis of LDH Zn-Al, biochar magnet, and composite LDH Zn-Al/magnetic biochar has been successfully carried out (Ahmad et al., 2023; Rahmadan et al., 2021).

Using nitrogen adsorption and desorption, BET analysis is performed to learn more about a material's surface area and pore dispersion (Bagheri et al., 2021). Table 1 lists the outcomes of nitrogen adsorption and desorption tests on each adsorbent. The table shows that after modification into a layered double hydroxide Zn-Al/magnetic biochar composite, the surface area increased. This increase occurs because the layered double hydroxide materials have properties that allow them to expand more when composited in an aqueous medium.

The nitrogen adsorption-desorption isotherms for the different adsorbents utilized are shown on the graph in Figure 5. A hysteresis phenomena is depicted in the illustration. All the materials, i.e., LDH Zn-Al, magnetic biochar, and composite LDH Zn-Al/magnetic biochar, follow type IV in the nitrogen adsorption-desorption isotherm curve. Type IV indicates that the material belongs to the mesoporous category because the desorption curve is different from the adsorption curve, resulting in a hysteresis phenomenon. According to IUPAC, mesoporous materials have pore sizes between 2 to 50 nm. The isotherm graphs of various materials, Zn-Al LDH, biochar magnetic, and composite LDH Zn-Al/magnetic biochar are grouped into H2 type. According to Hu et al. (2020) type H2 indicates that the material has a mesoporous structure with pores that have wide loops.

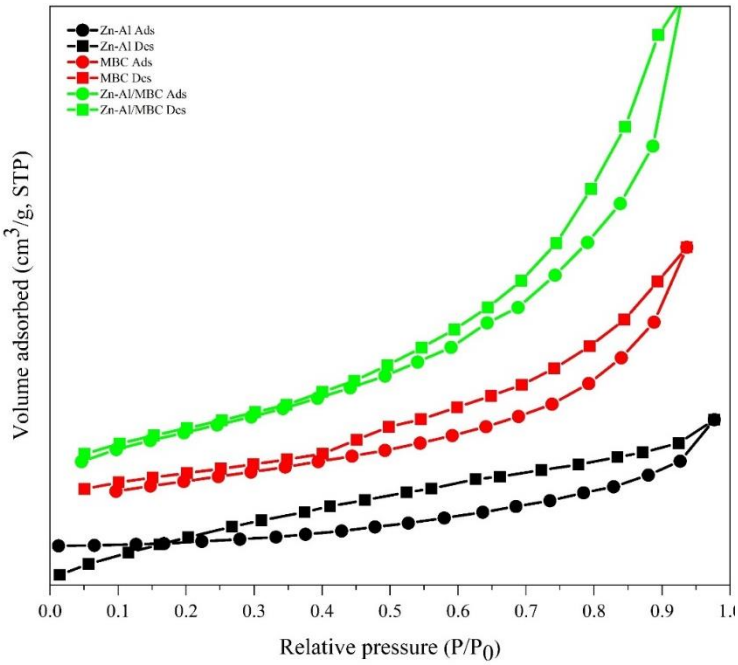

Figure 5. Graph nitrogen adsorption-desorption isotherms of adsorbents

Table 1 displays data on the surface area, pore volume, and pore diameter of the adsorbent materials. The Zn-Al LDH has a surface area of 9.621 m^2/g, while the surface area of magnetic biochar is 81.843 m^2/g. However, after undergoing the modification process into a layered double hydroxide Zn-Al/magnetic biochar composite material, the surface area of the adsorbent successfully increased to 99.473 m^2/g. It can be seen that the higher the carbon content in the material, the larger the surface area. The information in Table 1 also demonstrates that the relationship between surface area and pore volume is direct. In other words, the pore volume increases with surface area. However, there is a trend in the pore diameter size that is inversely related to the surface area and pore volume. The pore diameter gets narrower as the surface area grows in proportion to the pore volume. The Zn-Al material has the smallest surface area, which is 9.621 m^2/g, but has a pore volume of 0.017 cm^3/g. Although it has a small surface area, the pore diameter size in this material is the largest, reaching 12.094 nm. The XRD, FTIR, and BET characterization results proved that the Zn-Al LDH material, magnetic biochar, and Zn-Al/magnetic biochar layered double hydroxide composite have a stable structure. The modification process of this composite material successfully increased the surface area of the Zn-Al starting material.

Table 1. Adsorption-desorption isotherm analysis results of Zn-Al layered double hydroxide material, magnetic biochar, and Zn-Al layered double hydroxide material/magnetic biochar composite

Materials	Surface area (m^2/g)	Volume pore (cm^3/g)	Diameter pore (nm)
Zn-Al	9.621	0.017	12.094
Magnetic	81.843	0.127	4.136
Komposit	99.473	0.238	4.802

VSM (Vibrating Sample Magnetometer) characterization was performed to help understand the magnetic properties of biochar magnetic material and Zn-Al/magnetic biochar layered double hydroxide composite. The Hysteresis loop obtained can be seen in Figure 6. where the Hysteresis loop of magnetization appears like an S. Based on Figure 6 explaining the soft magnetic properties of the magnetite formed, it is observed that in the magnetic biochar and the layered double hydroxide Zn-Al/magnetic biochar composite, the magnetization is completely saturated at a value of 13.04 emu/g for pure magnetite and 9.67 emu/g in the composite. Coercivity (Hci), Magnetization (Ms), and Retentivity (Mr) values for magnetic biochar and layered double hydroxide Zn-Al/magnetic biochar composites, obtained from VSM.

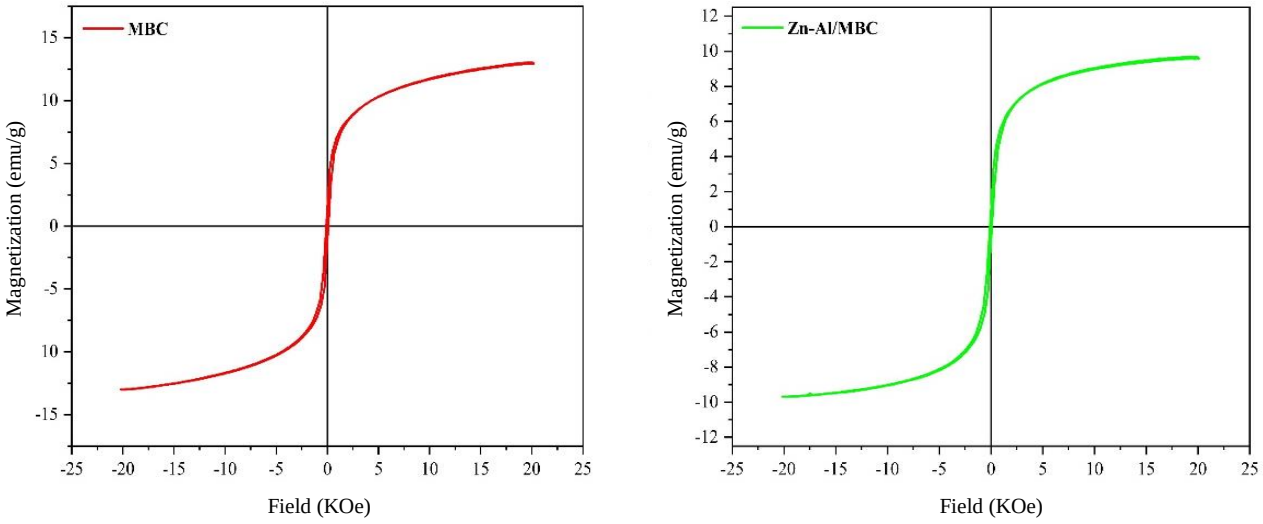

Figure 6. Graph vibrating sample magnetometer of adsorbents

The sharp decrease in Ms value for the layered double hydroxide Zn-Al/magnetic biochar composite may be due to the magnetic incorporation of biochar in the LDH Zn-Al framework, the LDH Zn-Al wall acts as a shield for the magnetic strength of Fe_3O_4. The low saturation magnetization in the composite may be due to the dispersion of nanoparticles in the layered double hydroxide Zn-Al matrix. The particle weight used for magnetic measurements is constant, hence the decrease in saturation magnetization is due to the increase in the amount of layered double hydroxide present in the magnetic composite layer. The layered double hydroxide on the surface of the magnetic composite decreases the surface moment resulting in a reduction in the magnetic moment in the magnetic composite. The magnetic composite has good magnetic stability so it has the ability an adsorption liquid waste. The magnetic composite also has the advantage of making regeneration easier when separating the adsorbent from the adsorbate. Figure 7 is a sample of magnetic biochar and layered double hydroxide Zn-Al/magnetic biochar composite.

Figure 7. Sample adsorbents of (a) magnetic biochar and (b) layered double hydroxide Zn-Al/magnetic biochar composite

3.4 Effect of time and kinetics

The adsorption ability of the prepared materials was proven through several parameters such as adsorption kinetics and thermodynamics. Kinetic parameters were carried out by making variations in adsorption time from 0 to 180 min which can be seen in Figure 8. The closest distance between the Qe_{exp} and Qe_{calc} values in Table 2 and the highest linear regression value are used to determine the PFO and PSO kinetic models (Sheikhmohammadi et al., 2019). While the PSO kinetic model assumes that the active sites of the adsorbent are available more than the potential bonding between the adsorbent and the adsorbate that occurs, the PFO kinetic model assumes that the bonding between the adsorbent and the adsorbate that occurs is proportional to the available active sites (Aqdam et al., 2021). The results of the variation of contact time of malachite green dye on layered double hydroxide Zn-Al and magnetic biochar seen in Figure 8 show that the equilibrium time is reached at 70 min and on the layered double hydroxide Zn-Al/magnetic biochar composite at 40 min. The

equilibrium time explains that the adsorption process has reached the optimum time where, after this time is reached, the resulting adsorption ability is not much different, resulting in a flat curve. This also shows the tendency towards the kinetics model of the adsorption process. It can be seen that all materials and their modifications are more likely to follow the PSO kinetics model than PFO. This determination is also evidenced by the data of linear regression values in Table 2.

Linear regression data on malachite green dye against Zn-Al ldh adsorbent, magnetic biochar, and composite LDH Zn-Al/magnetic biochar showed almost the same values of 0.9766, 0.9865, and 0.9896 in the PSO kinetic model. Based on this, it can be seen that the LDH Zn-Al, magnetic biochar, and LDH Zn-Al/magnetic biochar composites tend to follow the PSO kinetics model. The malachite green dye adsorbed using layered double hydroxide Zn-Al adsorbent, magnetic biochar, and layered double hydroxide Zn-Al/magnetic biochar composite all tend to follow the PSO kinetics model which can be seen from the linear regression values that are closer to 1. Based on these findings, it is established that the adsorption process happens on the active sites of the adsorbent that are available rather than the potential for adsorbent and adsorbate bonding. The Qe_{exp} value of each adsorbent, which is closer to Qe_{calc} from the PSO kinetics model, serves as more support for this.

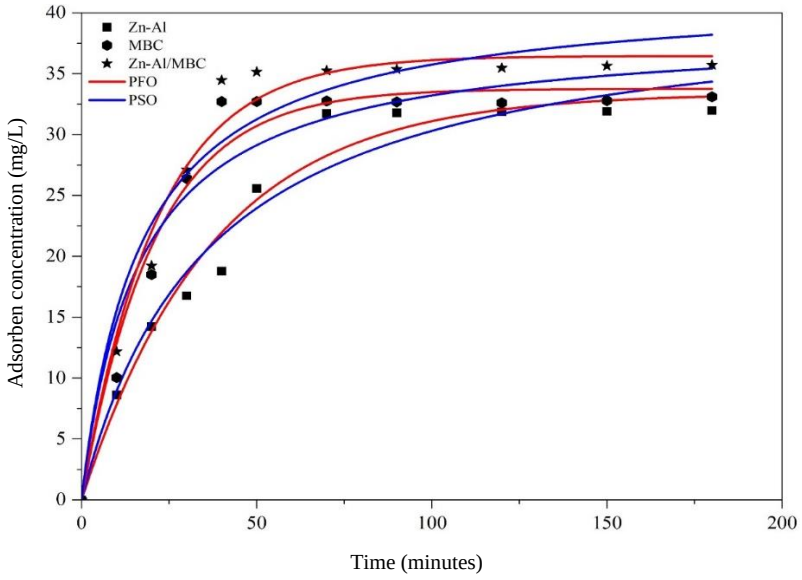

Figure 8. Model for adsorption kinetics

Table 2. Kinetic model of adsorption of malachite green dye on layered double hydroxide Zn-Al, magnetic biochar, and layered double hydroxide Zn-Al/magnetic biochar composite

Dye	Materials	Qe_{exp}	PFO			PSO		
		mg/g	k_1	Qe_{calc}	R^2	k_2	Qe_{calc}	R^2
Malachite green	Zn-Al	31.971	0.0325	20.8161	0.647	0.0008	39.5257	0.9766
	Magnetic biochar	33.114	0.0207	7.0340	0.4324	0.0021	36.2319	0.9865
	Composite	35.721	0.0272	10.7795	0.5991	0.0097	30.0030	0.9896

3.5 Effect of isotherms and thermodynamic studies

The adsorption isotherm and thermodynamic parameters were calculated using the effects of concentration and temperature on the adsorption of the dye malachite green. The Langmuir and Freundlich isotherm models are the two most often employed isotherm models. The Langmuir isotherm model, which presupposes the active side and energy contained on the adsorbent surface are homogeneous, explains that the adsorption process occurs chemically (chemisorption). In contrast to the Freundlich isotherm, which assumes that the adsorption process occurs physically (physisorption), this results in the interaction between the adsorbent and adsorbate only occurring in a single layer (monolayer) of the materials, resulting in a strong bond between the active side of the adsorbent and the adsorbate, namely the dye.

This assumes that the adsorption process occurs in many layers (multilayer). Table 3 shows the isotherm model can be done by looking at the linear regression value (R^2) which is closer to 1. The composite LDH Zn-Al/magnetic biochar and magnetic biochar tend to follow the Freundlich isotherm model, while the Zn-Al layered double hydroxide adsorbent and magnetic biochar tend to follow the Langmuir isotherm model, according to the data in Table 3. This is a result of the R^2 values becoming closer to 1. Table 3 also provides information on the adsorption capacity (Qm).

Table 3 shows the capacity of adsorption (Qm) of dye malachite green on Zn-Al layered double hydroxide, biochar magnetic, and composite LDH Zn-Al/magnetic biochar. The largest adsorption capacity of 25.907 mg/g occurs in LDH Zn-Al/magnetic biochar composite at 60℃, followed by magnetic biochar at 60℃ with an adsorption capacity (Qm) of 15.552 mg/g, and layered double hydroxide Zn-Al at 60℃ with an adsorption capacity (Qm) of 14.472 mg/g. The capacity of NiAl LDH/BC of 15.1 mg/g in the study of Palapa et al. (2022) achieved a satisfactory performance. This illustrates how effectively NiAl LDH/BC removes MG dye from aqueous samples. In Table 3, the Langmuir constant (KL) value is calculated to determine the strength of interaction between adsorbate and adsorbent surface. Data from Table 3 shows the KL value for each adsorbent tends to increase with increasing temperature. This indicates that the interaction between adsorbate and adsorbent is strong. This confirms that the layered double hydroxide Zn-Al/magnetic biochar composite has a greater adsorption capacity than its constituent materials, namely layered double hydroxide Zn-Al and magnetic biochar.

Table 3. Adsorption isotherm parameters of malachite green color on layered double hydroxide Zn-Al, magnetic biochar, and layered double hydroxide Zn-Al/magnetic biochar composites

Adsorbents	T(°C)	Qm	Model isotherms adsorption				
			Langmuir			Freundlich	
			Kl	R^2	n	Kf	R^2
ZnAl	30	0.227	0.015	0.9909	0.081	1.2331	0.8485
	40	0.361	0.017	0.9206	0.076	1.1015	06966
	50	0.432	0.018	0.5217	0.091	5.2601	0.2507
	60	14.472	0.030	0.9958	0.415	8.6139	0.9685
Magnetic	30	0.278	0.018	0.8785	0.047	2.4717	0.9942
	40	0.467	0.021	0.3777	0.049	3.9445	0.2615
	50	3.034	0.030	0.4541	0.162	1.7782	0.654
	60	15.552	0.085	0.9975	1.448	3.426	0.7634
Composites	30	2.125	0.019	0.9128	0.118	8.5703	0.9835
	40	2.124	0.020	0.8173	0.102	7.1285	0.9317
	50	4.274	0.034	0.5655	0.217	4.2785	0.7138
	60	25.907	0.143	0.9902	2.515	1.4564	0.5089

Enthalpy (ΔH), entropy (ΔS), and Gibbs free energy (ΔG) are three thermodynamic parameters that were identified during the adsorption of green malachite dye and are shown in Table 4-6. To ascertain whether the adsorption process is endothermic or exothermic, the enthalpy value (ΔH) in dye adsorption is measured. The entropy value (ΔS) of dye adsorption is determined to determine the degree of disorder during the process. Whether or not the adsorption process is spontaneous can be determined by looking at the value of Gibbs free energy (ΔG).

Table 4 shows the thermodynamic parameter data of malachite green dye adsorption on ZnAl layered double hydroxide adsorbent. In Table 4, the enthalpy (ΔH) is positive for layered double hydroxide ZnAl, which is 2.037-14.828 KJ/mol. This indicates that, during the adsorption phase, the reaction is endothermic. The entropy value (ΔS) is positive at 0.007-0.054 KJ/mol. This suggests that there is little chaos during the adsorption process. Given that the Gibbs free energy (ΔG) is negative, the adsorption of the dye malachite green occurs voluntarily. The thermodynamic parameter information for the adsorption of malachite green on biochar magnetic is displayed in Table 5. Biochar magnetic also exhibits a positive enthalpy value (ΔH) of 9.957-25.107 kJ/mol, similar to Zn-Al layered double hydroxide. This

indicates that the reaction that takes place during the adsorption process is endothermic. The entropy value (ΔS) on the biochar magnetic also shows a positive value of 0.033-0.90 j/mol/K. This indicates that the biochar magnetic when adsorbing green malachite has a small degree of irregularity during the adsorption process. The Gibbs free energy (ΔG) of the biochar magnetic when adsorbing green malachite is also negative, indicating that the adsorption process takes place spontaneously.

Table 4. Thermodynamic parameter data of adsorption of malachite green dye on layered double hydroxide adsorbent ZnAl

Concentration (mg/L)	Temperature (K)	Qe (mg/g)	ΔH (kJ/mol)	ΔS (J/K mol)	ΔG (kJ/mol)
	303	25.471	2.037	0.007	-0.080
	313	25.900			-0.150
50	323	26.150			-0.220
	333	26.400			-0.290
	303	31.079	8.653	0.029	-0.096
	313	32.186			-0.384
60	323	33.614			-0.673
	333	35.757			-0.962
	303	39.329	11.047	0.038	-0.531
	313	41.579			-0.914
70	323	43.329			-1.296
	333	46.186			-1.678
	303	48.150	12.899	0.046	-0.981
	313	51.079			-1.439
80	323	53.757			-1.897
	333	56.614			-2.355
	303	58.579	14.828	0.054	-1.481
	313	62.150			-2.020
90	323	65.579			-2.558
	333	68.614			-3.096

Table 5. Thermodynamic parameter data of adsorption of malachite green dye on biochar magnetic adsorbent

Concentration (mg/L)	Temperature (K)	Qe (mg/g)	ΔH (kJ/mol)	ΔS (J/K mol)	ΔG (kJ/mol)
	303	25.971	9.957	0.033	-0.167
	313	27.400			-0.501
50	323	29.186			-0.836
	333	30.257			-1.170
	303	34.293	14.149	0.049	-0.697
	313	37.150			-1.187
60	323	39.293			-1.677
	333	41.471			-2.167
	303	44.043	16.786	0.059	-1.217
	313	46.900			-1.811
70	323	50.471			-2.405
	333	52.971			-2.999
	303	53.043	19.714	0.070	-1.628
	313	56.614			-2.333
80	323	61.614			-3.037
	333	63.757			-3.741
	303	62.900	25.107	0.090	-2.026
	313	67.900			-2.922
90	323	74.329			-3.817
	333	76.471			-4.713

Table 6. Thermodynamic parameter data of adsorption of malachite green dye on layered double hydroxide ZnAl/magnetic biochar composite adsorbent

Concentration (mg/L)	Temperature (K)	Qe (mg/g)	ΔH (kJ/mol)	ΔS (J/K mol)	ΔG (kJ/mol)
	303	28.829	9.505	0.034	-0.652
	313	29.543			-0.987
50	323	30.257			-1.323
	333	33.114			-1.658
	303	37.221	14.810	0.052	-1.074
	313	38.650			-1.599
60	323	40.793			-2.123
	333	44.329			-2.647
	303	46.829	16.500	0.060	-1.577
	313	48.257			-2.173
70	323	52.650			-2.770
	333	54.757			-3.367
	303	55.507	20.605	0.074	-1.876
	313	57.650			-2.618
80	323	62.864			-3.360
	333	65.900			-4.102
	303	64.757	29.316	0.104	-2.070
	313	66.543			-3.106
90	323	76.471			-4.142
	333	78.614			-5.178

Table 6 shows the thermodynamic parameter data of green malachite dye adsorption on composite LDH Zn-Al/magnetic biochar adsorbent material. Similar to the LDH Zn-Al and magnetic biochar, the composite LDH Zn-Al/magnetic biochar adsorbent also has a positive enthalpy value (ΔH) of 9.505-29.316 kJ/mol. This informs that when adsorbing green malachite dye, the composite LDH Zn-Al/magnetic biochar has an endothermic reaction during the adsorption process. The entropy value (ΔS) of the composite LDH Zn-Al/magnetic biochar is the same as the LDH Zn-Al and magnetic biochar which shows a positive value of 0.034-0.104 j/mol/K. This indicates that the LDH Zn-Al/magnetic biochar composite, when adsorbing malachite green dye, has a small degree of disorder. The Gibbs free energy (ΔG) of the layered double hydroxide ZnAl/magnetic biochar composite is also the same as the layered double hydroxide Zn-Al and magnetic biochar when the adsorption of malachite green is negative, indicating that the adsorption process takes place spontaneously. Table 7 provides information on the adsorption capacities that have been made by other researchers.

Table 7. Adsorption of malachite green using other adsorbents

Adsorbent	Adsorption capacity (mg/g)	References
Rice husk/MnO	68.534	Emilia et al. (2023)
NiFe-POM	8.81	Lesbani et al. (2020)
Apricot carbon activated	17.60	Abbas (2020)
Magnetic GO/Fe_3O_4	59	Li et al. (2021)
Magnetic reduced graphene oxide nanocomposite	77.1	Sadegh et al. (2021)
M-Sp	69.444	Hasanah et al. (2023)
Camphor leaf	68.9	Hu et al. (2019)
MBC	76.471	This Study
Zn-Al/MBC	78.614	This Study

3.6 Adsorbents' capacity for re-use

By employing ultrasonics to remove the adsorbate from the adsorbent surface, regeneration is the process of using the materials again. The regeneration process can be done through adsorption and desorption steps first. After going through the adsorption and desorption steps, 0.2 g aliquots of LDH Zn-Al, magnetic biochar, and composite LDH Zn-Al/magnetic biochar were used to adsorb malachite green dye. The results of the regeneration of LDH Zn-Al, magnetic biochar, and composite LDH Zn-Al/magnetic biochar against malachite green dye can be seen in Figure 9. Figure 9 shows that the composite LDH Zn-Al/magnetic biochar against malachite green dye can adsorb as much as 92.25% of maximum capacity after the first regeneration, 82.61% after the second regeneration, 72.20% after the third regeneration, 68.47% after the fourth regeneration, and 55.46% after the fifth regeneration. The magnetic biochar was able to adsorb as much as 85.05% malachite green dye after the first regeneration, 79.74% after the second regeneration, 67.89% after the third regeneration, 64.15% after the fourth regeneration, and 51.87% after the fifth regeneration. The Zn-Al layered double hydroxide material had the smallest adsorption ability to malachite green dye compared to the other two adsorbents, namely, 79.24% after the first regeneration, 61.78% after the second regeneration, third regeneration 46.34%, fourth regeneration 37.16% and fifth regeneration 29.60%. This can be seen from the instability in Figure 9 that results from the repeated use of LDH Zn-Al, magnetic biochar, and composite LDH Zn-Al/magnetic biochar. Adsorption of malachite green by Amri and Hanifah (2023) using graphene oxide material from the first cycle to the fifth cycle decreased by 40.19%. This shows that adsorption with composite LDH Zn-Al/magnetic biochar is more effective in regeneration.

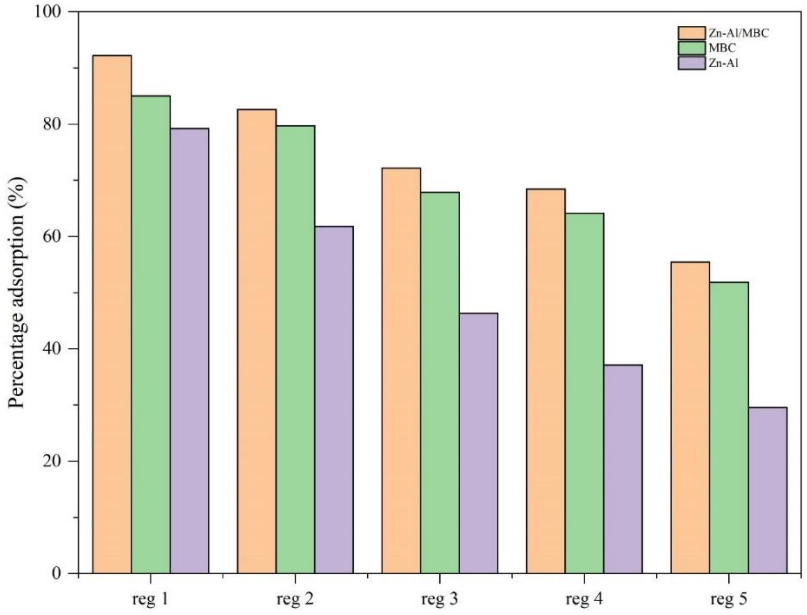

Figure 9. Reusability of adsorbent materials

3.7 Mechanism of malachite green adsorption

Figure 10 shows the adsorption mechanism of malachite green with the composite layered double hydroxide Zn-Al/magnetic biochar. Physical adsorption explains how malachite green can enter the pores of biochar and bind through van der Waals forces and capillary forces. Biochar with a large pore structure will provide a large surface area for malachite green to adsorb. Chemical adsorption allows composite layered double hydroxide on biochar to chemically interact with malachite green. This may involve the formation of chemical bonds or electrostatic interactions between the functional groups on malachite green and the layered double hydroxide groups on the hydroxy layer. These interactions can increase adsorption power and adsorption stability. Ion exchange occurs where malachite green is a charged compound, the layered double hydroxide on biochar can act as an ion exchange site, where positively charged malachite green can exchange with negative ions on the LDH, increasing the adsorption of the compound. The

adsorption capacity is optimized by applying optimum pH, optimum time, optimum concentration, and temperature (Palapa et al., 2022; Ahmad et al., 2017; Rahmadan et al., 2021; Dai et al., 2022).

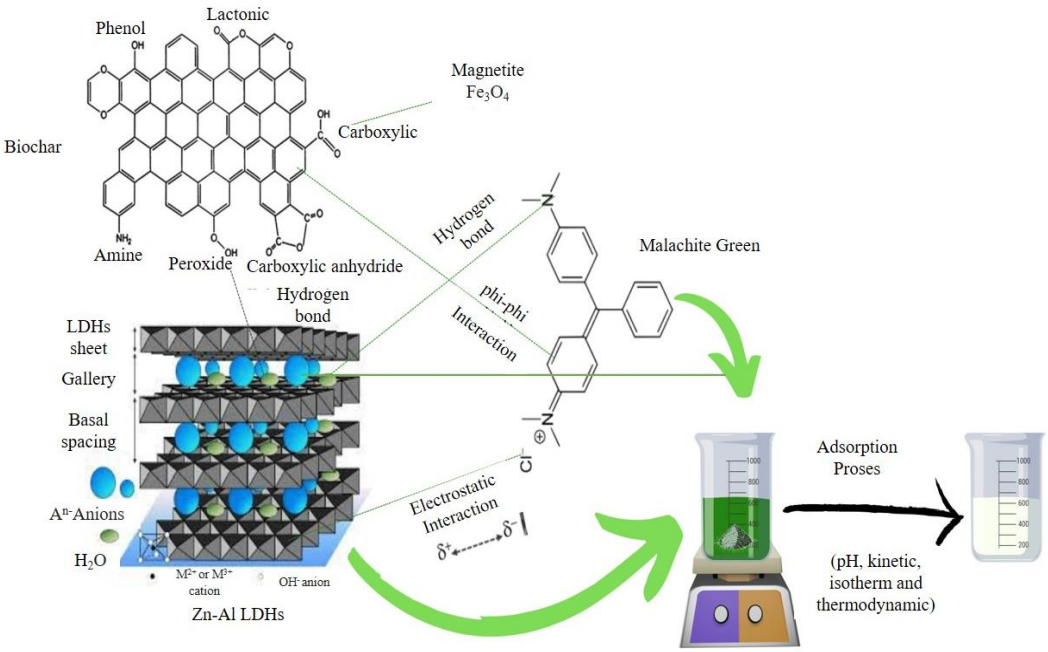

Figure 10. Adsorption mechanism of composite layered double hydroxide Zn-Al/magnetic biochar

4. CONCLUSION

According to this study's XRD, FTIR, BET, and VSM analyses, the Zn-Al, magnetic biochar, and Zn-Al/magnetic biochar composite were effectively synthesized. Regarding pH, Zn-Al and magnetic biochar had a pH of 6, whereas the composite of these two materials was pH 7. For Zn-Al, magnetic biochar, and composite Zn-Al/magnetic biochar, pH 8 is the ideal value for adsorption of malachite green. The PSO (pseudo-second order) kinetics model serves as the basis for this adsorption. The reaction is typically endothermic, the Gibbs Free Energy (ΔG) tends to occur spontaneously, and the isotherm parameters on Zn-Al, magnetic biochar, and Zn-Al/magnetic biochar composite against malachite green dye tend to follow the Langmuir isotherm model. The adsorption capacity of the magnetic Zn-Al/biochar composite at 60°C was found to be up to 25.907 mg/g. Regenerated magnetic Zn-Al/biochar composite showed superior performance of up to 92.25% of initial capacity.

ACKNOWLEDGEMENTS

The support and analytical assistance provided by the Research Center of Inorganic Materials and Coordination Complexes at Sriwijaya University allowed the author to complete this study.

REFERENCES

Abbas M. Experimental investigation of activated carbon prepared from apricot stones material (ASM) adsorbent for removal of malachite green (MG) from aqueous solution. Adsorption Science and Technology 2020;38(1-2):24-45.

Ahmad MA, Afandi NS, Bello OS. Optimization of process variables by response surface methodology for malachite green dye removal using lime peel activated carbon. Applied Water Science 2017;7(2):717-27.

Ahmad N, Arsyad FS, Royani I, Lesbani A. Charcoal activated as template Mg/Al layered double hydroxide for selective adsorption of direct yellow on anionic dyes. Results in Chemistry 2023;5:Article No. 100766.

Amri A, Hanifah Y. Synthesis of graphene oxide using hummers method as adsorbent of malachite green dye. Indonesian Journal of Material Research 2023;1(1):29-34.

Aqdam SR, Otzen DE, Mahmoodi NM, Morshedi D. Adsorption of azo dyes by a novel bio-nanocomposite based on whey protein nanofibrils and nano-clay: Equilibrium isotherm and kinetic modeling. Journal of Colloid and Interface Science 2021;602:490-503.

Badhai P, Kashyap S, Behera SK. Adsorption of phenol red onto GO-Fe_3O_4 hybrids in aqueous media. Environmental Nanotechnology, Monitoring and Management 2020;13: Article No. 100282.

Bagheri A, Hoseinzadeh H, Hayati B, Mahmoodi NM, Mehraeen E. Post-synthetic functionalization of the metal-organic framework: Clean synthesis, pollutant removal, and antibacterial activity. Journal of Environmental Chemical Engineering 2021;9(1):Article No. 104590.

Bouteraa S, Saiah FBD, Hamouda S, Bettahar N. Zn-M-CO_3 layered double hydroxides (M=Fe, Cr, or Al): Synthesis, characterization, and removal of aqueous Indigo Carmine.

Bulletin of Chemical Reaction Engineering and Catalysis 2020;15(1):43-54.

Cheng S, Zhao S, Xing B, Liu Y, Zhang C, Xia H. Preparation of magnetic adsorbent-photocatalyst composites for dye removal by the synergistic effect of adsorption and photocatalysis. Journal of Cleaner Production 2022;348:Article No. 131301.

Dai X, Yi W, Yin C, Li K, Feng L, Zhou Q, et al. 2D-3D magnetic NiFe layered double hydroxide decorated diatomite as multi-function material for anionic, cationic dyes, arsenate, and arsenite adsorption. Applied Clay Science 2022;229:Article No. 106664.

dos Santos TC, Mancera RC, Rocha MV, da Silva AF, Furtado IO, Barreto J, et al. CO_2 and H_2 adsorption on 3D nitrogen-doped porous graphene: Experimental and theoretical studies. Journal of CO_2 Utilization 2021;48:Article No. 101517.

Emilia D, Hakim YM, Mohadi R. Mangan oxide-assisted in biochar improvement and application in malachite green removal. Indonesian Journal of Material Research 2023; 1(2):35-43.

Faggio N, Zuppardi F, Staiano C, Poggetto GD, D'Ayala GG, Cerruti P. Removal of anionic and cationic dyes from aqueous solution using thermo- and pH-responsive amphiphilic copolymers. Journal of Water Process Engineering 2022; 49:Article No. 103107.

Fitri ES, Ardiansyah R. Study and characterization of hydrochar from duku (*Lansium domesticum*) peel. Indonesian Journal of Material Research 2023;1(2):44-50.

Hasanah M, Juleanti N, Priambodo A, Arsyad F, Lesbani A, Mohadi R. Utilization of rambutan peel as a potential adsorbent for the adsorption of malachite green, procion red, and congo red dyes. Ecological Engineering and Environmental Technology 2022;23(3):148-57.

Hasanah M, Wijaya A, Arsyad FS, Mohadi R, Lesbani A. Preparation of c-based magnetic materials from fruit peel and hydrochar using snake fruit (*Salacca zalacca*) peel as adsorbents for the removal of malachite green dye. Environment and Natural Resources Journal 2023;21(1):67-77.

Ho ZH, Adnan LA. Phenol removal from aqueous solution by adsorption technique using coconut shell activated carbon. Tropical Aquatic and Soil Pollution 2021;1(2):98-107.

Hosseinabadi-Farahani Z, Hosseini-Monfared H, Mahmoodi NM. Graphene oxide nanosheet: Preparation and dye removal from binary system colored wastewater. Desalination and Water Treatment 2015;56(9):2382-94.

Hu H, Wageh S, Al-Ghamdi AA, Yang S, Tian Z, Cheng B, et al. NiFe-LDH nanosheet/carbon fiber nanocomposite with enhanced anionic dye adsorption performance. Applied Surface Science 2020;5(11):Article No. 145570.

Hu Y, Zhu Y, Zhang Y, Lin T, Zeng G, Zhang S, et al. An efficient adsorbent: Simultaneous activated and magnetic ZnO doped biochar derived from camphor leaves for ciprofloxacin adsorption. Bioresource Technology 2019;288:Article No. 121511.

Lee SY, Choi JW, Song KG, Choi K, Lee YJ, Jung KW. Adsorption and mechanistic study for phosphate removal by rice husk-derived biochar functionalized with Mg/Al-calcined layered double hydroxides via co-pyrolysis. Composites Part B: Engineering 2019;176:Article No. 107209.

Lesbani A, Taher T, Palapa

NR, Mohadi R, Rachmat A, Mardiyanto. Preparation and utilization of Keggin-type polyoxometalate intercalated Ni-Fe layered double hydroxides for enhanced adsorptive removal of cationic dye. SN Applied Sciences 2020;2(3):Article No. 470.

Li W, Xu M, Cao Q, Luo J, Yang S, Zhao G. Magnetic GO/Fe_3O_4 for rapid malachite green (MG) removal from aqueous solutions: A reversible adsorption. RSC Advances 2021; 11(32):19387-94.

Li L, Cheng M, Qin L, Almatrafi E, Yang X, Yang L, et al. Enhancing hydrogen peroxide activation of CuCo layered double hydroxide by compositing with biochar: Performance and mechanism. Science of the Total Environment 2022;828:Article No. 154188.

Liao W, Zhou X, Cai N, Chen Z, Yang H, Zhang S, et al. Simultaneous removal of cadmium, lead, chromate by biochar modified with layered double hydroxide with sulfide intercalation. Bioresource Technology 2022;360:Article No. 127630.

Lv HW, Jiang HL, He FA, Hu QD, Zhong ZR, Yang YY. Adsorption of anionic and cationic dyes by a novel crosslinked cellulose-tetrafluoroterephthalonitrile-tannin polymer. European Polymer Journal 2022;180:Article No. 111602.

Mahmoodi NM, Mokhtari-Shourijeh Z. Preparation of aminated nanoporous nanofiber by solvent casting/porogen leaching technique and dye adsorption modeling. Journal of the Taiwan Institute of Chemical Engineers 2016;65:378-89.

Mahmoodi NM, Hosseinabadi-Farahani Z, Chamani H. Dye adsorption from single and binary systems using NiO-MnO_2 nanocomposite and artificial neural network modeling. Environmental Progress and Sustainable Energy 2017;36(1):111-9.

Mahmoodi NM, Karimi B, Mazarji M, Moghtaderi H. Cadmium selenide quantum dot-zinc oxide composite: Synthesis, characterization, dye removal ability with UV irradiation, and antibacterial activity as a safe and high-performance photocatalyst. Journal of Photochemistry and Photobiology B: Biology 2018;188:19-27.

Mohadi R, Palapa NR, Lesbani A. Preparation of ca/al-layered double hydroxides/biochar composite with high adsorption capacity and selectivity toward cationic dyes in aqueous. Bulletin of Chemical Reaction Engineering and Catalysis 2021;16(2):244-52.

Mokhtari-Shourijeh Z, Langari S, Montazerghaem L, Mahmoodi NM. Synthesis of porous aminated pan/pvdf composite nanofibers by electrospinning: characterization and direct red 23 removals. Journal of Environmental Chemical Engineering 2020;8(4):Article No. 103876.

Normah N, Palapa NR, Taher T, Mohadi R, Utami HP, Lesbani A. The ability of composite Ni/Al-carbon-based material toward readsorption of iron(II) in aqueous solution. Science and Technology Indonesia 2021;6(3):156-65.

Palapa NR, Rahayu BR, Taher T, Lesbani A, Mohadi R. Kinetic adsorption of direct yellow onto Zn/Al and Zn/Fe layered double hydroxides. Science and Technology Indonesia 2019;4(4):Article No. 101.

Palapa NR, Taher T, Rahayu BR, Mohadi R. CuAl LDH / rice husk biochar composite for enhanced adsorptive removal of cationic dye from aqueous solution. Science and Technology Indonesia 2020;16(3):540-8.

Palapa NR, Taher T, Normah N, Lesbani A. NiAl layered double hydroxide/rice husk composite for the efficient removal of malachite green. Indonesian Journal of Chemistry 2022; 22(1):142-56.

Rabeie B, Mahmoodi NM. Heterogeneous MIL-88A on MIL-88B hybrid: A promising eco-friendly hybrid from green synthesis to dual application (Adsorption and photocatalysis) in tetracycline and dye removal. Journal of Colloid and Interface Science 2024;654:495-522.

Rahmadan J, Parhusip V, Palapa NR, Taher T, Mohadi R, Lesbani A. ZnAl-humic acid composite as adsorbent of cadmium(II) from aqueous solution. Science and Technology Indonesia 2021;6(4):247-55

Rathee G, Awasthi A, Sood D, Tomar R, Tomar V, Chandra R. A new biocompatible ternary layered double hydroxide adsorbent for ultrafast removal of anionic organic dyes. Scientific Reports 2019;9(1):Article No. 16225.

Sadegh N, Haddadi H, Arabkhani P, Asfaram A, Sadegh F. Simultaneous elimination of rhodamine B and malachite green dyes from the aqueous sample with magnetic reduced graphene oxide nanocomposite: Optimization using experimental design. Journal of Molecular Liquids 2021; 343:Article No. 117710.

Selvanathan M, Yann KT, Chung CH, Selvarajoo A, Arumugasamy SK, Sethu V. Adsorption of copper(II) ion from aqueous solution using biochar derived from rambutan (*Nephelium lappaceum*) peel: Feedforward neural network modeling study. Water, Air, and Soil Pollution 2017; 228(8):Article No. 299.

Sheikhmohammadi A, Yazdanbakhsh A, Moussavi G, Eslami A, Rafiee M, Sardar M, et al. Degradation and COD removal of trichlorophenol from wastewater using sulfite anion radicals in a photochemical process combined with a biological reactor: Mechanisms, degradation pathway, optimization, and energy consumption. Process Safety and Environmental Protection 2019;123:263-71.

Siregar PMSBN, Palapa NR, Wijaya A, Fitri ES, Lesbani A. Structural stability of Ni/Al layered double hydroxide supported on graphite and biochar toward adsorption of congo red. Science and Technology Indonesia 2021;6(2):85-95.

Siregar PMSBN, Lesbani A, Mohadi R. Mg/Al-chitosan as a selective adsorbent in the removal of methylene blue from aqueous solutions. Science and Technology Indonesia 2022;7(2):170-8.

Vithanage M, Ashiq A, Ramanayaka S, Bhatnagar A. Implications of layered double hydroxides assembled biochar composite in adsorptive removal of contaminants: Current status and future perspectives. Science of the Total Environment 2020;737: Article No. 139718.

Wijaya A, Siregar PMSBN, Priambodo A, Palapa NR, Taher T, Lesbani A. Innovative modified of Cu-Al/c (c=biochar, graphite) composites for removal of procion red from aqueous solution. Science and Technology Indonesia 2021;6(4): 228-34.

Yan J, Li K, Yan J, Fang Y, Liu B. A magnetically recyclable magnetic graphite oxide composite functionalized with polydopamine and β-cyclodextrin for cationic dyes wastewater remediation: Investigation on adsorption performance, reusability, and adsorption mechanism. Applied Surface Science 2022;602:Article No. 154338.

Yuliasari N, Badri AF, Wijaya A, Siregar PMSBN, Amri A, Mardiyanto M, et al. Modification of Mg/Al-LDH intercalated metal oxide (Mg/Al-Ni) to improve the performance of methyl orange and methyl red dyes adsorption process. Science and Technology Indonesia 2022;7(3):275-83.

Zain ZM, Abdulhameed AS, Jawad AH. A pH-sensitive surface of chitosan/sepiolite clay/algae biocomposite for the removal of malachite green and remazol brilliant blue r dyes: Optimization and adsorption mechanism study. Journal of Polymers and the Environment 2023;31:501-18.

Zubair M, Aziz HA, Ihsanullah I, Ahmad MA, Al-Harthi MA. Engineered biochar supported layered double hydroxide-cellulose nanocrystals composite-: Synthesis, characterization, and azo dye removal performance. Chemosphere 2022; 307:Article No. 136054.

Environment and Natural Resources Journal

Volume 22
Issue 2
2024

Monitoring Land Surface Temperature Relationship to Land Use and Land Cover in Hai Duong Province, Vietnam

Bui B. Thien[1*], Asya E. Ovsepyan[1], and Vu T. Phuong[2,3]

[1]*Institute of Earth Sciences, Southern Federal University, Rostov-on-Don, 344090, Russian Federation*
[2]*Innovation Startup Support Center, Hong Duc University, Thanh Hoa, 40130, Vietnam*
[3]*Faculty of Social Sciences, Hong Duc University, Thanh Hoa, 40130, Vietnam*

ARTICLE INFO

Received: 21 Jul 2023
Received in revised: 21 Jan 2024
Accepted: 23 Jan 2024
Published online: 13 Feb 2024
DOI: 10.32526/ennrj/22/20230194

Keywords:
Land surface temperature/ Land use and land cover/ Vegetation cover/ Normalised Difference Vegetation Index/ Hai Duong Province

*** Corresponding author:**
E-mail:
buibaothienha@gmail.com

ABSTRACT

This study utilised remote sensing data and ArcGIS 10.8 software to evaluate changes in land use and land cover (LULC) and their effects on land surface temperature (LST) in Hai Duong Province, Vietnam, from 1992 to 2022. Landsat satellite data were pre-processed and classified using supervised methods for the years 1992, 2010, and 2022. In 1992, vegetation cover accounted for 57.89% of land cover, increasing to 84.49% in 2010, but then decreasing again to 66.67% in 2022. In contrast, the built-up area consistently increased, from 2.88% in 1992 to 29.35% in 2022, as most of the barren land present in 1992 became built-up area in 2022. The LST values were calculated from the thermal bands for the years 1992, 2010, and 2022 and ranged from 16.09°C to 34.27°C, 17.04°C to 36.74°C, and 11.03°C to 28.44°C, respectively. In addition, the Normalized Difference Vegetation Index (NDVI) values were calculated using the near-infrared band and the red band, with values ranging from -0.40 to 0.70 over the study period. A linear regression analysis indicated a shift in the correlation between NDVI and LST from positive to negative. This study highlights the significant transformation that occurred in Hai Duong Province due to rapid population density increases, urban growth and infrastructure development, leading to a decline in greenery. These LULC changes can cause severe environmental damage. These research findings will assist policymakers in formulating management strategies and sustainable land-use plans to minimize potential harm and promote sustainable development in the area.

1. INTRODUCTION

Climate change has a considerable influence on agriculture, both direct and indirect, making it a significant environmental issue worldwide. Its effects include changes in precipitation patterns, extreme temperature stress and alterations in land surface temperature (LST), which reduce crop health and productivity (Laux et al., 2017; Zia et al., 2017; Praveen and Sharma, 2019; Hammad et al., 2019; Zamin et al., 2019; Celik, 2020; Skendžić et al., 2021). These changes have driven to rural-to-urban migration, significantly affecting land use and land cover (LULC) patterns (Silva et al., 2018; Ritse et al., 2020). Understanding LST patterns is crucial for climate change research and protecting the environment (Donelson et al., 2018; Monroe et al., 2019). Multiple factors, including soil composition, changes in vegetation cover and the presence of permeable and impermeable surfaces, can affect LST patterns. Furthermore, green cover and vegetation play critical roles in mitigating LST in urban areas, making them more resilient to the effects of climate change (Ahmed et al., 2009; Winsemius et al., 2018; Mubeen et al., 2021; Hussain and Karuppannan, 2023).

LULC changes exert a significant influence on the provision of ecosystem services and affect ecosystem functions at the local, regional and global levels (Das and Das, 2019; Li et al., 2021; Phuong and

Citation: Thien BB, Ovsepyan AE, Phuong VT. Monitoring land surface temperature relationship to land use and land cover in Hai Duong Province, Vietnam. Environ. Nat. Resour. J. 2024;22(2):145-157. (https://doi.org/10.32526/ennrj/22/20230194)

Thien, 2023a). These changes also affect human variables, such as environmental and political plans (Roberts et al., 2018). Studying LULC changes provides valuable information to understand past practices, current models, and future directions. Change detection techniques, classified by whether they use pixel-, feature- or object-level image processing, are used to categorise LULC changes and different techniques can be used to detect changes (Tang and Di, 2019; Xu et al., 2019; Sahin et al., 2022; Thien et al., 2023a). Earlier research has established that LULC changes can have considerable environmental effects, particularly on the urban climate (Yao et al., 2020; Sahin et al., 2022).

Remote sensing (RS) and geographic information systems (GIS) have proven very effective in analysing and evaluating LULC and LST changes (Owolabi et al., 2020; Hu et al., 2023; Hussain and Karuppannan, 2023; Zeren Cetin et al., 2023). Satellite-based RS provides general LULC data at specific times and locations, and RS and GIS together can be used to map and identify LULC and LST changes. Recently, studies have relied heavily on remote spatial information from satellites to map individual plant species and describe changes in plant types. The Normalised Difference Vegetation Index (NDVI) is essential for monitoring vegetation cover and its response to climate change (Estrella et al., 2021; Fayech and Tarhouni, 2021; Phuong and Thien, 2023b). NDVI values reflect plants' biological activities (Guha, 2021; Bohanon and Crane, 2022). Daily changes in LST can be described through NDVI values, indicating the state of the vegetation cover (Fatemi and Narangifard, 2019; Mukherjee and Singh, 2020; Nse et al., 2020; Hussain and Karuppannan, 2023). NDVI values also help with the study of plants' global and regional ecological cycles. The vegetation response to environmental changes, plant life cycles and vegetation health can all be observed by NDVI (Workie and Debella, 2018; Rizvi et al., 2021; Sajan et al., 2023).

In Vietnam, studies of LST have primarily been conducted in large urban areas, such as Hanoi, Ho Chi Minh City, and Da Nang (Son et al., 2017; Thanh Hoan et al., 2018; Nguyen et al., 2019; Veettil et al., 2023; Veettil and Van, 2023). However, no such work has been performed in the neighbouring areas, such as Hai Duong Province, which are also starting to encounter problems as the expansion of impermeable surface areas causes surface temperatures to rise. Monitoring such issues can help policymakers take early steps to adopt appropriate policies to correct and mitigate the resulting problems. This study's main aim is to investigate the impact of LULC changes on LST in Hai Duong Province from 1992 to 2022 by utilising RS techniques, particularly NDVI. The investigation will also assess the relationship between LULC changes and the effects of climate change in the area. The results will provide policymakers and land managers with essential information to make informed decisions regarding LULC changes in the province. The specific objectives of this study are to (i) assess LULC changes; (ii) calculate LST; (iii) examine changes in vegetation cover using NDVI; and (iv) analyse the relationship between NDVI and LST in Hai Duong Province in 1992, 2010, and 2022.

2. METHODOLOGY

2.1 Study area

This research focuses on Hai Duong Province located in the Red River Delta region of Vietnam. The province spans approximately 1,668.24 km^2, ranging between longitude 106°09′47″ E to 107°04′37″ E and latitude 20°40′38″ N to 21°42′38″ N (General Statistics Office, 2022). It consists of two cities, one town, and nine districts, with Hai Duong City serving as its economic, political, and cultural center. The province is known for its agricultural activities, particularly rice cultivation, due to its relatively flat topography. Additionally, it hosts several industrial zones, such as the Nam Sach and Dai An Industrial Zones, which contribute significantly to its economic growth. The climate of the province is of the tropical monsoon type, featuring warm and humid summers and cool and dry winters. The yearly temperature in the area usually varies between 24 and 26°C, while the average annual precipitation amounts to 1,500-1,800 mm. Natural disasters such as floods, typhoons, and landslides, however, occasionally affect the province's agricultural sector, infrastructure, and people. The study area map was shown in Figure 1.

2.2 Landsat data

Satellite images from Landsat 5-TM (1992 and 2010) and Landsat 8-OLI/TIRS (2022) were downloaded freely from the United States Geological Survey (USGS) website (https://earthexplorer.usgs.gov/) (Table 1) to study LULC changes in the study area. A total of six images were downloaded, covering two frames with path/rows of 126/045 and 126/046, and were collected in winter to minimize the impact of cloud cover on the detection of LULC changes. The

LULC model was classified into four groups: vegetation, build-up, barren land, and water bodies, based on field survey information and high-resolution Google Earth Pro images. The accuracy of the LULC classification map was evaluated using 300 points for each year, with samples collected from Google Earth Pro for 1992 and 2010, and field surveys conducted for 2022.

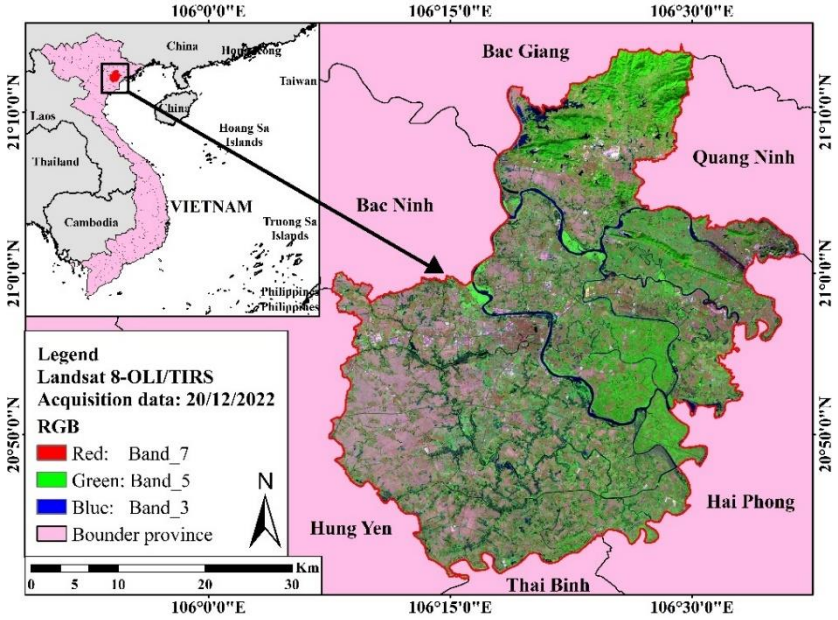

Figure 1. Study area map of Hai Duong Province, Vietnam

Table 1. Detailed data summary of satellite imagery used in the study

Landsat scene ID	Acquisition data	Satellite	Image quality	Cloud cover land (%)	Path/row
LT51260451992336BJC00	01/12/1992	Landsat 5-TM	9	0.00	126/045
LT51260461992336BJC00			7	0.00	126/046
LT51260452010305BKT00	01/11/2010	Landsat 5-TM	7	0.00	126/045
LT51260462010305BKT00			7	0.00	126/046
LC81260452022354LGN00	20/12/2022	Landsat 8-OLI/TIRS	9	9.96	126/045
LC81260462022354LGN00			9	4.62	126/046

2.3 Image processing and classification

In the preparation of Landsat satellite imagery for this study, co-registering to the UTM zone 48N projection using the WGS-84 datum was essential, accomplished through the utilisation of ArcGIS 10.8 software (Esri, USA) (Thien et al., 2023b). The spectral bands from Landsat 5-TM (bands 1-5 and band 7) and Landsat 8-OLI/TIRS (bands 1-7) were stacked to produce a multiband image using discrete bands (Hussain and Karuppannan, 2023). Mosaicking was then used to combine overlapping images, and the extract by mask tool was used to subset the image based on the study area (Chamling and Bera, 2020; Hussain et al., 2020; Thien et al., 2023b). Once pre-processing was complete, based on local knowledge supervised classification was performed on the satellite image datasets from 1992, 2010, and 2022 using a maximum likelihood algorithm. By drawing polygons around typical locations for each individual LULC type, training samples were chosen for each type (Viana et al., 2019). The spectral signatures of each LULC class were then retrieved from pixels surrounding the delineated polygons (Fayaz et al., 2020; Thien and Phuong, 2023). A detailed methodology is presented in Figure 2.

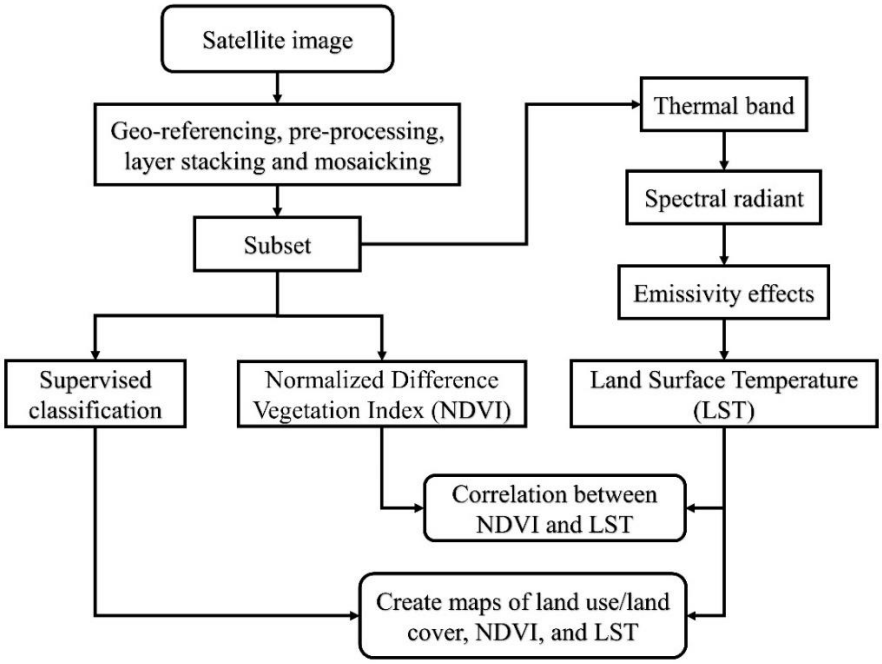

Figure 2. Schematic representation of the methodology followed in the study

2.4 Accuracy assessment

In this study, a process of accuracy evaluation was carried out to authenticate the generated image classifications and minimize errors in digital imagery (Alganci et al., 2020). Two techniques were utilised to assess accuracy: the error matrix and the kappa coefficient (Feizizadeh et al., 2022; Thien and Phuong, 2023). The error matrix offers the most comprehensive and mutual means of determining the current accuracy outcomes, which can be utilised to derive various statistical measures for accuracy assessment. These include the percentage of the producer's accuracy, the user's accuracy, and overall accuracy, which address errors produced by chance (Hussain et al., 2020). The kappa coefficient, ranging from 0 to 1, expresses the difference between classified results and reference points (Cvitić et al., 2021). Equations (1), (2), (3), and (4) were used as optimal quantitative measures to classify satellite imagery.

$$\text{Producer's accuracy} = \frac{x_{kk}}{x_{+k}} \times 100 \quad (1)$$

$$\text{User's accuracy} = \frac{x_{kk}}{x_{k+}} \times 100 \quad (2)$$

$$\text{Overall accuracy} = \frac{1}{N}\sum_{k=1}^{r} n_i \times 100 \quad (3)$$

$$\text{Kappa coefficient} = \frac{N\sum_{k=1}^{r} x_{kk} - \sum_{k=1}^{r}(x_{k+} . x_{+k})}{N^2 - \sum_{k=1}^{r}(x_{k+} . x_{+k})} \quad (4)$$

Where; N stands for the pixels in total, r for the classes number, and x_{kk} for the sum of the pixels in rows "k" and columns "k", respectively. In the error matrix, the total samples in column "k" are represented by subscription x_{+k}, while the total samples in row "k" are represented by x_{k+}.

2.5 Estimation of NDVI

The NDVI is a widely used criterion for detecting and monitoring vegetation areas (Estrella et al., 2021; Fayech and Tarhouni, 2021). The Landsat images were used to estimate the NDVI, which has values ranging between −1 and +1 (Thien and Phuong, 2023). The NDVI values were calculated using formula (5), which is as follows:

$$\text{NDVI} = \frac{\text{NIR} - \text{RED}}{\text{NIR} + \text{RED}} \quad (5)$$

Where; NIR is the near-infrared band and RED is the red band.

2.6 Estimation of LST

The LST is usually measured using the RS technique, which refers to the temperature of the Earth's surface (Zhang et al., 2019). It can be utilised to gain insights into the Earth's energy balance, urban heat island effects, and vegetation stress, among other applications. To compute LST, different researchers

have used defined measurements on Landsat data (Sekertekin and Bonafoni, 2020; Balew and Korme, 2020; Moazzam et al., 2022; Rendana et al., 2023). In this study, LST values were estimated from the thermal bands of Landsat 5-TM and Landsat 8-OLI/TIRS (bands 6 and 10). All steps for the LST calculation are provided below.

Equations (6) and (7) were used to convert digital numbers (DN) to radiance for Landsat 5-TM and Landsat 8-OLI/TIRS, respectively (Rendana et al., 2023).

$$L_\lambda = \left(\frac{L_{max\lambda} - L_{min\lambda}}{QCal_{max} - QCal_{min}}\right) \times (QCal - QCal_{min}) + L_{min\lambda} \quad (6)$$

Where; L_λ represents the sensor radiance, $L_{max\lambda}$ is the maximum radiance of band 6, $L_{min\lambda}$ is the minimum radiance of band 6, QCal is the quantized calibrated pixel value in DN, $QCal_{max}$ is the maximum quantized calibrated pixel value in DN, and $QCal_{min}$ is the minimum quantized calibrated pixel value in DN.

$$L_\lambda = M_L \times QCal + A_L \quad (7)$$

Where; M_L is the radiance multiplicative scaling factor, A_L is the radiance additive scaling factor for band10.

Equation (8) was then applied to obtain the Brightness Temperature (BT) in ℃.

$$BT = \left(\frac{K_2}{\ln\left(\frac{K_1}{L_\lambda} + 1\right)}\right) - 273.15 \quad (8)$$

Where; K_1 and K_2 are the calibration constants of thermal bands (Landsat 5-TM (K_1 =607.76 and K_2 =1260.56); Landsat 8-OLI/TIRS (K_1 =774.8853 and K_2=1321.0789)).

Then, equation (9) was utilised to determine the LST.

$$LST = \frac{BT}{1 + \left(\frac{\lambda \times BT}{\rho}\right)} \times \ln(\varepsilon) \quad (9)$$

Where; λ is the central band wavelength of emitted radiance, BT is the Brightness temperature, and ε is the emissivity (evaluated by using equation (10)):

$$\varepsilon = 0.004 \times Pv + 0.986 \quad (10)$$

Where; Pv is the proportion of vegetation evaluated by using equation (11):

$$Pv = \left(\frac{NDVI - NDVI_{min}}{NDVI_{max} - NDVI_{min}}\right)^2 \quad (11)$$

Where; NDVI has been estimated by equation (5).

2.7 Regression analysis

Regression analysis was used to measure the correlation between NDVI and LST in Hai Duong Province for the years 1992, 2010, and 2022 (Alam et al., 2022). To perform the regression analysis, 200 random points data were created within the study area boundary using the Create Random Points tool in ArcGIS 10.8. Then, the extract multi values to points tool was used to extract one value for each point from the NDVI and LST pixels (Alam et al., 2022). Finally, these points were exported to Excel 2016 software (Microsoft, USA) to estimate the regression equation between NDVI and LST. The correlation coefficient values generated by the regression analysis ranged from -1 to +1 (Rendana et al., 2023).

3. RESULTS AND DISCUSSION

3.1 Land use and land cover changes

The study utilised supervised classification techniques to analyse the LULC changes in Hai Duong Province, Vietnam, from 1992 to 2022. The findings indicate that the study area contains diverse land features, such as vegetation, barren land, built-up areas, and bodies of water (Figure 3). In 1992, vegetation accounted for 57.89% (965.71 km^2) of the total study area, followed by barren land, which accounted for 35.65% (594.78 km^2), water, which accounted for 3.58% (59.76 km^2) and, finally, built-up areas, which accounted for at least 2.88% (47.99 km^2) (Table 2). By 2010, the vegetation area had increased to 84.49% (1,409.49 km^2), while the barren land area had decreased sharply to 4.59% (76.58 km^2). The built-up and water areas had also increased to 7.01% (117.02 km^2) and 3.91% (65.15 km^2), respectively (Table 2). By 2022, the vegetation area had decreased to 66.67% (1,112.23 km^2), the barren land area had decreased to only 0.76% (12.73 km^2), the built-up area had increased to 29.35% (489.71 km^2), and the water area had decreased to 3.21% (53.57 km^2) (Table 2). These results show that the built-up area has increased continuously from 1992 to 2022 in the study area.

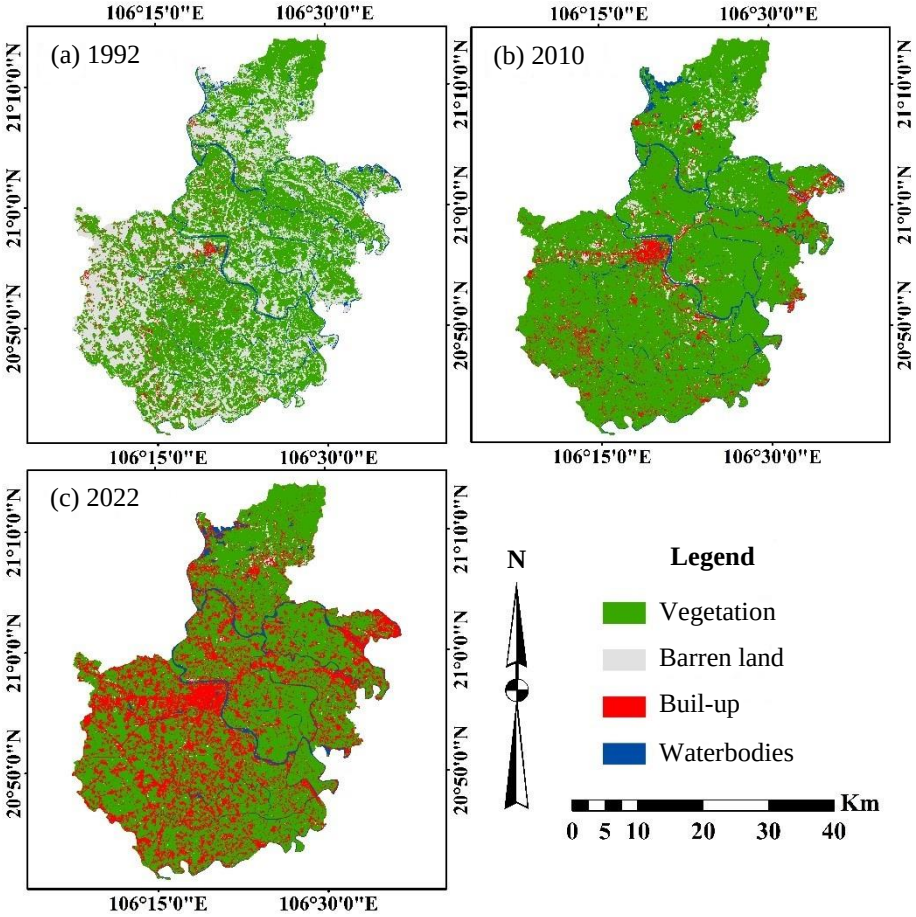

Figure 3. Land use/land cover maps of Hai Duong Province in (a) 1992, (b) 2010, and (c) 2022

Table 2. Area and percentage of land use/land cover classes distribution in 1992, 2010, and 2022

LULC classes	1992		2010		2022	
	Area (km^2)	%	Area (km^2)	%	Area (km^2)	%
Vegetation	965.71	57.89	1409.49	84.49	1112.23	66.67
Barren land	594.78	35.65	76.58	4.59	12.73	0.76
Built-up	47.99	2.88	117.02	7.01	489.71	29.35
Waterbodies	59.76	3.58	65.15	3.91	53.57	3.21
Total	1668.24	100.00	1668.24	100.00	1668.24	100.00

Changes in LULC in Hai Duong Province from 1992 to 2022 are presented in Table 3. From 1992 to 2010, the areas covered by vegetation, built-up areas, and bodies of water increased, while the area of barren land significantly decreased. The vegetation cover experienced the most positive shift, increasing by 443.78 km^2 (26.60%), whereas the barren land showed a negative shift, decreasing by 518.20 km^2 (31.06%) (Table 3). Meanwhile, the built-up area and bodies of water increased by 69.03 km^2 (4.14%) and 5.39 km^2 (0.32%), respectively (Table 3). From 2010 to 2022, built-up area showed a strong increasing trend, gaining 372.69 km^2 (22.34%), while the other land cover classes, vegetation, barren land, and bodies of water, tended to decrease, losing 297.26 km^2 (17.82%), 63.85 km^2 (3.83%), and 11.58 km^2 (0.69%), respectively (Table 3).

3.2 Accuracy assessment

The quality of the LULC maps for the years 1992, 2010, and 2022 was evaluated with an error matrix, which returned overall accuracies of 93.31%, 92.98%, and 96.67%, respectively (Table 4). The producer's accuracy assessment showed that the relative accuracies of land cover classification for 1992 and 2010 were 96.82% and 96.43% for the vegetation category, respectively, and for 2022, the built-up category achieved the highest accuracy

(97.94%) (Table 4). The user accuracy for different land cover classes each year was relatively high. The highest user accuracy occurred in 2010 for the vegetation category (97.59%), while the lowest user accuracy was observed in 1992 for the built-up category (80.77%) (Table 4). The kappa coefficients for 1992, 2010, and 2022 were 0.893, 0.887, and 0.946, respectively (Table 4).

Table 3. Land use/land cover changes of Hai Duong Province during 1992-2010, 2010-2022, and 1992-2022

LULC classes	Changes 1992-2010		Changes 2010-2022		Changes 1992-2022	
	Area (km^2)	%	Area (km^2)	%	Area (km^2)	%
Vegetation	443.78	26.60	-297.26	-17.82	146.52	8.78
Barren land	-518.20	-31.06	-63.85	-3.83	-582.05	-34.89
Built-up	69.03	4.14	372.69	22.34	441.72	26.48
Waterbodies	5.39	0.32	-11.58	-0.69	-6.19	-0.37

Table 4. Accuracy assessments for classified maps

LULC classes	1992		2010		2022	
	Producer's accuracy (%)	User's accuracy (%)	Producer's accuracy (%)	User's accuracy (%)	Producer's accuracy (%)	User's accuracy (%)
Vegetation	96.82	93.83	96.43	97.59	97.39	97.39
Barren land	92.16	96.91	81.08	81.08	87.50	87.50
Built-up	87.50	80.77	94.12	96.00	97.94	96.94
Waterbodies	83.87	89.66	88.37	82.61	92.86	95.12
Overall accuracy (%)	93.31		92.98		96.67	
Kappa coefficient	0.893		0.887		0.946	

3.3 NDVI variation in the study area

The NDVI values shifted noticeably over the study period, indicating changes in vegetation and land use. In 1992, the NDVI values in the study area ranged from -0.35 to +0.63, which changed by 2010 to a minimum of -0.40 and a maximum of +0.70 (Figure 4). By 2022, the NDVI values had changed again to a minimum of -0.24 and a maximum of +0.54 in the study area (Figure 4). Higher NDVI values in the study area represent vegetation and forests and signify increased productivity and efficiency, while lower values, associated with bare soil, bodies of water, and built-up areas, indicate reduced productivity.

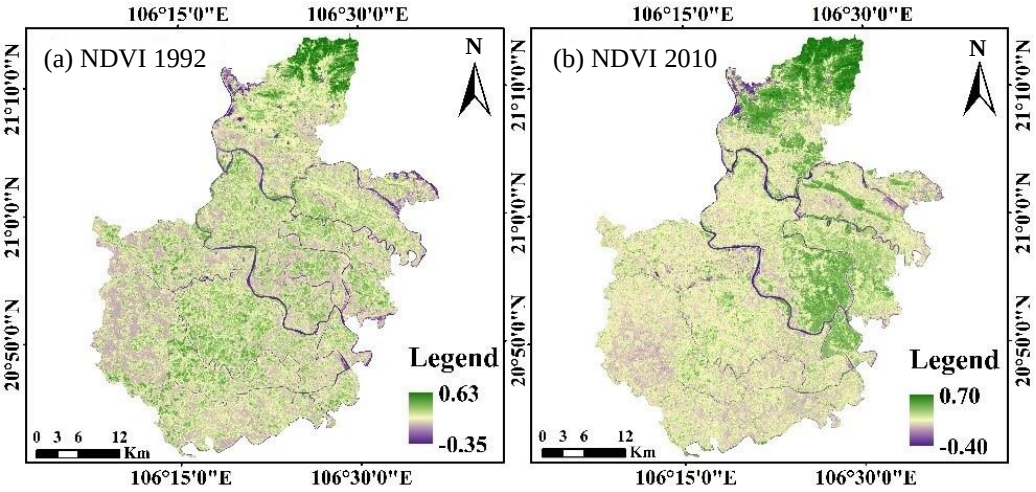

Figure 4. The NDVI maps of Hai Duong Province in (a) 1992, (b) 2010, and (c) 2022

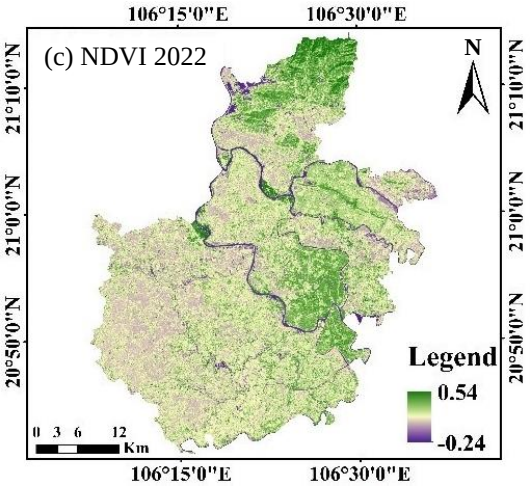

Figure 4. The NDVI maps of Hai Duong Province in (a) 1992, (b) 2010, and (c) 2022 (cont.)

3.4 LST variation in the study area

Figure 5 presents a visual representation of the spatial distribution and patterns of LST in Hai Duong Province in the three study years (1992, 2010, and 2022) and shows how the LST values and spatial patterns change over time in response to changes in LULC. The estimated LST values ranged from 16.09°C-34.27°C in 1992, 17.04°C-36.74°C in 2010, and 11.03°C-28.44°C in 2022. Notably, LST increased significantly between 1992 and 2010 in most parts of the study area, although some small regions adjacent to water bodies showed stable temperatures. However, by 2022, the overall LST had decreased significantly compared to 1992 and 2010.

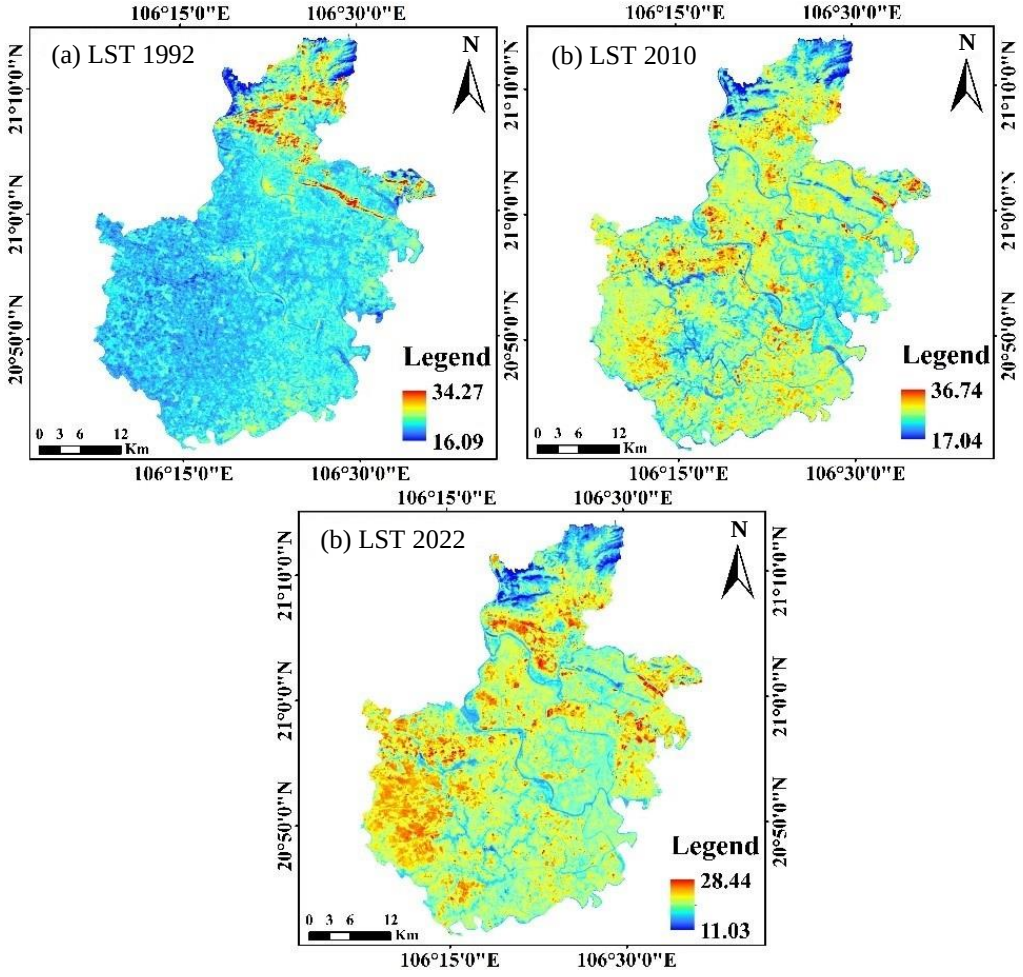

Figure 5. The LST maps of Hai Duong Province in (a) 1992, (b) 2010, and (c) 2022

3.5 Relationship between NDVI and LST

Figure 6 illustrates the correlation between NDVI and LST during the three study years (1992, 2010, and 2022), with a regression line showing the distinct relationship between these two indices. The correlation coefficients (R^2) obtained from linear regression analysis of the data in 1992, 2010, and 2022 were 0.0965, 0.0035, and 0.2277, respectively (Figure 6). The regression line between the NDVI and LST values for the year 1992 indicates a positive correlation; when NDVI values are high, LST values are also high, and vice versa. In 2010, the regression line and correlation coefficient were close to 0, suggesting that NDVI and LST values were less interdependent. However, in 2022, the regression line between these two variables demonstrates a negative correlation. That is, areas with low NDVI values, such as impermeable surfaces and built-up areas, exhibited high LST values, while areas with dense, healthy vegetation have high NDVI values and low LST values.

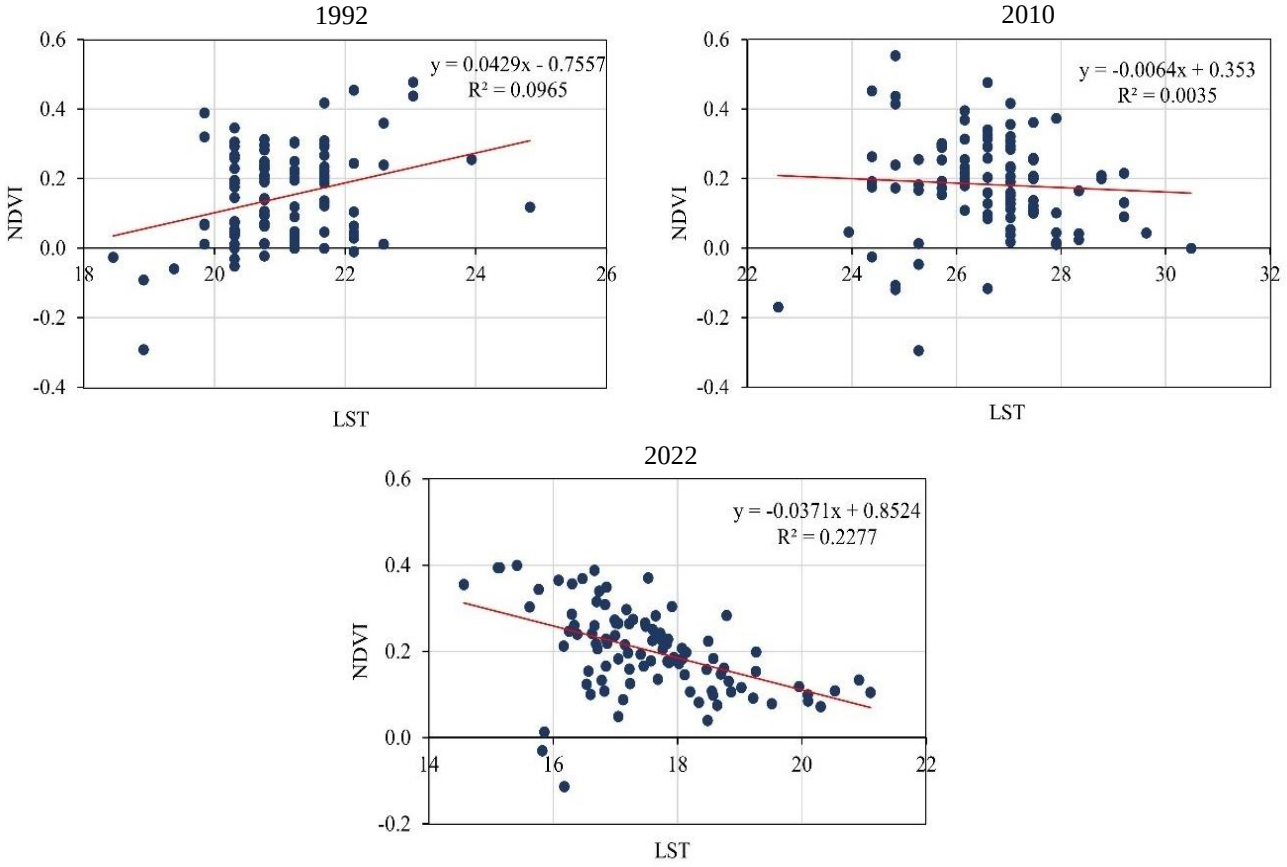

Figure 6. Relationship between NDVI and LST for the years 1992, 2010, and 2022 in Hai Duong Province

4. DISCUSSION

This study applied modern time- and cost-effective methods to investigate the drivers of LULC and LST changes from 1992 to 2022 in Hai Duong Province, Vietnam. Landsat satellite images (TM and OLI/TIRS) from 1992, 2010, and 2022 were classified using the supervised classification method with four LULC classes, vegetation, barren land, built-up area and bodies of water (Figure 3). The area of each LULC class is also presented in Table 2. Accuracy assessment is important to confirm the correctness of the generated image classifications (Alganci et al., 2020; Hussain et al., 2020; Thien and Phuong, 2023). The classification results were also evaluated for accuracy and returned kappa coefficients above 0.8. These high-accuracy results indicate the reliability of the land cover classification and confirm good consistency between the reference and classification maps. These results confirm that the categorized images meet the necessary accuracy standards and are viable data for subsequent analyses and applications (Cvitić et al., 2021; Thien et al., 2023b).

Spatial analysis of the multi-temporal LULC map of Hai Duong Province shows significant changes over the past 30 years (1992-2022). LULC changes occur continuously and are influenced by many

natural and human factors. These changes have both positive and negative effects. According to socioeconomic reports about Hai Duong Province, the four key economic sectors of the region are agriculture, forestry and fisheries; industry and construction; services; and taxes and subsidies on products. In 2022, the industrial and construction sector accounted for 56.1% of economic activity, while the service sector accounted for 26.5% and the remaining two sectors together only accounted for about 17.0% (Hai Duong Statistical Office, 2022). This suggests that the LULC changes in the study area may reflect the expansion of land used for economic development and urbanization, including the construction of new infrastructure, such as roads, railways, bridges, and industrial zones (Rahaman et al., 2022; Thien et al., 2023a). In addition, climate change may contribute to changes in areas covered by vegetation, barren areas, and bodies of water (Ahmad et al., 2014; Mahmoud and Gan, 2018; Sadiq Khan et al., 2020). The research results highlight the need to implement effective land-use planning and management strategies to minimize the negative effects of these changes on the environment and local communities.

This study was conducted because rapid urbanization has had significant effects on the thermal environment of the study area, which are reflected in the distribution of NDVI and LST values. Using Landsat 5-TM and Landsat 8-OLI/TIRS satellite images, the NDVI index was calculated for the period from 1992 to 2022 by leveraging the spectral characteristics related to vegetation cover, including its ability to absorb visible light, use photosynthetic energy and reflect near-infrared (NIR) radiation (Zeng et al., 2019; Kumar et al., 2022; Thien et al., 2023b). Areas of bare land typically have lower NDVI values than areas with many trees, suggesting the potential effect of increasing vegetation cover as measured by satellite-based assessments of vegetation greenness across the study area. As Ahmad et al. (2014) demonstrated, NDVI is an important component in various vegetation indices due to its stable performance, characterized by non-systematic variation.

These findings highlight the dynamism of LST and its sensitivity to LULC changes. Notably, this study identified a correlation between the expansion of built-up areas and the reduction of vegetation cover, especially in the central and western portions of the study area, leading to increased LSTs in these localities (Balew and Korme, 2020; Alam et al., 2022). These results emphasize the importance of incorporating LULC dynamics into urban planning and management policies to mitigate the adverse effects of urbanization on the local climate and generally improve the quality of life in urban environments (Hussain et al., 2020; Moazzam et al., 2022; Phuong and Thien, 2023a). The deep insights gained from this study can serve as valuable inputs for decision-making processes related to land-use management and planning and contribute to promoting sustainable urban development.

The spatial relationship between NDVI and LST values from 1992-2022 shows that their positive relationship gradually becomes negative. The average LST is low in areas with vegetation cover and flooded areas, indicating a relatively higher rate of water evaporation and favourable conditions for latent exchange between the surface and the atmosphere compared to areas with many impermeable surfaces, such as built-up and barren areas (Thanh Hoan et al., 2018; Rendana et al., 2023; Veettil et al., 2023). Meanwhile, the low NDVI values observed in barren and built-up areas and the high NDVI values seen in areas of mixed vegetation cover and flooded areas reflect a common trend reported in NDVI land cover studies (Alam et al., 2022; Moazzam et al., 2022). The determination coefficient between NDVI and LST values also shows that the positive correlation gradually becomes negative. The density of built-up areas and vegetation cover are important factors determining LST in the study area. The surface density of built-up areas increases LST, while high vegetation cover density significantly reduces LST (Mukherjee and Singh, 2020; Nse et al., 2020).

5. CONCLUSION

This study utilised Landsat satellite imagery to assess alterations in LULC and their effects on LST in Hai Duong Province, Vietnam, from 1992 to 2022. The supervised classification method in ArcGIS 10.8 software was used to classify Landsat satellite data, which was evaluated for accuracy and resulted in kappa coefficients of 0.893 for 1992, 0.887 for 2010, and 0.946 for 2022. The classification results showed significant changes in land cover in the study area. Vegetation was the dominant land cover throughout the study period (1992-2022). Meanwhile, the built-up area, which comprised 47.99 km^2 (2.88%) in 1992, exhibited a consistent upward trend and eventually reached 489.71 km^2 (29.35%) in 2022. The Landsat

data indicated swift changes from barren land in 1992 to vegetation cover in 2010, which then transitioned into built-up area by 2022. Although LST values overall decreased from 34.27°C in 1992 to 28.44°C in 2022, the rising built-up area in Hai Duong Province caused an expansion of high-LST areas in 2022. The regression analysis of NDVI and LST values also showed a shift from a positive to a negative correlation between the two variables. Our study findings suggest that the surge in built-up area and the reduction in bodies of water are among the primary factors contributing to the decline in vegetation cover quality and area, leading to the loss of natural ecosystems and biodiversity. Furthermore, the increasing built-up area may cause further environmental issues. The evaluation of LULC changes can help define the effects of various development activities on LULC classes during the planning process. The use of RS and GIS technologies also enables spatiotemporal analysis, which cannot be achieved through conventional mapping techniques. This study will enhance local and national authorities' ability to develop comprehensive strategies for land management in the study area.

The use of satellite imagery, while beneficial for large-scale analysis, may not capture the fine details of land use and land cover changes that occur at a smaller scale. For future studies, the inclusion of socioeconomic data could provide a more comprehensive understanding of the drivers of the observed LULC changes. Long-term monitoring and prediction models could also be developed to forecast future LULC changes and their potential effects on the local climate and biodiversity. These recommendations, if implemented, could result in more robust and comprehensive insights into land use and land cover changes and their implications for sustainable urban development.

REFERENCES

Ahmad F, Ghazi S, Ahmad SR, Ahmad I, Khan RMA, Raoof A, et al. Spectral characteristics and mapping of rice fields using multi-temporal landsat and MODIS data: A case of District Narowal. Global Journal of Human-Social Science Research 2014;14(6):Article No. 2.

Ahmed J, Ahmed M, Laghari A, Lohana W, Ali S, Fatmi Z. Public private mix model in enhancing tuberculosis case detection in District Thatta, Sindh, Pakistan. Journal of the Pakistan Medical Association 2009;59(2):Article No. 82.

Alam HE, Arafat MdY, Ahmed KT, Uddin MN. Temporal variation of land surface temperature in response to changes in vegetation index of Bhawal National Park, Bangladesh. In: Pal I, Kolathayar S, editors. Sustainable Cities and Resilience. Singapore: Lecture Notes in Civil Engineering Springer Singapore; 2022. p. 329-37.

Alganci U, Soydas M, Sertel E. Comparative research on deep learning approaches for airplane detection from very high-resolution satellite images. Remote Sensing 2020;12(3): Article No. 458.

Balew A, Korme T. Monitoring land surface temperature in Bahir Dar City and its surrounding using landsat images. The Egyptian Journal of Remote Sensing and Space Science 2020;23(3):371-86.

Bohanon A, Crane K. Structural and biological analysis of faults in basalts in Sheepshead Mountains, Oregon as an earth analogue to mars. Icarus 2022;385:Article No. 115121.

Celik S. The effects of climate change on human behaviors. In: Fahad S, Hasanuzzaman M, Alam M, Ullah H, Saeed M, Khan IA, et al. editors. Environment, Climate, Plant and Vegetation Growth. Cham: Springer International Publishing; 2020; p. 577-89.

Chamling M, Bera B. Spatio-temporal patterns of land use/land cover change in the Bhutan-Bengal Foothill region between 1987 and 2019: Study towards geospatial applications and policy making. Earth Systems and Environment 2020;4(1): 117-30.

Cvitić I, Peraković D, Periša M, Gupta B. Ensemble machine learning approach for classification of IoT devices in smart home. International Journal of Machine Learning and Cybernetics 2021;12(11):3179-202.

Das M, Das A. Dynamics of urbanization and its impact on urban ecosystem services (UESs): A study of a medium size town of West Bengal, Eastern India. Journal of Urban Management 2019;8(3):420-34.

Donelson JM, Salinas S, Munday PL, Shama LN. Transgenerational plasticity and climate change experiments: Where do we go from here? Global Change Biology 2018;24(1):13-34.

Estrella EH, Stoeth A, Krakauer NY, Devineni N. Quantifying vegetation response to environmental changes on the Galapagos Islands, Ecuador using the normalized difference vegetation index (NDVI). Environmental Research Communications 2021;3(6):Article No. 065003.

Fatemi M, Narangifard M. Monitoring LULC changes and its impact on the LST and NDVI in district 1 of Shiraz City. Arabian Journal of Geosciences 2019;12(4):Article No. 127.

Fayaz A, Shafiq MU, Singh H, Ahmed P. Assessment of spatiotemporal changes in land use/land cover of North Kashmir Himalayas from 1992 to 2018. Modeling Earth Systems and Environment 2020;6(2):1189-200.

Fayech D, Tarhouni J. Climate variability and its effect on normalized difference vegetation index (NDVI) using remote sensing in semi-arid area. Modeling Earth Systems and Environment 2021;7(3):1667-82.

Feizizadeh B, Darabi S, Blaschke T, Lakes T. QADI as a new method and alternative to Kappa for accuracy assessment of remote sensing-based image classification. Sensors 2022; 22(12):Article No. 4506.

General Statistics Office. Statistical yearbook of Viet Nam. Statistical publishing house [Internet]. 2022 [cited 2023 Jul 10]. Available from: https://www.gso.gov.vn/wp-content/uploads/2023/06/Sach-Nien-giam-TK-2022-update-21.7_file-nen-Water.pdf.

Guha S. Dynamic seasonal analysis on LST-NDVI relationship and ecological health of Raipur City, India. Ecosystem Health and Sustainability 2021;7(1):Article No. 1927852.

Hai Duong Statistical Office. Report: Socio-economic situation in December and the whole year of 2022, Hai Duong province [Internet]. 2022 [cited 2023 Jul 10]. Available from: https://web01.haiduong.gov.vn/Lists/TinTuc/Attachments/14460/BC%20KTXH%20T12.2022%20tinh%20Hai%20Duong.pdf.

Hammad HM, Ashraf M, Abbas F, Bakhat HF, Qaisrani SA, Mubeen M, et al. Environmental factors affecting the frequency of road traffic accidents: A case study of sub-urban area of Pakistan. Environmental Science and Pollution Research 2019;26(12):11674-85.

Hu Y, Raza A, Syed NR, Acharki S, Ray RL, Hussain S, et al. Land use/land cover change detection and NDVI estimation in Pakistan's Southern Punjab Province. Sustainability 2023; 15(4):Article No. 3572.

Hussain S, Karuppannan S. Land use/land cover changes and their impact on land surface temperature using remote sensing technique in District Khanewal, Punjab Pakistan. Geology, Ecology, and Landscapes 2023;7(1):46-58.

Hussain S, Mubeen M, Ahmad A, Akram W, Hammad HM, Ali M, et al. Using GIS tools to detect the land use/land cover changes during forty years in Lodhran District of Pakistan. Environmental Science and Pollution Research 2020;27 (32):39676-92.

Kumar S, Arya S, Jain K. A SWIR-based vegetation index for change detection in land cover using multi-temporal landsat satellite dataset. International Journal of Information Technology 2022;14(4):2035-48.

Laux P, Nguyen PNB, Cullmann J, Kunstmann H. Impacts of land-use/land-cover change and climate change on the regional climate in the Central Vietnam. In: Nauditt A, Ribbe L. editors. Land Use and Climate Change Interactions in Central Vietnam: Water Resources Development and Management. Singapore: Springer Singapore; 2017. p. 143-51.

Li C, Wu Y, Gao B, Zheng K, Wu Y, Li C. Multi-scenario simulation of ecosystem service value for optimization of land use in the sichuan-yunnan ecological barrier, China. Ecological Indicators 2021;132:Article No. 108328.

Mahmoud SH, Gan TY. Impact of anthropogenic climate change and human activities on environment and ecosystem services in arid regions. Science of the Total Environment 2018; 633:1329-44.

Moazzam MFU, Doh YH, Lee BG. Impact of urbanization on land surface temperature and surface urban heat island using optical remote sensing data: A case study of Jeju Island, Republic of Korea. Building and Environment 2022;222:Article No. 109368.

Monroe MC, Plate RR, Oxarart A, Bowers A, Chaves WA. Identifying effective climate change education strategies: A systematic review of the research. Environmental Education Research 2019;25(6):791-812.

Mubeen M, Bano A, Ali B, Islam ZU, Ahmad A, Hussain S, et al. Effect of plant growth promoting bacteria and drought on spring maize (*Zea Mays* L.). Pakistan Journal of Botany 2021;53(2):731-9.

Mukherjee F, Singh D. Assessing land use-land cover change and its impact on land surface temperature using LANDSAT data: A comparison of two urban areas in India. Earth Systems and Environment 2020;4(2):385-407.

Nguyen TM, Lin TH, Chan HP. The environmental effects of urban development in Hanoi, Vietnam from satellite and meteorological observations from 1999-2016. Sustainability 2019;11(6):Article No. 1768.

Nse OU, Okolie CJ, Nse VO. Dynamics of land cover, land surface temperature and NDVI in Uyo City, Nigeria. Scientific African 2020;10:e00599.

Owolabi ST, Madi K, Kalumba AM, Orimoloye IR. A groundwater potential zone mapping approach for semi-arid environments using remote sensing (RS), geographic information System (GIS), and Analytical Hierarchical Process (AHP) techniques: A case study of buffalo catchment, Eastern Cape, South Africa. Arabian Journal of Geosciences 2020;13(22):Article No. 1184.

Phuong VT, Thien BB. A multi-temporal landsat data analysis for land-use/land-cover change in the Northwest Mountains Region of Vietnam Using Remote Sensing Techniques. Forum Geografic 2023a;22(1):54-66.

Phuong VT, Thien BB. Using landsat satellite images to detect forest cover changes in the Northeast Region of Vietnam. Bulletin of the Transilvania University of Brasov Series II: Forestry Wood Industry Agricultural Food Engineering 2023b;16(1):19-36.

Praveen B, Sharma P. A review of literature on climate change and its impacts on agriculture productivity. Journal of Public Affairs 2019;19(4):e1960.

Rahaman ZA, Kafy AA, Faisal AA, Al Rakib A, Jahir DMA, Fattah MA, et al. Predicting microscale land use/land cover changes using cellular automata algorithm on the Northwest Coast of Peninsular Malaysia. Earth Systems and Environment 2022;6(4):817-35.

Rendana M, Razi Idris WM, Abdul Rahim S, Ghassan Abdo H, Almohamad H, Abdullah Al Dughairi A, et al. Effects of the built-up index and land surface temperature on the mangrove area change along the Southern Sumatra Coast. Forest Science and Technology 2023;19(3):179-89.

Ritse V, Basumatary H, Kulnu AS, Dutta G, Phukan MM, Hazarika N. Monitoring land use land cover changes in the Eastern Himalayan Landscape of Nagaland, Northeast India. Environmental Monitoring and Assessment 2020;192(11): Article No. 711.

Rizvi SH, Fatima H, Alam K, Iqbal MJ. The surface urban heat island intensity and urban expansion: A comparative analysis for the Coastal Areas of Pakistan. Environment, Development and Sustainability 2021;23(4):5520-37.

Roberts C, Geels FW, Lockwood M, Newell P, Schmitz H, Turnheim B, et al. The politics of accelerating low-carbon transitions: Towards a new research agenda. Energy Research and Social Science 2018;44:304-11.

Sadiq Khan M, Ullah S, Sun T, Rehman AU, Chen L. Land-use/land-cover changes and its contribution to urban heat island: A case study of Islamabad, Pakistan. Sustainability 2020;12(9):Article No. 3861.

Sahin G, Cabuk SN, Cetin M. The change detection in coastal settlements using image processing techniques: A case study of Korfez. Environmental Science and Pollution Research 2022;29(10):15172-87.

Sajan B, Kanga S, Singh SK, Mishra VN, Durin B. Spatial variations of LST and NDVI in Muzaffarpur District, Bihar using google earth engine (GEE) during 1990-2020. Journal of Agrometeorology 2023;25(2):262-7.

Sekertekin A, Bonafoni S. Sensitivity analysis and validation of daytime and nighttime land surface temperature retrievals from landsat 8 using different algorithms and emissivity models. Remote Sensing 2020;12(17):Article No. 2776.

Silva JS, da Silva RM, Santos CAG. Spatiotemporal impact of land use/land cover changes on urban heat islands: A case study of Paço Do Lumiar, Brazil. Building and Environment 2018;136:279-92.

Skendžić S, Zovko M, Živković IP, Lešić V, Lemić D. The impact of climate change on agricultural insect pests. Insects 2021;12(5):Article No. 440.

Son NT, Chen CF, Chen CR, Thanh BX, Vuong TH. Assessment of urbanization and urban heat islands in Ho Chi Minh City, Vietnam using landsat data. Sustainable Cities and Society 2017;30:150-61.

Tang J, Di L. Past and future trajectories of farmland loss due to rapid urbanization using landsat imagery and the markov-CA model: A case study of Delhi, India. Remote Sensing 2019;11(2):Article No. 180.

Thanh Hoan N, Liou YA, Nguyen KA, Sharma RC, Tran DP, Liou CL, et al. Assessing the effects of land-use types in surface urban heat islands for developing comfortable living in Hanoi City. Remote Sensing 2018;10(12):Article No. 1965.

Thien BB, Phuong VT. Using landsat satellite imagery for assessment and monitoring of long-term forest cover changes in Dak Nong Province, Vietnam. Geographica Pannonica 2023;27(1):69-82.

Thien BB, Phuong VT, Komolafe AA. Assessment of forest cover and forest loss using satellite images in Thua Thien Hue Province, Vietnam. AUC Geographica 2023a;58(2):172-86.

Thien BB, Yachongtou B, Phuong VT. Long-term monitoring of forest cover change resulting in forest loss in the capital of Luang Prabang Province, Lao PDR. Environmental Monitoring and Assessment 2023b;195(8):Article No. 947.

Veettil BK, Puri V, Van DD, Quang NX. Variations in land surface temperatures in small-scale urban areas in Vietnam during Covid-19 restrictions: Case studies from Da Nang, Hue and Vinh City. Environmental Monitoring and Assessment 2023;195(7):Article No. 822.

Veettil BK, Van DD. Did the Covid-19 restrictions influence land surface temperatures in Southeast Asia? A study from Ho Chi Minh City, Vietnam. Environmental Science and Pollution Research 2023;30(25):66812-21.

Viana CM, Girão I, Rocha J. Long-term satellite image time-series for land use/land cover change detection using refined open source data in a rural region. Remote Sensing 2019;11(9): Article No. 1104.

Winsemius HC, Jongman B, Veldkamp TI, Hallegatte S, Bangalore M, Ward PJ. Disaster risk, climate change, and poverty: Assessing the global exposure of poor people to floods and droughts. Environment and Development Economics 2018;23(3):328-48.

Workie TG, Debella HJ. Climate change and its effects on vegetation phenology across ecoregions of ethiopia. Global Ecology and Conservation 2018;13:e00366.

Xu L, Jing W, Song H, Chen G. High-resolution remote sensing image change detection combined with pixel-level and object-level. IEEE Access 2019;7:78909-18.

Yao N, Huang C, Yang J, Konijnendijk van den Bosch CC, Ma L, Jia Z. Combined effects of impervious surface change and large-scale afforestation on the surface urban heat island intensity of Beijing, China based on remote sensing analysis. Remote Sensing 2020;12(23):Article No. 3906.

Zamin M, Khattak AM, Salim AM, Marcum KB, Shakur M, Shah S, et al. Performance of aeluropus lagopoides (mangrove grass) ecotypes, a potential turfgrass, under high saline conditions. Environmental Science and Pollution Research 2019;26(13):13410-21.

Zeng Y, Badgley G, Dechant B, Ryu Y, Chen M, Berry JA. A practical approach for estimating the escape ratio of near-infrared solar-induced chlorophyll fluorescence. Remote Sensing of Environment 2019;232:Article No. 111209.

Zeren Cetin I, Varol T, Ozel HB. A geographic information systems and remote sensing-based approach to assess urban micro-climate change and its impact on human health in Bartin, Turkey. Environmental Monitoring and Assessment 2023;195(5):Article No. 540.

Zhang X, Zhou J, Göttsche F-M, Zhan W, Liu S, Cao R. A method based on temporal component decomposition for estimating 1-Km all-weather land surface temperature by merging satellite thermal infrared and passive microwave observations. IEEE Transactions on Geoscience and Remote Sensing 2019;57(7):4670-91.

Zia Z, Bakhat HF, Saqib ZA, Shah GM, Fahad S, Ashraf MR, et al. Effect of water management and silicon on germination, growth, phosphorus and arsenic uptake in rice. Ecotoxicology and Environmental Safety 2017;144:11-8.

Environment and Natural Resources Journal

Volume 22
Issue 2
2024

Assessment of Landslide Susceptibility in the Intermontane Basin Area of Northern Thailand

Kritchayan Intarat[1,2*], Patimakorn Yoomee[1,2], Areewan Hussadin[2,3], and Wanjai Lamprom[3]

[1]*Department of Geography, Faculty of Liberal Arts, Thammasat University, Thailand*
[2]*Research Unit in Geospatial Applications (Capybara Geo Lab), Faculty of Liberal Arts, Thammasat University, Thailand*
[3]*Faculty of Liberal Arts, Rajamangala University of Technology Thanyaburi, Thailand*

ARTICLE INFO

Received: 7 Sep 2023
Received in revised: 22 Jan 2024
Accepted: 23 Jan 2024
Published online: 12 Feb 2024
DOI: 10.32526/ennrj/22/20230241

Keywords:
Landslide susceptibility/ Machine learning/ Ensemble model/ Intermontane basin/ Chiang Mai

*** Corresponding author:**
E-mail: intaratt@tu.ac.th

ABSTRACT

In mountainous terrain, landslides are common, particularly in intermontane basin locations. Such regions can adversely affect both human beings and the environment. In the assessment of landslide susceptibility, machine learning (ML) algorithms are increasingly popular due to their compatibility with geospatial data and tools. Herein, this study evaluated the performance of four ML algorithms: namely, random forest (RF), gradient boost (GB), extreme gradient boost (XGB), and stacking ensemble (STK). These algorithms were implemented to create a practical model of landslide susceptibility. The site under investigation is in the province of Chiang Mai, an intermontane basin area in northern Thailand where populations are settled. To address issues of multicollinearity, the variance inflation factor (VIF) was used. Eight out of fourteen factors were selected for examination; hyperparameters of each model were tested to acquire the best combination. Results indicated that the STK model outperforms all other models, providing evaluation metrics (precision, recall, F1-score, and overall accuracy) of 82.92%, 81.18%, 82.04%, and 81.75%, respectively. The area under the receiver operating characteristic (ROC) curve also reveals the high efficiency of the model, achieving 0.8928. However, further analysis of the appropriate model or base learner is necessary for achieving even higher predictive results.

1. INTRODUCTION

Across the globe, natural disasters are becoming more frequent and severe, spanning from storms and floods to droughts, forest fires, and earthquakes. Among these natural phenomena, landslides threaten both human life and natural habitats, often resulting in widespread damage and destruction of property (Sim et al., 2022). The rise in landslides can be attributed to changes in climate and topography, including specific geological conditions (Kumar and Anbalagan, 2016). With mountainous regions and ongoing changes in urbanization and climate, Thailand is no exception to this trend. Thunderstorms, which bring heavy rainfall and flash floods, are the major catalysts for landslides, while geological factors are essential in triggering them.

The mapping of landslides has proven to be a valuable tool in reducing the risk of landslides in mountainous regions (Wang et al., 2021). With the rapid development of urbanization and infrastructure, assessing landslide susceptibility has become increasingly crucial to ensure the safety of communities residing in landslide-prone areas. Geoinformatics also plays a fundamental role in the prediction of landslide susceptibility, allowing for the integration and analysis of various spatial data to identify susceptibility areas and generate maps of landslide hazard zones (Lee, 2005; Van Westen et al., 2008; Pham et al., 2017). However, traditional methods regarding the mapping of landslide susceptibility often rely on expert knowledge and experience, which can be subjective and time-

Citation: Intarat K, Yoomee P, Hussadin A, Lamprom W. Assessment of landslide susceptibility in the Intermontane Basin Area of Northern Thailand. Environ. Nat. Resour. J. 2024;22(2):158-170. (https://doi.org/10.32526/ennrj/22/20230241)

consuming (Kumar and Anbalagan, 2016; Myronidis et al., 2016; Thongley and Vansarochana, 2021).

In the modelling of landslide susceptibility, statistical approaches have been developed and applied. Such approaches have been categorized into classical statistics, index-based statistics, machine learning, artificial neural networks, and multiple-criteria decision analysis (Reichenbach et al., 2018). Of these approaches, machine learning (ML) has shown great promise in developing accurate and reliable maps to predict the occurrence of landslides (Wu et al., 2020). Many ML algorithms have been associated with geoinformatics analytical tools and have demonstrated the ability to predict landslide occurrences (Pham et al., 2017; Hu et al., 2020; Wang et al., 2021; Huan et al., 2023). However, the complex nonlinear relationships between conditioning factors and landslide occurrences continue to pose a challenge (Lee et al., 2018; Hu et al., 2021). Recently, ensemble learning techniques have gained much interest in producing landslide susceptibility maps as they can combine with multiple models to produce more accurate and robust predictions. Ensemble methods can expand the hypothesis space of the fitting function, providing better predictions than single algorithms (Huan et al., 2023). Generally, the single algorithm used to constitute an ensemble is called the "base learner", which can be homogeneous or heterogeneous. Zeng et al. (2023a) adopted various ensemble ML models (bagging, boosting, and stacking) and found that the stacking method surpassed its complements. Several landslide studies have investigated meta-learning techniques for assembling homogeneous base learners (Pham et al., 2017; Hu et al., 2021) and discovered that a stacking-based scoring model can improve predictive performance by reducing overfitting and increasing the model's generalization (Wang et al., 2021; Huan et al., 2023). The stacking method proved to be superior to single ML models as it yielded stronger robustness and optimal accuracy (Huan et al., 2023; Zeng et al., 2023b).

The present study aims to investigate the efficacy of ML methods, including bagging (RF), boosting (GB and XGB), in assessing the susceptibility of landslide occurrences. The novel STK is a combination of both the bagging and boosting techniques, and is also employed. To the best of our knowledge, previously, there has been no research related to the STK ensemble modelling of landslide susceptibility in our experimental area. The study will be conducted in Chiang Mai Province, Thailand, which is known for its intermontane basin topography and is highly susceptible to landslides, particularly in hilly areas (Wattananikorn et al., 1995; Mankhemthong, 2019). Almost 10% of the region's population lives in landslide-prone areas. In previous years, many landslides were reported in Thailand, with Chiang Mai being the most affected area (Yongsiri et al., 2023). Hence, the area of Chiang Mai is an appropriate location for constructing a landslide susceptibility map. To evaluate the efficiency of the prediction, the model and result accuracies will be tested statistically. The findings of this study can provide valuable information for land use planning and mitigation efforts in the study location and other intermontane basin regions.

2. METHODOLOGY

2.1 Study area

The study site is in Chiang Mai, the westernmost part of northern Thailand province, with coordinates N 18°47'46.1148" and E 98°58'45.3468" (Figure 1). Within an area of approximately 20,200 km^2, Chiang Mai is the second-largest province in Thailand, consisting of 25 districts and 204 sub-districts. Mountainous landscapes mark its topography with several towering peaks, including Doi Inthanon, which is the country's highest mountain (2,580 m above mean sea level). The province's climate falls under the tropical savanna climate (Aw) category of the Köppen-Geiger classification system, characterized by wet and dry seasons throughout the year (Peel et al., 2007). The dry season typically lasts from November to April, while the wet season persists from May to October. During the wet season in Chiang Mai, heavy rainfall is typical, with an average precipitation of 1,100 to 1,200 mm. The average temperature in the region is 25.4°C, with maximum and minimum temperatures of 31.8 and 20.1°C, respectively (Chittrakorn and Chakpitak, 2019).

In addition to the mountainous landscape of Chiang Mai's westernmost region, the province boasts a variety of other diverse terrains i.e., dense forests, valleys, and rolling hills. This province is the northern region's largest intermontane basin, characterized by its location within the Chiang Mai Basin (Mankhemthong, 2019). The area is notable for its complex geological processes and formations. The geological structure of Chiang Mai Basin, the result of divergent geological forces, such as tectonic activity, sedimentation, and erosion, has formed a distinctive

landscape of flat and mountainous terrains with steep gradients. This region is geologically diverse, primarily consisting of sedimentary and metamorphic rocks alongside igneous formations (Yongsiri et al., 2023). These rock types' differential weathering rates lead to soils forming with varying cohesion and erosion resistance (Dechkamfoo et al., 2022). These geological and soil characteristics significantly influence the region's susceptibility to landslides.

2.2 Data acquisition

2.2.1 Training and validation data

The dataset used in this study comprised historical landslide incidents gathered from the Department of Mineral Resources' inventory spanning from 1989 to 2019. A total of 4,247 points were extracted to represent locations at risk of landslides in the Chiang Mai region. An equal number of non-landslide locations were randomly generated using a 1,000 m buffer distance from areas where landslides had occurred (Huan et al., 2023). The landslide dataset was split into both training and validation sets, with a 70:30 inventory sample ratio. This method ensures that the models can be trained using most data while reserving a portion for assessment purposes (Hu et al., 2020; Wang et al., 2021).

2.2.2 Intrinsic factors of landslide susceptibility

In Table 1, intrinsic factors outlining landslide susceptibility are given. Such factors highlight the elevation, slope, aspect, plan curvature, profile curvature, lithology, normalized difference vegetation index (NDVI), normalized difference water index (NDWI), stream power index (SPI), terrain ruggedness index (TRI), topographic wetness index (TWI), distance from fault, distance from stream, and distance from road (Hu et al., 2020; Huan et al., 2023; Das et al., 2023). All data was spatially aggregated into a 30 m resolution raster.

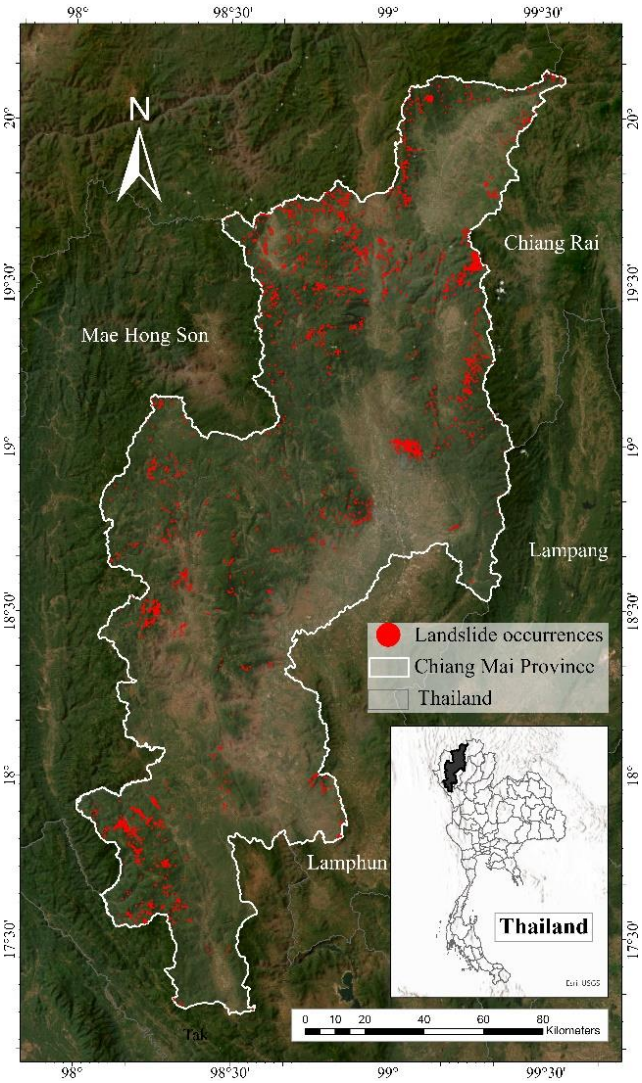

Figure 1. Location of Chiang Mai Province (the white border line boundary) courtesy of the satellite image from ArcGIS Pro software e-contract number ELC_T21-3057 (ESRI, Redlands, CA, USA). Red dots reveal the distribution of previous landslide occurrences that occurred in the province of Chiang Mai.

Table 1. Intrinsic factors' data format and acquired sources

Intrinsic factors	Format	Data source
Landslide occurrences	Point vector	Department of Mineral Resources
Elevation (m)	Raster	Earth Data, NASA (https://search.earthdata.nasa.gov)
Slope	Raster	DEM processing
Aspect	Raster	DEM processing
Plan curvature	Raster	DEM processing
Profile curvature	Raster	DEM processing
Lithology	Raster	Department of Mineral Resources
NDVI	Raster	Landsat 8-OLI (USGS)
NDWI	Raster	Landsat 8-OLI (USGS)
SPI	Raster	DEM processing

Table 1. Intrinsic factors' data format and acquired sources (cont.)

Intrinsic factors	Format	Data source
TRI	Raster	DEM processing
TWI	Raster	DEM processing
Distance from fault	Raster	Department of Mineral Resources
Distance from stream	Raster	Department of Mineral Resources
Distance from road	Raster	Department of Provincial Administration

2.3 Multicollinearity

Pham et al. (2020) reported that the issue of multicollinearity poses a significant challenge in selecting related variables for the susceptibility model. This phenomenon of high correlation among predictors can interfere with landslide susceptibility mapping, hindering the identification of significant contributors to landslide occurrence (Yu et al., 2023). The stability and reliability of susceptible models are also affected when independent variables exhibit strong interrelationships. In Equation (1), the variance inflation factor (VIF) is employed as a diagnostic tool to evaluate the extent of correlation between variables (Hair et al., 2010):

$$\mathrm{VIF}\ (X_i) = \frac{1}{1-R_i^2} \quad (1)$$

Where; VIF (X_i) represents the VIF value for the predictor variable X_i, and R_i^2 is the coefficient of determination (R-squared) obtained by regressing X_i on all other predictor variables.

According to Equation (1), a commonly used threshold of 10 indicates that variables with a VIF value exceeding ten may exhibit problematic multicollinearity (Aleotti and Chowdhury, 1999; Lee, 2005). A tolerance (TOL), an inverted fraction of VIF, is also considered to support inappropriate independent variables. Recent studies have considered lower thresholds for more conservative variable selection, aiming to minimize the effects of multicollinearity and ensure precise estimation of regression coefficients (Yu et al., 2023).

2.4 Ensemble machine learning algorithms

2.4.1 Random forest (RF) method

The RF algorithm, a bagging technique, has emerged as a potent ML approach for assessing landslide susceptibility. First developed by Breiman (2001), this ensemble learning method has gained popularity due to its capability to handle complex spatial relationships and capture the nonlinear nature of landslide occurrences. The RF algorithm combines the predictions of multiple decision trees to create a robust and accurate model. Moreover, its ability to handle intricate spatial relationships, capture nonlinear interactions, and provide essential rankings for input variables makes it a practical tool for prediction (Jhonnerie et al., 2015). Several studies have successfully applied the RF algorithm to landslide susceptibility mapping in various geographic regions (Van Den Eeckhaut et al., 2019). The RF model can be represented as shown in Equation (2):

$$\hat{Y} = \mathrm{mode}\ (C_k\ (x)) \quad (2)$$

Where; $\hat{Y}$ represents the predicted class label for input x, mode is the function that selects the most frequent occurring class label among the decision trees in the RF ensemble, and $C_k(x)$ denotes the predicted class label by the k-th decision tree.

2.4.2 Gradient-boosting (GB) method

The GB method operates by iteratively training new models, focusing on samples that preceding models misclassified. The final prediction of the boosting ensemble is obtained by combining the predictions of all the models in the ensemble (Friedman, 2001; Schapire and Freund, 2013; Ke et al., 2017). GB effectively combines multiple weak prediction models, often decision trees, to create a robust predictive model. The term "gradient" in GB refers to the optimization technique for updating the model's predictions. As such, it involves computing the gradient (partial derivatives) of the loss function concerning the predictions and adjusting them in a direction that minimizes the loss. Typically, gradient descent or a similar optimization algorithm is utilized for this purpose (Friedman, 2001). Equation (3) provides a formal representation of GB:

$$F(x) = F_0(x) + \sum_{m=1}^{M}(\eta \times h_m(x)) \quad (3)$$

Where; $F_o(x)$ denotes an initial prediction as a target value derived from $\frac{1}{N}\sum_i y_i$, and m refers to

iteration, M denotes the total number of iterations, η refers to learning rate, and $h_m(x)$ denotes weak learner.

2.4.3 eXtreme gradient boosting (XGB) method

The gradient-boosting ensemble method has been widely employed in predictive modelling to achieve improved accuracy. Among its many variants, the XGB algorithm has emerged as a widespread implementation of gradient-boosting classification (Chen and Guestrin, 2016). Hence, the algorithm incorporates regularization techniques like shrinkage and column subsampling. It also introduces both L1 and L2 regularization terms in the objective function to control the model's complexity and reduce the influence of individual features. Additionally, the XGB function supports various loss functions, making it suitable for diverse problem domains, including linear regression, logistic regression, and ranking. The XGB function can be expressed as:

$$\hat{y}_i = \sum_{k=1}^{K} f_k(x_i) \quad (4)$$

Where; $\hat{y}_i$ is the predicted output for the i^{th} sample, x_i represents the feature vector for the i^{th} sample, K denotes the number of weak learners (decision tree), and $f_k(x_i)$ reveals the output of the i^{th} weak learner for the i^{th} sample.

Further, it is seen that the XGB algorithm employs pruning techniques during the boosting process to control the growth of decision trees. Eliminating insignificant splits can help improve the model's overall performance and results in more compact and efficient trees, as demonstrated. It is significant that both XGB and the other gradient boosting algorithms have shown success in various applications, including landslide susceptibility mapping (Ke et al., 2017; Prokhorenkova et al., 2018).

2.4.4 Stacking ensemble (STK) method

In 1992, Wolpert introduced a comprehensive model (STK). Herein, the aim was to integrate multiple diverse algorithms into the training process. This approach involved using base learner classifiers with lower efficiency than data-independent coaching (Dou et al., 2020; Huan et al., 2023). In this experiment, RF, GB, and XGB were employed as the base learners. In Equation (5), a logistic regression (LR) is utilized (Hu et al., 2020). LR is designed to benefit binary classification where the outcome variable contains two categories (Hamid et al., 2023):

$$P(Y = 1) = \hat{p} = \frac{1}{1+e^{(\hat{\alpha}+\hat{\beta}_1 x_1+\hat{\beta}_2 x_2+\cdots+\hat{\beta}_i x_i)}} \quad (5)$$

Where; $\hat{p}$ is a landslide occurrence probability. The probability varies from 0 to 1 within an S-shape curve. $\hat{\alpha}$ is the intercept of the logistic model, $\hat{\beta}_i$ denotes the slope coefficients, and x_i represents independent variables or intrinsic predictors used in our prediction.

During the training phase, STK incorporates several instances of the same model. Unlike other ensemble techniques, the stacking algorithm is seen to divide the training data independently, and each base learner model is trained separately. After training, each base learner model is able to verify predictions, which are then combined by the meta-learner to make a final decision. This method leads to highly accurate prediction results.

2.5 Evaluation of model performance

The study utilized testing data split from the sample to collect measurement data. To assess the model, forecasted outcomes were matched against actual results, and the precise number of accurately identified incidents i.e., landslides and non-landslides were registered as true positives (TP) and true negatives (TN), respectively. In Table 2, the misclassification of incidents: landslides or non-landslides is indicated by false positives (FP) and false negatives (FN).

Table 2. Confusion matrix of each ML model, containing TP, TN, FP, and FN, respectively.

		Predicted results	
		Landslide (1)	Non-landslide (0)
Actual results	Landslide (1)	TP	FP
	Non-landslide (0)	FN	TN

The model's effectiveness was evaluated using various metrics, such as precision, recall, overall accuracy (OA), area under the receiver operating characteristic curve (ROC), and the F1-score. The F1-score is a critical measure used to assess the efficacy of machine learning models as it combines precision

and recall. OA, which ranges between 0 and 1, represents the ratio of accurately classified landslides and non-landslides among all occurrences. The higher the accuracy is to 1, the more influential the overall accuracy of the model is. Equation (6)-(9) express these metrics:

$$\text{Precision} = \frac{\text{TP}}{\text{TP} + \text{FP}} \quad (6)$$

$$\text{Recall} = \frac{\text{TP}}{\text{TP} + \text{FN}} \quad (7)$$

$$\text{F1} - \text{score} = 2 \times \frac{(\text{Precision} \times \text{Recall})}{(\text{Precision} + \text{Recall})} \quad (8)$$

$$\text{Overall accuracy} = \frac{\text{TP} + \text{TN}}{\text{TP} + \text{TN} + \text{FP} + \text{FN}} \quad (9)$$

The ROC curve represents the relationship between the false positive rate (FPR) and the true positive rate (TPR) of a classification model (Muschelli, 2020). A higher FPR on the horizontal axis indicates that more actual negative instances are incorrectly classified as positive. In contrast, a higher TPR on the vertical axis demonstrates that more actual positive instances are correctly classified as positive. The optimal prediction scenario is when FPR is 0 and TPR is 1, corresponding to the point (0, 1) on the coordinate axis. The ROC curve is an evaluation metric for the classification model's accuracy, ranging from 0.5 to 1. A higher value under curve (closer to 1) signifies better prediction performance (Huan et al., 2023).

3. RESULTS AND DISCUSSION

3.1 Independent variables' multicollinearity determination and importance

To diagnose the issue of multicollinearity, this research utilized both VIF and TOL. Such applications aim to facilitate the selection of relevant factors. Notably, a VIF value lower than 5 and a TOL value above 0.2 collectively signify the absence of substantial collinear tendencies among landslide predictors (Yu et al., 2023). In Table 3, the predictors selected are listed.

Table 3. Multicollinearity diagnosis: Variables selected for the susceptibility models

Variables	VIF	TOL	Selection
Elevation	12.66	0.08	No
Aspect	3.61	0.28	Yes
Slope	2.05	0.49	Yes
Plan curvature	52.53	0.02	No
Profile curvature	69.67	0.01	No
NDVI	37.14	0.03	No
NDWI	34.96	0.03	No
SPI	1.00	0.99	Yes
TRI	1.09	0.99	Yes
TWI	29.45	0.03	No
Geology	1.03	0.97	Yes
Distance from fault	2.31	0.43	Yes
Distance from stream	1.91	0.52	Yes
Distance from road	2.47	0.40	Yes

Based on Table 3, variables with a VIF value greater than 5 and a TOL value less than 0.2 were excluded from the susceptibility model (Huan et al., 2023). As a result, eight independent variables, including aspect, slope, SPI, TRI, geology, distance from fault, distance from stream, and distance from road, were selected for the model's training. As noted by Pham et al. (2020), this process of removing insignificant factors can improve the predictive accuracy of landslide susceptibility models. Subsequently, the selected variables in each model were evaluated. In Figure 2, the importance of the variables in the different models are illustrated.

According to Figure 2, the RF model exhibits a predilection for assigning substantial importance to variables, such as aspect, SPI, distance from fault, slope, and distance from stream. Conversely, the GB model manifests a pronounced emphasis on SPI, succeeded by aspect, distance from stream, slope, and distance from fault. The XGB model, in its evaluation,

accords high significance to the distance from fault, followed by aspect, SPI, distance from stream, and slope. The STK model allocates considerable significance to aspect, supplemented by distance from fault, stream, SPI, and slope. In contrast, TRI, geology, and distance from road are seen to be of minimum relative importance. Collectively, all models highlight the vital contribution of factors, such as aspect, slope, SPI, distance from fault, and distance from stream, as evidenced by their respective significant percentages about landslide susceptibility.

Figure 2. Importance of the variables in different models

In this research, aspect is identified as a critical factor across all models, focusing on the western region of Chiang Mai, which forms the edge of the intermontane basin adjoining the mountainous areas that extend into the Republic of the Union of Myanmar. This positioning leaves the eastern quadrant, extending from northeast to southeast (Yongsiri et al., 2023), more exposed to increased solar radiation, rainfall, and seepage, alongside other factors contributing to heightened landslide vulnerability (Zeng et al., 2023a). It is evident, therefore, that the intermontane basin topography characterizing this area of the study is quite unique. In different terrains, the significance of aspect varies. In Nepal, Tanoli et al. (2017) observed that landslide incidents predominantly occur on southern to western slopes, highlighting the directions that receive more intense monsoon rainfall, thereby escalating the likelihood of landslides. Besides, the correlation between steeper slope angles and the likelihood of

landslides is obvious. In the context of Chiang Mai, many landslides are noted on slopes with angles ranging from 15° to 35°. This finding aligns with the research by Dechkamfoo et al. (2022), signifying that slope angles of 15° to 30° are prone to triggering landslides in northern Thailand.

In the work by Sevgen et al. (2019), SPI demonstrates the erosive power of flowing water. As reported, the area's terrain is exposed to land erosion caused by stream power. Herein, the landscape gives rise to valleys and high plains. The points of landslide occurrence are located near these steep ridges, where the water flow from rain is most intense due to the steep terrain and not far from the stream (Zeng et al., 2023a). The proximity to fault lines is a significant factor in landslides within the study area. A number of landslides are observed in areas close to active faults. This observation is consistent with the findings of Wu et al. (2020), who identified a linear relationship between the distance from fault lines and the distribution of landslides. This pattern suggests an increased likelihood of landslides in areas closer to fault lines, underscoring the importance of fault proximity in assessing landslide risk.

3.2 Best combination of model's hyper parameter

During the training of the susceptibility model, hyperparameter tuning was performed using a grid search technique (Ageenko et al., 2022; Abbas et al., 2023). Each discrete model was evaluated using a 10-fold cross-validation approach to determine the most appropriate parameter combinations. In Table 4, the results of this evaluation are presented, showing the optimal hyperparameter combination for the ML model.

According to Table 4, every hyperparameter combination was chosen for the final model and fitted to the training dataset using an empirical approach, which achieved the most favorable results (Kuhn and Johnson, 2019).

Table 4. The best combination of hyperparameters in ML models' training

ML models	Hyperparameters	Value / Method
RF	max_depth	50
	min_sample_left	1
	n_estimators	200
GB	learning_rate	0.05
	n_estimators	500
	min_samples_leaf	2
	min_samples_split	10
	max_depth	20
XGB	booster	gbtree
	colsample_bytree	0.7
	eta	0.2
	max_depth	10
STK	subsample	1
	final estimator	logistic regression
	stack_method	predict_proba

3.3 Accuracy assessment for the modeling results

In Table 5, to evaluate the performance of the four ML models, several metrics, including precision, recall, F1-score, OA, and area under ROC curve, were utilized. In Figure 3, the ROC curves for each of the four models are shown, highlighting their respective areas under the curve.

In Table 5, a comparative analysis of all the landslide susceptibility models under consideration is shown. Results demonstrate that the STK model outperformed the GB, XGB, and RF models, with an OA of 81.75%. Furthermore, the F1-score of the STK model (82.04%) confirmed its superior performance compared to the other models. These results are consistent with previous studies exploring landslide susceptibility (Hu et al., 2020; Huan et al., 2023).

As observed in Figure 3 and Table 5, the STK model has been identified as the most effective approach for mapping landslide susceptibility, with a ROC value of 0.8928, represented by the dark red curve. In comparison, GB (dark green curve) with 0.8914, XGB (dark orange curve) with 0.8872, and RF

(dark blue curve) with 0.8762 models exhibited lower areas under the ROC curve. A ROC value exceeding 0.8 indicates good prediction ability, as highlighted in previous research studies (Huan et al., 2023). Therefore, the findings of this study suggest that the STK model should be preferred when selecting a model for landslide susceptibility mapping. However, in cases where models exhibit comparable evaluation accuracy, it is essential to simultaneously consider accuracy metrics and areas under the ROC curve to select the best candidate model (Pham et al., 2016; Zeng et al., 2023a).

Table 5. The models' performance: Validation data

Model	Precision	Recall	F1-score	OA	ROC
RF	77.43%	80.54%	78.95%	77.47%	0.8762
GB	80.13%	81.14%	80.61%	80.63%	0.8916
XGB	81.72%	79.24%	80.46%	80.23%	0.8872
STK	**82.92%**	**81.18%**	**82.04%**	**81.75%**	**0.8928**

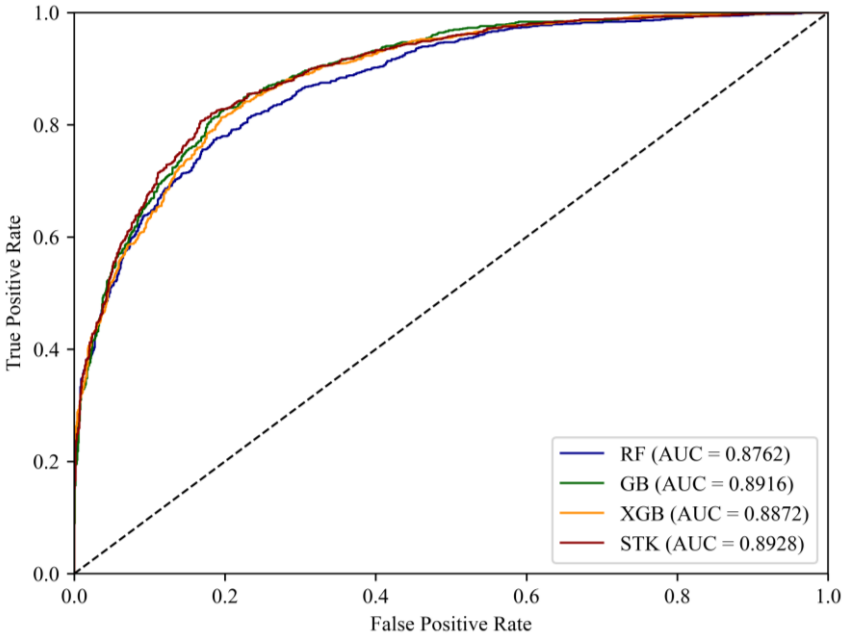

Figure 3. Area under the ROC for each ML model predicting landslide susceptibility: x refers to FPR and y refers to TPR; RF model (dark blue curve), GB model (dark green curve), XGB model (dark orange curve), and STK model (dark red curve).

3.4 Predicted landslide susceptibility

During the prediction stage, the four landslide susceptibility models were reclassified into five classes: namely, very high, high, moderate, low, and very low, following the natural breaks (Jenks) principle (Anis et al., 2019; Zeng et al., 2024), as depicted in Figure 4. To validate the contrast of each predicted class between the susceptible models, the ratio of each susceptible class (Rs) was calculated and presented, as in Table 6.

Table 6. Ratio of susceptible classes predicted from different ML models

Class prediction	Ratio of susceptible classes (Rs)			
	RF	GB	XGB	STK
Very low	0.26	0.51	0.48	0.48
Low	0.26	0.15	0.17	0.18
Moderate	0.21	0.11	0.12	0.11
High	0.17	0.10	0.11	0.10
Very high	0.10	0.13	0.13	0.13

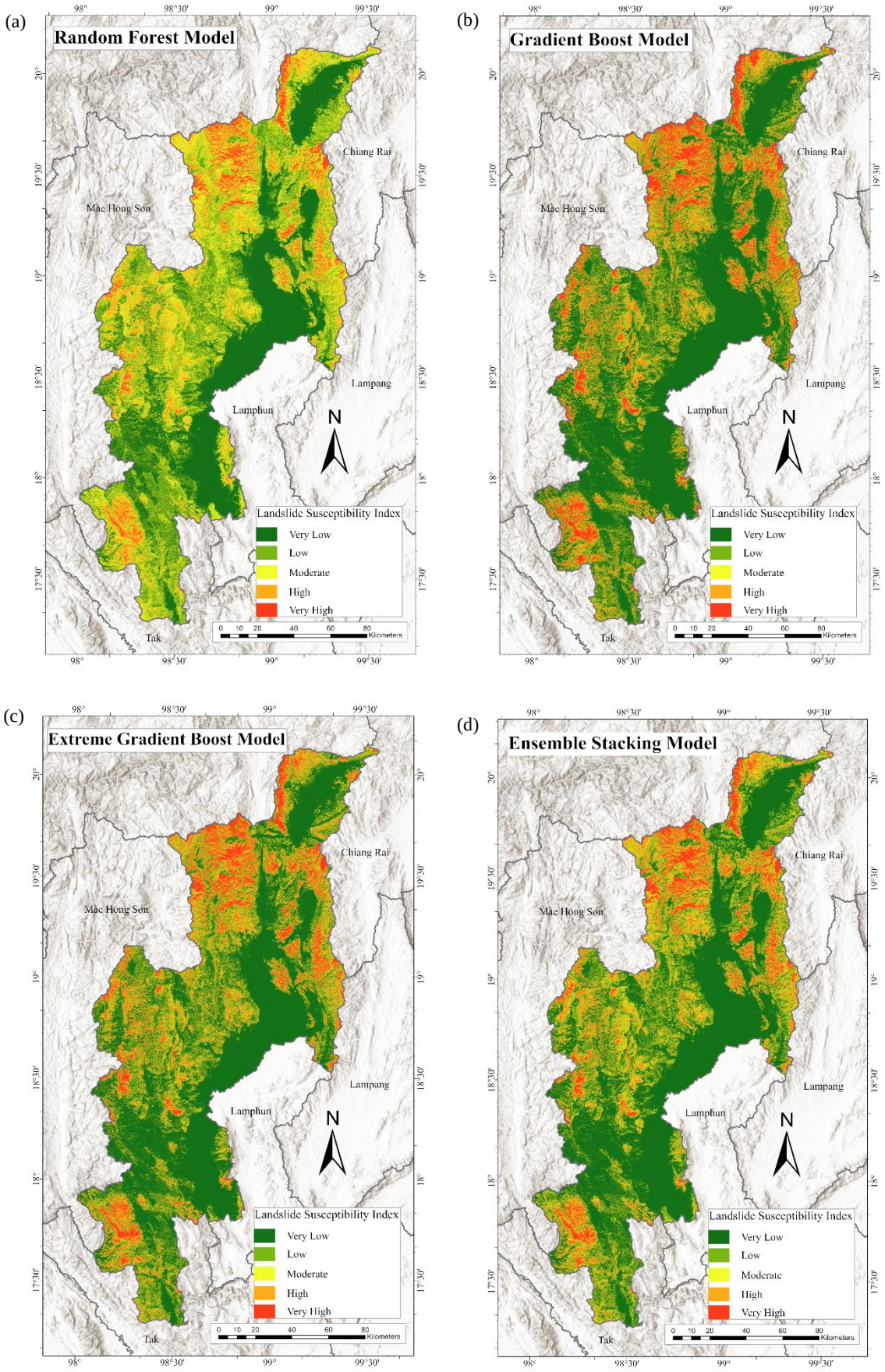

Figure 4. A comparison of predictions for the four ML landslide susceptibility models: (a) RF, (b) GB, (c) XGB, and (d) STK. The susceptibility of landslide is classified as very high (red), high (orange), moderate (yellow), low (light green), and very low (green), respectively.

According to Figure 4 and Table 6, the STK, GB, and XGB models exhibit more uniform Rs values, from very-low to very-high susceptibility classes. In the case of RF, previous works have reported the highest performance among its counterparts (Goetz et al., 2015; Yu et al., 2023). In contrast, our results confirm that the landslide susceptibility prediction from the RF model exhibited a more moderate susceptible area (0.21) than the other models (0.11, 0.12, and 0.11 for GB, XGB, and STK), corresponding to a lower precision score (77.43%) in the RF model's evaluation. Conversely, the predicted results from STK, XGB, and GB models reveal comparable outcomes with better precision scores of 82.92%, 81.72%, and 80.13%, respectively. Furthermore, compared with its contenders, RF reported differences between its low and very low class, with the low class Rs revealing high density. Thus, it is seen that the very-low class Rs value (0.26) was much lower than in the other models. The bagging technique is explicitly employed in the RF algorithm to mitigate variance. Contrasting this, the boosting approach effectively reduces bias and variance (Wu et al., 2020). This dual reduction capability is a cornerstone of boosting methods. Moreover, in the context of GB and XGB, the boosting framework is seen to enhance the ensemble model's performance (Table 5). Such an outcome was achieved by minimizing overfitting in GB and regulating model complexity in XGB, primarily through adjusting the minimized loss function (Huan et al., 2023).

In the realm of experimental models for landslide prediction, the STK model emerges as superior in performance compared to other singular ML models, aligning with prior research in this field (Hu et al., 2020; Huan et al., 2023). This enhanced performance is attributed to integrating bagging and boosting techniques as its foundational learners, collaboratively diminishing bias and variance in classification. This synergy notably augments the STK model's fitness to the training data (Wu et al., 2020). Critically, the primary advantage of the STK model lies in its amplified predictive capacity. Thus, prudent selection of the combination of models or base learners is recommended. Such a selection necessitates a thorough evaluation of each learner prior to their incorporation into ensemble models (Dou et al., 2020).

4. CONCLUSION

In this paper, results demonstrated that factors like aspect, slope, SPI, distance from faults, and distance from streams play a crucial role in determining landslide susceptibility. Compared to its counterparts, the novel STK model proved to be most effective for predicting landslide hazards in the intermontane basin terrain. It is significant that the STK model achieved the highest ROC value of 0.8928, validating its high prediction ability and justifying its selection as best candidate model. This model is recommended for creating landslide susceptibility maps in intermontane basin areas. Further research needs to be undertaken to refine model selection and base learner optimization for enhanced predictive accuracy.

ACKNOWLEDGEMENTS

This research was supported by the Faculty of Liberal Arts, Thammasat University, Research Unit in Geospatial Applications (Capybara Geo Lab). We express our gratitude towards the reviewers who have offered recommendations to enhance the quality of the writing.

REFERENCES

Abbas F, Zhang F, Ismail M, Khan G, Iqbal J, Alrefaei AF, et al. Optimizing machine learning algorithms for landslide susceptibility mapping along the Karakoram Highway, Gilgit Baltistan, Pakistan: A comparative study of baseline, bayesian, and metaheuristic hyperparameter optimization techniques. Sensors 2023;23(15):Article No. 6843.

Ageenko A, Hansen LC, Lyng KL, Bodum L, Arsanjani JJ. Landslide susceptibility mapping using machine learning: A Danish case study. ISPRS International Journal of Geo-Information 2022;11(6):Article No. 324.

Aleotti P, Chowdhury R. Landslide hazard assessment: Summary review and new perspectives. Bulletin of Engineering Geology and the Environment 1999;58:21-44.

Anis Z, Wissem G, Vali V, Smida H, Mohamed Essghaier G. GIS-based landslide susceptibility mapping using bivariate statistical methods in North-western Tunisia. Open Geosciences 2019;11(1):708-26.

Breiman L. Random forests. Machine Learning 2001;45:5-32.

Chen T, Guestrin C. Xgboost: A scalable tree boosting system. Proceedings of the 22nd ACM SIGKDD International Conference on Knowledge Discovery and Data Mining; 2016 Aug 13; San Francisco, CA: USA; 2016.

Chittrakorn K, Chakpitak N. Weather in Chiang Mai. Chiang Mai Journal of Science 2019;46(2):188-206.

Das J, Saha P, Mitra R, Alam A, Kamruzzaman M. GIS-based data-driven bivariate statistical models for landslide susceptibility prediction in Upper Tista Basin, India. Heliyon 2023;9(5):e16186.

Dechkamfoo C, Sitthikankun S, Ayutthaya TKN, Manokeaw S, Timprae W, Tepweerakun S, et al. Impact of rainfall-induced landslide susceptibility risk on mountain roadside in northern Thailand. Infrastructures 2022;7(2):Article No. 17.

Dou J, Yunus AP, Bui DT, Merghadi A, Sahana M, Zhu Z, et al. Improved landslide assessment using support vector machine with bagging, boosting, and stacking ensemble machine learning framework in a mountainous watershed, Japan. Landslides 2020;17:641-58.

Friedman JH. Greedy function approximation: A gradient boosting machine. Annals of Statistics 2001;1:1189-232.

Goetz JN, Brenning A, Petschko H, Leopold P. Evaluating machine learning and statistical prediction techniques for landslide susceptibility modeling. Computers and Geosciences 2015;81:1-1.

Hair JF, Anderson RE, Tatham RL, Black WC. Multivariate Data Analysis. 7th ed. Englewood Cliff, New Jersey: Prentice Hall; 2010.

Hamid B, Massinissa B, Nabila G. Landslide susceptibility mapping using GIS-based statistical and machine learning modeling in the city of Sidi Abdellah, Northern Algeria. Modeling Earth Systems and Environment 2023;9(2):2477-500.

Hu X, Zhang H, Mei H, Xiao D, Li Y, Li M. Landslide susceptibility mapping using the stacking ensemble machine learning method in Lushui, Southwest China. Applied Sciences 2020;10(11):Article No. 4016.

Hu X, Mei H, Zhang H, Li Y, Li M. Performance evaluation of ensemble learning techniques for landslide susceptibility mapping at the Jinping County, Southwest China. Natural Hazards 2021;105:1663-89.

Huan Y, Song L, Khan U, Zhang B. Stacking ensemble of machine learning methods for landslide susceptibility mapping in Zhangjiajie City, Hunan Province, China. Environmental Earth Sciences 2023;82(1):Article No. 35.

Jhonnerie R, Siregar VP, Nababan B, Prasetyo LB, Wouthuyzen S. Random Forest classification for mangrove land cover mapping using Landsat 5 TM and ALOS PALSAR imageries. Procedia Environmental Sciences 2015;24:215-21.

Ke G, Meng Q, Finley T, Wang T, Chen W, Ma W, et al. Lightgbm: A highly efficient gradient boosting decision tree. Proceedings of the 31st Annual Conference on Neural Information Processing Systems (NIPS2017); 2017 Dec 4-9; Long Beach, California: USA; 2017.

Kuhn M, Johnson K. Feature Engineering and Selection: A Practical Approach for Predictive Models. Milton: Chapman and Hall/CRC; 2019.

Kumar R, Anbalagan R. Landslide susceptibility mapping using analytical hierarchy process (AHP) in Tehri reservoir rim region, Uttarakhand. Journal of the Geological Society of India 2016;87:271-86.

Lee S. Application of logistic regression model and its validation for landslide susceptibility mapping using GIS and remote sensing data. International Journal of Remote Sensing 2005;26(7):1477-91.

Lee JH, Sameen MI, Pradhan B, Park HJ. Modeling landslide susceptibility in data-scarce environments using optimized data mining and statistical methods. Geomorphology 2018;303:284-98.

Mankhemthong N, Morley CK, Takaew P, Rhodes BP. Structure and evolution of the Ban Pong Basin, Chiang Mai Province, Thailand. Journal of Asian Earth Sciences 2019;172:208-20.

Muschelli J. ROC and AUC with a binary predictor: A potentially misleading metric. Journal of Classification 2020;37:696-708.

Myronidis D, Papageorgiou C, Theophanous S. Landslide susceptibility mapping based on landslide history and analytic hierarchy process (AHP). Natural Hazards 2016;81:245-63.

Peel MC, Finlayson BL, McMahon TA. Updated world map of the Köppen-Geiger climate classification. Hydrology and Earth System Sciences 2007;11:1633-44.

Pham BT, Pradhan B, Bui DT, Prakash, I, Dholakia MB. A comparative study of different machine learning methods for landslide susceptibility assessment: A case study of Uttarakhand area (India). Environmental Modelling and Software 2016;84:240-50.

Pham BT, Bui DT, Prakash I. Landslide susceptibility assessment using bagging ensemble based alternating decision trees, logistic regression and J48 decision trees methods: A comparative study. Geotechnical and Geological Engineering 2017;35:2597-611.

Pham BT, Pradhan B, Bui DT, Indra P. Analyzing the impact of multicollinearity on landslide susceptibility mapping using GIS-based machine learning techniques. Geocarto International 2020;35(11):1199-223.

Prokhorenkova L, Gusev G, Vorobev A, Dorogush AV, Gulin A. CatBoost: unbiased boosting with categorical features. Proceedings of the 32nd Conference on Neural Information Processing Systems (NeurlPS 2018); 2018 Dec 3-8; Montreal: Canada; 2018.

Reichenbach P, Rossi M, Malamud BD, Mihir M, Guzzetti F. A review of statistically-based landslide susceptibility models. Earth-Science Reviews 2018;180:60-91.

Schapire RE, Freund Y. Boosting: Foundations and algorithms. Kybernetes 2013;42(1):164-6.

Sevgen E, Kocaman S, Nefeslioglu HA, Gokceoglu C. A novel performance assessment approach using photogrammetric techniques for landslide susceptibility mapping with logistic regression, ANN and random forest. Sensors 2019;19:Article No. 3940.

Sim KB, Lee ML, Wong SY. A review of landslide acceptable risk and tolerable risk. Geoenvironmental Disasters 2022; 9(1):Article No. 3.

Tanoli JI, Ningsheng C, Regmi AD, Jun L. Spatial distribution analysis and susceptibility mapping of landslides triggered before and after Mw7. 8 Gorkha earthquake along Upper Bhote Koshi, Nepal. Arabian Journal of Geosciences 2017;10:1-24.

Thongley T, Vansarochana C. Spatial zonation of landslide prone area using information value in the geologically Fragile Region of Samdrup Jongkhar-Tashigang National Highway in Bhutan. Environment and Natural Resources Journal 2021;19(2):122-31.

Van Westen CJ, Castellanos E, Kuriakose SL. Spatial data for landslide susceptibility, hazard, and vulnerability assessment: An overview. Engineering Geology 2008;102(3-4):112-31.

Van Den Eeckhaut M, Kerle N, Poesen J, Hervás J. Support vector machines for landslide susceptibility mapping: A comparison of relative feature importance and model performance. Geomorphology 2019;328:85-97.

Wang H, Zhang L, Luo H, He J, Cheung RWM. AI-powered landslide susceptibility assessment in Hong Kong. Engineering Geology 2021;288:Article No. 106103.

Wattananikorn K, Beshir JA, Nochaiwong A. Gravity interpretation of Chiang Mai Basin, Northern Thailand:

Concentrating on ban Thung Sieo area. Journal of Southeast Asian Earth Sciences 1995;12(1-2):53-64.

Wolpert DH. Stacked generalization. Neural Networks 1992;5(2):241-59.

Wu Y, Ke Y, Chen Z, Liang S, Zhao H, Hong H. Application of alternating decision tree with AdaBoost and bagging ensembles for landslide susceptibility mapping. Catena 2020;187:Article No. 104396.

Yongsiri P, Soytong P, Laongmanee W, Uthaisri P. Development of a landslide risk area display system by using the geospatial technology with daily rainfall data via the internet network in the Northern region of Thailand. Technology 2023; 19(4):1953-68.

Yu H, Pei W, Zhang J, Chen G. Landslide susceptibility mapping and driving mechanisms in a vulnerable region Based on multiple machine learning models. Remote Sensing 2023;15(7):Article No. 1886.

Zeng T, Wu L, Peduto D, Glade T, Hayakawa YS, Yin K. Ensemble learning framework for landslide susceptibility mapping: Different basic classifier and ensemble strategy. Geoscience Frontiers 2023a;14(6):Article No. 101645.

Zeng T, Guo W, Wang L, Jin B, Wu F, Guo R. Tempo-spatial landslide susceptibility assessment from the perspective of human engineering activity. Remote Sensing 2023b;15:Article No. 4111.

Zeng T, Jin B, Glade T, Xie Y, Li Y, Zhu Y, et al. Assessing the imperative of conditioning factor grading in machine learning-based landslide susceptibility modeling: A critical inquiry. Catena 2024;236:Article No. 107732.

Environment and Natural Resources Journal

Volume 22
Issue 2
2024

Interaction between Rhizobacteria and *Andrographis paniculata* Under Water Limitation

Butsakorn Yodphet[1], Nisachon Jangpromma[2], Wanwipa Kaewpradit Polpinit[3], and Nuntavun Riddech[4*]

[1]*Graduate school of Microbiology Program, Faculty of Science, Khon Kaen University, Thailand 40002*
[2]*Protein and Proteomics Research Center for Commercial and Industrial Purposes (ProCCI), Department of Biochemistry, Faculty of Science, Khon Kaen University, Thailand 40002*
[3]*Department of Agronomy, Faculty of Agriculture, Khon Kaen University, Thailand 40002*
[4]*Department of Microbiology, Faculty of Science, Khon Kaen University, Thailand 40002*

ARTICLE INFO

Received: 2 Nov 2023
Received in revised: 23 Jan 2024
Accepted: 26 Jan 2024
Published online: 14 Feb 2024
DOI: 10.32526/ennrj/22/20230310

Keywords:
ACC-deaminase/ IAA production/ PGPR/ *Andrographis paniculata*/ Water limitation

*** Corresponding author:**
E-mail: nunrid@kku.ac.th

ABSTRACT

Drought stress is a major agricultural problem that leads to increased accumulation of ethylene in plants. It also has negative effects on plant productivity and growth. *Andrographis paniculate* is an important herb widely used in medical applications to inhibit diseases caused by viruses. In order to improve the production quality and growth of the *A. paniculata*, ACC-deaminase plant growth-promoting rhizobacteria were isolated from rice rhizosphere soil. All bacterial isolates were screened for their plant growth-promoting properties, including ACC deaminase, IAA production, biofilm formation, and exopolysaccharide production. Among the bacterial isolates, Rh-01 and Rh-22 exhibited positive results (cutting-edge) in all tests and were identified as *Paenibacillus polymyxa* Rh-01 and *Stenotrophomonas maltophilia* Rh-22, respectively. These strains were selected for further pot experiment study. Our results revealed that treatment with chemical fertilizer showed the highest potential to promote *A. paniculata* seedlings under normal moisture conditions. However, under water limitation conditions, the application of ACC-deaminase plant growth-promoting rhizobacteria led to a higher chlorophyll content compared to the control treatment. In addition, under normal irrigation conditions, plant growth promoting rhizobacterial increased relative water content and total biomass. In terms of plant stress markers, the proline content in *Andrographis paniculate's* seedling stage was low under water limitation conditions. In conclusion, to enhance the growth of *A. paniculate* seedlings during water limitation stress, a combination of microbial biofertilizers and chemical fertilizers is beneficial.

HIGHLIGHT

- ACC-deaminase plant growth-promoting rhizobacteria offer sustainable solutions for mitigating biotic and abiotic stress.
- ACC-deaminase plant growth-promoting rhizobacteria were able to promote the growth of *A. paniculata* when cultivated under water limitation
- The first report to indicate that *Paenibacillus polymyxa* Rh-01 and *Stenotrophomonas maltophilia* Rh-22 can stimulate the growth of *A. paniculata* under normal irrigation and water limitation
- Combined application of chemical fertilizers and microbial bio-fertilizers is recommended for sustainable agricultural practices.

1. INTRODUCTION

Herbs or medicinal plants are natural products widely used in medical applications for their numerous health benefits. Thailand has a variety of native herbs, including *Andrographis paniculata*, which is known for its medicinal properties in treating fever, common cold, diarrhea, and acting as an

Citation: Yodphet B, Jangpromma N, Polpinit WK, Riddech N. Interaction between rhizobacteria and Andrographis paniculata under water limitation. Environ. Nat. Resour. J. 2024;22(2):171-183. (https://doi.org/10.32526/ennrj/22/20230310)

antioxidant. Recently, researchers have discovered its potential in treating fever caused by COVID-19 infections (Jiang et al., 2021). *A. paniculata* grows well in tropical areas. However, the changing climate and rising ambient temperatures are affecting plant growth, with drought stress becoming a significant agricultural problem.

Drought stress is abiotic stress caused by water deficit, and has severe implications for ecosystems, agriculture and connected livelihoods. Water is essential for plant growth as it is a key factor that influences photosynthesis, dissolution, and transportation of nutrients in the soil (Selvakumar et al., 2012). Drought affects plant cells, resulting in reduced nutrient absorption and pigment synthesis, and increased accumulation of ethylene and reactive oxygen species (ROS), causing damage to plant organs and plant development (Rahdari et al., 2012). These substances are damaging to growth (Smirnoff, 1993) and significantly impact crop production in arid and semi-arid regions (Ahmadizadeh et al., 2012). In general, plants respond to biotic and abiotic stress by scavenging ROS through antioxidant enzyme activity and accumulating compatible solutes like flavonoid, proline, and phenolic compounds, including secreted phytohormones such as ethylene. However, many previous studies found that high levels of ethylene in plants can lead to early flowering and aging. Hence, the bacterial community surrounding plant roots has a crucial role in influencing plant resistance to drought stress. Several studies have shown that ACC-deaminase-producing bacteria can alleviate the negative effect of drought stress by converting ethylene into α-ketobutyrate and ammonia. Additionally, indole-3-acetic acid (IAA), synthesized by plant growth-promoting rhizobacteria (PGPR), can improve root and shoot growth. Zhou et al. (2016) demonstrated that the *Bacillus megaterium* BOFC15 released polyamine and abscisic acid (ABA), which play important roles in plant resistance to water limitation conditions by controlling the plant stomata and preventing water loss from plant cells.

Ethylene is a gaseous phytohormone released in large amounts by plants, especially during ripening prior to leaf shedding and flowering. Ethylene plays an important role in regulating plant growth and development. High accumulation of ethylene in plants can accelerate plant maturity and senescent of plant cells. While ethylene is beneficial in agriculture, its gaseous form limits its utilization. Furthermore, ethylene is also responsible for other abiotic stress, such as salt stress, floods, and heavy metal contamination. Water deficit conditions induce ethylene biosynthesis in plants, and high ethylene content can limit root and shoot growth (Liu et al, 2013).

The diverse microbial organisms in soil can be classified into two groups: beneficial microorganisms and non-beneficial microorganisms. Plant growth promoting rhizobacteria (PGPR) are beneficial microorganisms applicable in agriculture. Rhizobacteria live in the rhizosphere soil of plants and promote plant growth through various mechanisms. Direct mechanisms include phosphate solubilization, production of phytohormones, and nitrogen-fixing activities, while siderophore and antibiotic production are indirect mechanisms for improving the growth of plants. Several groups of PGPR exist, such as IAA-producing rhizobacteria, nitrogen-fixing rhizobacteria, phosphate-solubilizing rhizobacteria, and ACC deaminase-producing rhizobacteria. ACC-deaminase-producing rhizobacteria are capable of producing 1-aminocyclopropane-1-carboxylate (ACC)-deaminase enzyme, which degrades ethylene in plants by breaking down ACC into ammonia and α-ketobutyrate. Under water stress, ACC accumulates in plant cells. PGPR has shown significant ability to increase the fresh and dry weight of pepper and tomato seedlings whilst reducing ethylene content (Mayak et al., 2004). ACC deaminase-producing rhizobacteria promote plant growth and development and have proven to be effective strategies in alleviating drought-related problems. Therefore, the aims of this study were to explore the relationship between ACC deaminase-producing rhizobacteria and herb roots, as well as to evaluate the alleviation of water limitation stress using the ACC deaminase-producing rhizobacteria.

2. METHODOLOGY

2.1 Screening of rhizobacteria from rhizosphere soil samples under water limitation

Rice rhizosphere soil samples were collected from Ban Had, Khon Kaen, Thailand (GPS site: 16.166540°N 101.915853°W). Ten grams of the soil was mixed with 90 mL of 0.85% NaCl solution, and serially diluted using same solution as diluent. The samples were then spread on tryptic soya agar (TSA) (Himedia, India) supplemented with polyethylene glycol 6000 (PEG6000) up to 30% (w/w), and incubated at 30°C for 24-48 h. Rhizobacteria colonies that appeared on agar plates were selected based on different colony characteristics to pure culture and further tested for other plant growth-promoting traits.

2.2 Screening of ACC deaminase-producing rhizobacteria under water limitation

Thirty-seven bacterial isolates of rhizobacteria were obtained from rhizosphere soil. ACC deaminase-producing rhizobacteria were screened by using the modified DF salt minimal media (Dworkin and Foster, 1958). The media consisted of glucose, gluconic, citric acid, K_2HPO_4, Na_2HPO_4, $Mg.SO_4 \cdot 7H_2O$ amended with various concentrations of polyethylene glycol 6000 up to 35% by (w/v). The turbid in the medium was presented as a positive result and used for further study.

2.3 Measurement of the amount of ACC deaminase content in PGPR under water limitation

The two most effective ACC deaminase-producing rhizobacteria were grown in tryptic soya broth (TSB), and incubated at 28°C on a shaker incubator at 120 rpm for 24-48 h. The culture broth was diluted with 0.85% NaCl solution, and the optical density of the bacterial suspension was measured using a spectrophotometer at 500 nm, adjusted to OD 0.5 for use as inoculum size of starter culture. The suspension was then transferred into DF minimal salt broth supplemented with 3 mM ACC, incubated at 30°C, and shaken at 120 rpm for 24-72 h. After that, in the first step, the culture broth was centrifuged at 4,000 rpm for 10 min and the pellet was rinsed with 0.1 M Tris-HCl pH 7.5. In the second step, the bacterial cells were suspended in 0.1 M Tris-HCl pH 8.5, and 30 µL of toluene was added, and mixed on the vortex mixer for 30 s. In the third step, 200 µL of toluene and 20 µL of 0.5 M HCl were added and mixed on a vortex mixer, then incubated at 30°C for 30 min. In the fourth step, 1 mL of 0.56 M HCl was added and mixed on the vortex mixer and centrifuged at 13,000 rpm for 5 min. In the fifth step, 1 mL of supernatant was added to 800 µL of 0.56 M HCl and 300 µL dinitrophenylhydrazine, mixed, and incubated at 30°C for 30 min. For the last step, 2 mL of 2 N NaOH was added and absorbance was measured at 540 nm (Penrose and Glick, 2003). The experiment was conducted under two conditions: water limitation condition with the addition of 20% PEG6000 into the DF minimal salt medium, and normal condition without PEG6000.

2.4 Screening the biofilm formation and exopolysaccharide production in plant growth promoting rhizobacteria

The selected isolates were tested for biofilm formation using the crystal violet staining method (Latorre, 2016). The bacterial isolates were grown in TSB in a 15 mL centrifuge tube, and incubated at 30°C for 24 h. After incubation, a positive result was observed from the ring of biofilm which was adhered inside the surface of the tube, and the TSB medium was removed and the tube gently washed with distilled water. Then the 0.1% crystal violet solution was added to the tube to stain the adhered biofilm, then placed at room temperature for 25 min. After that, the crystal violet solution was discarded and the tube was washed with sterile distilled water. The detection of exopolysaccharide production in the bacterial isolates was performed by inoculating bacterial cells in TSB, incubating at 30°C for 24 h, then dropping the bacterial suspension on a paper disc and placing it on a minimal salt medium before incubation at 30°C for 4-5 days. After that, the paper disc was soaked in a test tube containing absolute ethanol. A positive result was indicated by the solution presenting a transparent color. This indicated that the bacteria could produce exopolysaccharides. (Paulo et al., 2012).

2.5 Study on the root colonization of PGPR in herb

2.5.1 Plant preparation

Two-month-old *A. paniculata* seedlings were washed with tap water to eliminate soil and debris.

2.5.2 Evaluation of root colonization in vitro by conventional method (spread plate technique)

In this experiment, *A. paniculata* seedlings were used. The seedlings were washed with sterile distilled water and soaked in bacterial suspension, both single isolates and co-inoculation, for 2 h. Then, the roots of the plant were transferred to 0.85% NaCl solution, diluted by 10-fold dilution up to 10^{-7} and spread on tryptone soya agar (TSA) and incubated for 24 h, after which the number of bacterial colonies on the agar plate was counted (Gamalero et al., 2004).

2.5.3 Microbial inoculant and plant preparation by scanning electron microscope (SEM) study

The two rhizobacterial isolates, in the form of single inoculum and co-inoculum (in the ratio of 1:1 (v/v)), were prepared in tryptone soya broth (TSB). The culture broth was centrifuged and the cell density was adjusted to 10^8 CFU/ mL. The rhizobacterial suspension was then transferred to Hoagland solution and the *A. paniculata* seedling was soaked in each rhizobacterial isolate's inoculum for 2 h. After that, the root of the plant was cut to 2-3 centimeters, fixed with 2.5% glutaraldehyde, and covered with

aluminum foil, before storage at 4°C for 2 h. The root sample was washed with sterile 0.1 M phosphate saline buffer for 10 min, three times. The sample was soaked in ethanol at varying concentrations up to 100% for 15 min, except for the 100% ethanol concentration which was soaked for 30 min, and this step was repeated. After that, the samples were stored in a desiccator before dehydration using the critical point dryer machine for 2 h. Finally, the sample was placed on carbon tape and stub respectively before being observed under the scanning electron microscope (modified from Kim and Krcmcr, 2005; Lombardi et al., 2018).

2.5.4 Characterization of PGPR isolates by morphology study and molecular assay

Bacterial isolates were characterized by studying the colony morphology and observing the appearance trait. The identification of PGPR was performed by PCR amplification and sequencing of bacterial 16s rRNA gene. Bacterial genomic DNA was obtained from the overnight grown cells using a genomic DNA extraction kit (Tiangen biotech (Beijing, China)). The sequence of nucleotide primer used for amplification of 16s rRNA genes was universal 8F primer: 5'-AGA GTT TGA TCM TGG CTC AG-3'and reverse universal 1512R primer: 5'-ACG GYT ACC TTG TTA CGA CTT-3'. DNA samples were purified and amplified on thermal PCR machine (PCR MJ Research-PTC-200). The program was used for the amplification of 16s rRNA gene: preheating at 95°C for 10 min denaturation at 94°C for 1 min, annealing at 55°C for 1 min, extension at 72°C for 1.30 min, and final extension at 72°C for 10 min, followed by cooling at 4°C when the PCR product was purified and sequenced at services of ATCG Co., Ltd., Thailand. The obtained nucleotide sequences were compared with the NCBI database using the BLASTN program. The nucleotide sequence was compared by using MEGA 7.0.9 software, and a phylogenetic tree was constructed. Additionally, 16s rRNA nucleotide sequences in both strains were deposited in the DDBJ database following the submission instructions at https://www.ddbj.nig.ac.jp/index-e.html.

2.5.5 Pot experiment

A. paniculata seedlings were transferred to pots containing a mixture of soil and coconut fiber in a 1:1 ratio, with a total weight of 5 km. One month after transplantation, the seedlings were exposed to drought stress, and their growth parameters were measured two months later. The treatment of the pot experiment was shown in Table 1.

Table 1. Experimental design for growing *A. paniculata*

No.	Treatments
1	Control without PGPR + irrigated 100% FC
2	Control without PGPR + irrigated 50% FC
3	PGPR + irrigated 100% FC
4	PGPR + irrigated 50% FC
5	Organic fertilizer + irrigated 100% FC
6	Organic fertilizer + irrigated 50% FC
7	Chemical fertilizer + irrigated 100% FC
8	Chemical fertilizer + irrigated 50% FC

2.5.6 Statistical analysis

Mean and standard deviation were calculated for the experiment data. Statistical analysis of the data was carried out by using the Statistix 10 program. Analysis of variance (ANOVA) and Least Significant Difference (LSD) were used for comparison of significant differences among all experimental treatments.

3. RESULTS AND DISCUSSION

3.1 Isolation and screening of plant growth promoting rhizobacteria

The total microorganisms in the soil sample are shown in Table 2. Thirty-two bacterial isolates were isolated from the rice rhizosphere soil. Among them, 16, 16, and 17 bacterial isolates were able to grow in TSB supplemented with polyethylene glycol 6000 (PEG6000) at concentrations of 20%, 30%, and 35%, respectively. Of all these bacterial isolates, only 17 isolates were able to produce the ACC-deaminase enzyme.

Table 2. Total microorganisms in rice rhizosphere soil sample

Sample	Log CFU/g soil
1	6.63±0.33
2	6.57±0.23
3	6.59±0.42

All of the bacterial isolates that showed ACC-deaminase activity were selected for detecting other plant growth-promoting properties, including IAA production (Table 3), biofilm formation, and exopolysaccharide production. The most effective ACC-deaminase plant growth-promoting rhizobacteria were chosen for quantitative analysis in a further experiment.

Table 3. IAA content in plant growth promoting rhizobacteria under normal and water limitation condition. ANOVA was performed with mean and standard deviation in each column with the same letter indicating no significant difference ($p<0.05$) by LSD test.

isolates	IAA content (µL/mL) without PEG (normal condition)	IAA content (µL/mL) with PEG (water limitation)
Rh-01	16.49±0.92^{b}	20.37±0.38^{c}
Rh-06	16.52±1.52^{b}	14.14±0.92^{d}
Rh-10	11.94±0.42^{c}	11.92±0.22^{ef}
Rh-13	7.29±0.88^{ef}	10.91±0.93^{fg}
Rh-22	29.78±0.88^{a}	56.75±1.52^{a}
Rh-23	5.48±0.59^{f}	13.13±0.22^{de}
Rh-28	12.31±0.70^{c}	24.82±0.09^{b}
Rh-32	8.87±0.12d^{e}	11.82±0.18^{ef}
Rh-37	10.38±1.39^{cd}	9.70±1.44^{g}

Two high-potential isolates of PGPR containing ACC-deaminase were examined for quantitative ACC-deaminase enzyme activity under normal and drought stress conditions. The results showed that the rhizobacteria could produce the ACC-deaminase enzyme under both conditions (Table 4).

Table 4. Quantitative estimation of ACC-deaminase activity in plant growth-promoting rhizobacteria. ANOVA analysis was performed with Mean and standard deviation in each column with the same letter indicating no significant difference ($p<0.05$) and by LSD test.

isolate	ACC-deaminase activity (µmol of α-ketobutyrate/mg protein/h)	
	With PEG6000	Without PEG6000
Rh-01	21.66±0.37^{b}	39.72±1.35^{b}
Rh-22	27.01±0.07^{a}	50.20±0.64^{a}

The most efficient ACC-deaminase plant growth-promoting rhizobacteria were further evaluated for quantitative ACC-deaminase enzyme activity under both normal and water limitation conditions. Under normal irrigation, all bacterial isolates showed a more effective production of the ACC-deaminase enzyme compared to the drought stress condition. However, PGPR was also able to produce the ACC-deaminase enzyme even under water limitation. Bacterial isolate Rh-22 seemed to produce more ACC-deaminase enzyme than isolate Rh-01 under both conditions.

Observation of root colonization by ACC-deaminase-producing rhizobacteria with plant growth-promoting properties under a scanning electron microscope revealed that both rhizobacteria isolates were capable of colonizing roots (Figure 1). This was similar to the results found in conventional experiments, where spreading plates were used to count the number of rhizobacteria invading plant roots; we found that the number of bacteria for both isolates was in a similar profile. Interestingly, co-inoculated treatment resulted in higher bacteria numbers compared to other treatments (Table 5).

Table 5. Root colonization of plant growth-promoting rhizobacteria by viable plate count

isolate	Log CFU/root	
	With PEG	Without PEG
control	6.08±0.022	6.19±0.043
Rh-01	9.28±0.034	9.19±0.043
Rh-22	10.18±0.071	9.29±0.034
Co-inoculated	10.10±0.089	9.78±0.300

3.2 Colony morphology and molecular identification of bacterial isolates

Characteristics of colony morphology that appeared on culture medium Nutrient agar (NA) plant growth-promoting rhizobacteria isolate Rh-01 colonies are round, flat, white, small-sized, jagged edged, gram-positive, and rod-shaped. For Rh-22 isolates, the colonies are white, jagged edged, wrinkled, gram-positive isolate (Table 6 and Figure 2). For molecular identification, the sequence of the 16S rRNA gene was analyzed. Rhizobacteria isolate Rh-01 was identified as *Paenibacillus polymyxa* Rh-01 with 99.6% similarity. Rh-22 showed 100% similarity with *Stenotrophomonas maltophilia* Rh-22 species (Table 7). The nucleotide accession number of strains Rh-01 and Rh-22 are LC775011 and LC775012, respectively. The phylogenetic tree was constructed from the 16S rRNA sequence of genus *Bacillus* and *Stenotrophomonas* (Figure 3).

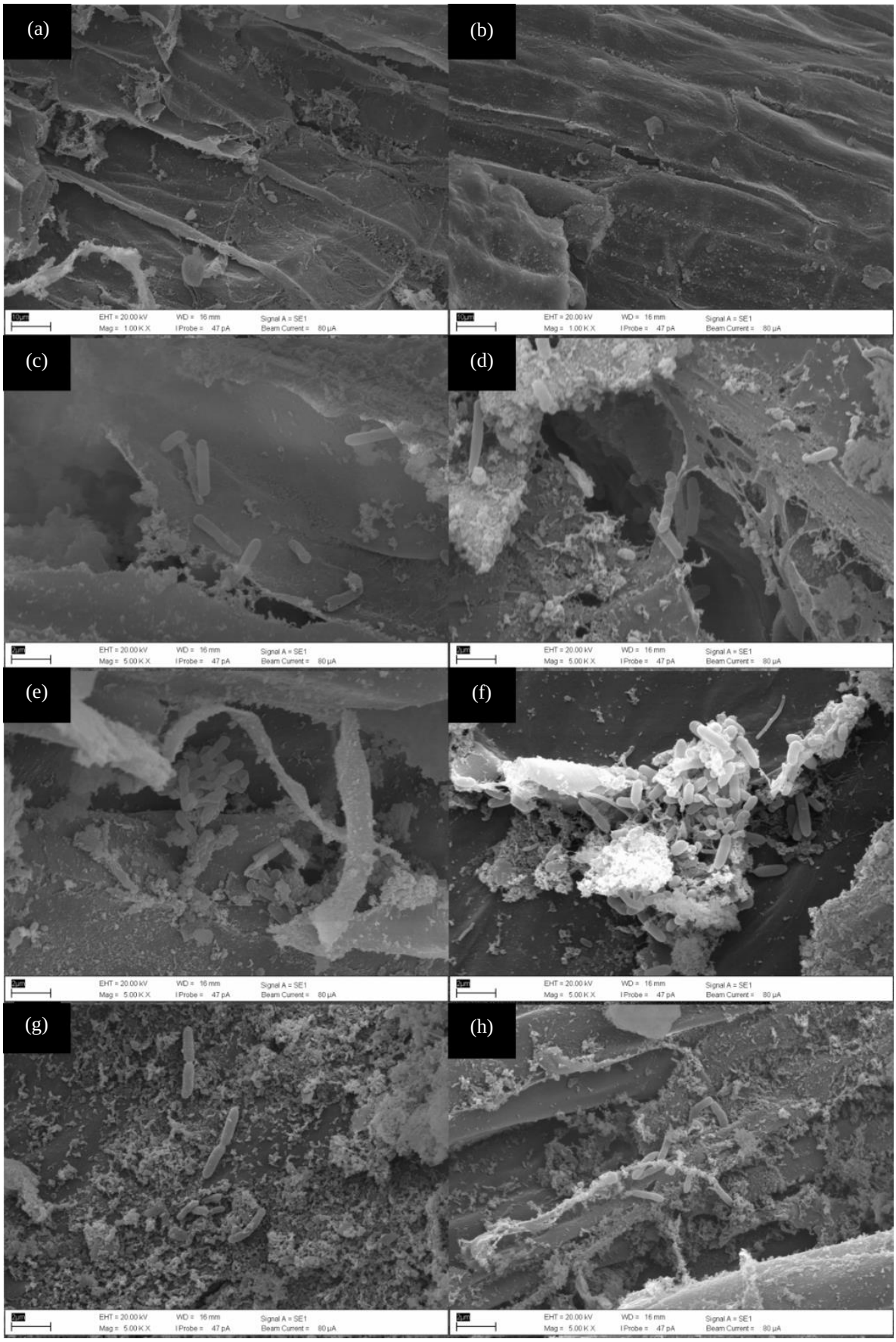

Figure 1. Root colonization of plant growth-promoting rhizobacteria observed under a scanning electron microscope, control without PEG and with PEG (a, b), strain Rh-01 without PEG (c), strain Rh-01 with PEG (d), strain Rh-22 without PEG (e), strain Rh-22 with PEG (f), mix of 2 strains without PEG (g), co-inoculation of 2 strains with PEG (h), with magnification 5000X.

3.3 Appearance of *A. paniculata* growth when simulated with plant growth-promoting rhizobacteria containing ACC-deaminase.

After 2 months of planting, A. paniculata plants were harvested and measured for growth parameters and stress markers (proline and relative water content).

Table 6. Morphological of plant growth-promoting rhizobacteria containing ACC-deaminase activity

Colony morphology	PGPR isolates	
	Rh-01	Rh-22
Form	Circular	Irregular
Color	White	Yellow
Margin	Entire	Curled
Structure	Opaque	Opaque
Surface	Smooth	Rough

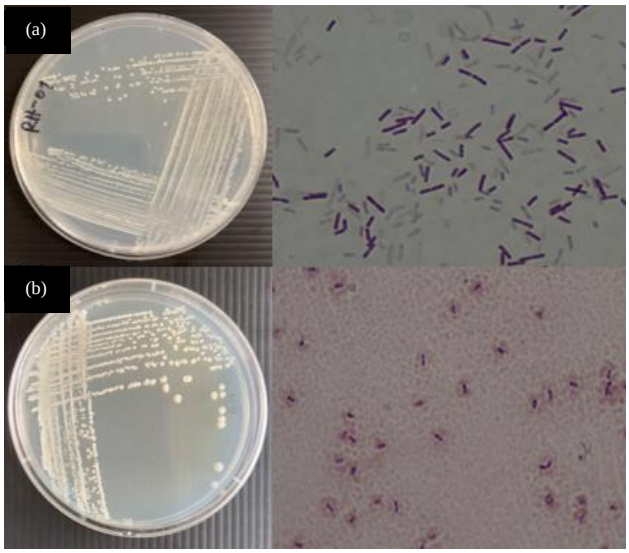

Figure 2. Colony morphology and gram stain of isolate Rh-01 (a), Rh-22 (b)

Table 7. Molecular identification of ACC-deaminase plant growth-promoting rhizobacteria

Bacterial isolates	Molecular identification		
	Closet NCBI match	Accession NO.	Similarity
Rh-01	*Paenibacillus polymyxa* Rh-01	LC775011	99.64%
Rh-22	*Stenotrophomonas maltophilia* Rh-22	LC775012	100%

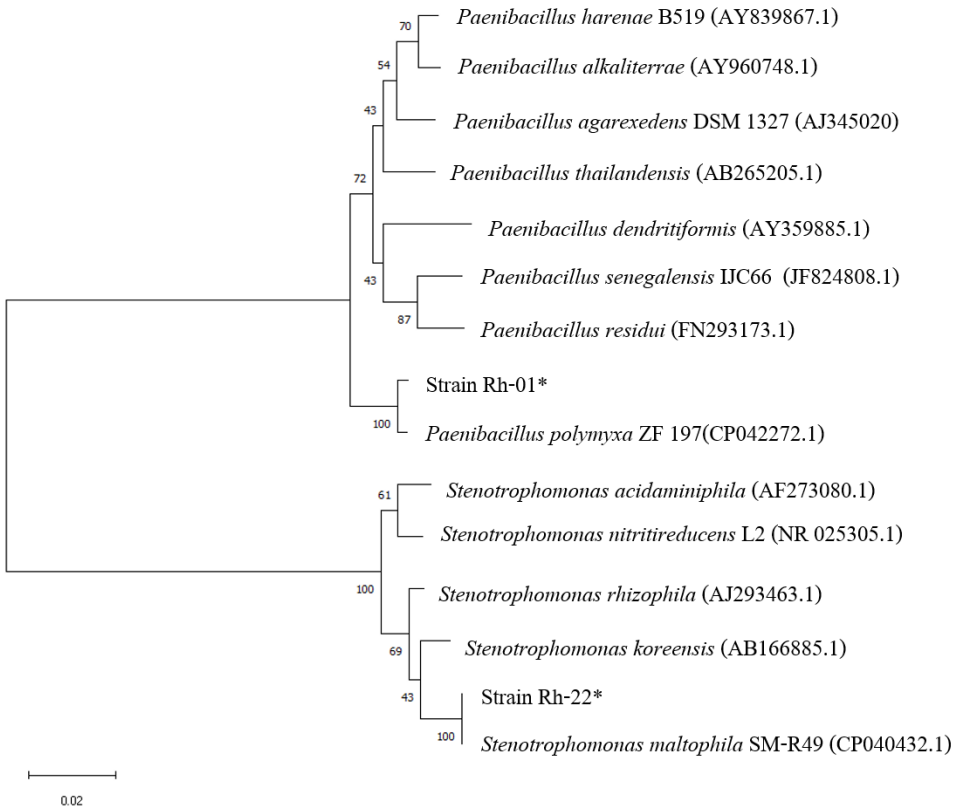

Figure 3. The phylogenetic tree was constructed from the 16S rRNA gene sequence from selected bacterial isolates by using Mega 11 software

3.4 Plant height and chlorophyll content

Water limitation at 50% FC of irrigation in all treatments had an effect on plant height, especially with plants treated with organic fertilizer (T6) and chemical fertilizer (T8). The reduction in plant height might be due to the limited water content available to solubilize nutrients in the soil. However, a non-significant difference was observed in treatment T3 (supplemented with PGPR, 100% FC, and 50% FC irrigation). Moreover, the plant height in T4 (PGPR and 50% irrigation) and T8 (Chemical and 50% irrigation) revealed a similar profile with a non-significant difference in statistical calculation. This indicated that PGPR and chemical fertilizer have equal potential to stimulate plant height under water limitation conditions (Figure 4).

For the chlorophyll content in plant leaves, the result showed that at 50% FC of irrigation in treatments, the chlorophyll content of the plants was lower than in treatment T7, which was treated with chemical fertilizer (100% FC irrigation). Moreover, our results indicated that PGPR in both treatments T3 (50% FC) and T4 (100% FC)) were able to enhance the growth of plants by expressing a higher content of chlorophyll than in the control (T2 with 50% FC irrigation) (Figure 4).

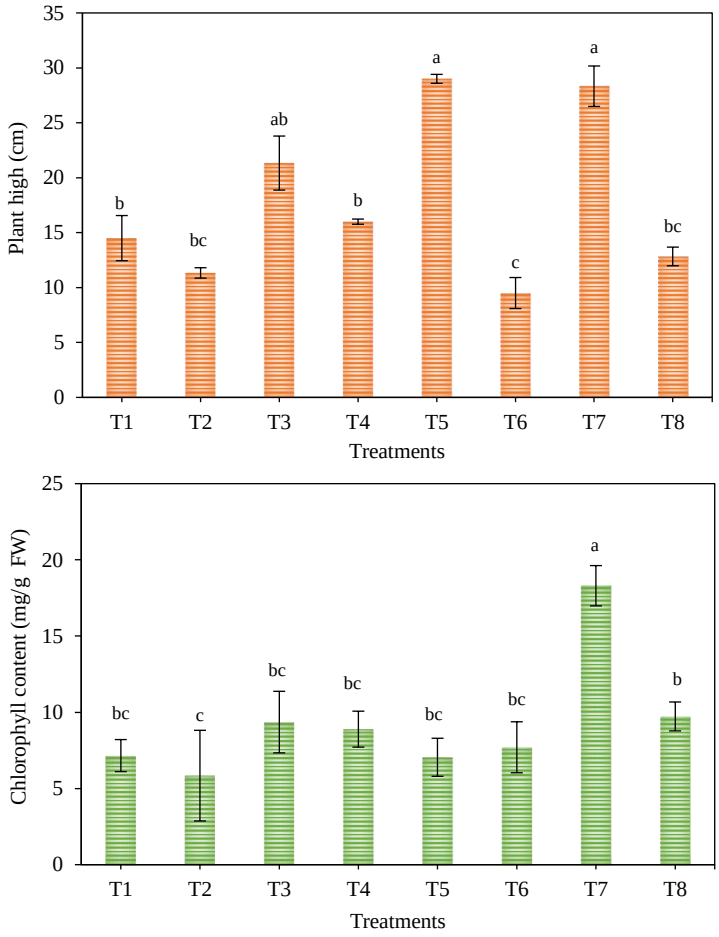

Figure 4. Effect of PGPR inoculant on Plant height and Chlorophyll content (T1=control + 100% FC, T2=control + 50% FC, T3=PGPR + 100% FC, T4=PGPR + 50% FC, T5=Organic Fertilizer + 50% FC, T6=Organic fertilizer + 100% FC, T7=Chemical fertilizer + 100% FC, T8=Chemical fertilizer + 50% FC).

3.5 Plant yield

Maximum total biomass was yielded in the treatment which applied chemical fertilizer with 100% FC irrigation (T7). It decreased when plants were treated with 50% FC irrigation in all treatments. However, when these values were compared to the control T1 and T2, there was a non-significant difference in the treatment that was treated with PGPR (T4), organic fertilizer (T6), and chemical fertilizer (T8). It seems that the PGPR's ability to solubilize nutrients in soil was similar to when the soil was applied with organic and chemical fertilizer. Moreover, we found that our PGPR was able to promote the biomass of roots when plants were treated

with PGPR under 100% FC irrigation. On the other hand, it decreased when treated with 50 % FC water irrigation. This indicates that water is important for supporting the microbial activities in soil that affect plant growth (Table 8).

Table 8. Effect of PGPR inoculant on root and shoot fresh weight, root & shoot dry weight, root and shoot biomass, and total biomass of *Andrographis paniculate (burm.f.) nees* under water limitation. ANOVA was performed with Mean and standard deviation in each column with the same letter indicating no significant difference *($p<0.05$) and **($p<0.01$) by LSD test.

Treatments	Shoot fresh weight (g)	Shoot dry weight (g)	shoot biomass (g)	Root fresh weight (g)	Root dry weight (g)	Root biomass (g)	Total biomass (g)
T1	3.583^{b}	1.003^{b}	2.580^{b}	2.013	0.338^{cd}	1.680	4.260^{bc}
T2	1.923^{cd}	0.790^{b}	1.133^{c}	1.620	0.346^{cd}	1.273	2.407^{d}
T3	2.910^{bcd}	0.823^{b}	2.087^{bc}	3.757	0.599^{ab}	3.157	5.243^{b}
T4	2.107^{bcd}	0.630^{b}	1.478^{bc}	3.757	0.323^{cd}	1.180	2.657^{cd}
T5	3.380^{bc}	0.887^{b}	2.493^{b}	3.517	0.573^{abc}	2.943	5.437^{b}
T6	1.777^{d}	0.533^{b}	1.243^{c}	2.350	0.265^{d}	2.083	3.327^{cd}
T7	13.467^{d}	3.797^{a}	9.670^{a}	2.637	0.690^{a}	1.947	11.617^{a}
T8	2.59^{3bcd}	0.940^{b}	1.653^{bd}	1.730	0.400^{bcd}	1.330	2.983^{cd}
%CV	22.52	23.44	25.67	47.92	32.03	56.27	21.40
F-test	**	**	**	ns	*	ns	**

3.6 Relative water content and accumulation of proline

Relative water content (RWC) refers to the current water content in the leaf of the plant. Normally, the reduction of relative water content was observed in drought stress condition. Our data showed that a lower content of RWC was found in all 50% FC irrigation. The RWC was in the range of 28-48% (Figure 5).

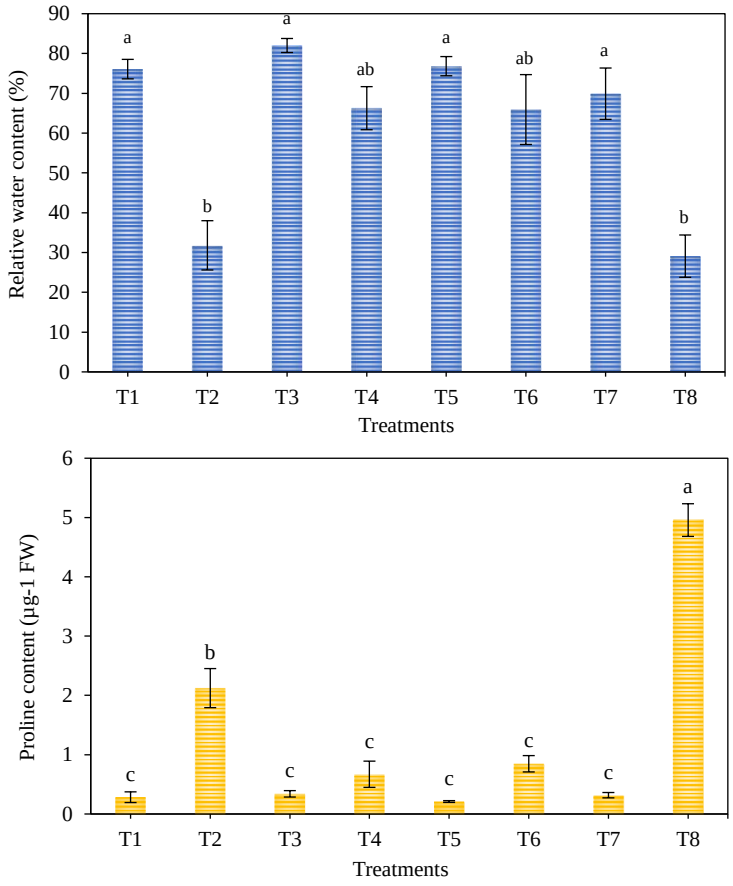

Figure 5. Effect of PGPR inoculant on proline content and relative water content in plant leaf (T1=control + 100% FC, T2=control + 50% FC, T3=PGPR + 100% FC, T4=PGPR + 50% FC, T5=Organic Fertilizer + 50% FC, T6=Organic fertilizer + 100% FC, T7=Chemical fertilizer + 100% FC, T8=Chemical fertilizer + 50% FC).

The growth of *A. paniculata* was affected by water limitation conditions as observed from the increasing accumulation of proline in plant leaves. The highest proline content was recorded in the treatment of chemical fertilizer with 50% FC irrigated (T8). However, the application of microbial inoculant (PGPR) for growing plants under water limitation (T3 and T4) presented a significantly decreased proline content when compared to the control treatment (T2) and T8 (supplemented with chemical fertilizer and 50% FC irrigation) (Figure 5). Meanwhile, there was no significant difference in other treatments when compared to the normal irrigation control treatment (T1). This indicated that irrigation had an effect on the accumulation of proline in plants, with the plant encountering stress due to low water content.

4. DISCUSSION

Water deficit affects plant growth, as water is an important factor for photosynthesis in plants and is necessary for the uptake and transport of nutrients in the soil (Lisar et al., 2012). The application of ACC-deaminase plant growth-promoting rhizobacteria is an environmentally sustainable option to alleviate the effect of biotic and abiotic stress on plant growth and productivity (Glick, 2005). In most higher plants the synthesis of ethylene is one of the response mechanisms utilized to cope with biotic and abiotic stress. A high level of ethylene has an impact on the growth and development of plants.

In the present study, two bacterial isolates, Rh-01 and Rh-22, exhibited large amounts of ACC deaminase activity and were selected from rice rhizosphere in arid regions for further assessment of growth promoting abilities such as IAA production, biofilm formation, and exopolysaccharide production. Phytohormones such as IAA, which are released by plant growth promoting bacteria, can promote plants by stimulating root elongation, the formation of lateral roots, and root hairs. This mechanism improves root system and enhances nutrient uptake in plants (Gupta and Panday, 2019).

According to our results, various types of fertilizer and water irrigation affect the growth of *A. paniculata* plant differently. Under normal irrigation conditions, the results showed that chemical fertilizer is the best fertilizer for promoting the growth of *Andrographis paniculate* in terms of improvement in plant height and chlorophyll content. In contrast, under water limitation conditions (50% FC irrigation), there was no significant difference in chlorophyll content among all three fertilizers, but a significant difference was found when compared to the water stress control treatment (T2; 50% FC irrigation without fertilizer). However, the highest increase in plant height was shown in the treatment with microbial bio-fertilizer (PGPR) (T4). This result suggests that at the 50% FC irrigation, ACC- deaminase plant growth-promoting bacteria could help to promote plant height under water stress treatment when compared to the control (without supplemented with fertilizer, T2), added organic fertilizer (T6) and chemical fertilizer. (T8). The improvement in plant height might be due to the reduction of stress ethylene levels by ACC-deaminase plant growth promoting bacteria. Danish et al. (2020) also demonstrated that ACC-deaminase producing bacteria enhanced the plant height of maize under drought stress. In addition, Yuan et al. (2023) reported that ACC-deaminase-producing bacteria *Pseudomonas* DY1-3 increased root growth and height of maize. They indicated the potential of plant growth-promoting bacteria to improve resistance to abiotic stress.

For the results of other plant growth parameters, chemical fertilizer treatment showed the highest increase in shoot fresh weight, shoot dry weight, root dry weight, and total biomass which was similar to the findings of Forouzandeh et al. (2012) who also reported that chemical fertilizers showed the highest effect on essential oil content in the medicinal plant Basil.

Biofilm formation of rhizobacteria promotes plants directly. Root exudate secreted by plants contains different types of sugar, vitamins, organic acid, and mucilage that attract PGPR for root colonization and form a biofilm around the root of the plant. The role of biofilm could promote root colonization of the microorganism located around the plant's root. Root colonization plays an important role in the survival of bacteria and protects the plant from the adverse effects of drought stress (Ansari and Ahmad, 2018). In addition, biofilm maintains the water and nutrient-holding capacity in the rhizosphere soil around the plant roots, improving the uptake of water and soluble nutrients. Exopolysaccharide (EPSs) production is one of the important traits of PGPR that has benefits on the formation of biofilm. Exopolysaccharides look like high molecular weight polymers of sugar, which contain both homopolysaccharides and heteropolysaccharides. Normally, EPSs are a key factor for promoting and protecting the microbial cell which maintains moisture, and thus increasing drought-tolerant

capability. Many research reports state that exopolysaccharides play a significant role in biofilm formation and also serve as an important component in biofilm formation (Salas-Jara et al., 2016; Lebeer et al., 2007; Czaczyk and Myszka, 2007).

The molecular identification and phylogenetic tree analysis revealed that the rhizobacterial isolate Rh-01 and isolate Rh-22 belong to *Paenibacillus polymyxa* Rh-01 and *Stenotrophomonas maltophilia* sm-Rh-22 respectively. A similar result was observed by Gupta and Pandey (2019), who reported the ACC-deaminase-producing ability of *Peanibacillus*. Moreover, Majeed et al. (2015) also indicated multiple plant growth promoting traits and the potential of *Stenotrophomonas* spp. for biofertilizer production.

According to pot experiment results, different types of fertilizer and different levels of water irrigation affected the growth of *A. paniculata* plant. Under the normal water conditions, chemical fertilizer best promoted the growth of *A. paniculata* in terms of improvement in plant height and chlorophyll content. In contrast, under water limitation conditions (50% FC), there was a non-significant difference in chlorophyll content among all three kinds of fertilizers, but a significant difference was found when compared to the water stress control treatment (T2). However, the highest increase in plant height was shown in microbial bio-fertilizer treatment (T4). This result suggested that ACC- deaminase plant growth-promoting bacteria could help promote plant height when compared to organic fertilizer with water stress treatment (T6), which showed the highest decrease in plant height. This result was consistent with the previous study of Ratnaningsih et al. (2023) who investigated ACC deaminase isolated from the rhizosphere of pine apple plants and found that these microbes promoted the growth of soybean. Similarly, Gupta et al. (2022) indicated that ACC deaminase producing PGPR could alleviate the adverse effect of osmotic and salinity stress in *Pisum sativum*.

Plant stress markers indicated the stress level in plants. In this study, we investigated relative water content and proline content in *A. paniculata* leaves. Our result revealed that relative water content exhibited a non-significant difference among all of the normal irrigation conditions (100% FC), supplemented with each type of fertilizer. On the other hand, under drought stress conditions the relative water content decreased when compared to normal irrigation as a control treatment (T1). A similar result was presented by Aslam et al. (2021), who found a reduction in leaf water content when using chemical fertilizer alone under severe evaporation for improved Canola growth, decreasing relative water content as a result of water limitation. In contrast, the application of microbial biofertilizer (PGPR) maintained relative water content in plant leaves.

Proline content is one of the most important osmoprotectants in higher plants. Our results showed proline content increased in water limitation treatment (T2). Furthermore, chemical fertilizers with water limitation condition also increased proline content in *A. paniculata* leaves, indicating that the accumulation of proline under stress in plants might be due to the high acidic and electro conductivity (pH and EC) of chemical fertilizer, while the application of microbial bio-fertilizer triggered a reduction in proline content in *A. paniculata* leaves. These results demonstrated that microbial bio-fertilizer alleviates stress in plants by increasing relative water content and decreasing proline accumulation in the plant. Furthermore, our results were consistent with a previous report showing that exopolysaccharide-producing bacteria significantly reduced proline content in inoculated plants (Khan and Bano, 2019). In our study indicates that ACC-deaminase-producing bacteria showed potential as a microbial biofertilizer for improving plant growth under biotic and abiotic stress.

5. CONCLUSION

Our results suggest that drought stress has a negative impact on the physiological and biochemical growth markers of the *A. paniculata* plant compared with the control treatment. However, plant growth promoting rhizobacteria can ameliorate plants via various mechanisms. These findings lead to a recommendation for the combined application of chemical fertilizers and microbial bio-fertilizers to accomplish sustainable agricultural goals.

DECLARATION OF COMPETING INTEREST

The authors confirm that they have not encountered any interpersonal or financial disputes that would have appeared to have an impact on the data presented in this study.

ACKNOWLEDGEMENTS

This study has been supported by Microbial Fertilizer Lab group, the Department of Microbiology, Faculty of Science Khon Kaen University and Protein

and Proteomics Research Center for Commercial and industrial Purposes (ProCCI). We would to thank Dr. Pornrapee Sarin and Dr. Natthawat Sritongon for assisting with the recommendations and statistical analysis. The author would like to thanks Mr. Matthew Savage for proofing English writing of this manuscript.

REFERENCES

Ahmadizadeh M, Valizadeh M, Shahbazi H, Nori A. Behavior of durum wheat genotypes under normal irrigation and drought stress conditions in the greenhouse. African Journal of Biotechnology 2012;11(8):1912-23.

Ansari FA, Ahmad I. Biofilm development, plant growth promoting traits and rhizosphere colonization by *Pseudomonas entomophila* FAP1: A promising PGPR. Advances in Microbiology 2018;8(3):Article No. 235.

Aslam MM, Farhat F, Siddiqui MA, Yasmeen S, Khan MT, Sial MA, et al. Exploration of physiological and biochemical processes of canola with exogenously applied fertilizers and plant growth regulators under drought stress. PloS One 2021;16(12):e0260960.

Czaczyk K, Myszka K. Biosynthesis of extracellular polymeric substances (EPS) and its role in microbial biofilm formation. Polish Journal of Environmental Studies 2007;16(6):799-806.

Danish S, Zafar-ul-Hye M, Mohsin F, Hussain M. ACC-deaminase producing plant growth promoting rhizobacteria and biochar mitigate adverse effects of drought stress on maize growth. PLoS One 2020;15(4):e0230615.

Dworkin M, Foster JW. Experiments with some microorganisms which utilize ethane and hydrogen. Journal of Bacteriology 1958;75(5):592-603.

Forouzandeh M, Fanoudi M, Arazmjou E, Tabiei H. Effect of drought stress and types of fertilizers on the quantity and quality of medicinal plant Basil (*Ocimum basilicum* L.). Indian Journal of Innovations and Developments 2012;1(9):696-9.

Gamalero E, Lingua G, Giusy Caprì F, Fusconi A, Berta G, Lemanceau P. Colonization pattern of primary tomato roots by *Pseudomonas fluorescens* A6RI characterized by dilution plating, flow cytometry, fluorescence, confocal and scanning electron microscopy. FEMS Microbiology Ecology 2004;48(1):79-87.

Glick BR. Modulation of plant ethylene levels by the bacterial enzyme ACC deaminase. FEMS Microbiology Letters 2005;251(1):1-7.

Gupta A, Rai S, Bano A, Sharma S, Kumar M, Binsuwaidan R. ACC deaminase produced by PGPR mitigates the adverse effect of osmotic and salinity stresses in Pisum sativum through modulating the antioxidants activities. Plants 2022;11(24):Article No. 3419.

Gupta S, Pandey S. ACC deaminase producing bacteria with multifarious plant growth promoting traits alleviates salinity stress in French bean (*Phaseolus vulgaris*) plants. Frontiers in Microbiology 2019;10:Article No. 1506.

Jiang M, Sheng F, Zhang Z, Ma X, Gao T, Fu C, et al. *A. paniculata* (Burm. f.) Nees and its major constituent andrographolide as potential antiviral agents. Journal of Ethnopharmacology 2021;272:Article No. 113954.

Khan N, Bano A. Exopolysaccharide producing rhizobacteria and their impact on growth and drought tolerance of wheat grown under rainfed conditions. PLoS One 2019;14(9):e0222302.

Kim SJ, Krcmcr RJ. Scanning and transmission electron microscopy of root colonization of morning glory (*Lpomoea* spp.) seedlings by rhizobacteria. Symbiosis 2005;39:117-24.

Latorre JD, Hernandez-Velasco X, Wolfenden RE, Vicente JL, Wolfenden AD, Menconi A, et al. Evaluation and selection of Bacillus species based on enzyme production, antimicrobial activity, and biofilm synthesis as direct-fed microbial candidates for poultry. Frontiers in Veterinary Science 2016;3:Article No. 95.

Lebeer S, Verhoeven TL, Perea Vélez M, Vanderleyden J, De Keersmaecker SC. Impact of environmental and genetic factors on biofilm formation by the probiotic strain *Lactobacillus rhamnosus* GG. Applied and Environmental Microbiology 2007;73(21):6768-75.

Lisar SY, Motafakkerazad R, Hossain MM, Rahman IM. Causes, effects and responses. Water Stress 2012;25(1):1-14.

Liu F, Xing S, Ma H, Du Z, Ma B. Cytokinin-producing, plant growth-promoting rhizobacteria that confer resistance to drought stress in *Platycladus orientalis* container seedlings. Applied Microbiology and Biotechnology 2013; 97:9155-64.

Lombardi N, Vitale S, Turrà D, Reverberi M, Fanelli C, Vinale F. Root exudates of stressed plants stimulate and attract Trichoderma soil fungi. Molecular Plant-Microbe Interactions 2018;31(10):982-94.

Majeed A, Abbasi MK, Hameed S, Imran A, Rahim N. Isolation and characterization of plant growth-promoting rhizobacteria from wheat rhizosphere and their effect on plant growth promotion. Frontiers in Microbiology 2015;6:Article No. 198.

Mayak S, Tirosh T, Glick BR. Plant growth-promoting bacteria that confer resistance to water stress in tomatoes and peppers. Plant Science 2004;166(2):525-30.

Rahdari P, Hoseini SM. Drought stress: A review. International Journal of Agronomy and Plant Production 2012;3(10):443-6.

Ratnaningsih HR, Noviana Z, Dewi TK, Loekito S, Wiyono S, Gafur A, et al. IAA and ACC deaminase producing-bacteria isolated from the rhizosphere of pineapple plants grown under different abiotic and biotic stresses. Heliyon 2023; 9(6):e16306.

Paulo EM, Vasconcelos MP, Oliveira IS, Affe HMDJ, Nascimento R, Melo ISD, et al. An alternative method for screening lactic acid bacteria for the production of exopolysaccharides with rapid confirmation. Food Science and Technology 2012; 32(4):710-4.

Penrose DM, Glick BR. Methods for isolating and characterizing ACC deaminase-containing plant growth-promoting rhizobacteria. Physiol Plant 2003;118(1):10-5.

Salas-Jara MJ, Ilabaca A, Vega M, García A. Biofilm forming Lactobacillus: New challenges for the development of probiotics. Microorganisms 2016;4(3):Article No. 35.

Selvakumar G, Panneerselvam P, Ganeshamurthy AN. Bacterial mediated alleviation of abiotic stress in crops. In: Bacteria in Agrobiology: Stress Management. Heidelberg, Germany: Springer; 2012. p. 205-24.

Smirnof N. The role of active oxygen in the response of plants to water deficit and desiccation. NewPhy-Tologist 1993; 125:27-58.

Yuan Y, Shi Y, Liu Z, Fan Y, Liu M, Ningjing M, et al. Promotional properties of ACC deaminase-producing bacterial strain DY1-3 and its enhancement of Maize resistance of salt and drought stresses. Microorganisms 2023;11(11):Article No. 2654.

Zhou C, Ma Z, Zhu L, Xiao X, Xie Y, Zhu J, et al. Rhizobacterial strain *Bacillus megaterium* BOFC1 5 induces cellular polyamine changes that improve plant growth and drought resistance. International Journal of Molecular Sciences 2016;17(6);Article No. 976.

Environment and Natural Resources Journal

Volume 22
Issue 2
2024

Evaluation of Tolerance and Uptake of Cd and Mn for Microfungi *Aspergillus flavus*, *Aspergillus oryzae*, and *Aspergillus terreus* Isolated from Landfill Soil Collected from Bangar, La Union Philippines

Jan Aizel E. Arellano[1], Irish Benja M. Argame[2], Francis Ruel G. Castillo[3], Christian Geen E. Salazar[1], and Mark Kevin S. Lopez[1*]

[1]*Faculty of Biology Department, College of Arts and Sciences, Don Mariano Marcos Memorial State University, North La Union Campus, Bacnotan, La Union, Philippines*
[2]*Graduate Student of Microbiology Division, Institute of Biological Sciences, Graduate Studies, University of the Philippines, Los Baños, College, Laguna, Philippines*
[3]*Medical Student of College of Medicine, University of Philippines, Manila, Philippines*

ARTICLE INFO

Received: 17 Sep 2023
Received in revised: 30 Jan 2024
Accepted: 7 Feb 2024
Published online: 4 Mar 2024
DOI: 10.32526/ennrj/22/20230254

Keywords:
Aspergillus/ Heavy metal tolerance and uptake/ Microfungi/ Mycoremediation

*** Corresponding author:**
E-mail: mlopez@dmmmsu.edu.ph

ABSTRACT

Excessive deposition of heavy metals into the environment due to anthropogenic activities necessitates an eco-friendly clean-up strategy. Among microorganisms, limited studies have been made on the mycoremediation potential of microfungi. This paper evaluated three landfill microfungal isolates of *Aspergillus* species for tolerance and uptake to Cd and Mn. Culture media optimization was also performed for the evaluation of the tolerance index and heavy metal analysis of soil samples from the landfill site. Among the nine heavy metals analyzed, Mn and Fe were detected in relatively high amounts, while Cd, Ni, and Cu were detected in a moderate range. Luxuriant mycelial growth of *A. oryzae* (MK120548.1) and *A. flavus* (MH864264.1) was observed in potato dextrose agar while *A. terreus* (MH047280.1) grew best in potato sucrose agar. In terms of tolerance index, *A. oryzae* (MK120548.1) and *A. flavus* (MH864264.1) demonstrated high tolerance to Cd up to 10 mg/kg. *A. oryzae* (MK120548.1) showed high tolerance to Mn up to 1,000 mg/kg while *A. flavus* (MH864264.1) exhibited a very high 10,000 mg/kg tolerance. In terms of metal uptake, *A. oryzae* (MK120548.1) showed the highest metal uptake of up to 654 mg/kg of Cd, while *A. terreus* (MH047280.1) exhibited the highest metal uptake of 997 mg/kg ofMn. With these findings, *A. oryzae* (MK120548.1), *A. flavus* (MH864264.1), and *A. terreus* (MH047280.1) have considerable mycoremediation potential. Bioremediation studies in conjunction with plants can be explored to further assess the potential of these *Aspergillus* species.

1. INTRODUCTION

The continuous rise of heavy metals and other toxicants as impacts of industrial activities and technological advancements poses a significant threat to human health and the environment in general. Due to their application and immutable nature, heavy metal pollution has become a serious environmental problem (Pawlowska and Charvat, 2004; Saba et al., 2017; Tiwari and Lata, 2018; Wijaya et al., 2019). Metals are naturally subjected to biogeochemical cycles determining their presence and concentration in different natural environments such as soil, groundwater-surface water, air, and living beings (Acosta-Rodríguez et al., 2018). However, heavy metals are among the most toxic inorganic substances that have contaminated large areas of soil or water resources due to the residues from metalliferous mines, the use of sludge, pesticides, fertilizers, and emissions from municipal wastes (Upadhyaya et al., 2010; Oso et al., 2015). Municipal solid waste in

Citation: Arellano JAE, Argame IBM, Castillo FRG, Salazar CGE, Lopez MKS. Evaluation of tolerance and uptake of Cd and Mn for microfungi *Aspergillus flavus*, *Aspergillus oryzae*, and *Aspergillus terreus* isolated from landfill soil collected from Bangar, La Union Philippines. Environ. Nat. Resour. J. 2024;22(2):184-196. (https://doi.org/10.32526/ennrj/22/20230254)

landfill sites produces leachates, which can be significant sources of environmental pollution due to organic and inorganic pollutants, including heavy metals. Problems with the possible release of these toxic chemicals, including heavy metals associated with landfill sites may result to groundwater pollution, plant phytotoxicity and a decline in crop and soil production near the dumpsite. Also, the absorption of heavy metals by plants marks the entry of heavy metals to food chain and their successive accumulation along food chain has a critical threat to the health of animals and humans (Nyiramigisha et al., 2021; Ayilara and Babalola, 2023; Beinabaj et al., 2023). The toxicity of heavy metals to living systems is well-recognized. A significant research effort has been directed towards the study of their cycling, levels in different habitats, and mechanisms of uptake by various organisms, as well as remediation of polluted environments (El-Moselhy et al., 2014; Verma and Kuila, 2019; Ayilara and Babalola, 2023). While many remediation techniques, including chemical and physical techniques, have been used for many years, their drawbacks and difficulties have encouraged the application of a more eco-friendly alternative known as bioremediation.

Bioremediation offers an economical and promising way of treating contaminated sites. Bioremediation is considered more environmentally friendly than conventional remediation techniques and is regarded as a green technology as it only depends on biological organisms and processes (Thabit and El-Naggar, 2014; Aishwarya et al., 2017). Many microbial species, including fungi and bacteria, can sequester heavy metals. However, fungal strains may better suit this goal than other microorganisms due to their excellent resistance toward most heavy metals, wall binding ability, and intracellular metals uptake abilities (Alzahrani et al., 2017). Fungi are among the dominating living biomass of soil but have not been widely exploited for bioremediation in contaminated soil environments. Fungi have a tremendous advantage over bacteria for the bioremediation of polluted soils due to their large biomass, massive hyphal networks, versatility in an extreme environment, and longer life cycles (Singh et al., 2014). Fungi could even be used as bioremediation agents in conjunction with other bioremediation agents like plants for a more efficient degradation or absorption of pollutants like heavy metals (Li et al., 2016).

Some fungal species have been studied for their tolerance, uptake, and mycoremediation potential to various heavy metals in the past several years. Ayilara and Babalora (2023) reviewed that *A. versicolor*, *A. fumigatus*, *Cladosporium* sp., and *Trichoderma* sp. are used in bioremediation of Cd, *Saccharomyces cerevisiae*, and *Aspergillus* sp. are used in bioremediation of As and *Penicillum* sp., *Trichoderma* sp., and *Aspergillus* sp. are used in bioremediation of Co and Cu. *A. flavus* CR500 showed metal tolerance and removal capability to As, Ni, and Pb (Kumar and Dwavedi, 2020) while another *A. flavus* strain in the study of Vajpai et al. (2019) showed tolerance and uptake of Cr. Khan et al. (2019) demonstrated the removal of Hg and Pb from contaminated soils by several *Aspergillus* species such as *A. niger*, *A. fumigatus*, *A. terreus*, and *A. flavus*. Moreover, *A. oryzae* showed capability to remove Mn, Al, and Fe in polluted freshwater samples (Mahmoud et al., 2017). Aside from that *A. oryzae* also showed tolerance, bioaccumulation or biosorption of Cu and Pb (Long et al., 2017), As (Liang et al., 2018) and Zn (Al-Obaid and Hashem, 1997). Studies on the tolerance and uptake of *A. terreus* for Cu (Oladipo et al., 2016; Palanivel et al., 2023; Zango et al., 2023), Pb and Fe (Oladipo et al., 2016; Zango et al., 2023) and Cr (Zango et al., 2023) have also been conducted.

Nowadays, mycoremediation using soil-borne fungi has received a great deal of attention due to their distinct attributes, such as the ability to thrive under extreme pH, temperatures, and nutrient variability conditions, as well as high tolerance to high metal concentrations (Oladipo et al., 2018). Several studies have even shown the promising potential of several soil-borne microfungal species isolated from contaminated areas like landfill sites or mining sites for mycoremediation (Joo and Hussein, 2012; Oladipo et al., 2018). Recognizing the limited preliminary studies conducted on the tolerance and uptake of landfill microfungal isolates *A. flavus*, *A. terreus*, and *A. oryzae* for Cd and Mn for possible bioremediation potential in landfill soil; hence, this study was conceptualized and aimed to evaluate in vitro the metal tolerance and uptake of Cd and Mn for the three *Aspergillus* species isolated from the landfill site of Bangar, La Union, Philippines. Also, their optimum culture media as well as analysis of the soil sample from the area were assessed.

2. METHODOLOGY

2.1 Description of the study site

The landfill site of Bangar, La Union, Philippines 2519 was the study site in this paper.

Forested areas, agricultural lands and nearby communities surround this open landfill site. Forested areas surround the landfill site in its northern and eastern parts, while agricultural land is situated in its western part and some of the southeastern parts. The nearby communities are settled several kilometers away in its southwestern portions. It serves as the dumpsite of municipal solid waste such as paper, plastic, metal, food, glass, etc., produced as solid waste by commercial, household, office, industrial, and the like. The collection and isolation of soil samples from this site, as well as the characterization and identification of microfungi from the soil samples collected, including the three *Aspergillus* species in this paper, was already conducted by Lopez (2023). For reference, however, the map of the landfill site, the sampling points, and their coordinates are shown in Figure 1.

Figure 1. Map of the landfill site showing the different sampling points where soil samples were collected

2.2 Soil analysis of the collection site

Composite soil sample collected from the landfill site of Bangar, La Union, Philippines 2519 was sent to the laboratories of CRL Environmental Corporation, Bldg. 2, Berthaphil Compound I, Berthaphil Industrial Park, Jose Abad Santos Ave., CFZ, Pampanga, Philippines 3115 for soil analysis to determine the heavy metal contents. Accordingly, metal analysis of the soil sample was carried out following the standard methods of metal analysis stipulated in the Standard Methods for the Examination of Water and Wastewater, 23rd Edition (Rice et al., 2017), in which the equipment used during the metals analysis was Inductively Coupled Plasma - Optical Emission Spectroscopy (ICP-OES, Shimadzu). A digested sample was nebulized, and the resulting aerosol was transported to the plasma torch. A radio-frequency inductively coupled plasma produces element-specific emission spectra. A grating spectrometer disperses the spectra, and the intensities of the emission lines were monitored by photosensitive devices.

2.3 The source of microfungal species and preparation of mycelial discs

The stock cultures of microfungal species *Aspergillus flavus* (MH864264.1), *Aspergillus oryzae* (MK120548.1), and *Aspergillus terreus* (MH047280.1) used in this study were obtained from the Microbiology Laboratory, Biology Department, College of Arts and Sciences, North La Union Campus, Don Mariano Marcos Memorial State University, Bacnotan, La Union, Philippines 2515. These microfungal species were isolated from soil samples collected from the landfill site of Bangar, La Union, Philippines 2519 (Figure 1), which were subsequently characterized and identified using molecular techniques by Lopez (2023).

In the preparation of the mycelial disc, a single-point inoculation technique was employed by

aseptically inoculating the microfungal spores using an inoculating needle onto inverted Petri plates with solidified potato dextrose agar (HIMEDIA, India). This technique prevents the scattered growth of fungal spores on the plate and ensures only one fungal colony growth. The plate cultures (inverted) were incubated at room temperature (≈28ºC) for 7 days. Using a cork borer (10 mm diameter), mycelial discs were taken near the margin of the growing mycelia on the plate to ensure a uniform age of mycelial disc inoculants.

2.3 Evaluation of optimum culture media for each of the three *Aspergillus* species

In this study, three indigenous culture media, namely coconut water agar (CWA), corn grit decoction agar (CGA), and potato sucrose agar (PSA) as well as three commercial culture media namely potato dextrose agar (PDA), sabouraud dextrose agar (SDA) and malt extract (HIMEDIA, India) + 2% agar (MEA) were evaluated for optimum culture media for the three *Aspergillus* species. The CWA was prepared by dissolving 24 g of agar into 1 L of mature coconut water. The mixture was, subsequently, heated at low heat (≈80ºC) with constant stirring until homogenously mixed. The CGA was prepared by boiling (≈100ºC) 250 g of corn cracklings in 1 L of distilled H_2O. When cooked, the mixture was cooled down (≈40ºC) for a few minutes and filtered using a clean cloth, then, the filtrate was mixed with 10 g of sugar and 24 g of agar. Subsequently, the mixture was heated at low heat (≈80ºC) with constant stirring until homogenously mixed. The PSA was prepared by boiling (≈100ºC) 250 g of cubed potatoes in 1 L of distilled H_2O. When cooked, the mixture was cooled down (≈40ºC) for a few minutes and filtered using a clean cloth; then, the filtrate was mixed with 10 g of sugar and 24 g of agar. Subsequently, the mixture was heated at low heat (≈80ºC) with constant stirring until homogenously mixed. Meanwhile, the commercial culture media PDA (HIMEDIA, India), SDA (HIMEDIA, India), and MEA (HIMEDIA, India) were prepared following the instructions indicated on their labels. Each of the prepared culture media was placed in an Erlenmeyer flask sealed with a cotton plug and autoclaved at 121ºC, 15 psi, for 15 min.

The sterilized culture media were cooled down (≈40ºC), pour-plated, solidified, and then aseptically inoculated with mycelial discs (10 mm) of each of the three *Aspergillus* species. Three replicates were made for each culture medium for every *Aspergillus* species. The inoculated plates were incubated at room temperature (≈28ºC) to allow mycelial growth. The mycelial growth (diameter of the fungal culture) was measured after 7 d of incubation. The culture medium where each of the three *Aspergillus* species showed the highest mycelial growth was considered suitable for each of them.

2.4 Evaluation of heavy metal tolerance

In the preparation of heavy metal-contaminated culture media, Dulay and De Castro's (2016) methods were followed with modifications. The optimum culture medium for each of the three *Aspergillus* species was used. Three replicates were made for each of the optimum culture media (respective of the *Aspergillus* species) contaminated with each of the two heavy metals (Cd and Mn) using cadmium nitrate ($Cd(NO_3)_2$) and manganese oxide (MnO_2), respectively, as sources. Varying concentrations of each heavy metal, such as 10 mg/kg, 100 mg/kg, 1,000 mg/kg, and 10,000 mg/kg, were prepared. Similarly, the heavy metal-contaminated media were autoclaved at 121ºC, 15 psi for 15 min. After sterilization, it was cooled (≈40ºC), pour-plated, solidified, and aseptically inoculated with the mycelial disc (10 mm) of each of the three *Aspergillus* species. The cultures were then incubated at room temperature (≈28ºC), allowing mycelial growth for 7 days.

The evaluation of the tolerance indices of the three *Aspergillus* species was based on the methods of Liaquat et al. (2020) with modifications. The radial mycelial growth was obtained by measuring the diameter of the growing mycelia on the plate across three orientations passing through the center and then averaged. All of these data were recorded per replicates. In the same period of mycelial growth, the tolerance index (TI) was then calculated using the following equation:

$$TI = \frac{RGwm}{RGwom} \quad (1)$$

Where; TI is the tolerance index, RGwm is radial mycelial growth with heavy metal, and RGwom is radial mycelial growth without heavy metal.

2.5 Determination of heavy metal uptake

The potato dextrose broth (HIMEDIA, India) was used to determine heavy metal uptake of the three *Aspergillus* species. A concentration of 10,000 mg/kg of each of the two heavy metal (Cd and Mn) was prepared using $Cd(NO_3)_2$ and MnO_2 in potato dextrose

broth (HIMEDIA, India). The culture media were dispensed in clean catsup bottles autoclaved at 121ºC, 15 psi for 15 min. After sterilization, the culture media were cooled down (≈28ºC) and aseptically inoculated with mycelial discs. The cultures were incubated at room temperature (≈28ºC), allowing mycelial growth for 10 days. The experiment was carried out in triplicates.

After 10 days of incubation, the mycelial mats from the culture broths were harvested using a strainer. The fresh mycelial mats were drained, packed, and labeled correctly which were then sent to the laboratories of CRL Environmental Corporation, Bldg. 2, Berthaphil Compound I, Berthaphil Industrial Park, Jose Abad Santos Ave., CFZ, Pampanga, Philippines 3115 for heavy metal quantitative analysis (methods were previously described above) for Cd and Mn. From the obtained results, the percent uptake (PU) of heavy metal was calculated using the equation:

$$PU = \frac{10{,}000\ mg/kg - MUmm}{10{,}000\ mg/kg} \times 100 \quad (2)$$

Where; PU is the percent metal uptake, 10,000 mg/kg is the known concentration of the medium, and MUmm is the metal uptake of the mycelial mats.

2.6 Statistical analysis

The Minitab ver. 21 statistical software was used for statistical analyses of data. The experiments were laid out in a completely randomized design (CRD). Analysis of variance (ANOVA) was used, and treatments that were declared significant by ANOVA were further compared using Tukey's comparison of means. The schematic diagram of the methods employed in this study is shown in Figure 2.

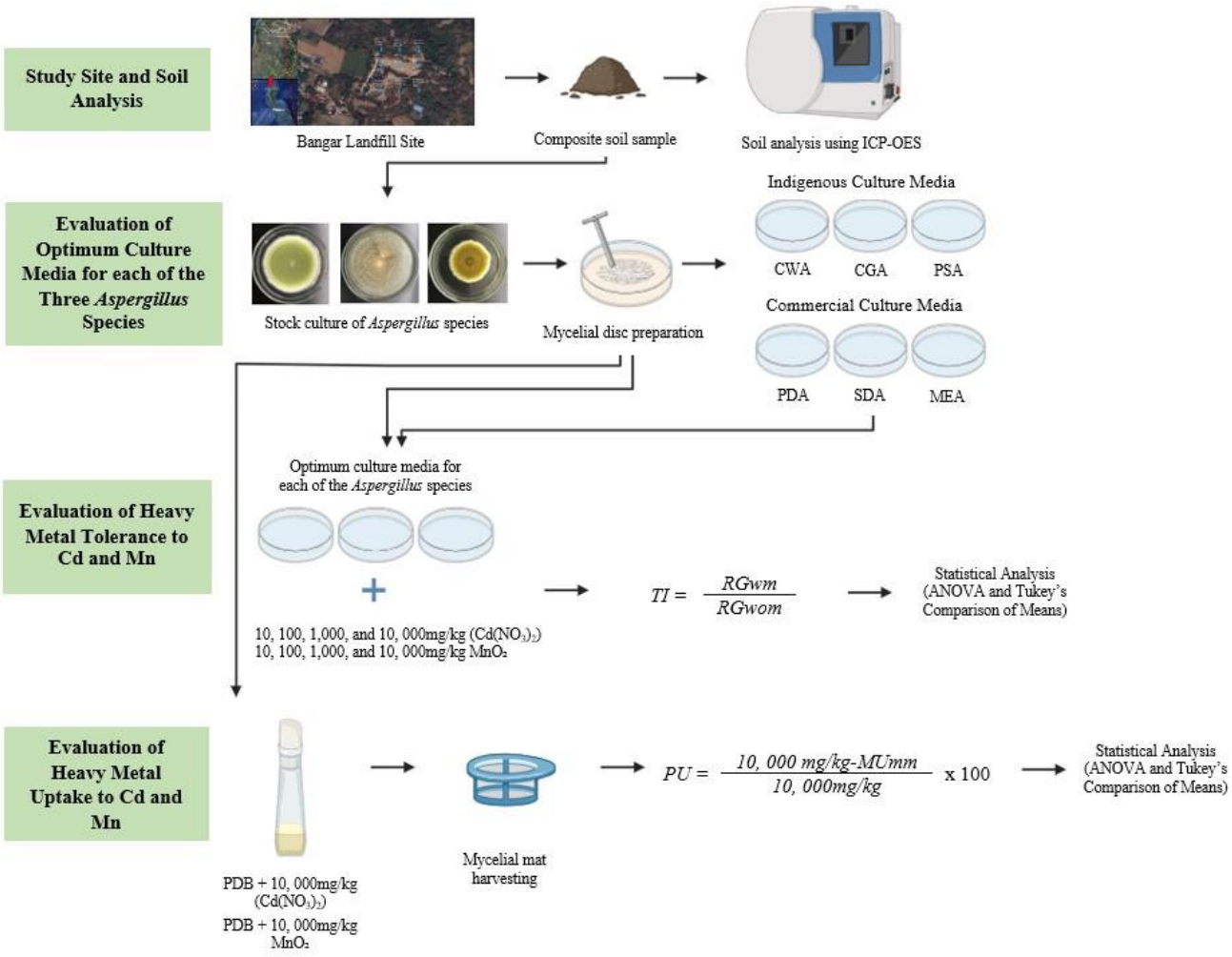

Figure 2. Schematic diagram of the procedure done in this study in the evaluation of tolerance and uptake to Cd and Mn for the three *Aspergillus* species

3. RESULTS AND DISCUSSION

3.1 Soil analysis

The results of the analysis of the soil sample collected from the landfill site are shown in Table 1. It can be inferred from the Table that Fe, Mn, and Cr have notable high concentrations of 31,100 mg/kg, 904 mg/kg, and 53 mg/kg, respectively, detected from the soil sample. However, the values detected are still within the permissible limits in soil based on available literature. On a positive note, the toxic heavy metals As, Pb, and Hg were not detected in the soil samples. All other heavy metals such as Cd, Cu, and Ni are in the moderate range or very minimal amounts and fall within the permissible limits. Due to the levels of toxicity and concentration, respectively, Cd and Mn were studied in this paper.

Table 1. Heavy metal concentration of toxic metals detected from the soil samples

Heavy metals	Result (mg/kg)	World permissible limits in soil (mg/kg)
Arsenic (As)	ND	20[a]
Cadmium (Cd)	1.1	0.8-3.0[b]
Copper (Cu)	7.8	36-100[b]
Chromium (Cr)	53	100[b]
Iron (Fe)	31,100	50,000[a]
Lead (Pb)	ND	50-85[b]
Manganese (Mn)	904	2,000[a]
Nickel (Ni)	16	35-50[b]
Mercury (Hg)	ND	0.05[c]

[a]Chiroma et al. (2014); [b]WHO (1996); [c]Kinuthia et al. (2020); ND: not detected

Generally, metals, as described by Rashid et al. (2023), are inorganic elements with atomic densities relatively higher than H_2O (1 g/cm^3). Over 40 elements in Mendeleev's periodic system with an atomic mass above 40 atomic units are identified as heavy metals which include Fe, Mn, Co, Ni, Cu, Zn, Mo, Cd, and others (Kucher et al., 2023). Heavy metals can be (i) essential elements (e.g., Cr, Fe, and Zn) needed in small amounts and are crucial for the physiological functions of organisms or (ii) non-essential elements of an unknown biological role (e.g., Cd, Pb, and Hg) which are toxic to living organisms (Gajewska et al., 2022). Heavy metals are naturally present in the environment, like the soil, however, excessive deposition of these metals may be caused by natural activities (e.g., geological weathering, volcanic activity, soil erosion, etc.) and intensified by human activities (landfilling of municipal solid wastes, irresponsible mining, etc.) makes them persistent environmental pollutants that could pose significant biological toxicity to living organisms. Aside from the biological toxicity, heavy metals cannot disappear from the soil but can only move from one natural layer to another, interacting with various living organisms; hence, the possibility to bioaccumulate and biomagnify in the food chain (Jamil Emon et al., 2023; Kucher et al., 2023).

It is then important to monitor the presence and concentration of these toxic heavy metals in the environment, especially in areas where introduction may occur, like in open landfill sites. The findings of this study on metal analysis of the soil sample from the landfill site coincide with the findings of Beinabaj et al. (2023) in which Fe had the highest concentration (22.94 mg/kg) among the metals they have detected in the landfill leachates from the new landfills in Tehran. They have also noted the high concentration of Mn (33.65-34.14 mg/kg) they have detected in the landfill soil. Like the present study, Beinabaj et al. (2023) also detected Cd at low concentration. In the present study, the high concentrations of Fe and Mn compared to the other metals analyzed in the soil sample collected can be attributed to sources such as cast iron from old tools, equipment, and alike for Fe while blade, bottle caps, galvanizing goods, insecticides, pigments and paints for Mn that are dumped in the landfill site (Kanmani and Gandhimathi, 2013; Beinabaj et al., 2023). Also, Li et al. (2011) regarded Fe as the fourth-most abundant element in the Earth's crust, widely used for production and life; hence, it is the most prevalent heavy metal in landfills. Other factors are explained and discussed by Wang et al. (2018), like the soil at landfill site may sometimes undergo reductive dissolution, thereby resulting in the release of Fe and Mn, thus increasing their solubility.

However, the detected heavy metals in the present study are within the permissible limits for soil based on available literature. Periodic monitoring of toxic heavy metals is a proactive measure to prevent the adverse toxic effects of these heavy metals on living organisms near the area by possibly applying an efficient and eco-friendly clean-up strategy because even though the concentrations of heavy metals are below the permissible levels, this may still interfere with the physiological metabolism of organisms, like plants, and may lead to the increased uptake of heavy metals due to the persistence of these toxic metals in the soil (Singh and Kalamdhad, 2011; Ojekunle et al., 2016). Also, Chibuike and Obiora (2014) observed that the combined effect of more than two heavy metals in contaminated soil was as harmful as the effect of the most toxic heavy metal.

3.2 Optimum culture medium for mycelial growth

In this study, three indigenous culture media namely coconut water agar (CWA), corn grit decoction agar (CGA), and potato sucrose agar (PSA) as well as three commercial culture media namely potato dextrose agar (PDA), sabaurud dextrose agar (SDA), and malt extract agar (MEA) were evaluated for optimum growth of the three *Aspergillus* species. Figure 3 shows the mean mycelial growth of the three *Aspergillus* species in indigenous and commercial culture media.

As shown in Figure 3, *A. oryzae* (MK120548.1) exhibited the highest mycelial growth in the commercial culture medium PDA (89.00±1.00 mm) although it is statistically comparable with MEA (85.00±1.73 mm) and the least mycelial growth in indigenous culture medium PSA (48.67±3.06 mm). Conversely, *A. terreus* (MH047280.1) exhibited the highest mycelial growth in indigenous culture medium PSA (76.00±2.00 mm) while it had the least growth in the commercial media MEA (37.67±2.52 mm). Interestingly, *A. flavus* (MH864264.1) also exhibited the highest mycelial growth in PDA (88.67±1.16 mm) although it is statistically comparable with SDA (88.33±1.53 mm). *A. flavus* (MH864264.1) exhibited the least mycelial growth in MEA (47.67±2.08 mm).

The optimum culture medium for mycelial growth of each of the three *Aspergillus* species is considered in this study so as not to interfere with the evaluation of their tolerance index. Luxuriant mycelial growth of *A. oryzae* (MK120548.1) and *A. flavus* (MH864264.1) was observed in potato dextrose agar while *A. terreus* (MH047280.1) grew best in potato sucrose agar as shown in Figure 3. Lopez et al. (2022) elaborated on the components of potato dextrose/sucrose agar relative to fungal growth in which potato dextrose agar is used in culturing wide range of fungi as it provides a rich source of carbohydrates and significant amounts of vitamins and minerals such as vitamin B6, potassium, phosphorus, magnesium, iron and low amount of sodium essential for many metabolic processes and growth. Also, it provides a significant amount of protein as nitrogen sources of various fungal species.

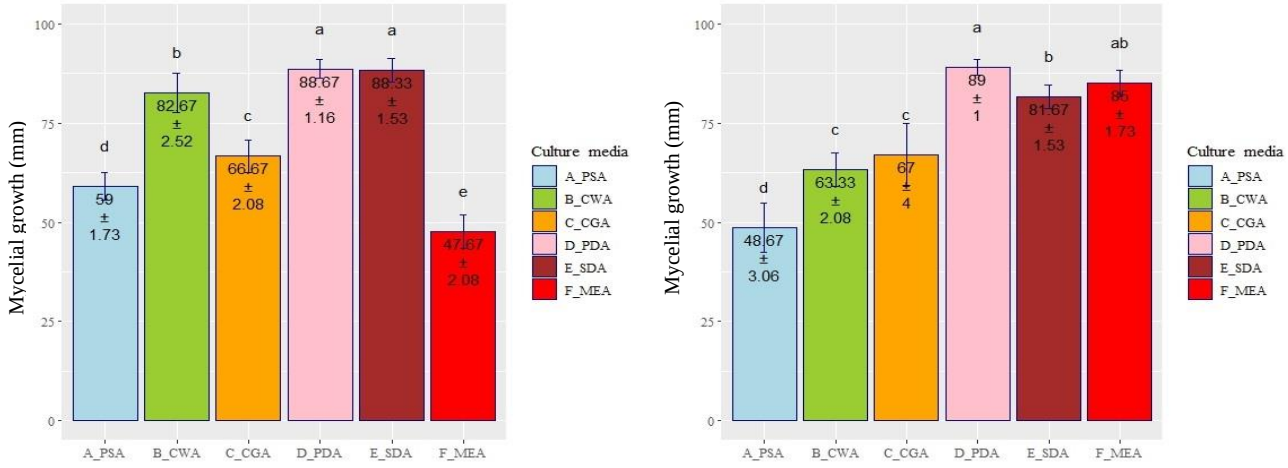

(a) *Aspergillus* (b) *Aspergillus oryzae*

Figure 3. The mycelial growth of (a) *A. flavus*, (b) *A. oryzae*, and (c) *A. terreus* in different culture media for the evaluation of optimum culture medium. Values are expressed in mean±SD and means that do not share a letter are significantly different.

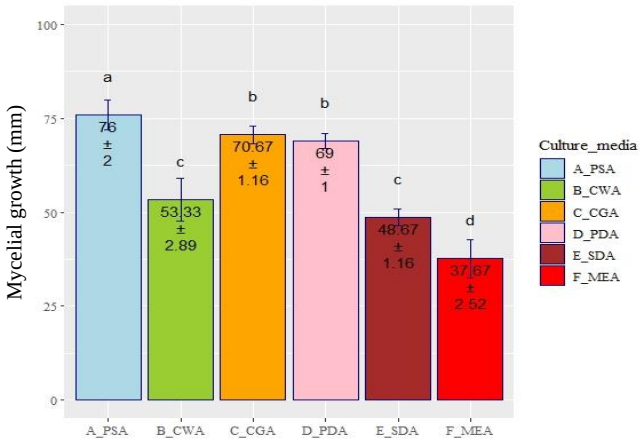

(c) *Aspergillus terreus*

Figure 3. The mycelial growth of (a) *A. flavus*, (b) *A. oryzae*, and (c) *A. terreus* in different culture media for the evaluation of optimum culture medium. Values are expressed in mean±SD and means that do not share a letter are significantly different (cont.).

3.3 Tolerance index of the three *Aspergillus* species to Cd and Mn

The optimum culture medium for each of the *Aspergillus* species was used to evaluate the tolerance index to Cd and Mn. Table 2 shows the tolerance index of the three *Aspergillus* species to Cd and Mn at 10, 100, 1,000, and 10,000 mg/kg concentrations. It can be inferred from the table that at 10 mg/kg Cd, *A. oryzae* (MK120548.1) and *A. flavus* (MH864264.1) exhibited a high metal tolerance index value while *A. terreus* (MH047280.1) (0.66±0.02) showed moderate metal tolerance to Cd. At 10 mg/kg Mn, *A. flavus* (MH864264.1) exhibited a remarkably high metal tolerance index of 1.03±0.04. *A. oryzae* (MK120548.1) exhibited a high metal tolerance index value of 0.97±0.02. However, *A. terreus* (MH047280.1) only showed a moderate metal tolerance index value. At 100, 1,000, and 10,000 mg/kg of Cd, all *Aspergillus* species showed very low to low metal tolerance.

Interestingly, at 100, 1,000, and 10,000 mg/Kg of Mn, *A. flavus* (MH864264.1) exhibited a consistently very high metal tolerance index while *A. terreus* (MH047280.1) exhibited a low to very low metal tolerance index to Mn. *A. oryzae* (MK120548.1) showed a high metal tolerance index only at 100 and 1,000 mg/kg of Mn. However, it showed very low metal tolerance at10,000 mg/kg. Figure 4 shows the mycelial growth of the three *Aspergillus* species grown in optimum medium contaminated with Cd and Mn at 10, 100, 1,000, and 10,000 mg/kg concentrations, as well as the trend of tolerance indexes of the three *Aspergillus* species at increasing concentrations (10, 100, 1,000, and 10,000 mg/kg) of Cd and Mn.

Table 2. Tolerance index of the three *Aspergillus* species to Cd and Mn at various heavy metal concentrations

Heavy metals	Microfungal species	*Tolerance index heavy metal concentration (mg/kg)			
		10	100	1,000	10,000
Cadmium (Cd)	*A. oryzae* (MK120548.1)	0.92±0.06	0.18±0.04	0.00±0.00	0.00±0.00
	A. terreus (MH047280.1)	0.66±0.02	0.30±0.04	0.04±0.01	0.00±0.00
	A. flavus (MH864264.1)	0.92±0.04	0.05±0.01	0.00±0.00	0.00±0.00
Manganese (Mn)	*A. oryzae* (MK120548.1)	0.97±0.02	0.89±0.02	0.85±0.01	0.16±0.02
	A. terreus (MH047280.1)	0.63±0.01	0.36±0.02	0.00±0.00	0.00±0.00
	A. flavus (MH864264.1)	1.03±0.04	1.02±0.07	1.10±0.04	1.22±0.06

*Tolerance index values are mean values that indicate: 0.00-0.39 - very low metal tolerance; 0.40-0.59 - low metal tolerance; 0.60-0.79 - moderate metal tolerance; 0.80-0.99 - high metal tolerance; 1.00->1.00 - very high metal tolerance (Oladipo et al., 2018)

It is noteworthy that the observed tolerance indices of *A. terreus* (MH047280.1) at 10 mg/kg to 100 mg/kg Cd coincide with the findings of Villalba-Villalba and Gonzalez-Mendez (2021). Sule et al. (2022) found that *A. flavus* along with other *Aspergillus* species such as *A. niger*, *A. fumigatus*, and *A. versicolor* exhibited tolerance to heavy metals such as Cd, Mn, and other heavy metals at different levels

of concentrations with most of their isolates found to tolerate at least up to 40 mg/kg of the heavy metals. This is consistent with the observations of the present study, where most of the three *Aspergillus* species still showed considerable tolerance to Cd and Mn at concentrations of 10 mg/kg to 100 mg/kg only. This observation can be attributed to heavy metal toxicity and its effect to fungal growth as discussed by Priyadarshini et al. (2021). They explained that excessive accumulation of heavy metal, like Cd, induces protein and nucleic acid damage, which may inhibit transcription and cell growth.

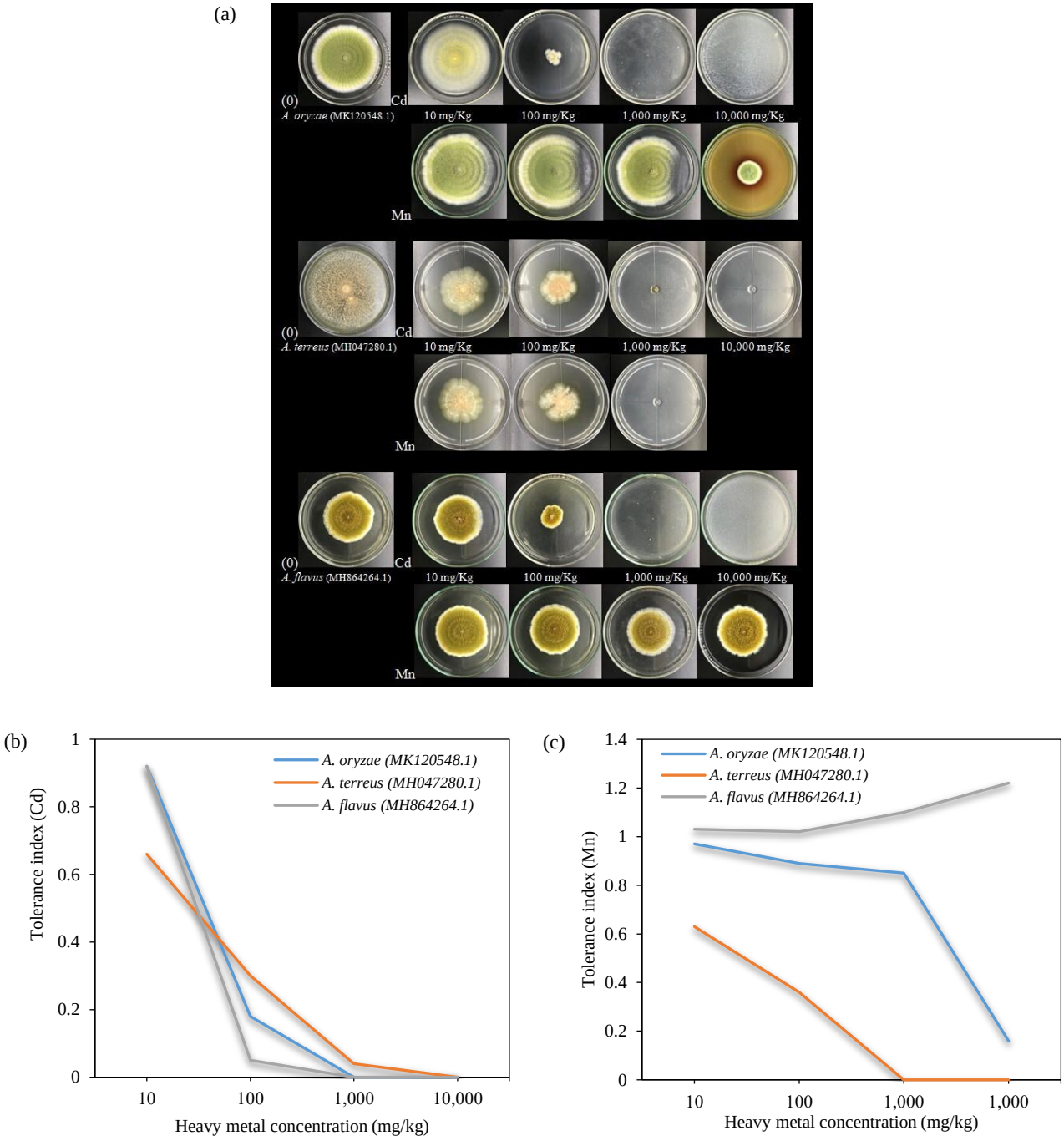

Figure 4. (a) Mycelial growth of the three *Aspergillus* species in their respective optimum culture medium enriched with Cd and Mn at varying concentrations; (b-c) Line graph showing the trend of the tolerance index of the three *Aspergillus* species to Cd and Mn at various concentrations

Interestingly, however, the present study found that *A. oryzae* (MK120548.1) showed a consistently high metal tolerance index of up to 1,000 mg/kg of Mn. *A. flavus* (MH864264.1) also showed a consistently very high tolerance index of up to 10,000 mg/kg of Mn. The result of the present study also

coincides with the findings of Kumar and Dwivedi (2020) that *A. flavus* CR500 tolerated Cd and Mn up to 100 mg/L and 1,600 mg/L concentrations, respectively. Heavy metal tolerance is the ability of an organism, like fungi, to survive metal toxicity through several mechanisms that serve as a direct response to the toxic metals present. These can be attributed to several mechanisms of metal tolerance adopted by fungi (which vary among species), which include enhanced metal efflux, suppressed influx, extracellular metal sequestration and precipitation, metal binding to cell walls, intracellular sequestration and complexation, and production of intracellular or extracellular enzymes (Oladipo et al., 2018).

3.4 Metal uptake of the three *Aspergillus* species to Cd and Mn

In evaluating the metal uptake of *Aspergillus* species to Cd and Mn, the mean percent uptake of heavy metal was determined using equation 2. The three *Aspergillus* species were grown in potato dextrose broth (PDB), each with 10,000 mg/kg of Cd and Mn. After ten (10) days of incubation, the mycelial mats were harvested and subjected to heavy metal analysis, and the results, which are presented in Table 3, were analyzed. Values in the table are percent uptake or the equivalent mg/kg concentration out of each heavy metal's 10,000 mg/kg concentration (Cd and Mn).

Table 3. Mean percent uptake of heavy metal Cd and Mn by the three *Aspergillus* species at a prepared concentration of 10,000 mg/kg of heavy metal in PDB

Microfungal species	Mean percent uptake of heavy metal (% of 10,000 mg/kg)	
	Cadmium (Cd)	Manganese (Mn)
Aspergillus oryzae (MK120548.1)	5.37±1.17%^{a} or ≤654 mg/kg	0.85±0.23%^{c} or ≤108 mg/kg
Aspergillus terreus (MH047280.1)	3.07±0.47%^{b} or ≤354 mg/kg	8.78±1.19%^{a} or ≤997 mg/kg
Aspergillus flavus (MH864264.1)	4.38±0.33%^{ab} or ≤471 mg/kg	2.66±0.26%^{b} or ≤292 mg/kg

*Means that do not share a letter are significantly different

Interestingly, all *Aspergillus* species showed uptake of heavy metals, with *A. oryzae* (MK120548.1) exhibiting the highest mean percent uptake of 5.37±1.17% to Cd or equivalent to ≤654 mg/kg of Cd. On the other hand, *A. terreus* (MH047280.1) showed the highest mean percent heavy metal uptake of 8.78±1.19% to Mn or equivalent to ≤997 mg/kg of Mn. *A. flavus* (MH864264.1) showed considerable mean percent heavy metal uptake to Cd and Mn. Various growth-dependent or growth-independent metabolic processes of living cells carry out heavy metal uptake or metal accumulation in fungi. However, even dead cells or polysaccharide secretions may also be involved in metal sorption (Shakya et al., 2016). Heavy metal uptake is affected by the mechanisms of fungi (often varied across fungal species) to resist heavy metal, which include biosorption capability, bioaccumulation and compartmentalization, metal chelation, intracellular formation of metal oxalates through secretions of organic acids, and efflux transport for metal exclusion. These mechanisms affect fungal species' uptake capability and capacity (Priyadarshini et al., 2021). The observed high metal uptake of Mn by *A.terreus* (MH047280.1), in the present study, can be related to the findings of Saha and Kennedy (2019) in the first reported relationship of Mn with medium components for utilization of sugar and production of itaconic acid (a building block platform chemical) by *A. terreus*.

Similarly, Sándor et al. (2021) observed that Mn ions in association with copper modulate the morphology of *A. terreus*. This suggests that the high Mn uptake of *A. terreus* can be associated with formation of metal oxalates from organic acid secretions from utilization of sugars although further studies should be done to confirm this claim. Interestingly, the present study also observed an initial Cd uptake capability of *A. oryzae* (MK120548.1) although several studies showed Cd uptake by other several *Aspergillus* species like *A. fumigatus*, *A. niger*, and *A. versicolor* but limited findings on *A. oryzae* (Al-Garni et al., 2009; Doku and Belford, 2015; Soleimani et al., 2016) suggesting more studies should be done to determine the various uptake mechanisms and assess the uptake potential of *A. oryzae* to biosorp Cd.

4. CONCLUSION

In conclusion, the landfill microfungal isolates such as *A. oryzae* (MK120548.1), *A. terreus* (MH047280.1), and *A. flavus* (MH864264.1) showed potential tolerance and metal uptake to Cd and Mn. Of note, the tolerance of *A. oryzae* (MK120548.1), and *A. flavus* (MH864264.1) in vitro to Mn is remarkable.

Interestingly, *A. oryzae* (MK120548.1), and *A. terreus* (MH047280.1) showed considerable metal uptake of Cd, and Mn, respectively. Regarding the optimum culture media, *A. oryzae* and *A. flavus* showed prolific growth in commercial medium potato dextrose agar while *A. terreus* showed prolific growth in indigenous medium potato sucrose agar. The soil sample collected has permissible amounts of heavy metals for Cd, Mn, Cu, Cr, and Ni while As, Pb, and Hg was not detected. The initial findings of this study are important in contributing to the discovery of the potential of landfill microfungal *Aspergillus* species such as *A. flavus*, *A. terreus*, and *A. oryzae* to tolerate and uptake Cd and Mn. With these data, studies in conjunction with plants can be made further to assess the mycoremediation potential of these microfungal isolates, and their tolerance and uptake to other heavy metals can be explored. The findings of this study on the heavy metal soil analysis to be within the permissible limits in soil are a good indication of the status of the heavy metals present in the landfill site. However, periodic monitoring and a thorough and wholistic assessment on the degree of soil contamination of the landfill site (using $PI_{Nemerow}$, for example) should be done for appropriate actions to be taken to prevent adverse health effect to public.

ACKNOWLEDGEMENTS

The "microfungi team" is very grateful to the Don Mariano Marcos Memorial State University (DMMMSU), particularly to the University Research and Extension Office and the DMMMSU North La Union Campus Research Unit for the financial support. Profound gratitude is also accorded to the Biology Department of the College of Arts and Sciences, DMMMSU, North La Union Campus.

REFERENCES

Acosta-Rodríguez I, Cárdenas-González JF, Rodríguez Pérez AS, Oviedo JT, Martínez-Juárez VM. Bioremoval of different heavy metals by the resistant fungal strain *Aspergillus niger*. Bioinorganic Chemistry Applications 2018;2018:Article No. 3457196.

Aishwarya SA, Nagam N, Vijaya T, Netala RV. Screening and identification of heavy metal-tolerant endophytic fungi *Lasiodiplodia theobromae* from *Boswellia ovalifoliolata* an endemic plant of tirumala hills. Asian Journal of Pharmaceutical and Clinical Research 2017;10(3):488-91.

Al-Garni S, Ghanem K, Bahobail A. Biosorption characteristics of *Aspergillus fumigatus* in removal of cadmium from an aqueous solution. African Journal of Biotechnology 2009;8(17): 4163-72.

Al-Obaid AM, Hashem AR. Zinc tolerance and accumulation in *Aspergillus oryzae*, *Penicillium citrinum* and *Rhizopus stolonifer* isolated from Saudi Arabian Soil. Qatar University Science Journal 1997;17(1):103-9.

Alzahrani NH, Alamoudi KH, El-Gendy MM. Molecular identification and nickel biosorption with the dead biomass of some metal tolerant fungi. Journal of Microbial and Biochemical Technology 2017;9(6):310-5.

Ayilara MS, Babalola OO. Bioremediation of environmental wastes: The role of microorganisms. Frontiers in Agronomy 2023;5:Article No. 1183691.

Beinabaj SM, Heydariyan H, Aleii HM, Hosseinzadeh A. Concentration of heavy metals in leachate, soil, and plants in Tehran's landfill: Investigation of the effect of landfill age on the intensity of pollution. Heliyon 2023;9(1):Article No. 13017.

Chibuike GU, Obiora SC. Heavy metal polluted soils: Effect on plants and bioremediation methods. Applied and Environmental Soil Science 2014;2014:Article No. 752708.

Chiroma TM, Ebewele RO, Hymore FK. Comparative assessment of heavy metal levels in soil, vegetables, and urban grey wastewater used for irrigation in Yola and Kano. International Refereed Journal of Engineering and Science 2014;3(2):1-9.

Doku TE, Belford EJ. The potential of *Aspergillus fumigatus* and *Aspergillus niger* in bioaccumulation of heavy metals from the Chemu Lagoon, Ghana. Journal of Applied Biosciences 2015;94:8907-14.

Dulay RM, De Castro ME. Cadmium and chromium tolerance and mycoremediation ability of tiger sawgill mushroom, *Lentinus tigrinus*. International Journal of Biology, Pharmacy and Allied Sciences 2016;5(11):3003-12.

El-Moselhy KM, Othman AI, Abd El-Azem H, El-Metwally ME. Bioaccumulation of heavy metals in some tissues of fish in the Red Sea, Egypt. Egyptian Journal of Basic and Applied Sciences 2014;1(2):97-105.

Gajewska J, Floryszak-Wieczorek J, Sobieszczuk-Nowicka E, Mattoo A, Arasimowicz-Jelonek M. Fungal and oomycete pathogens and heavy metals: An inglorious couple in the environment. IMA Fungus 2022;13:Article No. 6.

Jamil Emon F, Rohani MF, Sumaiya N, Tuj Jannat MF, Akter Y, Shahjahan M, et al. Bioaccumulation and bioremediation of heavy metals in fishes: A review. Toxics 2023;11(6):1-28.

Joo JH, Hussein KA. Heavy metal tolerance of fungi isolated from contaminated soil. Korean Journal of Soil Science and Fertilizer 2012;45(4):565-71.

Kanmani S, Gandhimathi R. Assessment of heavy metal contamination in soil due to leachate migration from an open dumping site. Applied Water Science 2013;3:193-205.

Khan I, Ali M, Aftab M, Shakir S, Qayyum S, Haleem KS, et al. Mycoremediation: A treatment for heavy metal-polluted soil using indigenous metallotolerant fungi. Environmental Monitoring and Assessment 2019;191:Article No. 622.

Kucher L, Krasnoshtan I, Nedilska U, Muliarchuk O, Manzii O, Menderetsky V, et al. Heavy metals in soil and plants during revegetation of coal mine spoil tips and surrounded territories. Journal of Ecological Engineering 2023;24(7):234-45.

Kumar V, Dwivedi SK. Multimetal tolerant fungus *Aspergillus flavus* CR500 with remarkable stress response, simultaneous multiple metal/loid removal ability and bioremediation potential of wastewater. Environmental Technology and Innovation 2020;20:Article No. 101075.

Kinuthia GK, Ngure V, Beti D, Lugalia R, Wangila A, Kamau L. Levels of heavy metals in wastewater and soil samples from open drainage channels in Nairobi, Kenya: Community health implication. Scientific Reports 2020;10(1):Article No. 8434.

Li WB, Yao J, Xia FF, Feng HJ, Feng H, Jiang CJ, et al. Leaching behavior of iron from simulated landfills with different operational modes. Bioresource Technology 2011;102(16): 7422-8.

Li X, Li W, Chu L, White Jr. JF, Xiong Z, Li H. Diversity and heavy metal tolerance of endophytic fungi from *Dysphania ambrosioides*, a hyperaccumulator from Pb-Zn contaminated soils. Journal of Plant Interactions 2016;11(1):186-92.

Liang J, Diao H, Song W, Li L. Tolerance and bioaccumulation of arsenate by *Aspergillus oryzae* TLWK-09 isolated from arsenic-contaminated soils. Water, Air and Soil Pollution 2018;229:Article No. 169.

Liaquat F, Munis MF, Haroon U, Arif S, Saqib S, Zaman W, et al. Evaluation of metal tolerance of fungal strains isolated from contaminated mining soil of Nanjing, China. Biology 2020;9(12):Article No. 469.

Long DD, Fu RR, Han JR. Tolerance and stress response of sclerotiogenic *Aspergillus oryzae* G15 to copper and lead. Folia Microbiologica 2017;62:295-304.

Lopez MK. Characterization, molecular identification, and phylogenetic analysis of microfungi isolated from the Landfill Site of Bangar, La Union, Philippines. International Journal of Agricultural Technology 2023;19(3):1085-96.

Lopez MKS, Kalaw SP, Dulay RMR, De Leon AM, Reyes RG. Optimization of mycelial growth of *Xylaria papulis* Lloyd (Xylariaceae) in indigenous liquid culture conditions, Science City of Muñoz, Nueva Ecija, Philippines. Studies in Fungi 2022;7(21):1-7.

Mahmoud A, Massoud M, Abdel-Motaal F, El-Zayat S. Tolerance and biosorption of manganese, iron and aluminium by five *Aspergillus* species isolated from freshwater. The International Journal of Environmental Sciences 2017;16(1):61-9.

Nyiramigisha P, Komariah, Sajidan. Harmful impacts of heavy metal contamination in the soil and crops grown around dumpsites. Reviews in Agricultural Science 2021;9:271-82.

Ojekunle OZ, Ojekunle OV, Adeyemi AA, Taiwo AG, Sangowusi OR, Taiwo AM, et al. Evaluation of surface water quality indices and ecological risk assessment for heavy metals in scrap yard neighbourhood. SpringerPlus 2016;5(1):Article No. 560.

Oladipo OG, Awotoye OO, Olayinka A, Bezuidenhout CC, Maboeta MS. Heavy metal tolerance traits of filamentous fungi isolated from gold and gemstone mining sites. Brazilian Journal of Microbiology 2018;49(1):29-37.

Oladipo OG, Awotoye OO, Olayinka A, Ezeokoli OT, Maboeta MS, Bezuidenhout CC. Heavy metal tolerance potential of *Aspergillus* strains isolated from mining sites. Bioremediation Journal 2016;20(4):287-97.

Oso BA, Olagunji MO, Okiki PA. Lead tolerance and bioadsorption potentials of indigenous soil fungi in Ado Ekiti, Nigeria. European Journal of Experimental Biology 2015; 5(9):15-9.

Palanivel TM, Pracejus B, Novo LAB. Bioremediation of copper using indigenous fungi *Aspergillus* species isolated from an abandoned copper mine soil. Chemosphere 2023;314:Article No. 137688.

Pawlowska TE, Charvat I. Heavy-metal stress and developmental patterns of arbuscular mycorrhizal fungi. Applied and Environmental Microbiology 2004;70(11):6643-9.

Priyadarshini E, Priyadarshini SS, Cousins BG, Pradhan N. Metal-Fungus interaction: Review on cellular processes underlyingheavy metal detoxification and synthesis of metal nanoparticles. Chemosphere 2021;274:Article No. 129976.

Rashid A, Schutte BJ, Ulery A, Deyholos MK, Sanogo S, Lehnhoff EA, et al. Heavy metal contamination in agricultural soil: Environmental pollutants affecting crop health. Agronomy 2023;13(6):Article No.1521.

Rice EW, Baird RB, Eaton AD. Standard Methods for the Examination of Water and Wastewater. 23rd ed. USA. American Public Health Association; 2017.

Saba G, Thirumarimurugan M, Sivakumar VM. Heavy metal tolerance potential of fungus isolated from copper smelting industry. International Research Journal of Pharmacy 2017;8(6):120-5.

Saha BC, Kennedy GJ. Phosphate limitation alleviates the inhibitory effect of manganese on itaconic acid production by *Aspergillus terreus*. Biocatalysis and Agricultural Biotechnology 2019;18:Article No. 101016.

Sándor E, Kolláth IS, Fekete E, Bíró V, Flipphi M, Kovács B, et al. Carbon-source dependent interplay of copper and manganese ions modulates the morphology and itaconic acid production in *Aspergillus terreus*. Frontiers in Microbiology 2021;12:Article No. 680420.

Shakya M, Sharma P, Meryem SS, Mahmood Q, Kumar A. Heavy metal removal from industrial wastewater using fungi: Uptake mechanism and biochemical aspects. Journal of Environmental Engineering 2016;142(9):1-18.

Singh J, Kalamdhad AS. Effects of heavy metals on soil, plants, human health and aquatic life. International Journal of Research in Chemistry and Environment 2011;1(2):15-21.

Singh D, Rathod V, Ninganagouda S, Hiremath J, Singh AK, Mathew J. Optimization and characterization of silver nanoparticle by endophytic fungi *Penicillium* sp. isolated from *Curcuma longa* (turmeric) and application studies against MDR *E. coli* and *S. aureus*. Bioinorganic Chemistry and Applications 2014;2014:Article No. 408021.

Soleimani N, MohammadianFazli M, Ramazani A, Mehrasbi MR. Application of live, dead and dried biomasses of *Aspergillus versicolor* for cadmium biotreatment. Journal of Human, Environment and Health Promotion 2016;1(2):87-98.

Sule AM, Inuwa B, Bello SZ, Gero M, Mohammed HA, Muhammad ZA. Isolation, characterization and heavy metals tolerance indices of indigenous fungal flora from a tannery located at Challawa Industrial Estate of Kano State, Nigeria. Journal of Applied Sciences and Environmental Management 2022;26(7):1289-98.

Thabit TMA, El-Naggar MAH. Potential impact of some soil-borne fungi on biodegradation of some organophosphorous-nematicides. American Journal of Environmental Protection 2014;3(6):299-304.

Tiwari S, Lata C. Heavy metal stress, signaling, and tolerance due to plant-associated microbes: An overview. Frontiers in Plant Science 2018;9:Article No. 452.

Upadhyaya H, Panda SK, Bhattacharjee MK, Dutta S. Role of arbuscular mycorrhiza in heavy metal tolerance in plants: Prospects for phytoremidiation. Journal of Phytological Research 2010;2(7):16-27.

Vajpai S, Taylor PE, Adholeya A, Ackland ML. Chromium tolerance and accumulation in *Aspergillus flavus* isolated from tannery effluent. Journal of Basic Microbiology 2019; 60(1):58-71.

Verma S, Kuila A. Bioremediation of heavy metals by microbial process. Environmental Technology and Innovation 2019;14: Article No. 100369.

Villalba-Villalba AG, González-Méndez B. Evaluating *Aspergillus terreus* tolerance to toxic metals. Revista Chapingo Serie Ciencias Forestales y del Ambiente 2021;27(3):449-64.

Wang Y, Pleasant S, Dubey B, Rhue D, Bonzongo JC, Townsend T. Assessing the propensity of landfill soils to undergo reductive iron dissolution. Environmental Earth Science 2018;77(8):Article No. 306.

World Health Organization (WHO). Permissible Limits of Heavy Metals in Soil and Plants. Geneva, Switzerland: World Health Organization; 1996.

Wijaya N, Priyani N, Munir E. Lead accumulation activity of fungi isolated from Batang Toru, South Tapanuli, North Sumatra. Proceedings of the IOP Conference Series: Earth and Environmental Science; 2018 Dec 8-9; Medan, North Sumatera, Indonesia; 2019.

Zango UU, Muhammad II, Sharma V, Sharma AK. Effective bioremediation of Cd, Cr, and Pb in tannery effluent using *Aspergillus fumigatus* and *Aspergillus terreus*: Synergistic effects of using the two strainst. Water Air and Soil Pollution 2023;234(12):Article No. 735.

INSTRUCTION FOR AUTHORS

Publication and Peer-reviewing processes of Environment and Natural Resources Journal

Environment and Natural Resources Journal is a peer reviewed and open access journal that is published in six issues per year. Manuscripts should be submitted online at https://ph02.tci-thaijo.org/index.php/ennrj/about/submissions by registering and logging into this website. Submitted manuscripts should not have been published previously, nor be under consideration for publication elsewhere (except conference proceedings papers). A guide for authors and relevant information for the submission of manuscripts are provided in this section and also online at: https://ph02.tci-thaijo.org/index.php/ennrj/author. All manuscripts are refereed through a **single-blind peer-review** process.

Submitted manuscripts are reviewed by outside experts or editorial board members of **Environment and Natural Resources Journal**. This journal uses double-blind review, which means that both the reviewer and author identities are concealed from the reviewers, and vice versa, throughout the review process. Steps in the process are as follows:

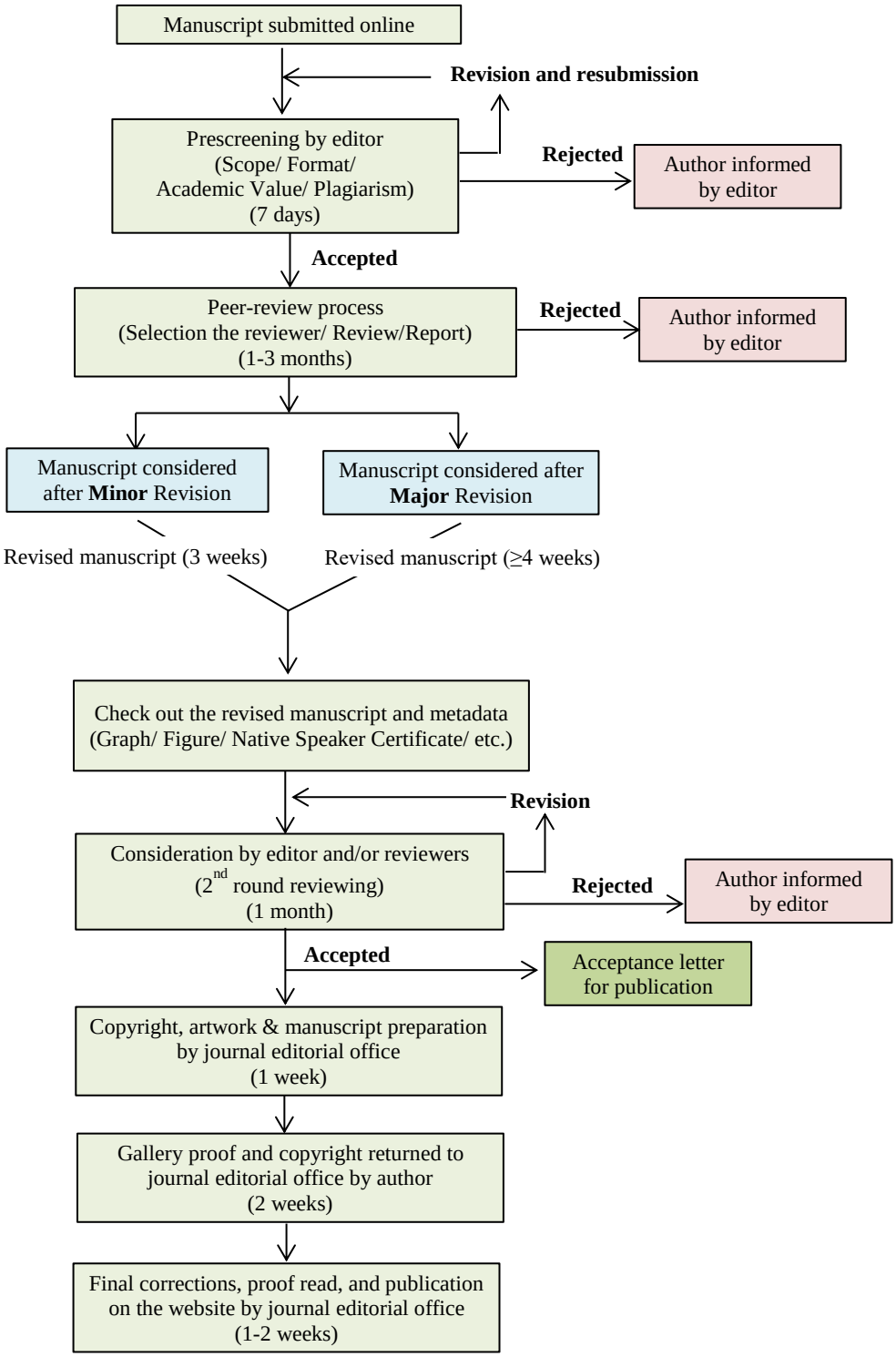

The Environment and Natural Resources Journal (EnNRJ) accepts 2 types of articles for consideration of publication as follows:

- *Original Research Article:* Manuscripts should not exceed 3,500 words (excluding references).
- *Review Article (by invitation):* This type of article focuses on the in-depth critical review of a special aspect in the environment and also provides a synthesis and critical evaluation of the state of the knowledge of the subject. Manuscripts should not exceed 6,000 words (excluding references).

Submission of Manuscript

Cover letter: Key points to include:

- Statement that your paper has not been previously published and is not currently under consideration by another journal
- Brief description of the research you are reporting in your paper, why it is important, and why you think the readers of the journal would be interested in it
- Contact information for you and any co-authors
- Confirmation that you have no competing interests to disclose

Manuscript-full: Manuscript (A4) must be submitted in Microsoft Word Files (.doc or .docx). Please make any identifying information of name(s) of the author(s), affiliation(s) of the author(s). Each affiliation should be indicated with superscripted Arabic numerals immediately after an author's name and before the appropriate address. Specify the Department/School/Faculty, University, Province/State, and Country of each affiliation.

Manuscript-anonymized: Manuscript (A4) must be submitted in Microsoft Word Files (.doc or .docx). Please remove any identifying information, such as authors' names or affiliations, from your manuscript before submission and give all information about authors at title page section.

Reviewers suggestion *(mandatory)*: Please provide the names of 3 potential reviewers with the information about their affiliations and email addresses. *The recommended reviewers should not have any conflict of interest with the authors. Each of the reviewers must come from a different affiliation and must not have the same nationality as the authors.* Please note that the editorial board retains the sole right to decide whether or not the recommended potential reviewers will be selected.

Preparation of Manuscript

Manuscript should be prepared strictly as per guidelines given below. The manuscript (A4 size page) must be submitted in Microsoft Word (.doc or .docx) with Times New Roman 12 point font and a line spacing of 1.5. *The manuscript that is not in the correct format will be returned and the corresponding author may have to resubmit*. The submitted manuscript must have the following parts:

Title should be concise and no longer than necessary. Capitalize first letters of all important words, in Times New Roman 12 point bold.

Author(s) name and affiliation must be given, especially the first and last names of all authors, in Times New Roman 11 point bold.

Affiliation of all author(s) must be given in Times New Roman 11 point italic.

Abstract should indicate the significant findings with data. A good abstract should have only one paragraph and be limited to 250 words. Do not include a table, figure or reference.

Keywords should adequately index the subject matter and up to six keywords are allowed.

Text body normally includes the following sections: 1. Introduction 2. Methodology 3. Results and Discussion 4. Conclusions 5. Acknowledgements 6. References

Reference style must be given in Vancouver style. Please follow the format of the sample references and citations as shown in this Guide below.

Unit: The use of abbreviation must be in accordance with the SI Unit.

Format and Style

Paper Margins must be 2.54 cm on the left and the right. The bottom and the top margin of each page must be 1.9 cm.

Introduction is critically important. It should include precisely the aims of the study. It should be as concise as possible with no sub headings. The significance of problem and the essential background should be given.

Methodology should be sufficiently detailed to enable the experiments to be reproduced. The techniques and methodology adopted should be supported with standard references.

Headings in Methodology section and Results and Discussion section, no more than three levels of headings should be used. Main headings should be typed (in bold letters) and secondary headings (in bold and italic letters). Third level headings should be typed in normal and no bold, for example;

2. Methodology
2.1 Sub-heading
2.1.1 Sub-sub-heading

Results and Discussion can be either combined or separated. This section is simply to present the key points of your findings in figures and tables, and explain additional findings in the text; no interpretation of findings is required. The results section is purely descriptive.
Tables Tables look best if all the cells are not bordered; place horizontal borders only under the legend, the column headings and the bottom.
Figures should be submitted in color; make sure that they are clear and understandable. Please adjust the font size to 9-10, no bold letters needed, and the border width of the graphs must be 0.75 pt. *(Do not directly cut and paste them from MS Excel.)* Regardless of the application used, when your electronic artwork is finalized, please 'save as' or convert the images to TIFF (or JPG) and separately send them to EnNRJ. The images require a resolution of at least 300 dpi (dots per inch). If a label needed in a figure, its font must be "Times New Roman" and its size needs to be adjusted to fit the figure without borderlines.

All Figure(s) and Table(s) should be embedded in the text file.

Conclusions should include the summary of the key findings, and key take-home message. This should not be too long or repetitive, but is worth having so that your argument is not left unfinished. Importantly, don't start any new thoughts in your conclusion.

Acknowledgements should include the names of those who contributed substantially to the work described in the manuscript but do not fulfill the requirements for authorship. It should also include any sponsor or funding agency that supported the work.

References should be cited in the text by the surname of the author(s), and the year. This journal uses the author-date method of citation: the last name of the author and date of publication are inserted in the text in the appropriate place. If there are more than two authors, "et al." after the first author' name must be added. Examples: (Frits, 1976; Pandey and Shukla, 2003; Kungsuwas et al., 1996). If the author's name is part of the sentence, only the date is placed in parentheses: "Frits (1976) argued that . . ."

Please be ensured that every reference cited in the text is also present in the reference list (and vice versa).

In the list of references at the end of the manuscript, full and complete references must be given in the following style and punctuation, arranged alphabetically by first author's surname. Examples of references as listed in the References section are given below.

Book
Tyree MT, Zimmermann MH. Xylem Structure and the Ascent of Sap. Heidelberg, Germany: Springer; 2002.

Chapter in a book
Kungsuwan A, Ittipong B, Chandrkrachang S. Preservative effect of chitosan on fish products. In: Steven WF, Rao MS, Chandrkachang S, editors. Chitin and Chitosan: Environmental and Friendly and Versatile Biomaterials. Bangkok: Asian Institute of Technology; 1996. p. 193-9.

Journal article
Muenmee S, Chiemchaisri W, Chiemchaisri C. Microbial consortium involving biological methane oxidation in relation to the biodegradation of waste plastics in a solid waste disposal open dump site. International Biodeterioration and Biodegradation 2015;102:172-81.

Published in conference proceedings
Wiwattanakantang P, To-im J. Tourist satisfaction on sustainable tourism development, amphawa floating marketSamut songkhram, Thailand. Proceedings of the 1st Environment and Natural Resources International Conference; 2014 Nov 6-7; The Sukosol hotel, Bangkok: Thailand; 2014.

Ph.D./Master thesis

Shrestha MK. Relative Ungulate Abundance in a Fragmented Landscape: Implications for Tiger Conservation [dissertation]. Saint Paul, University of Minnesota; 2004.

Website

Orzel C. Wind and temperature: why doesn't windy equal hot? [Internet]. 2010 [cited 2016 Jun 20]. Available from: http://scienceblogs.com/principles/2010/08/17/wind-and-temperature-why-doesn/.

Report organization:

Intergovernmental Panel on Climate Change (IPCC). IPCC Guidelines for National Greenhouse Gas Inventories: Volume 1-5. Hayama, Japan: Institute for Global Environmental Strategies; 2006.

Remark

** Please be note that manuscripts should usually contain at least 15 references and some of them must be up-to-date research articles.*

** Please strictly check all references cited in text, they should be added in the list of references. Our Journal does not publish papers with incomplete citations.*

Changes to Authorship

This policy of journal concerns the addition, removal, or rearrangement of author names in the authorship of accepted manuscripts:

Before the accepted manuscript

For all submissions, that request of authorship change during review process should be made to the form below and sent to the Editorial Office of EnNRJ. Approval of the change during revision is at the discretion of the Editor-in-Chief. The form that the corresponding author must fill out includes: (a) the reason for the change in author list and (b) written confirmation from all authors who have been added, removed, or reordered need to confirm that they agree to the change by signing the form. Requests form submitted must be consented by corresponding author only.

After the accepted manuscript

The journal does not accept the change request in all of the addition, removal, or rearrangement of author names in the authorship. Only in exceptional circumstances will the Editor consider the addition, deletion or rearrangement of authors after the manuscript has been accepted.

Copyright transfer

The copyright to the published article is transferred to Environment and Natural Resources Journal (EnNRJ) which is organized by Faculty of Environment and Resource Studies, Mahidol University. The accepted article cannot be published until the Journal Editorial Officer has received the appropriate signed copyright transfer.

Online First Articles

The article will be published online after receipt of the corrected proofs. This is the official first publication citable with the Digital Object Identifier (DOI). After release of the printed version, the paper can also be cited by issue and page numbers. DOI may be used to cite and link to electronic documents. The DOI consists of a unique alpha-numeric character string which is assigned to a document by the publisher upon the initial electronic publication. The assigned DOI never changes.

Mahidol University

Wisdom of the Land

Faculty of Environment and Resource Studies, Mahidol University, Thailand
999 Phutthamonthon Sai 4 Rd, Salaya, Phutthamonthon District, Nakhon Pathom 73170
E-mail: ennrjournal@gmail.com